

RECENT ADVANCES in MECHANICS, FLUID MECHANICS, HEAT and MASS TRANSFER

**Proceedings of the 2014 International Conference on Mechanics, Fluid
Mechanics, Heat and Mass Transfer (MFMHMT 2014)**

**Interlaken, Switzerland
February 22-24, 2014**

RECENT ADVANCES in MECHANICS, FLUID MECHANICS, HEAT and MASS TRANSFER

**Proceedings of the 2014 International Conference on Mechanics, Fluid
Mechanics, Heat and Mass Transfer (MFMHMT 2014)**

**Interlaken, Switzerland
February 22-24, 2014**

Copyright © 2014, by the editors

All the copyright of the present book belongs to the editors. All rights reserved. No part of this publication may be reproduced, stored in a retrieval system, or transmitted in any form or by any means, electronic, mechanical, photocopying, recording, or otherwise, without the prior written permission of the editors.

All papers of the present volume were peer reviewed by no less than two independent reviewers. Acceptance was granted when both reviewers' recommendations were positive.

Recent Advances in Mechanical Engineering Series - 9

ISSN: 2227-4596

ISBN: 978-1-61804-220-0

RECENT ADVANCES in MECHANICS, FLUID MECHANICS, HEAT and MASS TRANSFER

**Proceedings of the 2014 International Conference on Mechanics, Fluid
Mechanics, Heat and Mass Transfer (MFMHMT 2014)**

**Interlaken, Switzerland
February 22-24, 2014**

Organizing Committee

General Chairs (EDITORS)

- Professor Myriam Lazard
Institut Supérieur d'Ingenierie de la Conception
27 rue d'Hellieule, 88100 Saint Die
France
- Professor Olga Martin
Applied Sciences Faculty,
Politehnica University of Bucharest,
Romania
- Professor Pradip Majumdar
Department of Mechanical Engineering
Northern Illinois University
DeKalb, Illinois 60115, USA

Senior Program Chair

- Professor Gen Qi Xu
Department of Mathematics,
Tianjin University, Tianjin, China

Program Chairs

- Prof. Karel Frydrysek
Technical University of Ostrava,
Ostrava - Poruba,
Czech Republic
- Professor K. E. Vogiatzis
Civil Engineering Department
University of Thessaly
Greece
- Professor Pavla Bukovska
Department of Metal and Timber Structures,
Brno University of Technology
Czech Republic

Tutorials Chair

- Professor Pradip Majumdar
Department of Mechanical Engineering
Northern Illinois University
DeKalb, Illinois, USA

Special Session Chair

- Professor Olga Martin
Applied Sciences Faculty,
Politehnica University of Bucharest,
Romania

Workshops Chair

- Professor Gen Qi Xu
Department of Mathematics,
Tianjin University, Tianjin, China

Local Organizing Chair

- Professor Jan Awrejcewicz,
Technical University of Lodz,
Lodz, Poland

Publication Chair

- Professor Olga Martin
Applied Sciences Faculty,
Politehnica University of Bucharest,
Romania

Steering Committee

- Professor Aida Bulucea, University of Craiova, Romania (Chair)
- Professor Marcela Karmazínová, University of Technology, Brno, Czech Republic
- Professor Jan Awrejcewicz, Technical University of Lodz, Lodz, Poland
- Dr. Claudio Guarnaccia, Department of Industrial Engineering, University of Salerno, Italy

Program Committee

- Prof. A. C. Benim, Duesseldorf University of Applied Sciences, Duesseldorf, Germany
Prof. Mikhail Itskov, RWTH Aachen University, Germany
Prof. George G. Tsytkin, Russian Academy of Sciences, Russia
Prof. Ahmed Hassan, Assuit University, Assuit, Egypt
Prof. Beghidja Abdelhadi, Noisy le Grand, France
Prof. Bodo Ruck, University of Karlsruhe, Germany
Prof. Bouhadeef Malek, Universite des Sciences et de la Technologie Houari Boumediene, Alger, Algeria
Prof. Khaled Alhussan, King Abdulaziz City for Science and technology, S.Arabia
Prof. Krish Thiagarajan, The University of Western Australia, Australia
Prof. Luis Cortez, Cidade Universitaria Zeferino Vaz, Campinas, Sao Paulo, Brazil
Prof. Mahmoud Jamiolahmady, Heriot-watt University, Edinburgh, UK
Prof. Muthukumaran Packirisamy, Concordia University, Montreal, Quebec, Canada
Prof. Nicolas Galanis, University de Sherbrooke, Canada
Prof. Oh-hyun Rho, Seoul National University, Korea
Prof. Olga Mazhorova, Russia Academy of Science, Moscow, Russia
Prof. Pablo S. Casas, Depto. de Matematica Aplicada I, E.T.S. de Ingenieros Industriales de Barcelona, Spain
Prof. Pascal Roubides, University of Miami, Florida, USA
Prof. Roger Grimshaw, Loughborough University, UK
Prof. Ryszard Tadeusiewicz, AGH University of Science and Technology, Poland
Prof. Serkan Ozgen, Middle East technical University, Ankara, Turkey
Prof. Viorel Stoian, University of Craiova, Romania
Prof. Vitoriano Ruas, University Pierre et Marie Curie (Paris VI), France
Prof. Andrei G. Fedorov, Georgia Institute of Technology, Atlanta, Georgia, USA
Prof. Fotis Sotiropoulos, Georgia Institute of Technology, Atlanta, Georgia, USA
Prof. Shabaan Abdallah, University of Cincinnati, Ohio, USA
Prof. Oleg V. Vasilyev, University of Colorado, CO, USA
Prof. Shoaib Usman, University of Missouri-Rolla, USA
Prof. Bozidar, Liscic, President of IFHTSE, Zagreb, Croatia
Prof. Tatsuo Inoue, Head of the Department at Kyoto University, Kyoto, Japan
Prof. Michiharu Narazaki, Utsunomiya University, Utsunomiya, Tochgi, Japan

Prof. Boris Ushakov, State Metallurgical Univ. in Moscow, Russia
Prof. Pavel Krukovsky, Ukran. Nat. Academy of Sciences, Kiev, Ukraine
Prof. Gareth Thomas, University of California, Berkeley, CA, USA
Prof. Tamas Reti, Tech.Univ.of Budapest, Dept. Materials & Techn., Hungary
Prof. Claudia del Carmen Gutierrez-Torres, National Polytechnic Institute, Mexico
Prof. Hyung Hee Cho, Yonsei University, Seoul, Korea
Prof. K. P. Sandeep, North Carolina State University, USA
Prof. Jing Liu, Tech.Inst. of Physics & Chemistry, Chin Acad. of Sci, Beijing, China
Prof. Aly Elshamy, Menoufia University, Egypt
Prof. Rafael Royo, Universidad Politecnica de Valencia, Spain
Prof. Slawomir Smolen, Hochschule Bremen University, Germany
Prof. Junjie Gu, Dept. of Mech.& Aersp.Eng, Carleton Univ., Ottawa, Canada
Prof. C. J. Ho, Dept. of Mech.I Engin., Cheng Kung University, Tainan, Taiwan
Prof. Pradip Majumdar, Northern Illinois University, USA
Prof. Ivan Kazachkov, Royal Institute of Technology, Stockholm, Sweden
Prof. Jeong-se Suh Gyeongsang, National University, Korea
Prof. Abul-Fazal Arif, King Fahd Univ.of Petroleum &Minerals, Dhahran, S. Arabia
Prof. Yizhen Huang, Shanghai Jiaotong University, China
Prof. Asad Salem, Cleveland State University, USA
Prof. Suman Chakraborty, Indian Insitute of Technology, Kharagpur India
Prof. Ahmed Mohammadein ,Aswan Faculty of Science, Egypt
Prof. Joakim Wren, Linkoping University, Sweden
Prof. Agis Papadopoulos, Aristotle University Thessaloniki, Greece
Prof. Hany Mohamed, Assiut University, Egypt
Prof. Chin-Hsiang Cheng, Dep.Aeron&Astronautics, N. Cheng Kung Univ. Taiwan
Prof. Aydin Misirlioglu, Istanbul Technical University, Turkey
Prof. Valeri Bubnovich, Universidad de Santiago, Chile
Prof. Dragoljub Mirjanic, University of Banja Luka, Bosnia and Herzegovina
Prof. Hossein Shokouhmand, University of Tehran, Iran
Prof. Ramil Sharafutdinov, Bashkir State University, Bashkortostan Russia
Prof. Gunter K.F., Barwolff Inst. of Mathematics, Berlin, Germany
Prof. Kadir Bilen, Ataturk Univ, Dept of Mechanical Engineering, Erzurum,Turkey
Prof. Federico Mendez, Universidad Nacional Autonoma de Mexico, Mexico
Prof. Yinping Zhang, Tsinghua University, P.R. China
Prof. C.W. Leung, The Hong Kong Polytechnic University, Hong Kong
Prof. M. Abu-Zaid, Faculty of Eng., Mutah Univ., Jordan
Prof. Somchai Wongwises, King Mongkut's Univ. of Techn., Thonburi, Thailand
Prof. Chun-I Chen, I-Shou University, Taiwan
Prof. Mohd Al-Nimr, Jordan University of Science and Technology, Jordan
Prof. Mehmet C. Ece, Trakya Universitesi, Edirne, Turkey
Prof. Ali J. Chamkha, Public Authority for Applied Education & Training, Kuwait
Prof. C. Treviño, Facultad de Ciencias, UNAM, Mexico
Prof. Aroudam El hassan, Dept. of Physics, Tetouan, MAarocco
Prof. P.V.S.N Murthy,Dept Maths, Indian Inst.ofTechn. Kharagpur, W. Bengal, India
Prof. H.S. Takhar, Manchester Metropolitan University, UK
Prof. Federico Mendez, Universidad Nacional Autonoma de Mexico, Mexico
Prof. Nickolay Smirnov, Moscow M.V. Lomonosov State University, Russia

Additional Reviewers

Matthias Buyle	Artesis Hogeschool Antwerpen, Belgium
Lesley Farmer	California State University Long Beach, CA, USA
Deolinda Rasteiro	Coimbra Institute of Engineering, Portugal
Sorinel Oprisan	College of Charleston, CA, USA
Santoso Wibowo	CQ University, Australia
Yamagishi Hiromitsu	Ehime University, Japan
Kei Eguchi	Fukuoka Institute of Technology, Japan
Shinji Osada	Gifu University School of Medicine, Japan
Tetsuya Yoshida	Hokkaido University, Japan
Xiang Bai	Huazhong University of Science and Technology, China
Philippe Dondon	Institut polytechnique de Bordeaux, France
José Carlos Metrôlho	Instituto Politecnico de Castelo Branco, Portugal
João Bastos	Instituto Superior de Engenharia do Porto, Portugal
Takuya Yamano	Kanagawa University, Japan
Hessam Ghasemnejad	Kingston University London, UK
Konstantin Volkov	Kingston University London, UK
Eleazar Jimenez Serrano	Kyushu University, Japan
Jon Burley	Michigan State University, MI, USA
Manoj K. Jha	Morgan State University in Baltimore, USA
Frederic Kuznik	National Institute of Applied Sciences, Lyon, France
Stavros Ponis	National Technical University of Athens, Greece
Ole Christian Boe	Norwegian Military Academy, Norway
Imre Rudas	Obuda University, Budapest, Hungary
Masaji Tanaka	Okayama University of Science, Japan
Francesco Rotondo	Polytechnic of Bari University, Italy
George Barreto	Pontificia Universidad Javeriana, Colombia
Dmitrijs Serdjuks	Riga Technical University, Latvia
Andrey Dmitriev	Russian Academy of Sciences, Russia
Tetsuya Shimamura	Saitama University, Japan
Francesco Zirilli	Sapienza Universita di Roma, Italy
Minhui Yan	Shanghai Maritime University, China
Valeri Mladenov	Technical University of Sofia, Bulgaria
Jose Flores	The University of South Dakota, SD, USA
James Vance	The University of Virginia's College at Wise, VA, USA
Genqi Xu	Tianjin University, China
Zhong-Jie Han	Tianjin University, China
Kazuhiko Natori	Toho University, Japan
Moran Wang	Tsinghua University, China
M. Javed Khan	Tuskegee University, AL, USA
Bazil Taha Ahmed	Universidad Autonoma de Madrid, Spain
Alejandro Fuentes-Penna	Universidad Autónoma del Estado de Hidalgo, Mexico
Miguel Carriegos	Universidad de Leon, Spain
Angel F. Tenorio	Universidad Pablo de Olavide, Spain
Abelha Antonio	Universidade do Minho, Portugal

Table of Contents

Plenary Lecture 1: Discrete Lyapunov Controllers for an Actuator in Camless Engines <i>Paolo Mercorelli</i>	12
Plenary Lecture 2: EMG-Analysis for Intelligent Robotic based Rehabilitation <i>Thomas Schrader</i>	13
Plenary Lecture 3: Atmospheric Boundary Layer Effects on Aerodynamics of NREL Phase VI Windturbine in Parked Condition <i>Mohammad Moshfeghi</i>	14
Plenary Lecture 4: Laminar and Turbulent Simulations of Several TVD Schemes in Two-Dimensions <i>Edisson S. G. Maciel</i>	15
Plenary Lecture 5: The Flocking Based and GPU Accelerated Internet Traffic Classification <i>Zhiguang Xu</i>	17
Plenary Lecture 6: The State of Civil Political Culture among Youth: Goals and Results of Education <i>Irina Dolinina</i>	18
On a Scale Invariant Model of Statistical Mechanics and Derivation of Invariant forms of Conservation Equations from Invariant Boltzmann and Enskog Equations <i>Siavash H. Sohrab</i>	19
Analytical Solutions of Axysimmetric Problems of Compression (Expansion) of Thick-Walled Spherical and Cylindrical Shells Made of Incompressible Viscoplastic Material under Action of External Dynamic Loading <i>Alexey B. Kiselev</i>	38
Tracer Diffusion through Fiber Networks <i>K. Kang, J. K. G. Dhont</i>	42
Laminar Natural Convection in a Two-Dimensional Vertical Conical Partially Annular Space <i>B. Ould Said, N. Retiel, M. Aichouni</i>	49
Mathematical Modeling of Leather Fatliquoring <i>H. Charvátová, D. Janáčová, K. Kolomazník, V. Vašek, R. Drga, P. Mokrejš</i>	55
Experimental Investigation of Nozzle Shape Effect on Wall Shear Stress beneath Impinging Round Jet <i>B. Montagné, K. Sodjavi, P. Bragança, A. Meslem, M. Kristiawan</i>	60

Efficiency Evaluation of VHC: A CFD Comparison Study at Constant Flow	68
<i>Ricardo F. Oliveira, Senhorinha F. Teixeira, Helena C. Marques, José C. Teixeira</i>	
An Investigation on Development of Cooling Dual Discharge Fan Module	75
<i>Joo-Han Kim, Jung-Moo Seo, In Soung Jung</i>	
Laminar and Turbulent Simulations of Several TVD Schemes in Two Dimensions – Part I - Results II	79
<i>Edisson S. G. Maciel</i>	
Thermodynamic Performances of the Turbojet Combustion Chambers – Numerical Evaluation	86
<i>Constantin Rotaru, Mihai Mihaila-Andres, Pericle Gabriel Matei, Raluca Ioana Edu</i>	
Strength Verification of the Planetary Gear System	92
<i>Jae-Hwan Shim, Sung Gil Han, Yoo In Shin, Chan Heon Yoon, Jeong Se Suh, Chul Ki Song</i>	
Instability and Interaction of the Tourbillonner Macrostructure with the Boundary Layer in a Cavity Differentially Heated	97
<i>Taloub Djedid, Beghidja Abdelhadi</i>	
On Spectral Relaxation Method for an MHD Flow and Heat Transfer of a Maxwell Fluid	102
<i>Stanford Shateyi</i>	
Specific Heat and Volumetric Heat Capacity of Some Saudian Soils as Affected by Moisture and Density	107
<i>Nidal H. Abu-Hamdeh</i>	
Effect of Stent Porosity on Hemodynamics within Cerebral Aneurysm Models: Numerical Study	112
<i>Dai Thanh Phan, Minh Tuan Nguyen, Sang-Wook Lee</i>	
Investigation of Turbulence Characteristics of Burning Process of the Solid Fuel in BKZ 420 Combustion Chamber	116
<i>Askarova A. S., Bekmukhamet A., Bolegenova S. A., Beketaeva M. T., Maximov Yu. V., Ospanova Sh.</i>	
Atmospheric Boundary Layer Effects on Aerodynamics of NREL Phase VI Wind Turbine in Parked Condition	121
<i>Mohammad Moshfeghi, Nahmkeon Hur</i>	
Dynamics of Shock Oscillation across Second Throat of a Supersonic Diffuser under Geometry Variation	127
<i>Jintu K. James, Muruganandam T. M.</i>	

A Study of the Pressure and Potential Distribution by Two Model From Micro Fluidic Devices	132
<i>Maryam Ghelichkhani</i>	
Optimum Seismic Isolation System Design for Retrofitting and Upgrading Existing Concrete Bridges	135
<i>Mohammad Al Hamaydeh, Nader Aly</i>	
A Study of Pressure Distribution Droplets Motion in Convergence-Divergence Shape Microchannel	140
<i>Maryam Ghelichkhani</i>	
Design of Heat Exchanger	144
<i>Ahmed Lajili Ali, Abdulmunam Shaban</i>	
Authors Index	148

Plenary Lecture 1

Discrete Lyapunov Controllers for an Actuator in Camless Engines



Professor Paolo Mercorelli
Leuphana University of Lueneburg
Germany
E-mail: mercorelli@uni.leuphana.de

Abstract: This paper deals with a hybrid actuator composed by a piezo and a hydraulic part controlled using two cascade Lyapunov controllers for camless engine motor applications. The idea is to use the advantages of both, the high precision of the piezo and the force of the hydraulic part. In fact, piezoelectric actuators (PEAs) are commonly used for precision positionings, despite PEAs present nonlinearities, such as hysteresis, saturations, and creep. In the control problem such nonlinearities must be taken into account. In this paper the Preisach dynamic model with the above mentioned nonlinearities is considered together with cascade controllers which are Lyapunov based. The sampled control laws are derived using the well known Backward Euler method. An analysis of the Backward and Forward Euler method is also presented. In particular, the hysteresis effect is considered and a model with a switching function is used also for the controller design. Simulations with real data are shown.

Brief Biography of the Speaker: Paolo Mercorelli received the (Laurea) M.S. degree in Electronic Engineering from the University of Florence, Florence, Italy, in 1992, and the Ph.D. degree in Systems Engineering from the University of Bologna, Bologna, Italy, in 1998. In 1997, he was a Visiting Researcher for one year in the Department of Mechanical and Environmental Engineering, University of California, Santa Barbara, USA. From 1998 to 2001, he was a Postdoctoral Researcher with Asea Brown Boveri, Heidelberg, Germany. From 2002 to 2005, he was a Senior Researcher with the Institute of Automation and Informatics, Wernigerode, Germany, where he was the Leader of the Control Group. From 2005 to 2011, he was an Associate Professor of Process Informatics with Ostfalia University of Applied Sciences, Wolfsburg, Germany. In 2010 he received the call from the German University in Cairo (Egypt) for a Full Professorship (Chair) in Mechatronics which he declined. In 2011 he was a Visiting Professor at Villanova University, Philadelphia, USA. Since 2012 he has been a Full Professor (Chair) of Control and Drive Systems at the Institute of Product and Process Innovation, Leuphana University of Lueneburg, Lueneburg, Germany.

Research interests: His current research interests include mechatronics, automatic control, signal processing, wavelets; sensorless control; Kalman filter, camless control, knock control, lambda control, robotics.

The full paper of this lecture can be found on page 19 of the Proceedings of the 2014 International Conference on Circuits, Systems and Control, as well as in the CD-ROM proceedings.

Plenary Lecture 2

EMG-Analysis for Intelligent Robotic based Rehabilitation

Professor Thomas Schrader

University of Applied Sciences Brandenburg
Germany

E-mail: thomas.schrader@computer.org

Abstract: The establishment of wireless sensor network (WSN) technology in physiotherapy and rehabilitation is a clue for improvement of the therapeutic process, quality assessment and development of supporting technologies such as robotics. Especially for complex therapeutic interventions such as sensorimotor training, a continuous monitoring during the therapy as well as for all sessions would be quite useful. For the usage of robotic support in rehabilitation various input information about the status of patient and his/her activity status of various muscles have to be detected and evaluated. The critical point for robotic intervention is the response time. Under physiotherapeutic and rehabilitation conditions, the robotic device should be able to react differently and in various patterns. A complex analysis procedure of input signals such as EMG is essential to ensure an effective response of the robot. However sensor nodes in a wireless (body) area network have limited resources for calculating and storage processes. A stepwise procedure with distributed analysis tasks is proposed. Electromyogram (EMG) measurements of eight muscles were collected and evaluated in an experimental setting of a sensorimotor training using different types of balance boards. Fast and easy methods for detection of activity and rest states based on time domain analysis using low pass IIR filter und dynamic threshold adaption. These procedures can be done on the sensor nodes themselves or special calculation nodes in the network. More advanced methods in frequency domain or analysis of dynamical system behavior request much more system power in calculation as well as storage. These tasks could be done on the level of mobile devices such as mobile phones or tablet computer. A broad range of resources can be provided by cloud/internet. Such level based organization of analysis and system control can be compared with biological systems such as human nervous system.

Plenary Lecture 3

Atmospheric Boundary Layer Effects on Aerodynamics of NREL Phase VI Windturbine in Parked Condition



Professor Mohammad Moshfeghi
Sogang University, South Korea
E-mail: mmoshfeghi@sogang.ac.kr

Abstract: In a natural condition, the wind is affected by the groundcover and the type of terrains which impose vertical velocity profile to the wind. This wind profile, which is also called atmospheric boundary layer (ABL), dramatically influences the aerodynamic behaviors and loadings of horizontal axis wind turbines. However, for the sake of simplicity, many numerical simulations only deal with the uniform wind speed. To consider the effects of the ABL, numerical simulations of the two-bladed NREL Phase VI wind turbines aerodynamic at the parked condition are conducted under both uniform and ABL. The Deaves-Harris (DH) model is applied to the ABL. The wind turbine blades are kept at the six o'clock position and are considered at two different pitch angles. The aerodynamic forces and moments of the uniform and the DH model are compared. The results show that the pitch angle at which the HAWT is parked plays an important role on the blade loading. Also it is observed that for the fully separated conditions, the Down-blade and the blade in the uniform wind are under approximately similar aerodynamic loadings, while the Up-blade encounters more aerodynamic loads, which is even noticeable value for this small wind turbine. This in turn means that for an appropriate and exact design, effects of ABL should be considered with more care.

Brief Biography of the Speaker: Dr. Mohammad Moshfeghi works in Multi-phenomena CFD Engineering Research Center (ERC) Sogang University, Seoul, South Korea. He is also Lecturer in Qazvin Azad University. He has a registered patent: "Split-Blade For Horizontal Axis Wind Turbines" (Inventors: Mohammad Moshfeghi, Nahmkeon Hur).

Plenary Lecture 4

Laminar and Turbulent Simulations of Several TVD Schemes in Two-Dimensions



Professor Edison S. G. Maciel

Federal University of Great Dourados, Brazil

E-mail: edisavio@edissonsavio.eng.br

Abstract: This work, first part of this study, describes five numerical tools to perform perfect gas simulations of the laminar and turbulent viscous flow in two-dimensions. The Van Leer, Harten, Frink, Parikh and Pirzadeh, Liou and Steffen Jr. and Radespiel and Kroll schemes, in their first- and second-order versions, are implemented to accomplish the numerical simulations. The Navier-Stokes equations, on a finite volume context and employing structured spatial discretization, are applied to solve the supersonic flow along a ramp in two-dimensions. Three turbulence models are applied to close the system, namely: Cebeci and Smith, Baldwin and Lomax and Spalart and Allmaras. On the one hand, the second-order version of the Van Leer, Frink, Parikh and Pirzadeh, Liou and Steffen Jr., and Radespiel and Kroll schemes is obtained from a “MUSCL” extrapolation procedure, whereas on the other hand, the second order version of the Harten scheme is obtained from the modified flux function approach. The convergence process is accelerated to the steady state condition through a spatially variable time step procedure, which has proved effective gains in terms of computational acceleration (see Maciel). The results have shown that, with the exception of the Harten scheme, all other schemes have yielded the best result in terms of the prediction of the shock angle at the ramp. Moreover, the wall pressure distribution is also better predicted by the Van Leer scheme. This work treats the laminar first- and second-order and the Cebeci and Smith second- order results obtained by the five schemes.

Brief Biography of the Speaker: Professor Edison Sávio de Góes Maciel was born in Recife, Pernambuco, Brazil in 1969, February, 25. He studied in Pernambuco until obtains his Master degree in Thermal Engineering, in 1996, August. With the desire of study aerospace and aeronautical problems using numerical methods as tools, he obtains his Doctor degree in Aeronautical Engineering, in 2002, December, in ITA and his Post-Doctor degree in Aerospace Engineering, in 2009, July, also in ITA. He is currently Professor at UFGD (Federal University of Great Dourados) – Mato Grosso do Sul – Brasil. He is author in 47 papers in international journals, 2 books, 67 papers in international conference proceedings. His research interestes includes a) Applications of the Euler equations to solve inviscid perfect gas 2D and 3D flows (Structured and unstructured discretizations) b) Applications of the Navier-Stokes equations to solve viscous perfect gas 2D and 3D flows (Structured and unstructured discretizations) c) Applications of the Euler and Navier-Stokes to solve magneto gas dynamics flows 2D and 3D; (Structured and unstructured discretizations) d) Applications of algebraic, one-equation, and two-equations turbulence models to predict turbulent effects in viscous 2D flows (Structured and unstructured discretizations), e) Study of artificial dissipation models to centered schemes

in 2D and 3D spaces (Structured and unstructures discretizations) f)Applications of the Euler and Navier-Stokes equations to solve reentry flows in the Earth atmosphere and entry flows in Mars atmosphere in 2D and 3D (Structured and unstructured discretizations).

The full paper of this lecture can be found on page 79 of the present volume, as well as in the CD-ROM proceedings.

Plenary Lecture 5

The Flocking Based and GPU Accelerated Internet Traffic Classification



Professor Zhiguang Xu
Valdosta State University
USA
E-mail: zxu@valdosta.edu

Abstract: Mainstream attentions have been brought to the issue of Internet traffic classification due to its political, economic, and legal impacts on appropriate use, pricing, and management of the Internet. Nowadays, both the research and operational communities prefer to classify network traffic through approaches that are based on the statistics of traffic flow features due to their high accuracy and improved robustness. However, these approaches are faced with two main challenges: identify key flow features that capture fundamental characteristics of different types of traffic in an unsupervised way; and complete the task of traffic classification with acceptable time and space costs. In this paper, we address these challenges using a biologically inspired computational model that imitates the flocking behavior of social animals (e.g. birds) and implement it in the form of parallel programs on the Graphics Processing Unit (GPU) based platform of CUDA from NVIDIA™. The experimental results demonstrate that our flocking model accelerated by GPU can not only effectively select and prioritize key flow features to classify both well-known and unseen network traffic into different categories, but also get the job done significantly faster than its traditional CPU-based counterparts due to the high magnitude of parallelism that it exhibits.

Brief Biography of the Speaker: Prof. Zhiguang Xu received his Ph.D. in Computer Science from University of Central Florida, FL, USA in 2001. He is currently Professor of Computer Science in the Department of Math and Computer Science at Valdosta State University, GA, USA. His research and teaching interests include Computer Networking, Artificial Intelligence, Parallel and Distributed Computing, and Computer Science Education. Professor Xu is author or co-author of more than 25 published papers in refereed journals or conference proceedings. He has been awarded many grants from both academic and industrial entities. He is actively serving as committee member, reviewer, or lecturer of many national and international conferences and organizations.

The full paper of this lecture can be found on page 88 of the Proceedings of the 2014 International Conference on Mathematical Methods, Mathematical Models and Simulation in Science and Engineering, as well as in the CD-ROM proceedings.

Plenary Lecture 6

The State of Civil Political Culture among Youth: Goals and Results of Education



Professor Irina Dolinina

Perm National Research University, Russia

E-mail: irina_edu@mail.ru

Abstract: Political culture is viewed as a phenomenon of social reality. Attitudes toward it (its meaning or significance) are historically conditioned. This research studies enduring presuppositions about (dispositions toward) society and the state, and how these are reflected in conscious stereotypes and cognitive structures among young people within the sociocultural mechanisms that form and modify the basic characteristics of political culture.

Brief Biography of the Speaker: Prof. Irina Dolinina was born in 1960, in Perm, Russia. She is Team Leader in the Research Project «Formation of the political culture of the students», and Professor of Philosophy and Law of the Faculty of Humanities, Perm National Research Technical University since 2012. She has received a lot of honors and awards (2012 - Diploma of the All-Russian Roswitha fund national education and the Education Committee of the State Duma of the Federal Assembly of the Russian Federation. 2013 - Diploma of the All-Russian Roswitha fund national education and the Education Committee of the State Duma of the Federal Assembly of the Russian Federation. Diploma-Russian contest "Best Science Book in the humanitarian sphere - 2013). Prof. Dolinina has various professional organizations and activities.

(Expert on the legislative activities of the Council of Federation of Russia. Board member of the Interregional Association "For civic education." Director of the Research Centre of the political culture).

The full paper of this lecture can be found on page 57 of the Proceedings of the 2014 International Conference on Educational Technologies and Education, as well as in the CD-ROM proceedings.

On a Scale Invariant Model of Statistical Mechanics and Derivation of Invariant forms of Conservation Equations from Invariant Boltzmann and Enskog Equations

Siavash H. Sohrab

Abstract—A scale-invariant model of statistical mechanics is described and applied to introduce the invariant *Boltzmann* equation and the corresponding invariant *Enskog* equation of change. The invariant modified as well as classical forms of mass, thermal energy, linear momentum, and angular momentum conservation equations are derived. Also, an invariant definition of reaction rate $\mathfrak{R}_{\beta+1} = \sum_{\beta} \mathfrak{R}_{\beta}$

for any scale within the hierarchy of statistical fields is introduced. Following *Cauchy*, the total stress tensor for fluids $\mathbf{P}_{ij\beta} = p_{i\beta} \delta_{ij\beta} - (\mu_{i\beta} / 3) \nabla \cdot \mathbf{v}_{i\beta} \delta_{ij\beta}$ is introduced that is consistent with the fact that by definition fluids can only support compressive normal forces. Finally, the solution of the modified *Helmholtz* vorticity equation for the problem of flow within a droplet located at the stagnation point of opposed cylindrically-symmetric gaseous finite jets is presented.

Keywords—Invariant forms of conservation equations. Invariant *Boltzmann* and *Enskog* equations. TOE.

I. INTRODUCTION

IT is well known that the methods of statistical mechanics can be applied to describe physical phenomena over a broad range of scales of space and time from the exceedingly large scale of cosmology to the minute scale of quantum optics as schematically shown in Fig. 1. Although the universality of statistical nature of problems of stochastic quantum fields [1-17] and classical hydrodynamic fields [18-33] is well known, the extent to which exact correspondence exists between the laws of nature amongst the diverse scales of space-time from cosmic to photonic is as yet not recognized. Similarities between the statistical fields shown in Fig. 1 resulted in recent introduction of a scale-invariant model of statistical mechanics [34] and its application to the fields of thermodynamics [35], fluid mechanics [36], statistical mechanics [37] and quantum mechanics [38, 39].

This work was supported in part by NASA grant no. NAG3-1863.

S. H. Sohrab is with the Department of Mechanical Engineering, Northwestern University, Evanston, IL 60208 USA. (phone: 847-491-3572; fax: 847-491-3915; e-mail: s-sohrab@northwestern.edu).

In the present study, following the classical methods [18-22, 40-44] an invariant model of statistical mechanics is applied to introduce invariant *Boltzmann* equation and the corresponding invariant *Enskog* equation of change. From the equation of change invariant forms of mass, energy, linear momentum, and angular momentum conservation equations are derived. A modified form of the continuity equation is presented that in the absence of convection reduces to diffusion equation thus revealing the internal structure of normal shock wave in pure system. Also, a modified form of equation of motion is introduced with convective velocity distinguished from local velocity similar to *Carrier* equation [45]. Finally, a modified form of *Helmholtz* vorticity equation is introduced and its solution for the problem of laminar flow in a liquid droplet located at the stagnation point of gaseous counter flow finite jets is presented. By application of integral methods invariant classical forms of conservation equations are derived and connected to the modified forms in the last Section.

II. PROCEDURE FOR PAPER SUBMISSION

The scale-invariant model of statistical mechanics for equilibrium galactic-, planetary-, hydro-system-, fluid-element-, eddy-, cluster-, molecular-, atomic-, subatomic-, kromo-, and tachyon-dynamics corresponding to the scale $\beta = g, p, h, f, e, c, m, a, s, k,$ and t is schematically shown in Fig. 1 [31]. The statistical fields of equilibrium eddy-, cluster, and molecular-dynamics (EED, ECD, EMD) are shown in Fig. 2 in more details along with the corresponding non-equilibrium laminar fields (LED, LCD, LMD). Each statistical field is identified as the "system" and is composed of an ensemble of "elements" that is described by a distribution function $f_{i\beta}(\mathbf{x}_{i\beta}, \mathbf{u}_{i\beta}, t_{\beta}) d\mathbf{x}_{i\beta} d\mathbf{u}_{i\beta}$. Each element is composed of an ensemble of small particles called the "atoms" of the field that are viewed as *point-mass*. The most probable element (system) velocity of the smaller scale (j) becomes the velocity of the atom (element) of the larger scale ($j+1$) [38].

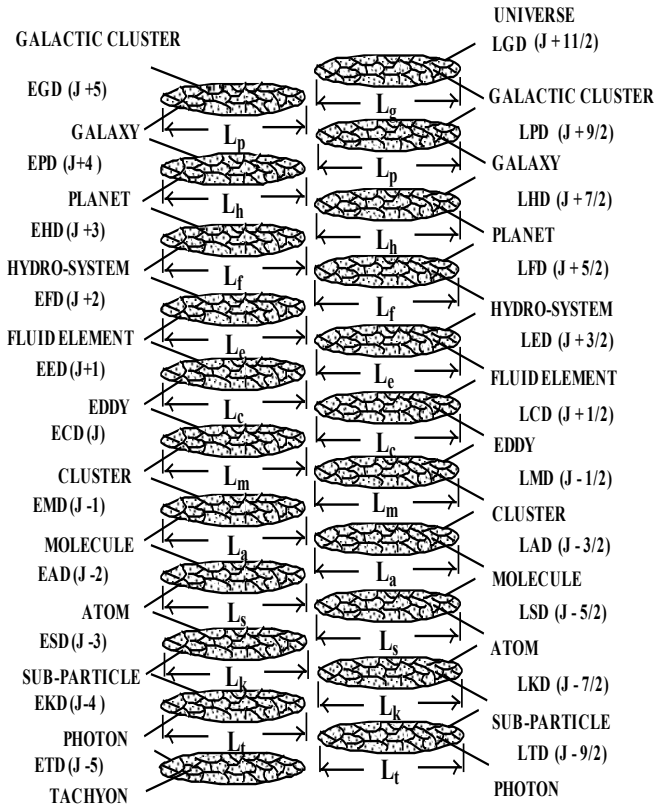


Fig. 1 A scale-invariant view of statistical mechanics from cosmic to tachyon scales.

Following the classical methods [18-22, 40-44] the invariant definition of density ρ_β , and velocity of *atom* $\mathbf{u}_{i\beta}$, *element* $\mathbf{v}_{i\beta}$, and *system* \mathbf{w}_β at the scale β are [38, 39]

$$\rho_{i\beta} = n_{i\beta} m_{i\beta} = m_{i\beta} \int f_{i\beta} d\mathbf{u}_{i\beta}, \quad \mathbf{u}_{i\beta} = \mathbf{v}_{i\beta-1} \quad (1)$$

$$\mathbf{v}_{i\beta} = \rho_{i\beta}^{-1} m_{i\beta} \int \mathbf{u}_{i\beta} f_{i\beta} d\mathbf{u}_{i\beta}, \quad \mathbf{w}_\beta = \mathbf{v}_{m\beta+1} \quad (2)$$

Similarly, the invariant definition of the peculiar and diffusion velocities are introduced as

$$\mathbf{V}'_{i\beta} = \mathbf{u}_{i\beta} - \mathbf{v}_{i\beta}, \quad \mathbf{V}_{i\beta} = \mathbf{v}_{i\beta} - \mathbf{w}_\beta \quad (3)$$

such that

$$\mathbf{V}_{i\beta} = \mathbf{V}'_{i\beta+1} \quad (4)$$

As shown in Fig. 2, the statistical field of ECD at an intermediate scale separates LED from LMD fields. The evidence for the existence of the statistical field of ECD is the phenomena of Brownian motions as discussed in an earlier study [39].

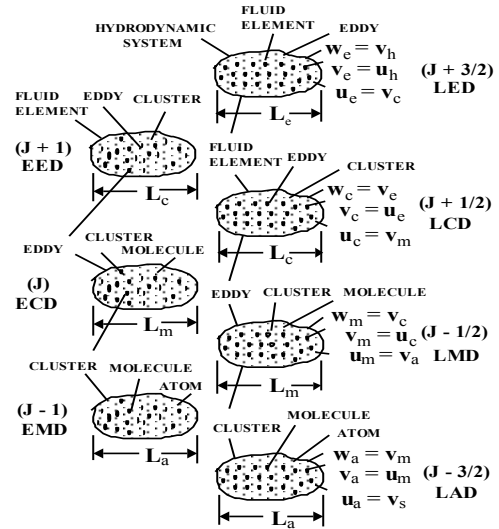


Fig. 2 Hierarchy of statistical fields for equilibrium eddy-, cluster-, and molecular-dynamic scales and the associated laminar flow fields.

For the statistical fields of EED, ECD and EMD, typical characteristic atom, element, and system lengths are

$$\text{EED} \quad (\ell_e, \lambda_e, L_e) = (10^{-5}, 10^{-3}, 10^{-1}) \text{ m} \quad (5a)$$

$$\text{ECD} \quad (\ell_c, \lambda_c, L_c) = (10^{-7}, 10^{-5}, 10^{-3}) \text{ m} \quad (5b)$$

$$\text{EMD} \quad (\ell_m, \lambda_m, L_m) = (10^{-9}, 10^{-7}, 10^{-5}) \text{ m} \quad (5c)$$

The relative system sizes of these statistical fields are schematically shown in Fig. 3.

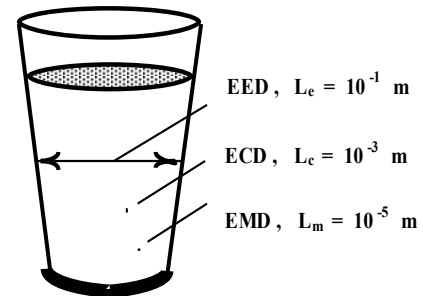


Fig. 3 The system sizes L_β of statistical fields EED, ECD, and EMD relative to a cup of water.

If one applies the same (atom, element, system) = $(\ell_\beta, \lambda_\beta, L_\beta)$ relative sizes in (5) to the entire spatial scale of Fig. 1 and considers the relation between scales as $\ell_\beta = \lambda_{\beta-1} = L_{\beta-2}$ then the resulting cascades or hierarchy of overlapping statistical fields will appear as schematically shown in Fig. 4.

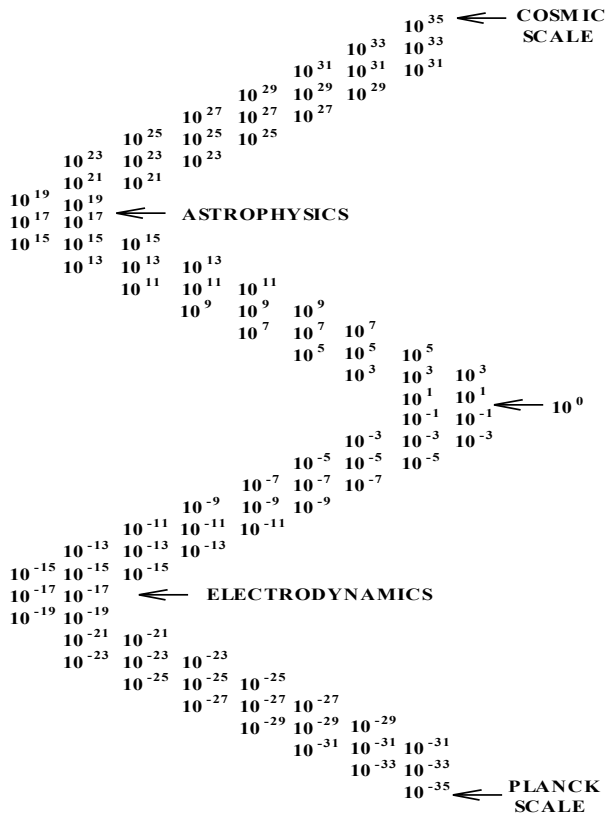


Fig. 4 Hierarchy of statistical fields with $(\ell_\beta, \lambda_\beta, L_\beta)$ from cosmic to Planck scales [38].

According to Fig. 4, starting from the hydrodynamic scale ($10^3, 10^1, 10^{-1}, 10^{-3}$) after seven generations of statistical fields one reaches the electro-dynamic scale with the element size 10^{-17} and exactly after seven more generations one reaches *Planck* length scale $(\hbar G / c^3)^{1/2} \approx 10^{-35}$ m, where $\hbar = h / 2\pi$, h is *Planck* constant and G is the gravitational constant. Similarly, seven generations of statistical fields separate the hydrodynamic scale ($10^3, 10^1, 10^{-1}, 10^{-3}$) from the scale of planetary dynamics (astrophysics) 10^{17} and the latter from galactic-dynamics (cosmology) 10^{35} m. There are no physical or mathematical reasons for the hierarchy shown in Fig. 4 not to continue to larger and smaller scales ad infinitum. Hence, according to Fig. 4 contrary to the often quoted statement by *Einstein* that God does not play dice; the Almighty appears to be playing with infinite hierarchies of embedded dice.

The left hand side of Figs. 1 and 2 correspond to equilibrium statistical fields when the velocities of elements of the field are random since at thermodynamic equilibrium particles i.e. oscillators of such statistical fields will have normal or *Gaussian* velocity distribution. For example, for stationary homogeneous isotropic turbulence at EED scale, the experimental data of *Townsend* [46] confirms the *Gaussian* velocity distribution of eddies as shown in Fig. 5.

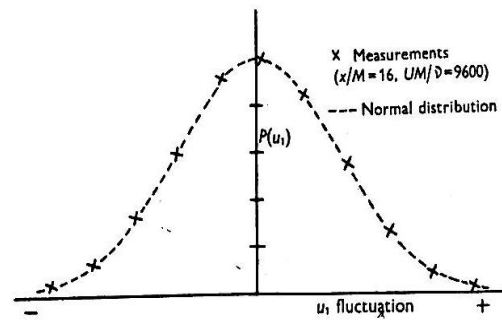


Fig. 5 Measured velocity distribution in isotropic turbulent flow by Townsend [46].

The invariant model of statistical mechanics (1)-(4) suggests that all statistical fields shown in Fig. 1 are turbulent fields [37, 38]. First, let us start with the field of laminar molecular dynamics LMD when molecules, clusters of molecules (cluster), and cluster of clusters of molecules (eddy) form the “atom”, the “element”, and the “system” with the velocities $(\mathbf{u}_m, \mathbf{v}_m, \mathbf{w}_m)$. Similarly, from (1)-(2) the fields of laminar cluster-dynamics LCD and eddy-dynamics LED will have the velocities

$$\text{LED} \quad (\mathbf{u}_e, \mathbf{v}_e, \mathbf{w}_e) \quad (6a)$$

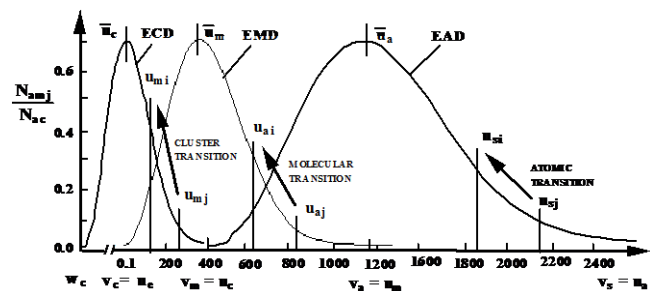
$$\text{LCD} \quad (\mathbf{u}_c, \mathbf{v}_c, \mathbf{w}_c) \quad (6b)$$

$$\text{LMD} \quad (\mathbf{u}_m, \mathbf{v}_m, \mathbf{w}_m) \quad (6c)$$

With *Gaussian* velocity distribution as in Fig. 5, the same chain of reasoning as employed in the classical kinetic theory of *Maxwell* and *Boltzmann* [18-20] requires that the distribution of the speeds of oscillators (eddy) in stationary isotropic turbulence be given by the invariant *Maxwell-Boltzmann* distribution function [38-39]

$$\frac{dN_{u\beta}}{N} = 4\pi \left(\frac{m_\beta}{2\pi kT_\beta}\right)^{3/2} u_\beta^2 e^{-m_\beta u_\beta^2 / 2kT_\beta} du_\beta \quad (7)$$

By (7), one arrives at a hierarchy of embedded *Maxwell-Boltzmann* distribution functions for ECD, EMD, and EAD scales shown in Fig. 6.



According to (1)-(2) and as shown in Fig. 6, the “atomic” velocity of ECD field will be the most probable speed of the adjacent lower scale of EMD $\mathbf{u}_c = \mathbf{v}_{m,mp}$. Similarly, the “system” speed of EMD scale will be the most probable speed of ECD and “atomic” speed of EED fields such that $\mathbf{w}_m = \mathbf{v}_{c,mp} = \mathbf{u}_e$.

Because at thermodynamic equilibrium particles’ velocity field is governed by a *Gaussian* profile (Fig. 5) namely *Boltzmann* distribution function and the particle speeds must follow *Maxwell-Boltzmann* distribution function, it was recently shown that the energy spectrum of particles will follow *Planck* spectrum of equilibrium radiation [37, 38, 47, 48]. This correspondence between monatomic gas and photon gas becomes possible because of the recent closure of the gap between ideal gas theory on the one hand and *Planck* equilibrium radiation theory on the other hand [39]. For example, the field of isotropic homogeneous turbulence is identified as equilibrium eddy dynamics EED, Figs.1 and 2, with turbulent eddies defined as clusters of molecular clusters or super-clusters constituting the elements of the field. At thermodynamic equilibrium the energy spectrum of eddies in such isotropic stationary turbulent field will be governed by invariant *Planck* energy distribution law [37, 47-48]

$$\frac{\epsilon_\beta dN_\beta}{V} = \frac{8\pi h}{u_\beta^3} \frac{v_\beta^3}{e^{hv_\beta/KT} - 1} dv_\beta \quad (8)$$

shown in Fig. 7.

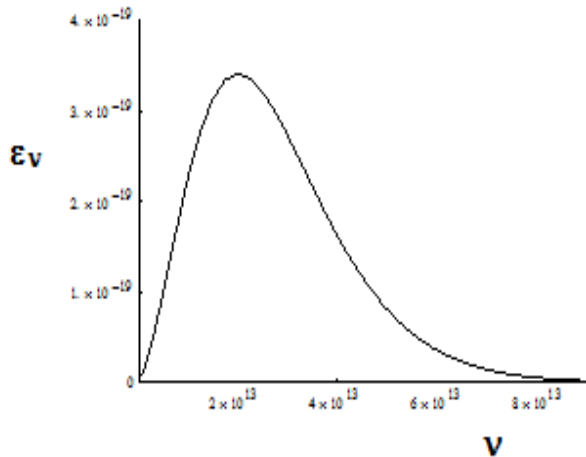


Fig. 7 Planck energy distribution law governing the energy spectrum of eddies at the temperature T = 300 K.

The three-dimensional energy spectrum E(k) for isotropic turbulence measured by *Van Atta and Chen* [49, 50] and shown in Fig. 8 is in qualitative agreement with *Planck* energy spectrum shown in Fig. 7.

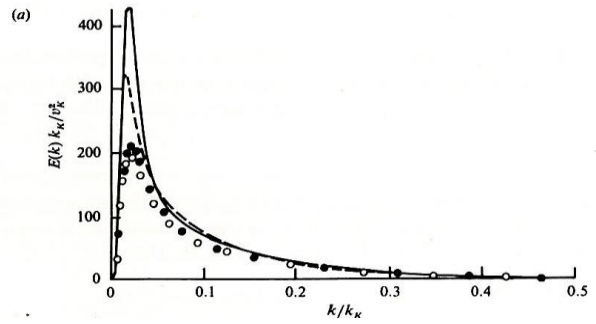


Fig. 8 Normalized three-dimensional energy spectra for isotropic turbulence [49].

In a more recent experimental investigation the energy spectrum of turbulent flow within the boundary layer in close vicinity of rigid wall was measured by *Marusic et al.* [51] and the reported energy spectrum have profiles quite similar to *Planck* distribution law.

To maintain stationary isotropic turbulence it is expected that both energy supply as well as energy dissipation spectrum should follow *Planck* law in (8). The experimental data obtained for one dimensional dissipation spectrum [52] along with *Planck* energy distribution (8) as well as this same distribution shifted by a constant amount of energy are shown in Fig. 9.

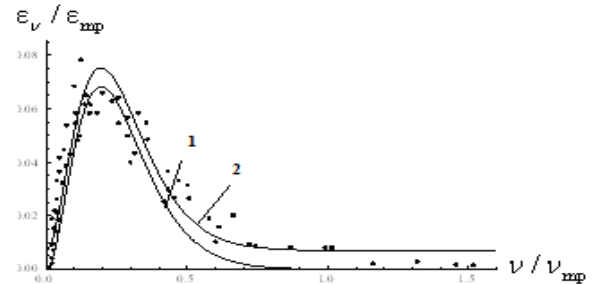


Fig. 9 One-dimensional dissipation spectrum [52] compared with (1) Planck energy distribution (2) Planck energy distribution with constant displacement.

Similar comparison with *Planck* energy distribution as shown in Fig. 9 is obtained with the experimental data of *Saddoughi and Veeravalli* [53] for one-dimensional dissipation spectrum of isotropic turbulence. Also, the normalized three-dimensional energy spectrum for homogeneous isotropic turbulence obtained from transformation of one-dimensional energy spectrum of *Lin* [54] by *Ling and Huang* [55]

$$E^* = \frac{\alpha^{*2}}{3} (K^* + \alpha^* K^{*2}) \exp(-\alpha^* K^*) \quad (9)$$

is in close agreement with *Planck* law (8).

An important aspect of *Planck* law (8) is that at a given fixed temperature the energy spectrum of equilibrium field is time invariant. Since one may view *Planck* distribution as energy spectrum of eddy cluster sizes [38] this means that cluster sizes are stationary. Therefore, even though the number

of eddies N_j and their energy ε_j in different fluid elements (energy levels) are different their product that is the total energy of all energy levels is the same [38]

$$U_j = \sum_j \varepsilon_j = N_j \varepsilon_j = U_{j+1} = \dots = U_{mp} = \bar{U} \quad (10a)$$

Thus *Boltzmann's* equipartition principle is satisfied in order to maintain time independent spectrum (Fig. 7) and avoid *Maxwell's* demon paradox [37]. Therefore, in stationary isotropic turbulence, energy flux occurs between fluid elements by transition of eddies of diverse sizes while leaving the fluid elements stochastically stationary in time. A schematic diagram of energy flux across hierarchies of eddies from large to small size is shown in Fig. 10 from the study by *Lumley et al.* [56].

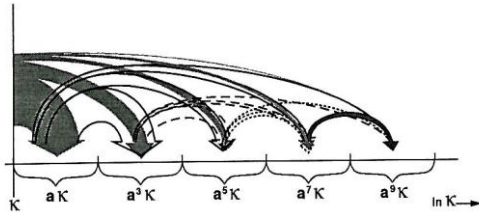


Fig. 10 A realistic view of spectral energy flux [56].

According to Fig. 6, *Maxwell-Boltzmann* distribution could be viewed as a spectrum of particle-cluster sizes that are stochastically stationary [38, 39]. Hence one arrives at a new paradigm of the physical foundation of quantum mechanics according to which *Bohr* stationary states will correspond to the stochastically stationary sizes of particle clusters, *de Broglie* wave packets, which will be governed by *Maxwell-Boltzmann* distribution function as shown in Fig. 6. Different energy levels of quantum mechanics could be identified as different size particle clusters (elements). Transfer of particle from a small rapidly- oscillating cluster j to a large slowly- oscillating cluster i constitutes transition from the high energy level j to the low energy level i (see Fig. 6). A scale invariant description of such transitions between energy levels at arbitrary scale β is schematically shown in Fig. 11.

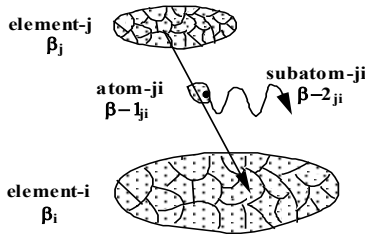


Fig. 11 Transition of “atom” a_{ij} from element- j to element- i leading to emission of sub-atomic particle s_{ij} .

Particle transitions will be accompanied with emission of a “sub-particle” that will carry away the excess energy

$$\Delta \varepsilon_{j\beta} = \varepsilon_{j\beta} - \varepsilon_{i\beta} = h(v_{j\beta} - v_{i\beta}) \quad (10b)$$

in harmony with *Bohr* theory of *atomic* spectra [38, 39].

III. SCALE INVARIANT FORMS OF CONSERVATION EQUATIONS FOR CHEMICALLY REACTIVE FIELDS

Following the classical methods [18-22, 40-44], the scale-invariant forms of mass, thermal energy, linear and angular momentum conservation equations [38, 39] at scale β are given as

$$\frac{\partial \rho_{i\beta}}{\partial t_\beta} + \nabla \cdot (\rho_{i\beta} \mathbf{v}_{i\beta}) = \mathfrak{R}_{i\beta} \quad (11)$$

$$\frac{\partial \varepsilon_{i\beta}}{\partial t_\beta} + \nabla \cdot (\varepsilon_{i\beta} \mathbf{v}_{i\beta}) = 0 \quad (12)$$

$$\frac{\partial \mathbf{p}_{i\beta}}{\partial t_\beta} + \nabla \cdot (\mathbf{p}_{i\beta} \mathbf{v}_{i\beta}) = -\nabla \cdot \mathbf{P}_{ij\beta} \quad (13)$$

$$\frac{\partial \boldsymbol{\pi}_{i\beta}}{\partial t_\beta} + \nabla \cdot (\boldsymbol{\pi}_{i\beta} \mathbf{v}_{i\beta}) = \rho_{i\beta} \boldsymbol{\omega}_\beta \cdot \nabla \mathbf{v}_{i\beta} \quad (14)$$

involving the *volumetric density* of thermal energy $\varepsilon_{i\beta} = \rho_{i\beta} \tilde{h}_{i\beta}$, linear momentum $\mathbf{p}_{i\beta} = \rho_{i\beta} \mathbf{v}_{i\beta}$, and angular momentum $\boldsymbol{\pi}_{i\beta} = \rho_{i\beta} \boldsymbol{\omega}_{i\beta}$. Also, $\mathfrak{R}_{i\beta}$ is the chemical reaction rate, $\tilde{h}_{i\beta}$ is the absolute enthalpy [34]

$$\tilde{h}_{i\beta} = \int_0^T c_{pi\beta} dT_\beta \quad (15)$$

In the energy conservation equation (12) instead of the classical practice of considering the internal energy the total thermal energy $\varepsilon_{i\beta} = \rho_{i\beta} \tilde{h}_{i\beta}$ namely absolute enthalpy (15) is considered. Therefore, the “potential” energy p/ρ of the moving fluid often referred to as “flow work” is also taken into account. Also, an important correction to invariant *Helmholtz* vorticity equation (14) is made herein by inclusion of *Coriolis* force that was neglected in earlier studies [38, 39] as discussed in Section 8. Finally, the scale dependence and quantum nature of physical “time” discussed in [38] is not addressed in the present study by taking $t_\beta = t$.

The partial stress tensor $\mathbf{P}_{ij\beta}$ is [40]

$$\mathbf{P}_{ij\beta} = m_\beta \int (\mathbf{u}_{i\beta} - \mathbf{v}_{i\beta})(\mathbf{u}_{j\beta} - \mathbf{v}_{j\beta}) f_\beta d\mathbf{u}_\beta \quad (16)$$

The derivation of (13) involves the definition of the peculiar velocity (3) along with the identity

$$\overline{\mathbf{V}'_{i\beta}\mathbf{V}'_{j\beta}} = \overline{(\mathbf{u}_{i\beta} - \mathbf{v}_{i\beta})(\mathbf{u}_{j\beta} - \mathbf{v}_{j\beta})} = \overline{\mathbf{u}_{i\beta}\mathbf{u}_{j\beta}} - \mathbf{v}_{i\beta}\mathbf{v}_{j\beta} \quad (17)$$

Also, summation of (13) over all the species results in *Cauchy* equation of motion at the next larger scale $\beta+1$

$$\frac{\partial}{\partial t}(\rho\mathbf{v}) + \nabla \cdot (\rho\mathbf{v}\mathbf{v}) = -\nabla \cdot \mathbf{P} \quad (18)$$

where $\rho = \rho_{\beta+1}$, $\mathbf{v} = \mathbf{v}_{\beta+1}$ and the total or mixture stress tensor is [40, 42]

$$\mathbf{P} = \sum_i \mathbf{P}_{i\beta} = \sum_i m_{i\beta} \int (\mathbf{u}_{i\beta} - \mathbf{v}_{i\beta})(\mathbf{u}_{j\beta} - \mathbf{v}_{j\beta}) f_{i\beta} d\mathbf{u}_{i\beta} \quad (19)$$

The subscript “i” in (11)-(14) that conventionally refers to chemical “specie i” is being also employed to identify the scale of “element” of the field. For example, in case of velocity with (atomic, element, and system) velocities denoted as $(\mathbf{u}_{i\beta}, \mathbf{v}_{i\beta}, \mathbf{w}_{\beta})$ one associates the average of a local group of specie i particles each with velocity $\mathbf{u}_{i\beta}$ as “element” or mean local velocity $\mathbf{v}_{i\beta}$. In moving to the next larger scale of $\beta+1$, the system velocity $\mathbf{w}_{\beta} = \langle \mathbf{v}_{i\beta} \rangle$ is then identified as the “mixture” velocity. When moving to the yet higher scale, one identifies $(\text{system})_{\beta} \Rightarrow (\text{element})_{\beta+1}$ such that $\mathbf{w}_{\beta} \Rightarrow \mathbf{v}_{j\beta+1}$ as the new “specie j” or “element” velocity and repeats the same procedure as before. According to this convention, the ordinary mass-average velocity of fluid mechanics \mathbf{v}_o will correspond to the system or “mixture” velocity $\mathbf{w}_m = \mathbf{v}_c$ of molecular-dynamic scale. This is because the mean thermal speed of molecules is the speed of sound $\mathbf{v}_{m,mp}$ that is a stationary random variable for a given temperature and constitutes the “atomic” velocity $\mathbf{u}_c = \mathbf{v}_{m,mp}$ of the next higher scale of ECD field by (1).

Considering (14), the classical definition of vorticity involves the curl of linear velocity $\nabla \times \mathbf{v}_{\beta} = \boldsymbol{\omega}_{\beta}$ thus giving rotational velocity of particle a secondary status in that it depends on its translational velocity \mathbf{v}_{β} . However, it is known that particle’s rotation about its center of mass is independent of the translational motion of its center of mass. In other words, translational, rotational, and vibrational (pulsational) motions of particle are independent degrees of freedom that should not be necessarily coupled.

To resolve this paradox, iso-spin of the particle at scale β is defined as the curl of the velocity at the next lower scale of $\beta-1$ [57]

$$\boldsymbol{\omega}_{i\beta} = \nabla \times \mathbf{v}_{i\beta-1} = \nabla \times \mathbf{u}_{i\beta} \quad (20)$$

With such a definition, the rotational velocity while having a connection to some type of translational motion at internal

scale of $\beta-1$, retains its independent degree of freedom at the external scale β as required. A schematic description of iso-spin and vorticity fields in cosmology is shown in Fig. 12.

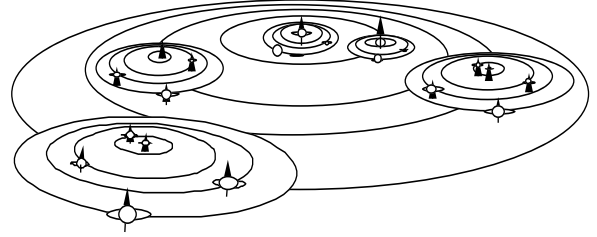


Fig. 12 Description of internal (iso-spin) versus external vorticity fields in cosmology.

Thus, what appears as rotational motion at scale β , when viewed at the lower scale $\beta-1$ is identified as orbital translational motion and a new local rotational motion is identified at this smaller scale. The nature of galactic vortices in cosmology and the associated dissipation have been discussed [29, 58].

The local velocity \mathbf{v}_{β} in (11)-(14) is expressed in terms of the convective \mathbf{w}_{β} and the diffusive \mathbf{V}_{β} velocities [34, 59]

$$\mathbf{w}_{\beta} = \mathbf{v}_{\beta} - \mathbf{V}_{\beta g} \quad , \quad \mathbf{V}_{\beta g} = -D_{i\beta} \nabla \ln(\rho_{i\beta}) \quad (21a)$$

$$\mathbf{w}_{\beta} = \mathbf{v}_{\beta} - \mathbf{V}_{\beta tg} \quad , \quad \mathbf{V}_{\beta tg} = -\alpha_{i\beta} \nabla \ln(\varepsilon_{i\beta}) \quad (21b)$$

$$\mathbf{w}_{\beta} = \mathbf{v}_{\beta} - \mathbf{V}_{\beta hg} \quad , \quad \mathbf{V}_{\beta hg} = -v_{i\beta} \nabla \ln(\mathbf{p}_{i\beta}) \quad (21c)$$

$$\mathbf{w}_{\beta} = \mathbf{v}_{\beta} - \mathbf{V}_{\beta rhg} \quad , \quad \mathbf{V}_{\beta rhg} = -v_{i\beta} \nabla \ln(\boldsymbol{\pi}_{i\beta}) \quad (21d)$$

where $(\mathbf{V}_{\beta g}, \mathbf{V}_{\beta tg}, \mathbf{V}_{\beta hg}, \mathbf{V}_{\beta rhg})$ are respectively the diffusive, the thermo-diffusive, the linear and the angular hydro-diffusive velocities and $v_{i\beta} = \mu_{i\beta} / \rho_{i\beta}$. Since for an ideal gas $\tilde{h}_{\beta} = c_{p\beta} T_{\beta}$, when $c_{p\beta}$ is constant and $T = T_{\beta}$, (21b) reduces to the *Fourier* law of heat conduction

$$\mathbf{q}_{i\beta} = \rho_{i\beta} \tilde{h}_{i\beta} \mathbf{V}_{\beta t} = -\kappa_{i\beta} \nabla T \quad (22)$$

where $\kappa_{i\beta}$ and $\alpha_{i\beta} = \kappa_{i\beta} / (\rho_{i\beta} c_{pi\beta})$ are the thermal conductivity and diffusivity. Similarly, (21c) may be identified as the shear stress associated with diffusional flux of linear momentum and expressed by the generalized *Newton* law of viscosity [34, 59]

$$\boldsymbol{\tau}_{i\beta} = \rho_{\beta} \mathbf{v}_{j\beta} \mathbf{V}_{i\beta h} = -\mu_{\beta} \partial \mathbf{v}_{j\beta} / \partial \mathbf{x}_i \quad (23)$$

Finally, (21d) may be identified as the torsional stress induced by diffusional flux of angular momentum and expressed as [36]

$$\boldsymbol{\tau}_{ij\beta} = \rho_\beta \boldsymbol{\omega}_{j\beta} \mathbf{V}_{ij\beta rh} = -\mu_\beta \partial \boldsymbol{\omega}_{j\beta} / \partial \mathbf{x}_i \quad (24)$$

Substituting from (21a)-(21d) into (11)-(14), neglecting the cross-diffusion terms and assuming constant transport coefficients with unity *Prandtl* and *Schmidt* numbers $Sc_\beta = Pr_\beta = 1$ result in

$$\frac{\partial \rho_{i\beta}}{\partial t} + \mathbf{w}_\beta \cdot \nabla \rho_{i\beta} = D_{i\beta} \nabla^2 \rho_{i\beta} + \mathfrak{R}_{i\beta} \quad (25)$$

$$\frac{\partial T_{i\beta}}{\partial t} + \mathbf{w}_\beta \cdot \nabla T_{i\beta} = \alpha_\beta \nabla^2 T_{i\beta} - \tilde{h}_{i\beta} \mathfrak{R}_{i\beta} / (\rho_{i\beta} c_{pi\beta}) \quad (26)$$

$$\frac{\partial \mathbf{v}_{i\beta}}{\partial t} + \mathbf{w}_\beta \cdot \nabla \mathbf{v}_{i\beta} = \nu_{i\beta} \nabla^2 \mathbf{v}_{i\beta} - \frac{\nabla \cdot \mathbf{P}_{ij\beta}}{\rho_{i\beta}} - \frac{\mathbf{v}_{i\beta} \mathfrak{R}_{i\beta}}{\rho_{i\beta}} \quad (27)$$

$$\frac{\partial \boldsymbol{\omega}_{i\beta}}{\partial t} + \mathbf{w}_\beta \cdot \nabla \boldsymbol{\omega}_{i\beta} = \nu_{i\beta} \nabla^2 \boldsymbol{\omega}_{i\beta} + \boldsymbol{\omega}_\beta \cdot \nabla \mathbf{v}_{i\beta} - \frac{\boldsymbol{\omega}_{i\beta} \mathfrak{R}_{i\beta}}{\rho_{i\beta}} \quad (28)$$

IV. THE INVARIANT BOLTZMANN EQUATION AND THE ASSOCIATED INVARIANT ENSKOG EQUATION OF CHANGE

Following the classical methods [19, 22, 40-44], the scale-invariant form of *Boltzmann* equation is introduced as

$$\frac{\partial f_{i\beta}}{\partial t} + \mathbf{u}_{i\beta} \cdot \nabla f_{i\beta} + \mathbf{f}_{i\beta} \cdot \nabla_v f_{i\beta} = \frac{\delta f_{i\beta}}{\delta t} \quad (29)$$

where $f_{i\beta}(\mathbf{x}_\beta, \mathbf{u}_{i\beta}, t_\beta)$ is the invariant distribution function at the scale β and \mathbf{f}_i is the external body force per unit mass of particle of specie i . Equation (29) is called *generalized Boltzmann* equation by *Williams* [42] because $\partial f_i / \partial t$ does not only account for contributions of binary collisions as in classical *Boltzmann* equation but also for contribution to changes of the volumetric number density n_i of particles of specie i due to chemical reactions. Multiplication of (29) with an arbitrary invariant function of velocity $\psi_{i\beta}$ for specie i and integration over all velocity space under appropriate assumptions [22, 40-43] results in the *Enskog* equation of change

$$\begin{aligned} & \frac{\partial}{\partial t} (\overline{n_{i\beta} \psi_{i\beta}}) + \nabla \cdot (\overline{n_{i\beta} \psi_{i\beta} \mathbf{u}_{i\beta}}) \\ & - \overline{n_{i\beta} \mathbf{f}_{i\beta} \cdot (\nabla \psi_{i\beta})} = \int \psi_{i\beta} \frac{\delta f_{i\beta}}{\delta t} d\mathbf{u}_{i\beta} \quad (30) \end{aligned}$$

Following the classical methods [40-43], the summational invariants $\Psi_{i\beta}$ for mass, thermal energy, linear, and angular momentum are defined as

$$\Psi_{i\beta} = m_{i\beta} \quad \text{Mass} \quad (31a)$$

$$\Psi_{i\beta} = m_{i\beta} \tilde{h}_{i\beta} \quad \text{Thermal energy} \quad (31b)$$

$$\Psi_{i\beta} = m_{i\beta} \mathbf{u}_{i\beta} \quad \text{Linear momentum} \quad (31c)$$

$$\Psi_{i\beta} = m_{i\beta} \boldsymbol{\omega}_{i\beta} \quad \text{Angular momentum} \quad (31d)$$

The new summational invariant (31d) involves the fluctuating iso-spin $\boldsymbol{\omega}_{i\beta}$ of particle [57] of mass $m_{i\beta}$ defined in (20).

V. THE INVARIANT FORMS OF CONTINUITY EQUATION

Following the classical methods [40-44], substitution of $\Psi_{i\beta} = m_{i\beta}$ into (30) with $\mathbf{f}_{i\beta} = 0$ gives invariant continuity equation

$$\frac{\partial \rho_{i\beta}}{\partial t} + \nabla \cdot (\rho_{i\beta} \mathbf{v}_{i\beta}) = \mathfrak{R}_{i\beta} \quad (32)$$

with the invariant reaction rate defined as

$$\mathfrak{R}_{i\beta} = m_{i\beta} \int (\delta f_{i\beta} / \delta t) d\mathbf{u}_{i\beta} \quad (33)$$

By summing (32) over all species one obtains the continuity equation for the next higher scale [36]

$$\frac{\partial \rho_{\beta+1}}{\partial t} + \nabla \cdot (\rho_{\beta+1} \mathbf{v}_{\beta+1}) = \mathfrak{R}_{\beta+1} \quad (34)$$

because

$$\begin{aligned} \sum_i \mathfrak{R}_{i\beta} &= \sum_i m_{i\beta} \int (\delta f_{i\beta} / \delta t) d\mathbf{u}_{i\beta} = \\ &= \frac{\delta}{\delta t} \sum_i m_{i\beta} \int f_{i\beta} d\mathbf{u}_{i\beta} = \frac{\delta}{\delta t} \sum_i m_{i\beta} n_{i\beta} = \\ &= \frac{\delta}{\delta t} \sum_i \rho_{i\beta} = \frac{\delta}{\delta t} \rho_{\beta+1} = \frac{\delta}{\delta t} (m_{\beta+1} n_{\beta+1}) = \\ &= m_{\beta+1} \int (\delta f_{\beta+1} / \delta t) d\mathbf{u}_{\beta+1} = \mathfrak{R}_{\beta+1} \quad (35) \end{aligned}$$

The result (35) is important since it represents a generalized expression for the reaction rate valid for all scales within the hierarchy shown in Fig. 1. The gravitational mass at any scale is therefore convertible into energy through “chemical reactions” at the rate defined by (35).

When the local velocity in (32) is expressed in terms of the convective and diffusive velocities from (21a) one obtains (25) that for a pure system $\rho_{i\beta} = \rho_\beta$ in the absence of reactions

$\mathfrak{R}_{i\beta} = 0$ results in the modified form of continuity equation [36] where

$$\frac{\partial \rho}{\partial t} + \mathbf{w} \cdot \nabla \rho - D \nabla^2 \rho = 0 \quad (36)$$

where D is the coefficient of self-diffusion. The importance of the modified form of the continuity equation (36) is that in the absence of convective velocity it reduces to diffusion equation. The second order derivative of diffusion equation allows for determination of internal structure of normal shock waves thus leading to the solutions [62] expressible as

$$\Theta = \text{erf}(0.2 - y) \quad (37)$$

with the dimensionless density and temperature defined as

$$\rho = \frac{\rho' - \rho'_{-\infty}}{\rho'_{\infty} - \rho'_{-\infty}}, \quad \theta = \frac{T - T_{-\infty}}{T_{\infty} - T_{-\infty}} \quad (38)$$

The predicted temperature profile (37) is in close agreement with the experimental data for normalized wire temperature Θ in normal shock reported by *Sherman* [63] as shown in Fig. 13

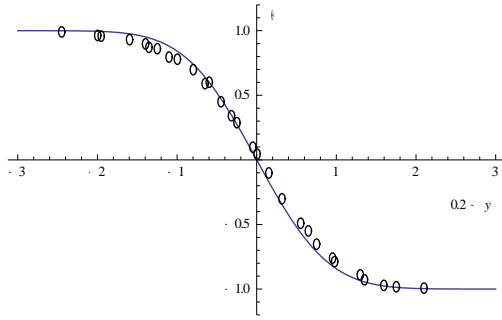


Fig. 13 Comparison between measured normalized wire temperature Θ versus position $(0.2 - y)$ in normal shock [63] and theory (37).

As a second example that reveals the important difference between (32) versus (36), let us consider the one-dimensional unsteady problem of diffusion of an infinite yz - plane source of mass placed at the origin $x = 0$ at time $t = 0$. Because of the symmetry of the problem the center of mass will remain stationary $\mathbf{w}_{\beta} = 0$ and (36) reduces to the diffusion equation

$$\frac{\partial \rho}{\partial t} = D \frac{\partial^2 \rho}{\partial x^2} \quad (39)$$

that governs the time evolution of density discontinuity in a background field composed of the same fluid. With appropriate boundary and initial conditions the solution of (39) is

$$\rho = \frac{M}{\sqrt{4\pi Dt}} \exp\left(-\frac{x^2}{4Dt}\right) \quad (40)$$

$$M = \int_{-\infty}^{+\infty} \rho dx \quad (41)$$

VI. THE INVARIANT FORM OF EQUATION OF MOTION

The invariant form of equation of motion is obtained by the classical methods [40-44] of substituting $\Psi_{i\beta} = m_{i\beta} \mathbf{u}_{i\beta}$ into (30) with $\mathbf{f}_{i\beta} = 0$ to obtain invariant *Cauchy* equation of motion

$$\frac{\partial(\rho_{i\beta} \mathbf{v}_{i\beta})}{\partial t} + \nabla \cdot (\rho_{i\beta} \mathbf{v}_{i\beta} \mathbf{v}_{j\beta}) = -\nabla \cdot \mathbf{P}_{ij\beta} \quad (42)$$

where the stress tensor on the right hand-side has been defined in (16).

The history of derivation of *Navier–Stokes* equation from (42) has been described in an excellent review by *Darrigol* [64]. The derivation begins with the introduction of *Cauchy* total stress tensor in the form [40-44, 64-66]

$$\sigma_{ij} = -p\delta_{ij} + \lambda' \nabla \cdot \mathbf{v} \delta_{ij} + 2\mu e_{ij} \quad (43)$$

where the rate of strain is

$$e_{ij} = \frac{1}{2} \left(\frac{\partial v_i}{\partial x_j} + \frac{\partial v_j}{\partial x_i} \right) \quad (44)$$

For fluids the two *Lame* constants (μ, λ') are called the first and the second viscosity coefficients [64-66]. The classical expression for the stress tensor of fluids (43) was introduced in close analogy with the stress tensor for deformation of elastic solids developed by the founders *Cauchy* and *Poisson* [64, 65]. Thus the role played by the strain tensor ε_{ij} in solids was related to the rate of strain tensor e_{ij} in liquids.

In view of the negative sign in (42) the total stress tensor for fluids is expressed as

$$\sigma_{ij\beta} = p_{i\beta} \delta_{ij\beta} - \lambda'_{i\beta} \nabla \cdot \mathbf{v}_{i\beta} \delta_{ij\beta} - 2\mu_{i\beta} e_{ij\beta} \quad (45)$$

By classical methods [64-66] the mean pressure of fluid in motion is defined as

$$\mathbf{P}_{ij\beta} = \frac{1}{3} \sigma_{i\beta} \delta_{ij\beta} = p_{i\beta} \delta_{ij\beta} - \left(\lambda'_{i\beta} + \frac{2}{3} \mu_{i\beta} \right) \nabla \cdot \mathbf{v}_{i\beta} \delta_{ij\beta} \quad (46)$$

Following the conventional practice one makes the *Stokes* assumption of zero bulk viscosity $b_{s\beta} = 0$ such that the two *Lame* constants $(\lambda'_{\beta}, \mu_{\beta})$ will be related by [66]

$$b_{s\beta} = \lambda'_{\beta} + \frac{2}{3}\mu_{\beta} = 0 \quad (47)$$

However, according to both *Cauchy* and *Poisson* as the intermolecular spacing vanish $R \rightarrow 0$ the two *Lame* constants must satisfy the limiting expression [65]

$$\lambda'_{\beta} + \mu_{\beta} = \lim_{R \rightarrow 0} R^4 f(R) = 0 \quad (48)$$

that by (47) leads to a finite coefficient of bulk viscosity [39]

$$b_{\beta} = \lambda'_{\beta} + \frac{2}{3}\mu_{\beta} = -\frac{\mu_{\beta}}{3} \quad (49)$$

Therefore, in *Cauchy-Poisson* limit (48) all tangential stresses will vanish as was emphasized by *Darrigol* [65]

“Then the medium loses its rigidity since the transverse pressures disappear.”

leaving only normal stresses. By (46) and (49) the total normal stress tensor for fluids becomes [39]

$$\mathbf{P}_{i\beta} = p_{i\beta} \delta_{ij\beta} - \frac{1}{3} \mu_{i\beta} \nabla \cdot \mathbf{v}_{i\beta} \delta_{ij\beta} = (p_{i\beta} + p_{hi\beta}) \delta_{ij\beta} \quad (50)$$

when the hydrodynamics pressure is defined as

$$p_{hi\beta} = -\frac{\mu_{i\beta}}{3} \nabla \cdot \mathbf{v}_{i\beta} \quad (51)$$

According to (50) a moving fluid besides the thermodynamic pressure $p_{i\beta}$ experiences the hydrodynamic pressures $p_{hi\beta}$ due to its motion.

The expression for hydrodynamic pressure in (50) could also be arrived at directly by first noting that classically hydrodynamic pressure is defined as the mean normal stress

$$p_{hi\beta} = (\tau_{xxi\beta} + \tau_{yyi\beta} + \tau_{zzi\beta}) / 3 \quad (52)$$

because shear stresses in fluids must vanish by definition. Next, normal stresses are expressed as diffusional flux of the corresponding momenta by (21c) as

$$\tau_{i\beta} = \rho_{i\beta} \mathbf{v}_{i\beta} \mathbf{v}_{i\beta} = -\mu_{i\beta} \nabla \cdot \mathbf{v}_{i\beta} \quad (53)$$

Substituting from (53) into (52) results in

$$p_{hi\beta} = \frac{1}{3} (\tau_{xxi\beta} + \tau_{yyi\beta} + \tau_{zzi\beta}) = -\frac{\mu_{i\beta}}{3} \nabla \cdot \mathbf{v}_{i\beta} \quad (54)$$

that is in accordance with (51).

Because by definition fluids satisfy *Cauchy-Poisson* limit (48) and hence are incapable of supporting tangential forces, the normal stress tensor (50) is the total stress tensor for fluids [39] and only involves a single *Lame* coefficient as anticipated by *Navier* [64]. Substituting from (50) into (42) results in the

modified invariant equation of motion for compressible fluids [39]

$$\frac{\partial(\rho_{i\beta} \mathbf{v}_{i\beta})}{\partial t} + \nabla \cdot (\rho_{i\beta} \mathbf{v}_{i\beta} \mathbf{v}_{i\beta}) = -\nabla p_{i\beta} + \frac{\mu_{i\beta}}{3} \nabla(\nabla \cdot \mathbf{v}_{i\beta}) \quad (55)$$

It is noted that unlike the classical result the diffusion term does not occur in (55). This is because by definition fluids are substances that cannot support any shear stress and hence shear force. As a result, in the application of *Newton* law of motion to fluids the only forces on the right-hand-side of *Cauchy* equation of motion (42) must be normal forces. Tangential or shear forces must therefore arise from diffusional flux of momentum and originate from the left-hand-side of (42) to be further described in the following.

A most significant aspect of the modified equation of motion (55) is that for an incompressible fluid $\nabla \cdot \mathbf{v}_{i\beta} = 0$ by continuity equation (11) it reduces to *Euler* equation

$$\frac{\partial \mathbf{v}_{i\beta}}{\partial t} + \mathbf{v}_{i\beta} \cdot \nabla \mathbf{v}_{i\beta} = -\frac{\nabla p_{i\beta}}{\rho_{i\beta}} \quad (56)$$

Therefore, for incompressible flows *Euler* equation (56) that has been conventionally only associated with potential hence non-viscous flows is now identified as exact equation of motion even for viscous flows. This is because the only viscous effect appears in the last term of (55) and vanishes due to solenoidal velocity field. In other words, in fluids shear stresses can only arise from diffusional flux of momenta that according to (21c) arise from difference between convective versus local velocities. However, such distinction between convective and local velocities does not occur in *Euler* equation (56).

If the local velocity that is coupled with the divergence operator $\mathbf{v}_{i\beta}$ in the second term of (55) is expressed in terms of the sum of convective and diffusive velocities from (21c), and following conventional practice the cross diffusion effects are neglected and transport coefficients are assumed to be constant, one obtains the modified invariant equation of motion for compressible fluids as

$$\frac{\partial \mathbf{v}_{i\beta}}{\partial t} + \mathbf{w}_{i\beta} \cdot \nabla \mathbf{v}_{i\beta} - v_{i\beta} \nabla^2 \mathbf{v}_{i\beta} = -\frac{\nabla p_{i\beta}}{\rho_{i\beta}} + \frac{v_{i\beta}}{3} \nabla(\nabla \cdot \mathbf{v}_{i\beta}) - \frac{\mathbf{v}_{i\beta} \mathfrak{R}_{i\beta}}{\rho_{i\beta}} \quad (57)$$

The result (57) is to be compared with the classical *Navier-Stokes* equation of motion

$$\frac{\partial \mathbf{v}}{\partial t} + \mathbf{v} \cdot \nabla \mathbf{v} - \nu \nabla^2 \mathbf{v} = -\frac{\nabla p}{\rho} + \frac{\nu}{3} \nabla(\nabla \cdot \mathbf{v}) \quad (58)$$

An important feature of the modified equation of motion (57) as compared to (58) is that it is linear since it involves a

convective velocity \mathbf{W}_β that is different from the local fluid velocity \mathbf{V}_β . Also, the diffusion term in (57) arises from the LHS of (42) and relates to diffusional flux of momentum [34, 59] by (21c). In (58) on the other hand, the diffusion term arises from the RHS of (42) as a force that relates to the classical form of the stress tensor (43). Finally, in the absence of convective velocity $\mathbf{W}_\beta = 0$, the temporal and diffusion terms in (57) remain finite. With the *Navier-Stokes* equation (58) on the other hand, the absence of velocity $\mathbf{V}_\beta = 0$ results in the vanishing of the entire equation of motion.

To clarify the physical significance of the different roles of $\mathbf{W}_{j\beta}$ versus $\mathbf{V}_{j\beta}$ in (57) we consider the problem of one-dimensional diffusion of momentum parallel to the steps (39)-(41) for diffusion of mass. Let a yz -plane source of momentum be placed at the origin $x = 0$ at time $t = 0$ in an infinite and otherwise stationary fluid. Because of the symmetry, momentum conservation leads to stationary center of mass $\mathbf{W}_\beta = 0$. Neglecting the pressure gradient, i.e. assuming that the total initial imparted momentum is small and for an incompressible fluid in the absence of chemical reactions $\mathfrak{R}_{i\beta} = 0$, (57) reduces to

$$\frac{\partial \mathbf{v}_\beta}{\partial t} = \nu_\beta \nabla^2 \mathbf{v}_\beta \quad (59)$$

With the appropriate initial and boundary conditions the solution of (59) is

$$\mathbf{v}_\beta = \frac{\Lambda_\beta}{\rho_\beta \sqrt{4\pi\nu t}} \exp\left(-\frac{x^2}{4\nu t}\right) \quad (60)$$

where

$$\Lambda_\beta = \int_{-\infty}^{+\infty} \rho \mathbf{v}_\beta dx \quad (61)$$

is linear momentum per unit area of the plane source. Derivation of results (59)-(61) from the nonlinear classical form of the equation of motion (58) will be more complex.

The scale invariant model of statistical mechanics naturally leads to a statistical theory of turbulence that is in accordance with the perceptions of *Heisenberg* and *Chandrasekhar* [38]. Hence, following *Heisenberg* the problem of turbulence is considered to be similar to that of *Maxwell* and *Boltzmann* kinetic theory of gas namely the problem of distribution of a given amount of energy amongst large numbers of degrees of freedom as described by *Heisenberg* [30]

“Turbulence is an essentially statistical problem of the same type as one meets in statistical mechanics, since it is

the problem of distribution of energy among a very large number of degrees of freedom. Just as in Maxwell theory this problem can be solved without going into details of the mechanical motions, so it can be solved here by simple considerations of similarity.”

The model shown in Figs. 1 and 2 suggests a hierarchy of flows that appear laminar at scale β but are actually bulk advection of turbulent flows at the smaller scale of $\beta-1$. Such hierarchies of embedded turbulent flows are most clearly seen in steady turbulent boundary layer over a flat plate when the solutions of (57) at scales β and $\beta+1$ were respectively found to be [67]

$$v_{\beta+1}^+ = 5 + 8(2/\sqrt{\pi})^2 \operatorname{erf}(y_\beta^+/32) \quad (62)$$

and

$$v_\beta^+ = 8(2/\sqrt{\pi}) \operatorname{erf}(y_{\beta-1}^+/8) \quad (63)$$

For example, the solutions in (62) and (63) at $\beta+1 = e$ and $\beta = c$ correspond to LED and LCD and their comparisons with experimental data [41, 50, 68-70] are shown in Fig.14a.

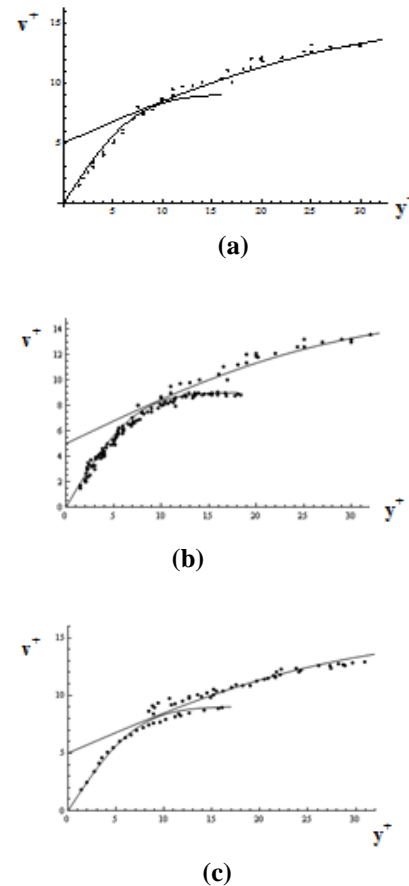


Fig. 14 Comparison between the predicted velocity profiles (a) LED-LCD, (b) LCD-LMD, (c) LCD-LAD with experimental data in the literature over spatial range of 10^8 [67].

Similarly, the solutions in (62) and (63) at $\beta+1 = c$ and $\beta = m$ correspond to LCD and LMD and at $\beta+1 = m$ and $\beta = a$ corresponding to LMD and LAD and their comparisons with experimental data of *Lancien et al.* [71] and *Meinhart et al.* [72] are shown in Figs. 14b and 14c, respectively.

VII. THE INVARIANT FORM OF ENERGY CONSERVATION EQUATION

To obtain the scale-invariant form of the energy equation the exact nature of the summational invariant ψ_{ip} to be substituted in (30) must first be identified. First the energy for translational oscillations of particles in two directions (x^+, x^-) is considered. According to (3), particle translational velocity is the sum of the mean or cluster velocity and the random peculiar velocity

$$\mathbf{u}_{mj} = \mathbf{v}_{mj} + \mathbf{V}'_{mj} = \mathbf{u}_{cj} + \mathbf{V}'_{mj} \quad (64)$$

The above definition is in the same spirit as in cosmology where the peculiar velocity of a galaxy is defined as the difference between its velocity and the mean velocity of the cluster of galaxies to which it belongs. The thermodynamic system being considered herein is composed of a spectrum of molecular clusters under stochastically stationary state. In a recent study [38], it was shown that three different flow regimes based on the nature of cluster velocity \mathbf{v}_m in (3) could be identified. For a system of ideal gas at thermodynamic equilibrium all three velocities in (64) will be random such that (64) when squared, averaged, and multiplied by particle mass leads to the kinetic energy

$$m\overline{u_{mj}^2} = m\overline{v_{mj}^2} + m\overline{V_{mj}'^2} = m\overline{u_{cj}^2} + m\overline{V_{mj}'^2} \quad (65)$$

since $\overline{\mathbf{u}_{cj} \cdot \mathbf{V}'_{mj}} = 0$. The internal energy of particle due to translational motion of particle in two directions (x^+, x^-) is expressed as

$$\begin{aligned} \hat{u}_t &= \frac{1}{2} \overline{mv_{mx+}^2} + \frac{1}{2} \overline{mv_{mx-}^2} = \\ &= \frac{1}{2} \overline{mu_{cx+}^2} + \frac{1}{2} \overline{mu_{cx-}^2} = \overline{mv_{mx+}^2} \end{aligned} \quad (66)$$

Next, the potential energy due to “stress” is related to the kinetic energy of peculiar velocity as

$$\begin{aligned} \hat{\varepsilon}_p &= \frac{1}{2} m\overline{V_{mx+}'^2} + \frac{1}{2} m\overline{V_{mx-}'^2} = \\ &= m\overline{V_{mx+}'^2} = \frac{1}{3} m\overline{V_{m+}'^2} = p\hat{v} \end{aligned} \quad (67)$$

where pressure is defined as $p = nm\overline{V_{m+}'^2} / 3$. Hence, the total energy associated with harmonic translational motion of particle will become [73]

$$\hat{\varepsilon}_t = \hat{u}_t + \hat{\varepsilon}_p = \hat{u}_t + p\hat{v} \quad (68)$$

Since particles are neither point masses without any physical extent nor absolutely rigid, their rotational and vibrational energies cannot be properly neglected as was emphasized by *Clausius* in his pioneering investigation of the mechanical theory of heat [74]

"In liquids, therefore, an oscillatory, a rotatory, and a translator motion of the molecules take place, but in such a manner that these molecules are not themselves separated from each other, but even in the absence of external forces, remain within a certain volume"

Therefore, following *Clausius* the internal kinetic energy of rotational and vibrational motion of particles in two directions (θ^+, θ^-), (r^+, r^-) are written as [35, 73]

$$\hat{u}_r = \varepsilon_r = \frac{1}{2} \overline{I\omega_{m\theta+}^2} + \frac{1}{2} \overline{I\omega_{m\theta-}^2} = \overline{I\omega_{m\theta+}^2} \quad (69)$$

$$\hat{u}_v = \varepsilon_v = \frac{1}{2} \overline{\chi r_{m+}^2} + \frac{1}{2} \overline{\chi r_{m-}^2} = \overline{\chi r_{m+}^2} \quad (70)$$

where (I, χ) are respectively the moment of inertia and the spring constant. Hence, the internal “atomic” energy of particle is defined as the sum of its translational, rotational, and vibrational kinetic energies from equations (66), (69) and (70)

$$\hat{u} = \hat{u}_t + \hat{u}_r + \hat{u}_v = \overline{mv_{x+}^2} + \overline{I\omega_{\theta+}^2} + \overline{\chi r_+^2} \quad (71)$$

Finally, by (67) and (71) the total atomic energy or the atomic enthalpy is defined as the sum of atomic internal kinetic energy and atomic external potential energy written as [73]

$$\hat{h} = \hat{u}_t + \hat{u}_r + \hat{u}_v + p\hat{v} = \hat{u} + p\hat{v} \quad (72)$$

such that the total enthalpy becomes

$$H = U + pV \quad (73)$$

where (H, U, V) = $N(\hat{h}, \hat{u}, \hat{v})$. According to equation (72) the system has four degrees of freedom and at equilibrium *Boltzmann* principle of equipartition of energy requires

$$\hat{u}_t = \hat{u}_r = \hat{u}_v = p\hat{v} \quad (74)$$

In view of (72) and (74) the atomic enthalpy per unit mass \tilde{h}_m is defined as

$$\tilde{h}_{i\beta} = \hat{h}_{i\beta} / m_{i\beta} \quad (75)$$

By (75) the expression for summational invariant for thermal energy in (31b) becomes

$$\Psi_{i\beta} = m_{i\beta} \tilde{h}_{i\beta} = \hat{h}_{i\beta} \quad (76)$$

Substituting (76) in *Enskog* equation of change (30) with $\mathbf{f}_{i\beta} = 0$ results in the invariant form of energy conservation equation (12)

$$\frac{\partial \varepsilon_{i\beta}}{\partial t} + \nabla \cdot (\varepsilon_{i\beta} \mathbf{v}_{i\beta}) = 0 \quad (77)$$

with the volumetric density of total thermal energy defined as $\varepsilon_{i\beta} = \rho_{i\beta} \tilde{h}_{i\beta}$. Substituting from (21b) in (77), neglecting the cross diffusion terms, assuming constant transport coefficients such that the absolute enthalpy of ideal gas could be expressed as $\tilde{h}_{i\beta} = c_{pi\beta} T_\beta$ results in scale invariant form of energy conservation equation [36]

$$\frac{\partial T_\beta}{\partial t} + \mathbf{w}_\beta \cdot \nabla T_\beta - \alpha_{i\beta} \nabla^2 T_\beta = -\tilde{h}_{i\beta} \mathfrak{R}_{i\beta} / (\rho_\beta c_{pi\beta}) \quad (78)$$

As an example of solution of (78) the simple problem of steady plane parallel laminar flow over a flat plate schematically shown in Fig. 15 is considered.

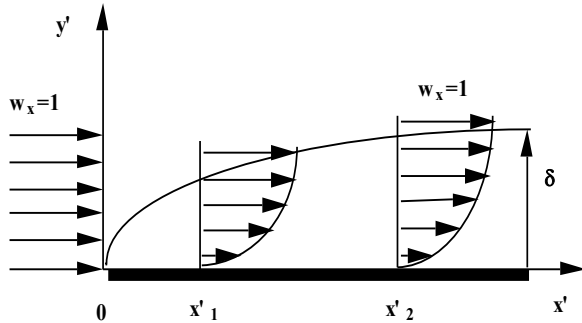


Fig. 15 Laminar boundary layer over a flat plate.

In the absence of chemical reactions and with negligible pressure gradient the equations governing partial density (36), velocity (57), and temperature (78) become identical for unity *Prandtl* and *Schmidt* numbers $Sc_\beta = Pr_\beta = 1$ [75]

$$\frac{d^2 g}{d\xi^2} + 2\xi \frac{dg}{d\xi} = 0 \quad g = \rho_i, \theta, v_x \quad (79)$$

where similarity variable ξ is defined as

$$\xi = \frac{y}{2\sqrt{2x}} = \frac{\eta}{2\sqrt{2}} \quad (80)$$

Furthermore, defining the dimensionless partial density, temperature, velocity, and coordinates as

$$\rho_i = \frac{\rho'_i - \rho'_{iw}}{\rho'_{i\infty} - \rho'_{iw}}, \quad \theta = \frac{T - T_w}{T_\infty - T_w}, \quad v_x = \frac{v'_x}{w'_{x0}} \quad (81a)$$

$$x = x' / \ell_H, \quad y = y' / \ell_H, \quad \ell_H = v / w'_{x0} \quad (81b)$$

leads to identical boundary conditions

$$\rho_i = \theta = v = 0 \quad \xi = 0 \quad (82a)$$

$$\rho_i = \theta = v = 1 \quad \xi = \infty \quad (82b)$$

such that the solution of (79) and (82) for concentration, temperature, and velocity profiles become identical [75]

$$\rho_i = \theta = v_x = \text{erf}(\eta / 2\sqrt{2}) \quad (83)$$

Comparison of the velocity profile in (83) with experimental data of *Dhawan* [76] is shown in Fig. 16.

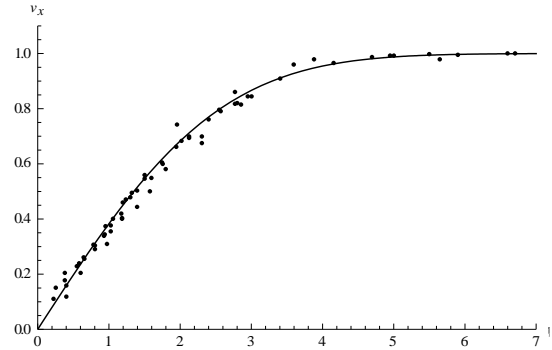


Fig. 16 Predicted velocity profile (83) compared with experimental data of *Dhawan* [76].

It is important to note however that the exact similarity between (ρ_i, θ, v) fields given by (83) will no longer be valid if instead of (57) the non-linear *Navier-Stokes* equation of motion (58) is considered to obtain the velocity field.

Following steps parallel to (39)-(41) for mass diffusion, the diffusion of a plane source of heat placed at the origin $x = 0$ at time $t = 0$ in a none-reactive $\mathfrak{R}_{i\beta} = 0$ field leaves the center of mass stationary hence $\mathbf{w}_\beta = 0$ and (78) reduces to diffusion equation

$$\frac{\partial T}{\partial t} = \alpha \frac{\partial^2 T}{\partial x^2} \quad (84)$$

that with the appropriate initial and boundary conditions has the solution

$$T = \frac{Q_\beta}{\rho c_p \sqrt{4\pi\alpha t}} \exp\left(-\frac{x^2}{4\alpha t}\right) \quad (85)$$

where

$$Q_\beta = \int_{-\infty}^{+\infty} \rho \tilde{h} dx = \int_{-\infty}^{+\infty} \rho c_p T dx \quad (86)$$

VIII. THE INVARIANT FORM OF ANGULAR MOMENTUM CONSERVATION EQUATION

To obtain the invariant form of the conservation equation of angular momentum, one introduces the new summational invariant $\Psi_{i\beta} = m_{i\beta} \boldsymbol{\omega}_{i\beta}$ from (31d) where $\boldsymbol{\omega}_{i\beta}$ is the iso-spin of particle [57] defined in (20). Next, parallel to the distribution function for translational velocity $f_{i\beta}(\mathbf{x}_{i\beta}, \mathbf{u}_{i\beta}, t_\beta)$ in *Boltzmann* equation (29) one introduces the distribution function for iso-spin or rotational velocity $f_{ri\beta}(\mathbf{x}_{i\beta}, \boldsymbol{\omega}_{i\beta}, t_\beta)$ at the scale β that gives the total number of rotators per unit volume as

$$n_{i\beta} = \int f_{ri\beta} d\boldsymbol{\omega}_{i\beta} \quad (87)$$

The introduction of particle iso-spin $\boldsymbol{\omega}_{i\beta}$ in (87) gives the mean iso-spin i.e. vorticity as

$$\boldsymbol{\omega}_{i\beta}(x_{i\beta}, t) = \int \boldsymbol{\omega}_{i\beta} f_{ri\beta} d\boldsymbol{\omega}_{i\beta} / n_{i\beta} \quad (88)$$

Substitutions from (31d) and (88) into equivalent of (30) with $\mathbf{f}_{i\beta} = 0$ and $f_{ri\beta}$ for rotational motion results in the modified invariant vorticity equation

$$\frac{\partial \boldsymbol{\pi}_{i\beta}}{\partial t} + \nabla \cdot (\boldsymbol{\pi}_{i\beta} \mathbf{v}_{i\beta}) = \rho_{i\beta} \boldsymbol{\Omega}_\beta \cdot \nabla \mathbf{v}_{i\beta} \quad (89)$$

In (89) diffusion vorticity $\boldsymbol{\Omega}_\beta$ is the mean of peculiar vorticity $\boldsymbol{\Omega}'_{i\beta}$ defined by curl of (3). The last term of (89) corresponds to vortex stretching and arises from *Coriolis* force [77] as

$$\begin{aligned} -\nabla \cdot (\rho_{i\beta} \boldsymbol{\Omega}_\beta \times \mathbf{v}_{i\beta}) &= -\nabla \cdot (\rho_{i\beta} \epsilon_{ijk} \boldsymbol{\Omega}_{j\beta} \mathbf{v}_{k\beta}) \\ &= \nabla \cdot (\rho_{i\beta} \epsilon_{ijk} \boldsymbol{\Omega}_{j\beta} \mathbf{v}_{i\beta}) = \rho_{i\beta} \boldsymbol{\Omega}_\beta \cdot \nabla \mathbf{v}_{i\beta} \end{aligned} \quad (90)$$

The issue of sign discrepancy of the vortex stretching term in *Helmholtz* vorticity equation has been a source of difficulty in past studies [38, 39]. The error is now identified to originate from the neglect of *Coriolis* force in the last term on the RHS of (89) to be further discussed in the following.

As stated before, vorticity diffusion $\boldsymbol{\Omega}_\beta$ arises from the difference between the bulk or mean vorticity $\bar{\boldsymbol{\omega}}_\beta$ and the local vorticity $\boldsymbol{\omega}_\beta$ given by the curl of equation (3) as

$$\boldsymbol{\omega}_{i\beta} - \bar{\boldsymbol{\omega}}_\beta = \boldsymbol{\Omega}_\beta \quad (91)$$

When the mean or bulk vorticity is absent $\bar{\boldsymbol{\omega}}_\beta = \nabla \times \mathbf{w} = 2\mathbf{w}_0 = 0$, i.e. the absence of what *Kundu* [77] calls *planetary vorticity*, by (91) the local vorticity and diffusion vorticity relate by

$$\boldsymbol{\omega}_{i\beta} = \boldsymbol{\Omega}_\beta \quad (92)$$

Substitution from (92) into (89) results in scale-invariant *Helmholtz* vorticity equation

$$\frac{\partial \boldsymbol{\pi}_{i\beta}}{\partial t} + \nabla \cdot (\boldsymbol{\pi}_{i\beta} \mathbf{v}_{i\beta}) = \rho_{i\beta} \boldsymbol{\omega}_\beta \cdot \nabla \mathbf{v}_{i\beta} \quad (93)$$

By expressing the local velocity in (93) in terms of convective and diffusive velocities from (21d) and neglecting cross diffusion terms and assuming constant transport coefficients one obtains the invariant modified *Helmholtz* vorticity equation

$$\frac{\partial \boldsymbol{\omega}_{i\beta}}{\partial t} + \mathbf{w}_\beta \cdot \nabla \boldsymbol{\omega}_{i\beta} = \boldsymbol{\omega}_\beta \cdot \nabla \mathbf{v}_{i\beta} + v_{i\beta} \nabla^2 \boldsymbol{\omega}_{i\beta} - \frac{\boldsymbol{\omega}_{i\beta} \mathfrak{R}_{i\beta}}{\rho_{i\beta}} \quad (94)$$

Equation (94) is to be compared with the classical form of *Helmholtz* vorticity equation

$$\frac{\partial \boldsymbol{\omega}}{\partial t} + \mathbf{v} \cdot \nabla \boldsymbol{\omega} = \boldsymbol{\omega} \cdot \nabla \mathbf{v} + \nu \nabla^2 \boldsymbol{\omega} \quad (95)$$

An important difference between the modified (94) and the classical (95) forms of *Helmholtz* vorticity equation is the occurrence of convective velocity \mathbf{w}_β as opposed to local velocity \mathbf{v}_β in the second term. Because local vorticity $\boldsymbol{\omega}_\beta$ in (95) is itself related to the curl of local velocity it cannot be convected by this same velocity. On the other hand, the advection of local vorticity by convective velocity \mathbf{w}_β in (94) is possible. Moreover, in absence of convection (94) reduces to the diffusion equation similar to that in (36), (57), and (78) for mass, momentum, and heat transport. However, the absence of local velocity in (95) will lead to the vanishing of the entire equation.

Parallel to diffusion of mass (39), momentum (59), and heat (84), for a plane source of vorticity placed at $x = 0$, at time $t = 0$, by symmetry the convection vanishes $\mathbf{w}_\beta = 0$ and in the absence of reaction $\mathfrak{R}_{i\beta} = 0$ (94) reduces to the diffusion equation

$$\frac{\partial \omega}{\partial t} = \nu \frac{\partial^2 \omega}{\partial x^2} \quad (96)$$

with the solution

$$\omega = \frac{S}{\sqrt{4\pi\nu t}} \exp\left(-\frac{x^2}{4\nu t}\right) \quad (97)$$

where

$$S = \int_{-\infty}^{+\infty} \omega dx \quad (98)$$

is the vorticity per unit area of the plane source.

To show that the modified *Helmholtz* vorticity equation (94) does lead to consistent predictions, we consider the problem of spherical flow within a droplet located at the stagnation point of two cylindrically-symmetric opposed gaseous finite jets. The convective velocity field is known and given as [41, 78]

$$\mathbf{w}_r = \xi \quad , \quad \mathbf{w}_z = -2\xi \quad (99)$$

and the dimensionless velocity and coordinates are defined as

$$\begin{aligned} (\mathbf{w}_r, \mathbf{w}_z) &= (\mathbf{w}'_r, \mathbf{w}'_z) / \sqrt{\nu\Gamma} \quad , \quad \xi = \mathbf{r} / \sqrt{\nu\Gamma} \\ \zeta &= \mathbf{z} / \sqrt{\nu\Gamma} \end{aligned} \quad (100)$$

where Γ is the stagnation flow velocity gradient. The modified steady *Helmholtz* vorticity equation (94) for axi-symmetric cylindrical coordinates in absence of chemical reactions $\mathfrak{R}_{ip} = 0$ reduces to

$$\begin{aligned} \mathbf{w}_r \frac{\partial \omega_0}{\partial \xi} + \mathbf{w}_z \frac{\partial \omega_0}{\partial \zeta} &= \frac{\omega_0 \mathbf{v}_r}{\xi} + \left[\frac{\partial^2 \omega_0}{\partial \xi^2} + \frac{1}{\xi} \frac{\partial \omega_0}{\partial \xi} \right. \\ &\quad \left. - \frac{\omega_0}{\xi^2} + \frac{\partial^2 \omega_0}{\partial \zeta^2} \right] \end{aligned} \quad (101)$$

The solution of (99)-(101) after substitution for local radial velocity $\mathbf{v}_{r\beta} = \mathbf{w}_{r\beta-1} = -\xi$ that is in opposite direction as compared to (99) in accordance with (105) and under appropriate boundary conditions is given as [79, 80]

$$\omega_0 = 14\xi\zeta/R^2 \quad (102)$$

and the corresponding flow within the droplet is described by the stream function

$$\Psi = \zeta\xi^2 [1 - (\xi/R)^2 - (\zeta/R)^2] \quad (103)$$

The dimensionless vorticity, stream function, and droplet radius R' are defined as $\omega_0 = \omega'_0/\Gamma$, $\Psi = \Psi'/(v^3/\Gamma)^{1/2}$, and $R = R'/\sqrt{\nu/\Gamma}$. Some of the streamlines calculated from (103) are shown in Fig. 17.

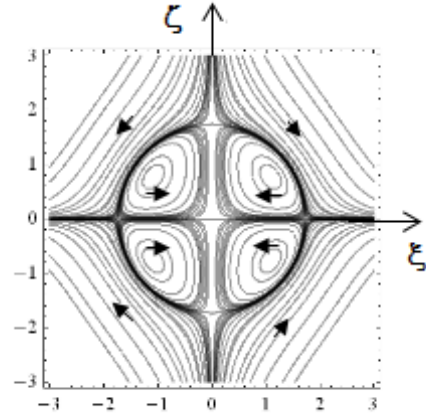


Fig. 17 Flow field within liquid droplet at the stagnation point of viscous counter flow [80].

The local radial and axial velocities corresponding to the stream function (103) are

$$\mathbf{v}_r = -\xi [1 - (\xi/R)^2 - 3(\zeta/R)^2]$$

$$\mathbf{v}_z = 2\xi [1 - 2(\xi/R)^2 - (\zeta/R)^2] \quad (104)$$

One notes that with the local velocity field given in (104) the solution (102) does not satisfy the classical form of *Helmholtz* vorticity equation (95). However, in close vicinity of the stagnation point ($r \approx 0$, $z \approx 0$) the local velocity field (104) reduces to

$$\mathbf{v}_{r\beta} = \mathbf{w}_{r\beta-1} = -\xi \quad , \quad \mathbf{v}_{z\beta} = \mathbf{w}_{z\beta-1} = 2\xi \quad (105)$$

that is identical in form but opposite in direction to the outer convective velocity field in (99). Therefore, as was noted earlier [80], because of the scale-invariant nature of the conservation equations, one expects a cascade of embedded concentric spherical flows at ever smaller scales to form around the stagnation point.

It is interesting to note that even if there were no liquid droplet at the stagnation point, it is expected that a small spherical region of gaseous recirculation flow like that shown in Fig. 17 will form around the stagnation point of viscous counter flow. In other words, for fluids with finite viscosity the critical singularity located at the stagnation point will be avoided by the global flow through the formation of such a closed region of secondary flow recirculation. The radius of such a secondary flow region is given by $R' = \sqrt{\nu/\Gamma}$ and hence depends on the viscosity and the rate of strain [79, 80].

Because of linearity of (101) the superposition principle applies such that the sum or products of solutions of (101) will also satisfy this equation. For example by (103) it can be shown that the flow within three concentric immiscible liquid droplets of radii $R_1 = 2$, $R_2 = 5$, and $R_3 = 10$ located at the stagnation point of gaseous counter flow finite jets is described by the product solution

$$\Psi = \xi^6 \zeta^3 (2 - \xi^2 / R^2 - \zeta^2 / R^2) (5 - \xi^2 / R^2 - \zeta^2 / R^2) (10 - \xi^2 / R^2 - \zeta^2 / R^2) \quad (106)$$

Some of the streamlines for flow within three concentric droplets calculated from (106) are shown in Fig. 18.

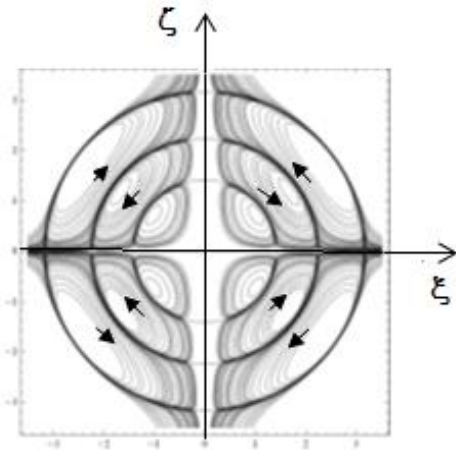


Fig. 18 Streamlines of concentric embedded spherical flows calculated from (106).

Looking at Figs. 17 and 18 it is seen that as one moves away from the central inner droplet the outer convective flow (99) is identified as the local feature of a larger spherical flow within the second droplet and hence $\mathbf{w}'_{\beta} = \mathbf{v}'_{\beta+1}$ gives

$$\begin{aligned} w_{r\beta} = v_{r\beta+1} &= \xi [1 - (\xi/R)^2 - 3(\zeta/R)^2] \quad , \\ w_{z\beta} = v_{z\beta+1} &= -2\zeta [1 - 2(\xi/R)^2 - (\zeta/R)^2] \quad (107) \end{aligned}$$

leading to the vorticity

$$\omega_{\theta\beta+1} = -14\xi\zeta / R^2 \quad (108)$$

with opposite sign of $\omega_{\theta\beta}$ in (102). The second droplet experiences yet a new “convective” velocity $\mathbf{w}_{\beta+1}$ at the next larger scale given by

$$\mathbf{w}_{r\beta+1} = -\xi \quad , \quad \mathbf{w}_{z\beta+1} = 2\zeta \quad (109)$$

that is similar to (99) but has opposite direction. The above hierarchy of embedded spherical flows with alternating sense of

rotation is recognized as one aspect of the important problem of cascades of vortices in turbulent flows and the well-known rhyme attributed to *Richardson* about big and little eddies [81].

**Big whirls have little whirls,
That feed on their velocity;
And little whirls have lesser whirls,
And so on to viscosity,**

Generation of cascades of embedded spherical vortices within locally strained flows (Fig. 18) could be identified as one possible mechanism of turbulent dissipation.

The result in Fig. 18 is also in harmony with perceptions of *Weizäcker* in cosmology as was emphasized by *Chandrasekhar* [81].

"Prominent role that Weizäcker ascribed to interplay between turbulence and rotation"

Another significant astrophysical aspect of the spherical flows shown in Figs. 17 and 18 is their relations to the well-known *Hill* spherical vortex [82, 83] formed within a liquid droplet in uniform gaseous flow. Hence, Fig. 17 could be viewed as two semi-spherical *Hill* vortices each vortex occupying a semi-spherical volume. Clearly the cascade of spherical flows in Fig. 18 is a good model of convective flows within stars. As an example it is known that the direction of magnetic polarization of volcanic rocks alternate every few million years with no known mechanism to account for such behavior. Clearly, reversal of polarization could not be due to change of the direction of the magnetic field of the entire planet earth that would be catastrophic. Examination of Fig. 18 suggests that successive generation and evolution of embedded spherical flows with alternating sense of rotation within the ionic plasma of a dynamo such as the planet earth discussed by *Elsasser* [84] could possibly account for such periodic changes in the direction of polarization.

IX. DERIVATION OF INVARIANT CLASSICAL FORMS OF CONSERVATION EQUATIONS

The invariant forms of conservation equations could be derived following classical integral methods by considering a volume element Γ shown in Fig. 19

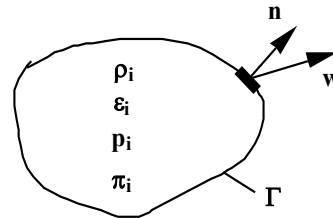


Fig. 19 Conservation of $(\rho_i, \epsilon_i, p_i, \pi_i)$ in an arbitrary domain Γ with unit outward normal \mathbf{n} .

with the unit outward normal \mathbf{n} and expressing mass, thermal energy, linear and angular momentum conservations as

$$\frac{\partial}{\partial t} \int \rho_{i\beta} dV_{\beta} = - \int \rho_{i\beta} \mathbf{w}_{\beta} \cdot \mathbf{n} dA_{\beta} + \int \mathfrak{R}_{i\beta} dV_{\beta} \quad (110)$$

$$\frac{\partial}{\partial t} \int \varepsilon_{i\beta} dV_{\beta} = - \int \varepsilon_{i\beta} \mathbf{w}_{\beta} \cdot \mathbf{n} dA_{\beta} \quad (111)$$

$$\frac{\partial}{\partial t} \int \mathbf{p}_{i\beta} dV_{\beta} = - \int \mathbf{p}_{i\beta} \mathbf{w}_{\beta} \cdot \mathbf{n} dA_{\beta} - \int \mathbf{P}_{ij\beta} \cdot \mathbf{n} dA_{\beta} \quad (112)$$

$$\frac{\partial}{\partial t} \int \boldsymbol{\pi}_{i\beta} dV_{\beta} = - \int \boldsymbol{\pi}_{i\beta} \mathbf{w}_{\beta} \cdot \mathbf{n} dA_{\beta} + \int \rho_{i\beta} \varepsilon_{ijk} \boldsymbol{\omega}_{j\beta} \mathbf{v}_i \cdot \mathbf{n} dA_{\beta} \quad (113)$$

For *Coriolis* force [77] in the last term of (113) substitution has been made from the identity

$$- \int \rho_{i\beta} \varepsilon_{ijk} \boldsymbol{\omega}_{j\beta} \mathbf{v}_i \cdot \mathbf{n} dA_{\beta} = \int \rho_{i\beta} \varepsilon_{ijk} \boldsymbol{\omega}_{j\beta} \mathbf{v}_i \cdot \mathbf{n} dA_{\beta} \quad (114)$$

By the application of *Gauss's* divergence theorem to (110)-(113) one arrives at

$$\frac{\partial \rho_{i\beta}}{\partial t} + \nabla \cdot (\rho_{i\beta} \mathbf{w}_{\beta}) = \mathfrak{R}_{i\beta} \quad (115)$$

$$\frac{\partial \varepsilon_{i\beta}}{\partial t} + \nabla \cdot (\varepsilon_{i\beta} \mathbf{w}_{\beta}) = 0 \quad (116)$$

$$\frac{\partial \mathbf{p}_{i\beta}}{\partial t} + \nabla \cdot (\mathbf{p}_{i\beta} \mathbf{w}_{\beta}) = - \nabla \cdot \mathbf{P}_{ij\beta} \quad (117)$$

$$\frac{\partial \boldsymbol{\pi}_{i\beta}}{\partial t} + \nabla \cdot (\boldsymbol{\pi}_{i\beta} \mathbf{w}_{\beta}) = \rho_{i\beta} \boldsymbol{\omega}_{\beta} \cdot \nabla \mathbf{v}_{i\beta} \quad (118)$$

In the above formulation the flux of quantities $(\rho_{i\beta}, \varepsilon_{i\beta}, \mathbf{p}_{i\beta}, \boldsymbol{\pi}_{i\beta})$ across the system boundary occurs by convective velocity that is now expressed as the vector sum of local plus diffusion velocities as

$$\mathbf{w}_{\beta} = \mathbf{v}_{j\beta} + \mathbf{V}_{ij\beta} \quad (119)$$

that is different from (21c). To examine the difference between (119) and (21c) it is first noted that diffusion velocity relates to the mean of the peculiar velocity

$$\mathbf{u}_{i\beta} - \mathbf{v}_{i\beta} = \mathbf{V}'_{ij\beta} \quad (120)$$

Also, one can express the peculiar and diffusion velocities of scale EMD from particle speed profiles shown in Fig. 6 as

$$\mathbf{u}_{im} - \mathbf{v}_{im} = \mathbf{V}'_{ijm} \quad \mathbf{v}_{m,mp} \leq \mathbf{v}_{im} \leq \mathbf{u}_{im} \quad (120a)$$

$$\mathbf{v}_{im} - \mathbf{w}_m = \mathbf{V}_{ijm} \quad \mathbf{w}_m \leq \mathbf{v}_{im} \leq \mathbf{v}_{m,mp} \quad (120b)$$

From the overlap region between velocity distribution of EMD and ECD fields in Fig. 6 one identifies the equivalence of (120b) with

$$\mathbf{u}_{ic} - \mathbf{v}_{ic} = \mathbf{V}'_{ijc} \quad \mathbf{v}_{c,mp} \leq \mathbf{v}_{ic} \leq \mathbf{u}_{ic} \quad (120c)$$

Therefore, according to (3) since the equality $\mathbf{w}_{\beta} = \mathbf{v}_{j\beta} >$ leads to the inequality $\mathbf{v}_{i\beta} > \mathbf{w}_{i\beta}$ the sign of the diffusion velocity $\mathbf{V}_{ij\beta}$ will be positive and this is insured by having a negative sign in its definition

$$\mathbf{V}_{\beta hg} = -v_{i\beta} \nabla \ln(\mathbf{p}_{i\beta}) \quad (121)$$

In (119) on the other hand the sign of the diffusion velocity vector is not anticipated by retaining the negative sign in its definition in (121),

Substituting from (119), (21) and from (48) for the stress tensor into (115)-(118) and assuming constant transport coefficients and unity *Schmidt* and *Prandtl* numbers $\text{Sc}_{\beta} = \text{Pr}_{\beta} = 1$ result in the *invariant forms of conservation equations for chemically reactive fields*

$$\frac{\partial \rho_{i\beta}}{\partial t} + \mathbf{v}_{\beta} \cdot \nabla \rho_{i\beta} = D_{i\beta} \nabla^2 \rho_{i\beta} + \mathfrak{R}_{i\beta} \quad (122)$$

$$\frac{\partial \mathbf{T}_{i\beta}}{\partial t} + \mathbf{v}_{\beta} \cdot \nabla \mathbf{T}_{i\beta} = \alpha_{i\beta} \nabla^2 \mathbf{T}_{i\beta} + h_{i\beta} \mathfrak{R}_{i\beta} / \rho_{i\beta} c_{pi\beta} \quad (123)$$

$$\begin{aligned} \frac{\partial \mathbf{v}_{i\beta}}{\partial t} + \mathbf{v}_{\beta} \cdot \nabla \mathbf{v}_{i\beta} &= \nu_{i\beta} \nabla^2 \mathbf{v}_{i\beta} - \frac{\nabla \mathbf{p}_{i\beta}}{\rho_{i\beta}} \\ &+ \frac{\nu_{i\beta}}{3} \nabla (\nabla \cdot \mathbf{v}_{i\beta}) - \mathbf{v}_{i\beta} \mathfrak{R}_{i\beta} / \rho_{i\beta} \end{aligned} \quad (124)$$

$$\begin{aligned} \frac{\partial \boldsymbol{\omega}_{i\beta}}{\partial t} + \mathbf{v}_{\beta} \cdot \nabla \boldsymbol{\omega}_{i\beta} &= \nu_{i\beta} \nabla^2 \boldsymbol{\omega}_{i\beta} + \boldsymbol{\omega}_{\beta} \cdot \nabla \mathbf{v}_{i\beta} - \boldsymbol{\omega}_{i\beta} \mathfrak{R}_{i\beta} / \rho_{i\beta} \\ & \end{aligned} \quad (125)$$

5that appear similar to the classical forms of conservation equations except for the reactive terms in (124)-(125). It is emphasized however that even though the final results are mathematically identical there are subtle and important fundamental differences between (122)-(125) and classical conservation equations besides the fact that the continuity equation (122) contains a diffusion term even for a pure fluid that is absent in the classical continuity equation (29).

To relate (122)-(125) to classical conservation equations one must start with the most elementary question namely the definition of fluid velocity. In classical fluid mechanics the local fluid velocity $\mathbf{v} = \mathbf{v}_{\beta} = \mathbf{v}_m$ is usually defined as the average of molecular velocity $\mathbf{u}_{\beta} = \mathbf{u}_m$ by (2). Therefore,

conventional fluid mechanics is considered to be associated with laminar-molecular-dynamics LMD scale (Fig. 2) with relevant velocities ($\mathbf{u}_m, \mathbf{v}_m, \mathbf{w}_m$). However, it is known that the most probable molecular speed is the velocity of sound, $\mathbf{v}_{m,mp} = 358 \text{ m/s}$ in air at standard conditions [73], that is a constant at constant temperature. As a result, the velocity of fluid mechanics should correspond to higher scale than LMD. This implies that stationary fluids should be identified with ECD and consequently conventional fluid dynamics should correspond to laminar-cluster-dynamics LCD scale with relevant velocities ($\mathbf{u}_c, \mathbf{v}_c, \mathbf{w}_c$) as shown in Figs. 2 and 6. The evidence for the existence of intermediate scale of ECD separating the statistical field of EMD from EED is the phenomenon of *Brownian* motions as discussed in [38, 39].

The exact nature of fluid mechanic velocity is best revealed in the field of combustion where distinction between molecular specie velocity \mathbf{u}_{im} , mean velocity of specie \mathbf{v}_{im} , and mass-average velocity \mathbf{v}_o of all species i.e. mixture velocity become necessary [42]. In the model being described herein, one associates “atomic”, “element”, and “system” velocities for identification of different scales as opposed to identity of specific molecular species. Accordingly, the velocity of conventional fluid mechanics should be identified as the mass-average velocity \mathbf{v}_o as noted by *Williams* [42] and be identified as $\mathbf{v}_o = \langle \langle \mathbf{u}_{im} \rangle \rangle = \langle \mathbf{v}_{im} \rangle = \mathbf{w}_m$.

The conservation equations (122)-(125) at LCD scale $\beta = c$ with local velocity $\mathbf{v}_c = \mathbf{w}_m$ given by *Navier-Stokes* equation (124) therefore represent the conventional field of fluid mechanics. This is because \mathbf{w}_m as system velocity of LMD cannot appear in differential equations since by definition it is not locally defined i.e. its value at any position will depend on velocity at other locations remote from this position as discussed earlier [34]. It appears therefore that due to the scale invariant nature of the problem the conservation equations (122)-(125) at LCD scale coincide with the classical forms of conservation equations that are conventionally conceived to correspond to the lower scale of LMD. Many of the concepts and results described in this study are in need of further future examination.

X. CONCLUDING REMARKS

A scale-invariant model of statistical mechanics was applied to introduce the invariant *Boltzmann* equation and the associated invariant *Enskog* equation of change. The invariant modified forms of mass, thermal energy, linear and angular momentum conservation equations were derived. The modified form of continuity equation with a diffusion term, even for pure fluid, was presented that allowed for the description of internal structure of normal shocks in pure gaseous systems. Also, a modified form of equation of motion with distinction between convective and local velocity was presented that is similar to *Carrier* equation of motion. Finally, vorticity was defined as the mean iso-spin of particles leading to a modified form of

Helmholtz vorticity equation that was solved for the problem of spherical flow within a liquid droplet located at the stagnation point of opposed gaseous axisymmetric finite jets. Finally, by application of integral methods classical forms of conservation equations were derived. The invariant nature of conservation equations across broad range of spatio-temporal scales described herein is in harmony with the observed universal occurrence of fractals in physical science [85].

REFERENCES

- [1] L. de Broglie, “Interference and corpuscular light,” *Nature* **118**, 2969, 1926, pp. 441-442; “Sur la possibilité de relier les phénomènes d’interférence et de diffraction à la théorie des quanta de lumière,” *C. R. Acad. Sci. Paris*, **183**, 1927, pp. 447-448; “La structure atomique de la matière et du rayonnement et la mécanique ondulatoire,” **184**, 1927, pp. 273-274; “Sur le rôle des ondes continues en mécanique ondulatoire,” **185**, 1927, pp. 380-382
- [2] L. de Broglie, *Non-Linear Wave Mechanics: A Causal Interpretation*, Elsevier, New York, 1960.
- [3] L. de Broglie, “The reinterpretation of wave mechanics,” *Found. Phys.* **1**, 5, 1970, pp. 5-15.
- [4] E. Madelung, “Quantentheorie in hydrodynamischer form,” *Z. Physik*. **40**, 1926, pp. 332-326.
- [5] E. Schrödinger, “Über die umkehrung der naturgesetze,” *Sitzber Preuss Akad Wiss Phys-Math Kl*, 1931, p. 144-153.
- [6] R. Fürth, “Über einige beziehungen zwischen klassischer statistik und quantenmechanik,” *Z. Phys.* **81**, 1933, pp. 143-162.
- [7] D. Bohm, “A suggested interpretation of the quantum theory in terms of “hidden” variables. I,” *Phys. Rev.* **85**, 2, 1952, pp.166-179.
- [8] T. Takabayasi, “On the foundation of quantum mechanics associated with classical pictures,” *Prog. Theor. Phys.* **8**, 2, 1952, pp. 143-182.
- [9] D. Bohm, and J. P. Vigier, “Model of the causal interpretation of quantum theory in terms of a fluid with irregular fluctuations,” *Phys. Rev.* **96**, 1, 1954, pp. 208-217.
- [10] E. Nelson, “Derivation of the Schrödinger equation from Newtonian mechanics,” *Phys. Rev.* **150**, 4, 1966, pp. 1079-1085.
- [11] E. Nelson, *Quantum Fluctuations*, Princeton University Press, Princeton, New Jersey, 1985.
- [12] L. de la Peña, “New foundation of stochastic theory of quantum mechanics,” *J. Math. Phys.* **10**, 9, 1969, pp. 1620-1630.
- [13] L. de la Peña, and A. M. Cetto, “Does quantum mechanics accept a stochastic support?” *Found. Phys.* **12**, 10, 1982, pp. 1017-1037.
- [14] A. O. Barut, “Schrödinger’s interpretation of ψ as a continuous charge distribution,” *Ann. der Phys.* **7**, 4-5, 1988, pp. 31-36.
- [15] A. O. Barut, and A. J. Bracken, “Zitterbewegung and the internal geometry of the electron,” *Phys. Rev. D* **23**, 10, 1981, pp. 2454-2463.
- [16] J. P. Vigier, “De Broglie waves on Dirac aether: A testable experimental assumption,” *Lett. Nuvo Cim.* **29**, 14, 1980, pp. 467-475; Ph. Gueret, and J. P. Vigier, “De Broglie’s wave particle duality in the stochastic interpretation of quantum mechanics: A testable physical assumption,” *Found. Phys.* **12**, 11, 1982, pp. 1057-1083; C. Cufaro Petroni, and J. P. Vigier, “Dirac’s aether in relativistic quantum mechanics,” *Found. Phys.* **13**, 2, 1983, pp. 253-286; J. P. Vigier, “Derivation of inertia forces from the Einstein-de Broglie-Bohm (E.d.B.B) causal stochastic interpretation of quantum mechanics,” *Found. Phys.* **25**, 10, 1995, pp. 1461-1494.
- [17] F. T. Arecchi, and R. G. Harrison, *Instabilities and Chaos in Quantum Optics*, Springer-Verlag, Berlin, 1987.
- [18] J. C. Maxwell, “On the dynamic theory of gases,” *Phil. Trans. Roy. Soc. London* **157**, 49 (1867).
- [19] L. Boltzmann, “Weitere Studien uber das Warmegleichgewicht unter Gasmoleculen,” *Sitzungsberichte Akad. Wiss., Vienna, Part II*, **66**, 275 (1872). English translation in: Brush, G., S., *Kinetic Theory*, Vol.1-3 (Pergamon Press, New York, 1965).
- [20] L. Boltzmann, *Lectures on Gas Theory* (Dover, New York, 1964).
- [21] O. Reynolds, “On the dynamical theory of incompressible viscous fluid and the determination of the criterion,” *Phil. Trans. Roy. Soc. A* **186**, 1, 1895, pp. 23-164.

- [22] D. Enskog, "Kinetische theorie der vorgänge in massig verdünnten gasen," by Almqvist and Wiksells Boktryckeri-A.B., Uppsala, 1917. English translation in Ref. [60], pp. 125-225.
- [23] G. I. Taylor, "Statistical theory of turbulence-Parts I-IV," *Proc. Roy. Soc. A* **151**, 873, 1935, pp. 421-478.
- [24] T. Kármán, and L. Howarth, "On the statistical theory of isotropic turbulence," *Proc. Roy. Soc. A* **164**, 917, 1938, pp. 192-215.
- [25] H. P. Robertson, "The invariant theory of isotropic turbulence," *Proc. Camb. Phil. Soc.* **36**, 1940, pp. 209-223.
- [26] A. N. Kolmogoroff, "Local structure on turbulence in incompressible fluid," *C. R. Acad. Sci. U. R. S. S.* **30**, 1941, pp. 301-305; "Dissipation of energy in locally isotropic turbulence," *C. R. Acad. Sci. U. R. S. S.* **32**, 1942, p. 19-21; "A refinement of previous hypothesis concerning the local structure of turbulence in a viscous incompressible fluid at high Reynolds number," *J. Fluid Mech.* **13**, 1962, pp. 82-85.
- [27] A. M. Obukhov, "On the distribution of energy in the spectrum of turbulent flow," *C. R. Acad. Sci. U. R. S. S.* **32**, 1941, pp. 19-22; "Some specific features of atmospheric turbulence," *J. Fluid Mech.* **13**, 1962, pp. 77-81.
- [28] S. Chandrasekhar, "Stochastic problems in physics and astronomy," *Rev. Mod. Phys.* **15**, 1, 1943, pp. 1-89.
- [29] S. Chandrasekhar, *Stochastic, Statistical, and Hydrodynamic Problems in Physics and Astronomy*, Selected Papers, vol.3, University of Chicago Press, Chicago, 1989, pp. 199-206.
- [30] W. Heisenberg, "On the theory of statistical and isotropic turbulence," *Proc. Roy. Soc. A* **195**, 1948, pp. 402-406; "Zur statistischen theorie der turbulenz," *Z. Phys.* **124**, 7-12, 1948, p. 628-657.
- [31] G. K. Batchelor, *The Theory of Homogeneous Turbulence*, Cambridge University Press, Cambridge, 1953.
- [32] L. D. Landau, and E. M. Lifshitz, *Fluid Dynamics*, Pergamon Press, New York, 1959.
- [33] H. Tennekes, and J. L. Lumley, *A First Course In Turbulence*, MIT Press, 1972.
- [34] S. H. Sohrab, "Transport phenomena and conservation equations in multicomponent chemically-reactive ideal gas mixtures," *Proceeding of the 31st ASME National Heat Transfer Conference*, HTD-Vol. **328**, 1996, pp. 37-60.
- [35] S. H. Sohrab, "A scale invariant model of statistical mechanics and modified forms of the first and the second laws of thermodynamics," *Rev. Gén. Therm.* **38**, 1999, pp. 845-853.
- [36] S. H. Sohrab, "Derivation of invariant forms of conservation equations from the invariant Boltzmann equation," In: *Theoretical and Experimental Aspects of Fluid Mechanics*, S. H. Sohrab, H. C. Catrakis, and F. K. Benra (Eds.), WSEAS Press, 2008, ISBN: 978-960-6766-30-5, pp. 27-35.
- [37] S. H. Sohrab, "Universality of a scale invariant model of turbulence and its quantum mechanical foundation," In: *Recent Advances in Fluid Mechanics & Aerodynamics*, S. Sohrab, H. Catrakis, and N. Kobasko (Eds.), WSEAS Press, 2009, ISBN: 978-960-474-106-9, pp. 134-140.
- [38] S. H. Sohrab, "Invariant Planck energy distribution law and its connection to the Maxwell-Boltzmann distribution function," *WSEAS Transactions on Mathematics* **6**, 2, 2007, pp. 254-262.
- [39] S. H. Sohrab, "Quantum theory of fields from Planck to cosmic scales," *WSEAS Transactions on Mathematics* **9**, 8, 2010, pp. 734-756.
- [40] R. S. de Groot, and P. Mazur, *Nonequilibrium Thermodynamics*, North-Holland, 1962.
- [41] H. Schlichting, *Boundary-Layer Theory*, McGraw Hill, New York, 1968.
- [42] F. A. Williams, *Combustion Theory*, Addison Wesley, New York, 1985.
- [43] J. O. Hirschfelder, C. F. Curtiss, and R. B. Bird, *Molecular Theory of Gases and Liquids*, Wiley, New York, 1954.
- [44] S. Chapman, and T. G. Cowling, *The Mathematical Theory of Non-uniform Gases*, Cambridge University Press, Cambridge, 1953.
- [45] G. Carrier, "On slow viscous flow," Nonr-653-00-1, 1953.
- [46] Townsend, A. A., "The measurement of double and triple Correlation derivatives in isotropic turbulence," *Proc. Camb. Phil. Soc.* **43**, 560, 1947, pp. 560-570.
- [47] M. Planck, *The Theory of Heat Radiation*, Dover, New York, 1991.
- [48] M. Planck, "On the Law of the Energy Distribution in the Normal Spectrum," *Ann. der Phys.* **4**, 1901, pp. 553-558.
- [49] C. W. Van Atta, and W. Y. Chen, "Measurements of spectral energy transfer in gridturbulence," *J. Fluid Mech.* **38**, 1969, pp. 743-763.
- [50] M. T. Landahl, and E. Mollo-Christensen, *Turbulence and Random Processes in Fluid Mechanics*, Cambridge University Press, Cambridge, 1992, p. 62.
- [51] I. Marusic, R. Mathis, and N. Hutchins, "Predictive model for wall-bounded turbulent flow" *Science* **329**, July 2010, pp. 193-196.
- [52] W. D. McComb, and V. Shanmugasundaram, "Numerical calculation of decaying isotropic turbulence using the LET theory," *J. Fluid Mech.* **143**, 1984, pp. 95-123.
- [53] G. S. Saddoughi, and V. S. Veeravalli, "Local isotropy in turbulent boundary layers at high Reynolds number," *J. Fluid Mech.* **268**, 1994, pp. 333-372.
- [54] C. C. Lin, *Turbulent Flows and Heat Transfer*, Princeton University Press, Princeton, 1959.
- [55] L. S. C. Ling, and T. T. Huang, "Decay of weak turbulence," *J. Phys. Fluids.* **13**, 12, 1970, pp. 2912-2924.
- [56] L. J. Lumley, G. Berkooz, J. Elezgaray, P. Holmes, A. Poje, and C. Volte, "Fundamental aspects of incompressible and compressible turbulent flows," In: *Simulation and Modeling of Turbulent Flows*. Gatski, B. T., Hussaini, M. Y., Lumley, L. J. (Eds.), Oxford University Press 1996, pp. 5-78.
- [57] S. H. Sohrab, "Some implications of a scale invariant model of statistical mechanics to transport phenomena," In: *Recent Advances in Systems*, N. Mastorakis, V. Mladenov, Z. Bojkovic, S. Kartalopoulos, A. Varonides, and M. Jha (Eds.), WSEAS Press, 2009, ISBN: 978-960-474-097-0, pp. 557-568.
- [58] H. J. Lugt, *Vortex Flow in Nature and Technology*, Wiley, New York, 1983.
- [59] R. B. Bird, E. W. Stewart, and N. E. Lightfoot, *Transport Phenomena*, Wiley, New York, 1960.
- [60] W. E. Olmstead, "Reciprocal relationships in viscous hydrodynamics," *Acta Mech.* **21** (1975), pp. 289-300.
- [61] M. Roper, and M. P. Brenner, "A nonperturbative approximation for the moderate Reynolds number Navier-Stokes equations," *PNAS* **106**, 9, 2009, pp. 2977-2982.
- [62] S. H. Sohrab, "A modified hydro-thermo-diffusive theory of shock waves," *WSEAS Transactions on Heat and Mass Transfer* **1** (5), pp: 606-611 (2007).
- [63] F. S. Sherman, "A low-density wind tunnel study of shock wave structure and relaxation phenomena in gases," *NACA Tech. Notes* 3298 (1955).
- [64] O. Darrigol, "Between hydrodynamics and elasticity theory: The first five births of the Navier-Stokes equation," *Arch. Hist. Exact Sci.* **56**, 2002, pp. 95-150.
- [65] O. Darrigol, *World of Flow*, Oxford University Press, New York, 2005.
- [66] A. B. Bahatia, and, R. N. Singh, *Mechanics of Deformable Media*, IOP publication, Boston, 1986, p. 153.
- [67] S. H. Sohrab, "A modified theory of turbulent flow over a flat plate," in *Fluid Mechanics and Aerodynamics*, S. H. Sohrab, H. Catrakis, and N. Kobasko, and S. Necasova (Eds), pp: 71-79, WSEAS Press, 2007, ISBN: 978-960-6766-99-7.
- [68] R. C. Martinelli, "Heat transfer to molten metals," *Transactions, ASME* **69**, 947 (1947).
- [69] H. Ueda, and J. O. Hinze, "Fine-structure in the wall region of a turbulent boundary layer," *J. Fluid Mech.* **67**, 57 (1989).
- [70] M. V. Zagarola, A. E. Perry, and, A. J. Smits, "Log laws or power laws: The scaling in the overlap region," *Phys. Fluids* **9** (7), 2094 (1997)
- [71] Lancien, E. Lajeunesse, and F. Metivier, "Near wall velocity measurements by particle-tracking," arXiv:physics/0701131v1 [physics.flu-dyn], 11 January 2007.
- [72] C. D. Meinhart, S. T. Wereley, and, J. G. Santiago, "PIV measurements of a micro channel flow," *Experiments in Fluids* **27**, 414 (1999).
- [73] S. H. Sohrab, "Some implications of a scale invariant model of statistical mechanics to classical and relativistic thermodynamics," in *Recent Researches in Electric Power and Energy Systems*, Ki Young

- Kim, Dario Assante, Marian Ciontu, and Jana Jirickova (Eds.), pp: 298-313, WSEAS press, 2013, ISBN: 978-960-474-328-5.
- [74] R. Clausius, "Ueber die Art der Bewegung, welche wir Wärme nennen", *Ann. der Phys.* **100**, 353 (1957). *Phil. Mag.* **14**, 108 (1957).
- [75] S. H. Sohrab, "Modified theory of laminar boundary layer flow over a flat plate," *IASME Transactions* **2**, (8), pp: 1389-1394 (2005).
- [76] S. Dhawan, "Direct measurements of skin friction," *NACA Technical Note* 2567 (1952).
- [77] P. K. Kundu, *Fluid Mechanics*, Academic Press, New York, 1990.
- [78] S. H. Sohrab, "Modified theories of axi-symmetric stagnation-point laminar boundary layer flow and counterflow jets," *IASME Transactions* **2** (7), pp: 1097- 1105 (2005).
- [79] S. H. Sohrab, "Hydrodynamics of spherical flows and geometry of premixed flames near the stagnation-point of axisymmetric viscous counterflows," *Fifth International Microgravity Combustion Workshop*, NASA, May 18-20, 1999, Cleveland, Ohio, pp.85-88.
- [80] S. H. Sohrab, "Modified form of the Helmholtz vorticity equation and its solution for spherical flow within a droplet in uniform or counter flow streams," *IASME Transactions*. Issue 4, Vol **1**, pp.634-640 (2004).
- [81] S. Chandrasekhar, "Turbulence- A physical theory of astrophysical interest," in Ref, 29 (1949).
- [82] M. J. M. Hill, "On a spherical vortex," *Phil. Trans. Roy. Soc. A* **185**, 213 (1894).
- [83] R. L. Panton, *Incompressible Flow*, Wiley, New York, 1996, p. 333.
- [84] W. M. Elsasser, "The earth as a dynamo," *Scientific American*, May, (1958).
- [85] H. Takayasu, *Fractals in Physical Science*, Wiley, New York, 1990.

Analytical solutions of axysymmetric problems of compression (expansion) of thick-walled spherical and cylindrical shells made of incompressible viscoplastic material under action of external dynamic loading

Alexey B. Kiselev

Abstract—Exact solutions of the one-dimensional problems of compression (expansion) of thick-walled spherical and cylindrical shells made of incompressible viscoplastic material Sokolovsky-Perzyna type under action of external dynamic loading. Problems solved in Lagrange variables.

Keywords—Analytical solutions, incompressibility, viscoplastic material, dynamic loading.

I. INTRODUCTION

Not many exact solutions of problems of dynamic elastoviscoplasticity with initial and boundary conditions are known, in view of their particular complexity (see [1-7] and the bibliography given there). In articles [4-6] exact solutions of one-dimensional non-stationary problems of the adiabatic compression and expansion of thick-walled spherical and cylindrical shells made of incompressible viscoplastic material are obtained, assuming that, at the initial instant of time, the radial velocity distributions satisfy the conditions of incompressibility of the shell material. In [4] solution obtained in assumption that first invariant of stress tensor equal zero. In [5, 6] this simplifying assumption not exploit and for obtaining solution was used low of conservation of total energy. Unlike of papers [2, 3], where investigated processes of collapse and expansion of spherical pores in incompressible viscoplastic material under constant action, exact solutions in present paper are obtained under dynamic external loading.

II. COMPRESSION OF A SPHERICAL SHELL

In one-dimensional approximation (all parameters depend on the radial Lagrange coordinate R and the time t), we will consider the process of adiabatic compression of a spherical

shell, the inner and outer radii vary with time as $r_0 = r(R_0, t)$ and $r_1 = r(R_1, t)$ respectively, where R_0 and R_1 are the inner and outer radii when $t = 0$ (see Fig. 1).

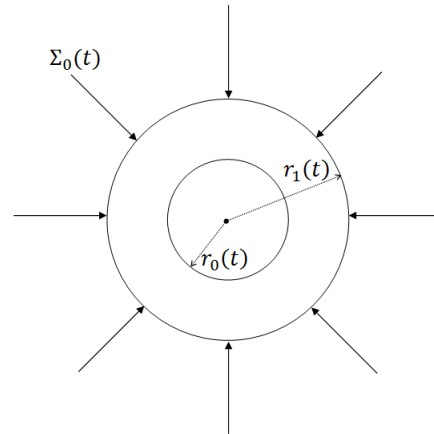


Fig. 1

We will make the following simplifying assumptions: the behavior of the shell material described by the equations of Sokolovsky-Perzyna type elastoviscoplastic model [8]:

$$\dot{\epsilon}_{ij}^e = \frac{\dot{S}_{ij}}{2\mu} + \frac{S_{ij}(\sqrt{S_{ij}S_{ij}} - \sqrt{\frac{2}{3}}Y_0)}{2\eta\sqrt{S_{ij}S_{ij}}} H(\sqrt{S_{ij}S_{ij}} - \sqrt{\frac{2}{3}}Y_0). \quad (1)$$

Here $\dot{\epsilon}_{ij}$ and S_{ij} are the deviators of the rates of deformations and stresses, Y_0 is the yield point for simple stretching, $H(x)$ is the Heaviside unit function, and μ and η are shear modulus and the dynamic viscosity of the material;

elastic deformations are neglected: $\dot{\epsilon}_{ij}^e = 0$, $\dot{\epsilon}_{ij} = \dot{\epsilon}_{ij}^p$ ($\dot{\epsilon}_{ij}^e$, $\dot{\epsilon}_{ij}^p$ and $\dot{\epsilon}_{ij} = \dot{\epsilon}_{ij}^e + \dot{\epsilon}_{ij}^p$ are the rates of elastic, plastic and

This work was supported by the Russian Foundation on Basic Research under Grant 12-01-00425.

Professor A. B. Kiselev is with Moscow Lomonosov State University, Mechanics and Mathematics Faculty (e-mail: akis2006r@yandex.ru).

complete deformations respectively); plastic flow is incompressible: $\dot{\epsilon}_{kk}^p = \dot{\epsilon}_{kk} = 0$.

By virtue of these assumptions, equations (1) reduce to a single equation

$$\sigma_R - \sigma_\theta = Y_0 + 2\eta(\dot{\epsilon}_R - \dot{\epsilon}_\theta). \quad (2)$$

Here v is a radial velocity, $\dot{\epsilon}_R = \partial v / \partial R$, $\dot{\epsilon}_\theta = v / R$ are the radial and circumferential rates of deformation, and σ_R and σ_θ are the radial and circumferential stresses.

The condition for the material to be incompressible $\dot{\epsilon}_R + 2\dot{\epsilon}_\theta = 0$ gives the equation for the velocity distribution of the velocities in the shell:

$$\frac{\partial v}{\partial R} + 2\frac{v}{R} = 0. \quad (3)$$

Its solution has the form:

$$v = \frac{C(t)}{R^2}. \quad (4)$$

Here $C(t) \leq 0$, since place compression of the shell occurs and $v \leq 0$.

The equation of motion has the form

$$\rho \dot{v} = \frac{\partial \sigma_R}{\partial R} + 2\frac{\sigma_R - \sigma_\theta}{R}. \quad (5)$$

Here ρ is the density of shell material; and a dot above a symbol here and henceforth denotes a material derivative with respect to time.

Set next boundary conditions:

$$\sigma_R|_{R=R_1} = \Sigma(t) < 0, \quad \sigma_R|_{R=R_0} = 0. \quad (6)$$

If value of external loading in initial instant of time $\Sigma(0)$ more some critical value, which we will indicate lower, then medium completely pass in plastic condition. Namely such loading are considered.

Substituted (2), (4) to equation of motion and integrate over radius R with taking account of boundary condition (6), we obtained ordinary differential equation for function $C(t)$:

$$\dot{C}(t) + \alpha C(t) = \beta \Sigma(t) + \gamma. \quad (7)$$

Here

$$\alpha = \frac{4\eta(R_1^2 + R_1R_0 + R_0^2)}{\rho_0 R_1^2 R_0^2}, \quad \beta = \frac{R_1 R_0}{\rho_0 (R_1 - R_0)},$$

$$\gamma = \frac{2Y_0 R_1 R_0}{\rho_0 (R_1 - R_0)} \ln \frac{R_1}{R_0}.$$

Taking into account the fact that, at the initial instant of time $C(0) = 0$, we obtain from equation (7)

$$C(t) = \beta e^{-\alpha t} \int_0^t e^{\alpha t} \Sigma(t) dt + \frac{\gamma}{\alpha} (1 - e^{-\alpha t}). \quad (8)$$

Taking into account the fact that acceleration of shell in initial instant of time under compression is negative, i.e. $\dot{C}(0) < 0$, taking restriction of external pressure on shell:

$$\Sigma(0) < -\frac{\gamma}{\beta} = -2Y_0 \ln \frac{R_1}{R_0}. \quad (9)$$

Value $\Sigma_{\min} = 2Y_0 \ln \frac{R_1}{R_0}$ is effective yield limit under multifold compression. This result are obtained earlier in paper [2].

In case when external pressure to shell is constant, i.e.

$\Sigma(t) = \Sigma_0 = \text{const} < -2Y_0 \ln \frac{R_1}{R_0}$, we will find that

$$C(t) = \frac{1}{\alpha} (\beta \Sigma_0 + \gamma) (1 - e^{-\alpha t}). \quad (10)$$

Moving value of Euler coordinate for material particle with Lagrange coordinate R is:

$$r(R, t) = R \left[1 + \frac{\beta \Sigma_0 + \gamma}{\alpha R^3} \left(t + \frac{e^{-\alpha t} - 1}{\alpha} \right) \right]. \quad (11)$$

Obtain equation for moment of collapse for incompressible spherical shell $t = t_s^*$ (i.e. when $r(R_0, t_s^*) = 0$), for which obtained solution have physical meaning:

$$e^{-\alpha t_s^*} = \alpha t_s^* + 1 - \frac{R_0^3 \alpha^2}{\beta \Sigma_0 + \gamma}. \quad (12)$$

Under condition (9) equation (12) always have unique solution which not express from elementary functions, but numerical solution of equation (12) not represent a problem.

III. COMPRESSION OF A CYLINDRICAL SHELL

In case of a cylindrical shell, with the above assumptions, and by virtue of the condition that there displacements of the points of the shell along the z axis, i.e., the deformation rate $\dot{\epsilon}_z = 0$, we reduce equation (1) to the form

$$\sigma_R - \sigma_\theta = \frac{2}{\sqrt{3}} Y_0 + 2\eta(\dot{\epsilon}_R - \dot{\epsilon}_\theta). \quad (13)$$

Taking into account the condition for the medium to be incompressible $\dot{\epsilon}_R + \dot{\epsilon}_\theta = 0$, similar to the case of a spherical shell, instead of relations (3) – (5), (7) – (12) we obtain

$$\frac{\partial v}{\partial R} + \frac{v}{R} = 0. \quad (14)$$

$$v = \frac{B(t)}{R}, \quad B(t) \leq 0. \quad (15)$$

$$\rho_0 \dot{v} = \frac{\partial \sigma_R}{\partial R} + \frac{\sigma_R - \sigma_\theta}{R}. \quad (16)$$

$$\dot{B}(t) + \bar{\alpha} B(t) = \bar{\beta} \Sigma(t) + \bar{\gamma}. \quad (17)$$

$$\bar{\alpha} = \frac{2\eta(R_1^2 - R_0^2)}{\rho_0 R_1^2 R_0^2 \ln(R_1 / R_0)}, \quad \bar{\beta} = \frac{1}{\rho_0 \ln(R_1 / R_0)}, \quad \bar{\gamma} = \frac{Y_0}{\sqrt{3} \rho_0}.$$

$$B(t) = \bar{\beta} e^{-\bar{\alpha} t} \int_0^t e^{\bar{\alpha} t} \Sigma(t) dt + \frac{\bar{\gamma}}{\bar{\alpha}} (1 - e^{-\bar{\alpha} t}). \quad (18)$$

$$\Sigma(0) < -\frac{\bar{\gamma}}{\bar{\beta}} = -\frac{Y_0}{\sqrt{3}} \ln \frac{R_1}{R_0}. \quad (19)$$

$$\Sigma(t) = \Sigma_0 = const < -\frac{Y_0}{\sqrt{3}} \ln \frac{R_1}{R_0}:$$

$$B(t) = \frac{1}{\bar{\alpha}} (\bar{\beta} \Sigma_0 + \bar{\gamma}) (1 - e^{-\bar{\alpha} t}). \quad (20)$$

$$r(R, t) = R \left[1 + \frac{\bar{\beta} \Sigma_0 + \bar{\gamma}}{\bar{\alpha} R^3} \left(t + \frac{e^{-\bar{\alpha} t} - 1}{\bar{\alpha}} \right) \right]. \quad (21)$$

$$e^{-\bar{\alpha} t_c^*} = \bar{\alpha} t_c^* + 1 - \frac{R_0 \bar{\alpha}^2}{\bar{\beta} \Sigma_0 + \bar{\gamma}}. \quad (22)$$

IV. ABOUT EXPRESSION OF A SPHERICAL AND CYLINDRICAL SHELLS

In case of a shells expression instead of boundary conditions (6), we set up the next conditions

$$\sigma_R |_{R=R_0} = 0, \quad \sigma_R |_{R=R_1} = \Sigma(t) > 0. \quad (23)$$

It is easy to see, that obtain solutions for one-dimensional problems of compression of thick-walled spherical and cylindrical shells made from incompressible viscoplastic material may be used and for problems of shells extension. For this sufficiently in all the formulae to replace Y_0 on $(-Y_0)$. In case of shells extension under $C(t) \geq 0$, $B(t) \geq 0$ lose sense concept of time shells collapse t_s^* , t_c^* . And condition for value of external loading in initial instant of time moment (9), (19) for spherical and cylindrical shells are next form respectively:

$$\Sigma(0) > -\frac{\gamma}{\beta} = 2Y_0 \ln \frac{R_1}{R_0}, \quad \Sigma(0) > -\frac{\bar{\gamma}}{\bar{\beta}} = \frac{Y_0}{\sqrt{3}} \ln \frac{R_1}{R_0}. \quad (24)$$

Consider case of extension of spherical shell then loading have graduated form:

$$\Sigma(t) = \Sigma_0 H(T - t), \quad \Sigma_0 = const > 2Y_0 \ln \frac{R_1}{R_0}. \quad (25)$$

Here T is the loading time.

Substituted (25) to (8) and change Y_0 on $(-Y_0)$, we obtain

$$C(t) = \frac{(\Sigma_0 - 2Y_0 \ln(R_1 / R_0)) R_0^3}{4\eta(1 - (R_0 / R_1)^3)} (1 - e^{-\alpha t}), \quad 0 \leq t \leq T. \quad (26)$$

$$C(t) = C(T) + \frac{\gamma}{\alpha} (e^{-\alpha t} - e^{-\alpha T}), \quad T < t \leq t_s^s. \quad (27)$$

In formula (27) $C(T)$ determine from (26), and t_s^s – is moment of stopping of extension of spherical shell, which determine from (27) under condition $C(t_s^s) = 0$:

$$t_s^s = -\frac{1}{\alpha} \ln \left(\frac{\alpha}{\gamma} C(T) + e^{-\alpha T} \right). \quad (28)$$

Function $C = C(t)$, described formulas (26), (27), show on Fig. 2.

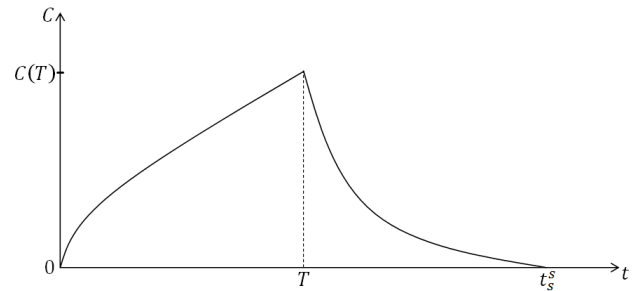


Fig. 2

Distribution of circumferential deformation in moment of stopping of spherical shell extension $t = t_s^s$ described next formula:

$$\varepsilon_{\theta} \Big|_{t=t_s^s} = \frac{1}{R^3} \left[\left(t_s^s (1 - e^{-\alpha t}) + T e^{-\alpha t} \right) \frac{\Sigma_0 - 2Y_0 \ln(R_1 / R_0)}{4\eta(1 - (R_0 / R_1)^3)} R_0^3 + \frac{\gamma}{\alpha} (t_s^s - T) e^{-\alpha t} \right].$$

In case of extension of cylindrical shell under graduated loading

$$\Sigma(t) = \Sigma_0 H(T - t), \quad \Sigma_0 = const > \frac{Y_0}{\sqrt{3}} \ln \frac{R_1}{R_0}. \quad (29)$$

We find to replace Y_0 by $(-Y_0)$, that

$$B(t) = \frac{(\Sigma_0 - Y_0 \ln(R_1 / R_0) / \sqrt{3}) R_0^2}{2\eta(1 - (R_0 / R_1)^2)} (1 - e^{-\bar{\alpha} t}), \quad 0 \leq t \leq T. \quad (30)$$

$$B(t) = B(T) + \frac{\bar{\gamma}}{\bar{\alpha}} (e^{-\bar{\alpha} T} - e^{-\bar{\alpha} t}), \quad T < t \leq t_c^s. \quad (31)$$

In formula (31) value $B(T)$ determine from (30), and t_c^s – is moment of stopping cylindrical shell expansion, which determine from (31) under condition $B(t_c^s) = 0$:

$$t_c^s = -\frac{1}{\bar{\alpha}} \ln \left(\frac{\bar{\alpha}}{\bar{\gamma}} B(T) + e^{-\bar{\alpha} T} \right). \quad (32)$$

Distribution of circumferential deformation in moment of stopping of cylindrical shell extension $t = t_c^s$ described next formula:

$$\varepsilon_{\theta} \Big|_{t=t_c^s} = \frac{1}{R^2} \left[\left(t_c^s (1 - e^{-\bar{\alpha} t}) + T e^{-\bar{\alpha} t} \right) \frac{\Sigma_0 - Y_0 \ln(R_1 / R_0) / \sqrt{3}}{2\eta(1 - (R_0 / R_1)^2)} R_0^2 + \frac{\bar{\gamma}}{\bar{\alpha}} (t_c^s - T) e^{-\bar{\alpha} t} \right].$$

V. CONCLUSION

Obtained exact solutions can be used to test numerical calculation programs and to estimate the effectiveness of numerical methods, similar to that employed previously [9] when using exact Verney solution [1] and similar to that employed previously [10] when using exact Kiselev solutions [4-6].

References

- [1] D. Verney, "Avaluation de la limite elastique du cuivre et de l'uranium par des experiences d'implosion "lente", in *Behavior of Dense Media under High Dynamic Pressures. Symposium H.D.P.* Paris, 1968. Gordon and Breach: New York, 1968. P. 293.
- [2] V. G. Grigoriev, S. Z. Dunin, and V. V. Surkov, "Collapse of spherical pore in viscoplastic material," *Mechanics of Solids*, vol. 16, issue 1, pp. 199-201, January-February 1981.
- [3] V. K. Golubev, "Pore expansion in plastic metal under spall," *J. of Applied Mechanics and Technical Physics*, vol. 24, issue 6, pp. 920-926, November-December 1983.
- [4] A. B. Kiselev, "Analytical solutions of the adiabatic compression of thick-walled spherical and cylindrical shells made of incompressible viscoplastic material," *J. of Applied Mathematics and Mechanics*, vol. 76, issue 4, pp. 489-492, July-August 2012.
- [5] A. B. Kiselev, "Unsteady expansion of thick-walled spherical and cylindrical viscoplastic shells," *Moscow University Mechanics Bulletin*, vol. 67, no. 5/6, pp.116-121, September-December 2012.
- [6] A.B. Kiselev, "To investigation of nonstationary processes of compression of thick-walled spherical and cylindrical viscoplastic shells (Published in Conference Proceedings Style)," in *Book of Abstracts 7th International Congress of Croatian Society of Mechanics*, Zagreb, 2012, pp. 209-213.
- [7] A.B. Kiselev, and A.V. Mischenko, "Elastoplastic problems in monoaxial deformed assumption. Analytical and numerical solutions," *Moscow University Mechanics Bulletin*, vol. 69, no. 1/2, January-April 2014.
- [8] P. Perzyna, *Fundamental Problems in Viscoplasticity*. N.Y.: Academic Press, 1968.
- [9] B. P. Howell, and G. J. Bally, "A Free-Lagrange augmented Godunov Method for the simulation of elastic-plastic solids," *J. of Computational Physics*, vol. 175, pp. 128-167, January 2002.
- [10] A.V. Mischenko, "Numerical modeling of dynamic deforming and fracture of solids in one-dimensional approach by using method of separation on physical processes (Thesis or Dissertation style)," Ph.D. dissertation (Candidate of Physics and Mathematics Sciences), Mechanics and Mathematics Faculty, Moscow Lomonosov State University, Moscow, 2013.

Tracer Diffusion Through Fiber Networks

K. Kang* and J.K.G. Dhont

Abstract—We discuss long-time diffusion of spherical Brownian particles through fiber networks. The long-time self-diffusion coefficient is related through the Einstein relation to an effective friction coefficient, which is determined by direct interactions and hydrodynamic interactions of the tracer sphere with the network. We present several approaches to calculate the effective friction coefficient, which relates the force on the tracer sphere to its thermally averaged velocity. For tracer spheres larger than the network mesh size, direct interactions are dominant, which can be expressed in terms of the distortion of the pair correlation function resulting from the force with which the tracer is pulled through the network. For tracer spheres smaller than the mesh size of the network, hydrodynamic interactions with the network are dominant. A theory is discussed to account for hydrodynamic interactions. We also discuss the case of charged tracers and a charged network, where both hydrodynamics and direct interactions affect the long-time self-diffusive behavior.

Keywords—Self diffusion, fiber network, effective friction, screened hydrodynamics, pair-correlation functions.

I. INTRODUCTION

THIS paper is concerned with the calculation of the long-time self-diffusion diffusion coefficient of a single spherical Brownian particle through a fiber network. Long-time self-diffusion has been studied for many different types of systems. A few examples are, concentrated suspensions of colloidal hard spheres and charged spheres (see, for example Refs.[1-7]), colloidal rods [8] and spheres in rod-networks [9-11], in dextran solutions [12], in polymeric gels [13, 14], in polymer solutions [15], semi-dilute DNA solutions [16], and in dispersions of Xanthan [17]. The central quantity for self-diffusion is the mean-squared-displacement (MSD), $\langle |\vec{r}(t) - \vec{r}(0)|^2 \rangle$, with $\vec{r}(t)$ the position coordinate of the tracer particle at time t , while the brackets stand for ensemble averaging. The typical time dependence of the MSD is sketched in Fig. 1. At very short times ballistic motion occurs, where the MSD varies like $\sim t^2$. When friction becomes important, for times larger than the Brownian time scale τ_B , the MSD becomes linear in time. The slope is proportional to the short-time self-diffusion coefficient. In a crowded

This work was supported in part by the European Soft Matter Infrastructure (ESMI), funded by FP7. K. Kang is with Institute of Complex systems (ICS-3) at the Forschungszentrum Juelich (FZJ), Juelich, 52425, Germany. (phone: +49-2461-61-6089; fax: +49-2461-61-2280; e-mail: k.kang@fz-juelich.de). J.K.G. Dhont is also with Institute of Complex systems (ICS-3) at Forschungszentrum Juelich (FZJ), Juelich, 52425, Germany. (e-mail: j.k.g.dhont@fz-juelich.de).

environment, the MSD crosses over to a second linear regime at later times, where the slope defines the long-time self-diffusion coefficient. The interaction time scale at which this cross over occurs marks the time at which the tracer particles diffuse within “cages” in the crowded environment to times at which diffusion from “cage-to-cage” occurs.

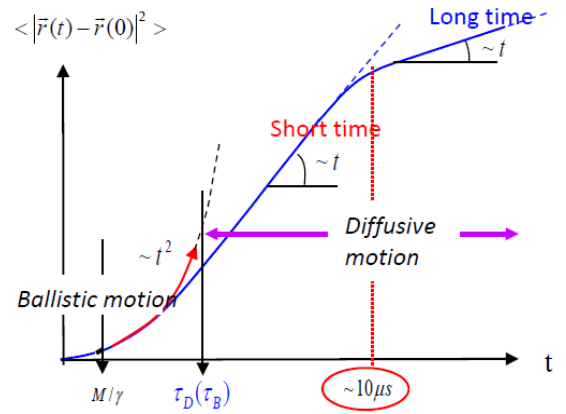


Fig. 1 A sketch of the time dependence of the mean-squared displacement.

The long-time self-diffusion coefficient D_s is related to the effective friction coefficient γ by the Einstein relation $D_s = k_B T / \gamma$. The friction coefficient is the ratio of the force and the resulting thermally averaged velocity: $\vec{F}^{ext} = \gamma \langle \vec{v} \rangle$. For a tracer sphere in a fiber network, the external force balances the force exerted by the network on the tracer through direct and hydrodynamic interactions, in addition to the friction force with the solvent, and is therefore referred to as an “effective friction coefficient”. The relative importance of

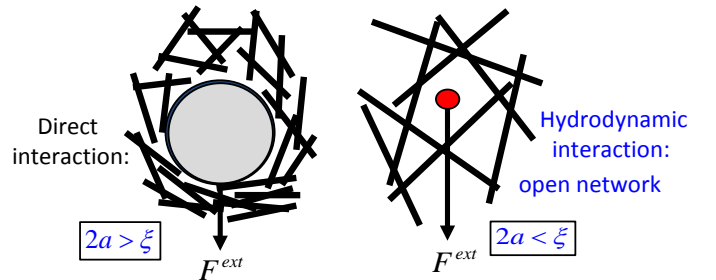


Fig. 2 Effective interactions of a tracer sphere in a network of rods: Direct interactions versus hydrodynamic interactions.

the direct and hydrodynamic interactions is determined by the size of the tracer sphere relative to the mesh size of the network (see the sketch in Fig.2). If the diameter $2a$ of the tracer is larger than the mesh size of the network, $2a > \xi$, the sphere deforms the network while moving, so that direct interactions are dominant (see left Fig.2). However, for a small sphere in an open network, $2a < \xi$, the network is essentially undistorted (see right Fig.2), and the effective friction coefficient is determined by hydrodynamic interactions with the network, as well as direct interactions of the tracer sphere with single fibers. The tracer sphere experiences a direct interaction force that acts against the external force as it passes along a fiber. As the tracer sphere is pulled past a fiber, the probability to find the tracer sphere on average at the front side of the fiber is enhanced, while it is diminished at the back side of the fiber. This probability “*shadowing effect*” is formally described by a deformation of the pair-correlation function, and contributes to the effective friction coefficient.

This paper is organized as follows. In section II we discuss long-time self-diffusion of a large sphere as compared to the mesh size, to leading order in concentration of the fibers. Section III is concerned with diffusion of small spheres. In section IIIA we discuss the influence of hydrodynamic interactions of the tracer with the network on a coarse-grained level, section IIIB contains a discussion on the shadowing effect for hard-core interaction, and in section IIIC we consider the combined effect of hydrodynamic interactions together with hard-core and charge-charge interactions between a charged tracer sphere and a charged network. In section IV a brief comparison with experiments for isotropic networks is made (with some remarks concerning diffusion in nematic networks as discussed in more detail in Refs.[10, 11]), where the fiber network is realized using suspensions of very long and thin rod-like colloids (fd-virus particles).

II. LONG-TIME SELF-DIFFUSION OF A LARGE TRACER

The long-time self-diffusion coefficient can be expanded in a power series of the volume fraction of the fiber network,

$$D_s = D_0 [1 - \alpha\phi + O(\phi^2)] \quad (1)$$

where $D_0 = k_B T / 6\pi\eta a$ is the Einstein diffusion coefficient of a single, non-interacting sphere with radius a , with η the solvent viscosity, and with k_B the Boltzmann constant, and T the temperature. Here, we calculate the first-order coefficient for a spherical tracer that is larger compared to the mesh-size of the network. To first order in the volume fraction of the network, we need to consider the interaction of the sphere with just a single fiber. As such this is not diffusion through a network, but rather characterizes the initial slope of the long-time self-diffusion coefficient as a function of the fiber concentration.

On the Brownian time scale, neglecting the hydrodynamics, force balance implies that,

$$\langle \vec{v} \rangle = \beta D_0 \left\{ \vec{F}^{ext} - N \left[\langle \nabla_1 V \rangle + k_B T \langle \nabla_1 \ln g \rangle \right] \right\} \quad (2)$$

where $\beta = 1/k_B T$, N is the number of hosting fibers in the system, and V is the pair-interaction potential of the sphere and rods. The last term is the Brownian force, which contains the probability distribution function (pdf) g of the position coordinate of the sphere and the position and orientation of a fiber, which is also referred to as the pair-correlation function. Here ∇_1 is the gradient operator with respect to the position coordinate \vec{r}_1 of the tracer sphere. The pdf can be found from the stationary Smoluchowski equation,

$$0 = \left\{ \hat{L}^{(0)} + \beta D \vec{F}^{ext} \hat{L}^{(1)} \right\} g(\vec{r}_1 - \vec{r}_2, \hat{u}) \quad (3)$$

where $\hat{L}^{(0)}$, $\hat{L}^{(1)}$ are the Smoluchowski operators without the external force acting on the sphere, and the contribution due to the external force, respectively. These operators are given in Ref.[9]. Furthermore, D is the diameter of the fibers, \vec{r}_2 is the position coordinate of the fiber, and \hat{u} its orientation. To determine the effective friction coefficient it suffices to consider linear response, so that the pdf is written as,

$$g(\vec{r}_1 - \vec{r}_2, \hat{u}) = g^{eq}(|\vec{r}_1 - \vec{r}_2|, \hat{u}) \left\{ 1 + \beta D \vec{F}^{ext} \Psi(\vec{r}_1 - \vec{r}_2, \hat{u}) \right\} \quad (4)$$

where $g^{eq} = \exp(-\beta V)$ is the equilibrium solution of the Smoluchowski equation without the external force, and the factor βD renders the function Ψ dimensionless. The Smoluchowski equation can be cast into a minimization problem. A functional of Ψ can be constructed, of which the function that minimizes that functional can be shown to be the solution Ψ of the Smoluchowski equation [12]. A physically plausible trial function is constructed with free parameters that can be adjusted to minimize that functional.

A plausible trial function which can be justified by representing the fiber of length L and diameter D as a string of spheres is,

$$\begin{aligned} \Psi^{adv}(\vec{R}, \hat{u}) = & \frac{\partial}{\partial z} \left\{ a_1 \frac{1}{R} \right. \\ & + \left(a_2 + a_3 Z^2 + a_4 \hat{u}_z^2 + a_5 (\hat{u} \cdot \vec{R})^2 \right) \int_{-\frac{1}{2}(\frac{L}{D}-1)}^{\frac{1}{2}(\frac{L}{D}-1)} dl \frac{1}{|\vec{R} - l\hat{u}|} \\ & \left. + a_6 \int_{-\frac{1}{2}(\frac{L}{D}-1)}^{\frac{1}{2}(\frac{L}{D}-1)} dl \frac{l^2}{|\vec{R} - l\hat{u}|} \right\}. \end{aligned} \quad (5)$$

A numerical minimization with respect to the coefficients leads to an approximate solution of the Smoluchowski equation (3),

which is substituted into (2) to obtain the effective friction coefficient, and thereby the first order coefficient α in the expansion (1) of the long-time self-diffusion coefficient. Fig.3 is a plot of α obtained from the trial function (5) as a function of the aspect ratio L/D of the fibers, for several values of $p=L/2a$.

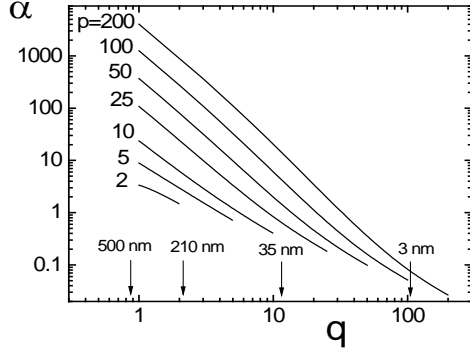


Fig.3 The first-order concentration coefficient as a function of $q=L/2a$ of the fibers for several values of $p=L/D$. The indicated radii refer to the experimental systems discussed in section IV (taken from Ref. [12])

III. LONG-TIME SELF-DIFFUSION OF A SMALL TRACER

In this section we consider diffusion of small spheres, where hydrodynamic interactions are discussed in subsection IIIA, while hard-core and charge-charged interactions are discussed in subsections IIIb and IIIc, respectively.

A. Hydrodynamic interactions

When a small sphere (with radius a) is pulled through the essentially undistorted network, it induces a solvent flow that is scattered back to the sphere by the fibers. This affects the effective friction of the sphere with its surroundings, and determines the long-time self-diffusion coefficient. Consider the tracer sphere with a velocity \vec{v}_p (see the red dot in Fig.4).

Let \vec{u}_0 denote the flow velocity generated by the tracer sphere, embedded by the network. Since this flow propagates through a network that is fixed in space (at least on the time scale at

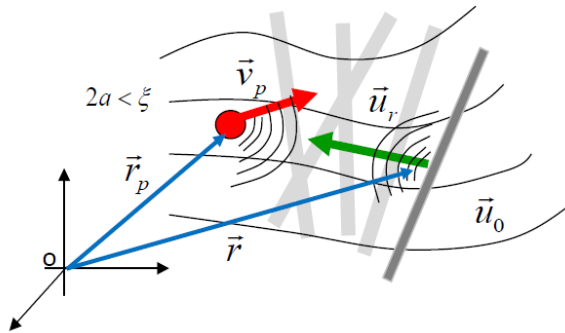


Fig.4 Screened hydrodynamic interaction of a tracer sphere and a rod in the fiber network.

which the small sphere reaches its long-time diffusive behavior), there is on average a resistance that is opposite to the flow velocity. On average, the network thus acts with a body force that is proportional to, and opposite in direction. The corresponding Navier-Stokes equation, including that body force, reads (with p the pressure),

$$\begin{aligned} \eta_0 [\nabla^2 - \kappa^2] \vec{u} - \nabla p &= 0 \\ \nabla \cdot \vec{u} &= 0 \end{aligned} \quad (6)$$

where $1/\kappa$ is referred to as the hydrodynamic screening length. This length characterizes the distance over which a shear wave damps out as it traverses through the network. The coarse-grained approach is only valid when the screening length is larger than the mesh size of the network: $\kappa^{-1} > \xi$. The Green's functions of this Debye-Büchse-Brinkman equation are the screened Oseen tensor \vec{T}_s . For the small tracer sphere under consideration, the flow it generates is equal to,

$$\vec{u}_0(\vec{r}) = 6\pi\eta_0 a \vec{T}_s(\vec{r} - \vec{r}_p) \cdot \vec{v}_p \quad (7)$$

This flow propagates through the network to a particular fiber (the dark grey rod in Fig.4), which reflects a flow field \vec{u}_r back to the sphere. The reflected flow field is equal to,

$$\begin{aligned} \vec{u}_r(\vec{r}) &= \sum_{\alpha} \vec{T}_s(\vec{r} - \vec{r}_c - D\alpha\hat{u}) \cdot \vec{F}_{\alpha}^h \\ \vec{F}_{\alpha}^h &= 3\pi\eta_0 D [\vec{v}_{\alpha} - \vec{u}_{\alpha}^*(\vec{r} = \vec{r}_c + D\alpha\hat{u})] \end{aligned} \quad (8)$$

where \vec{F}_{α}^h is the hydrodynamic force on bead α of the rod, which, as before, is represented by a string of such beads. Furthermore, \vec{r}_c is the center of the rod, \hat{u} is the orientation of the rod, and \vec{u}_{α}^* is the flow velocity at bead α that would have existed in the absence of that bead. The force acting on the sphere to maintain its velocity \vec{v}_p is equal to,

$$\vec{F}^{ext} = 6\pi\eta_0 a [\vec{v}_p - \vec{u}_r(\vec{r} = \vec{r}_p)] \quad (9)$$

with \vec{r}_p is the position of the center of the sphere. Since \vec{u}_r is proportional to \vec{v}_p , (9) leads to an expression for the effective friction coefficient once the proportionality constant between \vec{u}_r and \vec{v}_p is quantified. To this end we need to specify the hydrodynamic forces in (8). For the calculation of the hydrodynamic forces, first note that,

$$\vec{u}_{\alpha}^*(\vec{r}) = \vec{u}_0(\vec{r}) + \sum_{\beta \neq \alpha} \vec{T}_s(\vec{r} - \vec{r}_c - D\beta\hat{u}) \cdot \vec{F}_{\beta}^h \quad (10)$$

where \vec{F}_β^{h*} is the hydrodynamic force on bead β in the absence of bead α . For long and thin fibers, the mere absence of a single bead does not affect hydrodynamic forces significantly, and $\vec{F}_\alpha^h = 3\pi\eta_0 D \vec{u}_\alpha^*$, (10) evaluated at the position $\vec{r} = \vec{r}_c + D\alpha\hat{u}$ of bead α leads to an integral equation for the hydrodynamic forces,

$$\frac{\vec{F}_\alpha^h}{3\pi\eta_0 D} + \vec{u}_0(\vec{r}) + \sum_{\beta \neq \alpha} \vec{T}_s(D\hat{u}(\alpha - \beta)) \cdot \vec{F}_\beta^h = 0 \quad (11)$$

This integral equation can be solved in approximation for long and thin fibers, which can be used in (8, 9) to derive the following expression for the external force,

$$\vec{F}^{ext} = 6\pi\eta_0 a \left[\hat{I} + \sum_{j=1}^N \langle \vec{M}(\vec{R}_j, \hat{u}_j) \rangle \right] \cdot \vec{v}_p \quad (12)$$

where $\vec{M}(\vec{R}_j, \hat{u}_j)$ is a mobility tensor that depends on the dimensionless variables κD and κL (where, as before, L is the length of the fibers). The brackets $\langle \dots \rangle$ denote ensemble averaging with respect to the degrees of freedom of the sphere and rods. Equation (12) simply adds up all reflected fields from N rods, which neglects reflections of velocity fields between fibers, just as multiple reflections between the sphere and fibers is neglected.

This is a good approximation for small spheres and open networks. The mobility tensor is a multiple integral over phase-space coordinates of the screened Oseen tensor, which can be evaluated semi-analytically both for isotropic and nematic ordered networks (see Ref.18). For an isotropic network the long-time self-diffusion coefficient is found to be equal to,

$$D_s^h = \frac{D_0}{1 + \alpha^h \phi} \quad (13)$$

where ϕ is the volume fraction of the network, and, from a numerical evaluation of the phase-space integral,

$$\alpha^h = -\frac{\kappa a}{(\kappa D)^2 \ln(\kappa D)} \left[\frac{64}{10} - \frac{85}{10000} \kappa L - \frac{33}{10000} (\kappa L)^2 \right] \quad (14)$$

Analytical asymptotic results for $\kappa D \ll 1$ of the phase-space integral (also for nematic networks) can be found in Ref.[18]. The superscripts h on D_s^h and α^h are used to indicate that these quantities represent the effect of hydrodynamic interactions only. Direct interactions will be discussed in the next subsection.

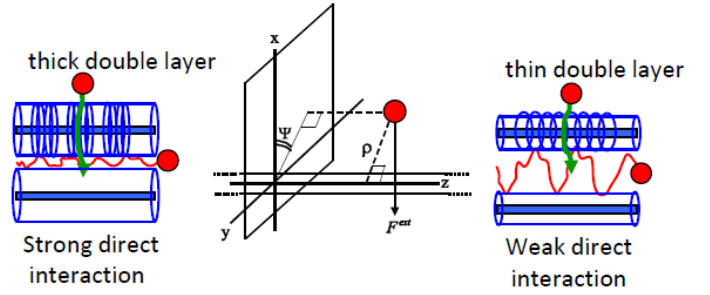


Fig. 5 Shadowing effect of a sphere: left for a thick double layer, right for a thin double layer. The middle panel defines the cylindrical coordinates, where the tracer moves in a direction perpendicular to the fiber.

B. Direct interactions and the shadowing effect for small tracer spheres with hard-core interactions

Besides hydrodynamic interactions, direct interactions may be important also for small spheres. Although direct-interaction contributions to the self-diffusion coefficient can be described both for isotropic and nematic networks [13, 14], here we will only consider isotropic networks. Direct interactions are important when the velocity of the tracer has a non-zero component perpendicular to a fiber. Point of departure is again the ensemble averaged force balance equation,

$$\langle \vec{v} \rangle = \beta D_s^h \left\{ \vec{F}^{ext} - \langle \nabla_1 V \rangle + k_B T \langle \nabla_1 \ln g \rangle \right\} \quad (15)$$

where the difference with (2) is that for the small sphere

and open network of interest here, the sphere interacts with a single fiber only (so that $N = 1$ in (2)), and that the sphere moves in an hydrodynamically effective medium with a diffusion coefficient D_s^h (as discussed in the previous subsection). Similar to what was done in section II, we write,

$$g(r, \varphi) = g^{eq}(r) \left[1 + \cos(\varphi) L(r) F^{ext} \right] \quad (16)$$

where, for this moment, the sphere is supposed to move past a rod with a velocity that is perpendicular to the orientation of the fiber, with φ and r the cylindrical coordinates (see the middle panel in Fig.5). Furthermore, $g^{eq} = \exp(-\beta V)$ is the pair-correlation function in the absence of the external force. Substitution of the Ansatz (16) into the Smoluchowski equation without hydrodynamic interactions, leads to the following equation for the function L ,

$$\begin{aligned} g^{eq}(r) \left[\frac{dL^2(r)}{dr^2} + \frac{1}{r} \frac{dL(r)}{dr} - \frac{L(r)}{r^2} \right] \\ = -\frac{dg^{eq}(r)}{dr} \left[\beta + \frac{dL(r)}{dr} \right]. \end{aligned} \quad (17)$$

Assuming hard-core interactions between the sphere and the fiber, thus leads to,

$$L(r) = \beta \frac{(a + D/2)^2}{r} \quad (18)$$

$$g(r, \varphi) = g^{eq}(r) \left[1 + \beta \cos(\varphi) \frac{(a + D/2)^2}{r} F^{ext} \right]$$

which expression quantifies the shadowing effect that was mentioned in the introduction. This result allows for the evaluation of the averages in (15), and thereby leads to an expression for the effective friction coefficient. It should be noted that in calculating ensemble averages, also averaging of the orientation of the fiber relative to the velocity of the sphere must be accounted for. This leads to different expressions for isotropic and nematic networks [13,14]. For the isotropic state we find,

$$D_s^s = D_s^h \frac{1}{1 + \alpha^s \phi} \quad (19)$$

with,

$$\alpha^s = \frac{2}{3} \left(1 + \frac{2a}{D} \right)^2 \quad (20)$$

where the superscripts s on D_s^s and α^s refer to the shadowing effect.

C. Direct interactions and the shadowing effect for small tracer spheres with hard-core and charge-charge interactions

For charged tracers and networks, in addition to hard-core interactions, charge-charge interactions between the tracer sphere and the network must be accounted for. In case of low ionic strengths, the double-layer thickness can be substantial as compared to the radius of the tracers sphere, in which case direct interactions become more significant (see the left and right panels in Fig.5). For the very long and thin fibers and the small diameter of the tracer sphere as compared to the length of the fibers, end-effects on charge-charge interaction potentials can be neglected. For sufficiently small surface charges the interaction potential V_Q between the tracer sphere and the rod is a superposition of Debye-Hückel interaction potentials,

$$\beta V_Q(r) = K \int_{-\infty}^{\infty} dx \frac{\exp\{-\kappa_Q \sqrt{r^2 + x^2 D^2}\}}{\sqrt{r^2 + x^2 D^2}}, \quad (21)$$

$$K = Z_s Z_{rod} \frac{D}{L} l_B \frac{\exp\{\kappa_Q (a + D/2)\}}{(1 + \kappa_Q a)(1 + \kappa_Q D/2)},$$

$$\kappa_Q \equiv \sqrt{\frac{e^2}{k_B T \epsilon} \sum_{\alpha} \rho_{\alpha}^0 z_{\alpha}^2}.$$

where $l_B = \beta e^2 / 4\pi\epsilon$ is the Bjerrum length (0.71 nm for water at room temperature), with ϵ as the static dielectric constant of the solvent, e is the elementary charge, and Z_s and Z_{rod} the number of elementary charges on the surface of the tracer sphere and a fiber, respectively. Furthermore, κ_Q is the inverse Debye-Hückel electrostatic screening length, which is a function of the bulk number concentrations ρ_{α}^0 of ion species α that carry z_{α} elementary charges. We use the same Ansatz in (16), with $L = L_{hc} + L_Q$, where L_{hc} is the contribution due to hard-core interaction (which is given in eq.(18)), and where L_Q accounts for the charge-charge interactions. Since on the pair-level we have $g^{eq} = g_{hc}^{eq} g_Q^{eq}$ (with g_{hc}^{eq} the equilibrium pair-correlation function for hard-core potentials, and g_Q^{eq} for charge-charge interactions) we find from (17),

$$g_{hc}^{eq}(r) \left[\frac{dL_Q^2(r)}{dr^2} + \frac{1}{r} \frac{dL_Q(r)}{dr} - \frac{L_Q(r)}{r^2} \right] = \left\{ \beta g_{hc}^{eq}(r) \frac{dV_Q(r)}{dr} - \frac{dg_{hc}^{eq}(r)}{dr} \right\} \times \left[\beta + \frac{dL_{hc}(r)}{dr} + \frac{dL_Q(r)}{dr} \right] \quad (22)$$

The solution for L_Q (using (21)) is,

$$L_Q(r) = -L_{hc}(r) \left[F^C + \beta \int_{a+D/2}^r dr' L_{hc}^{-1}(r') F(r') \right] \quad (23)$$

with,

$$F(r') = \int_{r'}^{\infty} dr'' \frac{dV_Q(r'')}{dr''} \left[\beta - \frac{L_{hc}(r'')}{r''} \right] \quad (24)$$

and where $F^C = F(r' = a + D/2)$ is the contact value of the function in (24). As before, this solution can be used to compute the effective friction coefficient after evaluation of the ensemble averages in (16), which leads to,

$$D_s^s = D_s^h \frac{1}{1 + \alpha^{s,Q} \phi} \quad (25)$$

with,

$$\alpha^{s,Q} = \frac{2}{3} \left(1 + \frac{2a}{D} \right)^2 \left\{ 1 - \int_{a+D/2}^{\infty} dr \frac{dV_Q(r)}{dr} \left[\beta - \frac{L_{hc}(r)}{r} \right] \right\} \quad (26)$$

where a Q is added to the superscript to indicate that charge-charge interactions are taken into account, on top of hard-core interactions. This expression can be used to obtain by numerical integration explicit values for the effective friction, and hence the long-time self-diffusion coefficient.

IV. COMPARISON TO EXPERIMENTS

As an experimental realization of a fiber network we use fd-virus particles. These particles consist of a DNA strand with a length of 880 nm, which is covered with coat proteins rendering a core thickness of 6.8 nm, and a relatively large persistence length of about 2500 nm. These very long and thin rods form an entangled network for concentrations that are a few times larger than the overlap concentration of 0.076 mg/ml. The lower panel in Fig.6 (a) shows the long-time self-diffusion coefficient (normalized to the Einstein diffusion coefficient) as a function of the fd-virus concentration, for tracer spheres of various radii, as indicated in the figure. For the large tracer sphere with a radius of 500 nm, the theory as discussed in section II can be used to predict the initial slope of the diffusion coefficient as a function of the fd-concentration, using that the fiber volume fraction is connected to the concentration c as $\phi = 0.0011 \times c [mg/ml]$. The corresponding initial slope is given by the dotted line in the Fig.6 (b), which quite accurately reproduces the experimental slope.

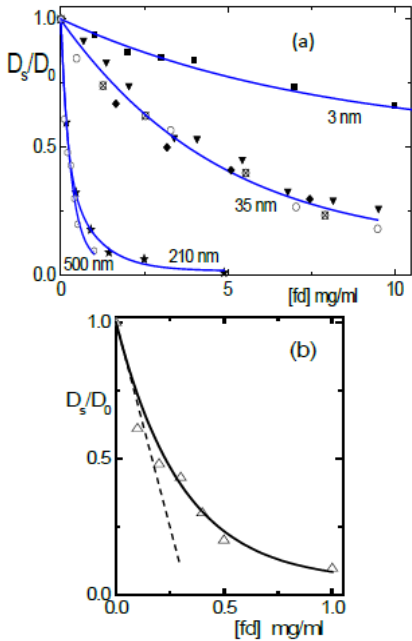


Fig.6 (a) Long-time self-diffusion coefficient (normalized to the Einstein coefficient) as a function of fd-concentration for various radii of the tracer sphere. The ionic strength is sufficiently high to guarantee hard-core interactions. The data points are obtained by Fluorescence Correlation Spectroscopy, Dynamic Light Scattering, and video image analysis. (b) The data for the tracer sphere with a radius of 500 nm, where the dotted straight line corresponds to the predicted initial slope as calculated in section II (taken from Ref. [9]).

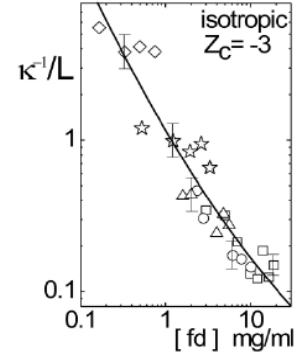


Fig.7 The hydrodynamic screening length κ^{-1} in units of the length of rod versus the concentration. $Z_c = -3$ is the charge of apoferritin in units of the elementary charge (taken from Ref. [11]).

The mesh size of the fd-network, for concentrations larger than the overlap concentration c^* , can be estimated from,

$$\xi \approx L\sqrt{c^*/c} \quad (27)$$

where, as before, $L=880$ nm is the length of the fibers. Experiments were performed on apoferritin, which has a radius of 6.4 nm (not shown in Fig.6), where the ionic strength is varied such that $\kappa_0 D$ ranges from 0.24 up to 7.17 [11]. With this variation of the range of charge-charge interactions, the relative contribution of the shadowing effect is varied. The long-time self-diffusion coefficient that includes both hydrodynamic interactions as well as the shadowing effect is, according to (13, 25), given by,

$$\frac{D_s}{D_0} = \frac{1}{1 + \alpha^h \phi} \frac{1}{1 + \alpha^{s,Q} \phi} \quad (28)$$

From the measured diffusion coefficient and the expressions for the coefficients on the right hand-side as derived in section III, the hydrodynamic screening length κ^{-1} can be obtained. The resulting dependence of κ^{-1}/L as a function of the fd-concentration is given in Fig.7. Variation of the ionic strength allows covering a large range of screening lengths. As can be seen from Fig.7, the screening length is always larger than about 88 nm. For the fd-concentration range, the ratio κ^{-1}/ξ varies from about 2 to 20, which validates the assumption underlying screened hydrodynamics, namely that the screening length should be at least as large as the mesh size. We have so far considered isotropic networks. The above theory can be extended to nematic networks, and similar experiments as for isotropic networks have been performed. Two diffusion coefficients can now be defined [10, 11, 19], one related to motion along, and one perpendicular to the nematic director.

For nematic networks, a simple scaling for the hydrodynamic screening length as a function of the fiber concentration as in Fig.7 for isotropic networks is not found. The simple reason for this is that the nematic orientational order parameter has a strong effect on the screening length. As the ionic strength and/or the fd-concentration is varied, the order parameter changes, which leads to a change of the screening length. This destroys scaling of the screening parameter as a function of fd-concentration alone. Contrary to an isotropic network, the hydrodynamic screening length in nematic networks increases with increasing concentration. This is due to the increase of the orientational order parameter. A more ordered nematic allows a shear wave to penetrate deeper into the network. The analysis for nematic networks in Refs. [10, 11] is based on an approximate Debye-Bücher-Brinkman equation as in (6). A more accurate approach would be to consider a truly anisotropic screening parameter (along- and perpendicular to the nematic director). Green's functions for such a Debye-Bücher-Brinkman equation have been calculated in Ref. [20], which could be used to improve the theory in Refs. [10, 11] for nematic networks.

V. CONCLUSIONS

A theory is developed for the effective friction coefficient (i.e. the long-time self-diffusion coefficient) of tracer spheres through fiber networks, and experiments are discussed for diffusion of tracers with various sizes in networks formed by fd-virus particles. Both hydrodynamic interactions of the tracers with the network and direct interactions (the so-called "shadowing effect") are discussed. When the sphere is large compared to the mesh-size, direct interactions are dominant, while for small spheres with hard-core interactions, hydrodynamic interactions are dominant. For small charged tracers and a charged network, however, direct interactions are also important, besides hydrodynamic interactions, when the Debye length is comparable or larger than the mesh size. Hydrodynamic interactions are formulated in terms of a hydrodynamic screening length, which is calculated from experimental data as a function of the fiber concentration (and hence, the mesh size of the network). Contrary to isotropic networks, no unique scaling relation for the hydrodynamic screening lengths (both for motion along- and perpendicular to the nematic director) as a function of the fiber concentration is found. The reason for this is that the hydrodynamic screening length is very sensitive to the nematic order parameter, while the nematic order parameter is not just set by the fiber concentration but also by the ionic strength (for the charged fibers under consideration).

REFERENCES

- [1] G. Szamel, and J. A. Leegwater, "Long-time self-diffusion coefficients of suspensions", *Phys. Rev. A.*, vol. 46, no. 8, pp. 5012-5019, Oct. 1992.
- [2] A. Imhof, A. van Blaaderen, J. Mellema, and J.K.G. Dhont, "A comparison between the long-time self-diffusion and low shear viscosity of concentrated dispersions of charged colloidal silica spheres", *J. Chem. Phys.* Vol. 100, no.3, pp. 2170-2181, Feb. 1994.
- [3] A.Imhof and J.K.G. Dhont, "Long-time self-diffusion in binary colloidal hard-sphere dispersions", *Phys. Rev. E.* vol. 52, no. 6, pp. 6344-6357, Dec. 1995.
- [4] G. Naegele, and P.Baur, "Influence of hydrodynamic interactions on long-time diffusion in charge-stabilized colloids", *Europhys. Lett.* Vol. 38, no. 7, pp. 557-562, Apr. 1997.
- [5] M.G. McPhie, and G. Naegele, "Long-time self-diffusion of charged colloidal particles: Electrokinetic and hydrodynamic interaction effects", *J. Chem. Phys.* Vol. 127, pp. 034906-1-14, July. 2007.
- [6] R.A. Lionberger, and W.B. Russel, "A Smoluchowski theory with simple approximations for hydrodynamic interactions in concentrated dispersions", *J. Rheol.* Vol. 41, pp. 399-425, April. 1997.
- [7] H.Loewen, and G.Szamel, "Long-time self-diffusion coefficient in colloidal suspensions: theory and simulation", *J. Phys.:Cond. Matt*, vol. 5, pp. 2295-2306, Feb. 1993.
- [8] M.P.B.van Bruggen, H.N.W.Lekkerkerker, G. Maret, and J.K.G. Dhont, "Long-time translational self-diffusion in isotropic and nematic dispersions of colloidal rods", *Phys. Rev. E*, vol. 58, no. 6, pp. 7668-7677, Dec. 1998.
- [9] K.Kang, J.Gapinski, M.P.Lettigna, J.Buitenhuis, G.Meier, M.Ratajczyk, J.K.G. Dhont, and A. Patkowski, "Diffusion of spheres in crowded suspensions of rods", *J. Chem. Phys.* Vol. 122, pp. 044905-1-13, Jan. 2005.
- [10] K.Kang, A.Wilk, J.Buitenhuis, A. Patkowski, and J.K.G. Dhont, "Diffusion of spheres in isotropic and nematic suspensions of rods", *J. Chem. Phys.* Vol. 124, pp. 044907-1-17, Jan. 2006.
- [11] K.Kang, A.Wilk, A. Patkowski, and J.K.G. Dhont, "Diffusion of spheres in isotropic and nematic suspensions of rods: Electrostatic interactions and hydrodynamics screening", *J. Chem. Phys.* Vol. 126, pp. 214501-1-17, June. 2007.
- [12] T.F. Kosar, R.J. Philips, "Measurement of protein diffusion in dextran solutions by holographic interferometry", *AIChE J.*, Vol 41, pp 701, Mar. 1995.
- [13] B. Schnurr, F. Gittes, F.C. MacKintosh, C.F. Schmidt, "Determining microscopical viscoelasticity in flexible and semiflexible polymer networks", *Macromolecules*, Vol 30, pp 7781, 1997
- [14] A. Pluen, P.A. Netti, R.K. Jain, D.A. Berk, "Diffusion of Macromolecules in agarose Gels: Comparison of Linear and Globular Configurations", *Biophys. J.*, Vol. 77, pp 542, Jul. 1999
- [15] J. van der Gucht, N.A. Besseling, W. Knoben, L. Bouteiller, M.A. Cohen-Stuart, "Brownian particles in supramolecular polymer solutions", *Phys. Rev. E*, Vol 67, pp 051106, May 2003.
- [16] S. Mangelot, S. Keller, J. Rädler," Transport of nucleosome core particles in semidilute DNA solutions", *Biophys. J.*, Vol 85, pp1817, Sep. 2003.
- [17] G.H. Koenderink, S. Sacanna, D.G. Aarts, A.P. Philipse, "Rotational and translational diffusion of fluorocarbon tracer spheres in semidilute xanthan solutions", *Phys. Rev. E*, Vol.69, pp 021804, Feb. 2004.
- [18] B. Cichocki, M.L. Ekiel-Jezewska, "Self-diffusion in an effective medium of rods", *J. Chem. Phys.* Vol 130, pp 214902, 2009.
- [19] H. Loewen, "Anisotropic self-diffusion in colloidal nematic phases", *Phys. Rev. E* Vol 59, pp 1989, Feb. 1999.
- [20] B. Cichocki, M.L. Ekiel-Jezewska, "Green tensors for Debye-Bücher-Brinkman equations", *J. Math. Phys.*, Vol 51, pp 103101, 2010.

Laminar Natural Convection in a Two-Dimensional Vertical Conical Partially Annular Space

B. Ould said, N. Retiel, and M. Aichouni

Abstract—The present paper is dedicated to present the numerical simulation of thermal convection in a two dimensional vertical conical partially annular space. The constant properties and the Boussinesq approximation for density variation is used to solve the governing equations of mass, momentum and energy using the CFD FLUENT 12.0. The results of streamlines and the isotherms of the fluid are discussed for different annuli with various boundary conditions and Rayleigh numbers. Emphasis is placed on the height influences of the inner vertical cone on the flow and the temperature distribution. In more, the effects on the heat transfer are treated for different values of physical parameters of the fluid in the annulus geometry. The heat transfer on the hot walls of the annulus is also computed in order to make comparisons the cylinder annulus for boundary conditions and several Rayleigh numbers. the results obtained of Nusselt number has been found between the present provisions and available data from the published literature data.

Keywords—Annular space, Conical partially, Natural convection, Heat transfer, Numerical simulation.

I. INTRODUCTION

The heat transfer analysis by natural convection in an enclosure is an large research topic owing to its wide variety of engineering applications involving energy conversion, storage and transmission systems. Instances of using annulus geometry solar energy collection and nuclear reactor design [1]. A comprehensive review of natural convection in various cavity shapes has been documented in the open literature. Among the very first investigations, [2] has been analyzed numerically the heat transfer problem by natural convection in rectangular enclosure is filled by micropolar fluid, to studied the influence of the conductive vertical divider. The case of square and cubic cavities was reported by [3] and [4]. Other investigations [5] has been studied by cfd simulation the effect of the physical and geometrical parameters in two-dimensional

vertical enclosure by heat transfer with correlations generalized. The complex shapes such that inclined cavities with wavy walls by [6], and trapezoidal cavities by [7]. Natural convection and fluid flow was studied for triangular enclosures mostly with boundary conditions, see [8] and [9]. [10] have carried investigations of heat transfer by protruding isothermal heater within an triangular enclosure. The study numerically of this phenomenon of natural convection flow in vertical concentric annular with isothermal inner and outer vertical walls. Several problem that has been extensively studied due to its several practical applications have received much attention. The studies conducted by [11] in a vertical cylindrical cavity, A parametric study numerically of the thermal convection in vertical annulus by a the heat generation rod variation centrally vertically by [12]. The study the effect of tilted angle and diameter ratio on natural convection heat transfer in the case of horizontal cylindrical annulus by [13]. Investigation the transition effect and turbulence flows on natural convection along a horizontal annular cavity with local and mean Nusselt number were presented by [14] and recently by [15]. Few research works have been reported for the case of conical, have numerically solved the heat transfer by natural convection and radiation problem in a conical annular cylinder porous fixed is presented by [16]. These studies were restricted to conduction heat transfer only. The present paper covers the laminar natural convection in a vertical conical cylinder partially annular space. On the other hand, the direct numerical simulation necessary for well resolved the study of heat transfer, (DNS) approach which requires computational resources well beyond actual capacities for the majority of real industrial problems. We will be concerned with the effect of the Rayleigh number and annulus radius ratio as well as the cavity geometry on the heat transfer.

II. PHYSICAL AND MATHEMATICAL FORMULATION

A. Physical Domain

In this present problem the geometry is schematized for studied the flow produced by natural convection in a vertical conical partial annulus; where the annulus is filled with air. The analysis domain is delimited by two concentric, conics with isothermal walls of the inner and outer axial height h , H respectively. The top and bottom walls of the outer cone are considered adiabatic, as shown in Fig. 1. The bottom radius of inner and outer conics are r_i and r_o and the inner and outer wall temperature are T_i and T_o , respectively. The horizontal walls

B. O. Author is with the Laboratory of Numerical and Experimental Modeling of Mechanical phenomena, Department of Mechanical, University of Mostaganem Abdelhamid Ibn Badis, UMAB, BP300, Route Belhacel, Mostaganem (27000), Algeria; e-mail: kazemou@ yahoo.fr).

N. R. Author, was with Laboratory of Numerical and Experimental Modeling of Mechanical phenomena, Department of Mechanical, University of Mostaganem Abdelhamid Ibn Badis, UMAB, BP300, Route Belhacel, Mostaganem (27000), Algeria; e-mail: retieln@ yahoo.fr).

M. A. Author is with Associate Professor, Engineering College (I Research Chair in Quality & Productivity Improvement in Construction Industry, Université, Hail University, S.A. Saudi BinLaden); Faculty of engineering, University of Hail, Hail, PO Box 2440, Hail 43385, Saudi Arabia, (e-mail: m.aichouni@uoh.edu.sa).

of the outer cone are insulated. The buoyancy induced flow is assumed to be laminar, and the fluid studied is incompressible with constant fluid properties except the density variation. The Boussinesq approximation is used for calculated the density variation with the temperature. Then, the mathematical model used is based on the hypothesis of a two-dimensional (axisymmetric) flow.

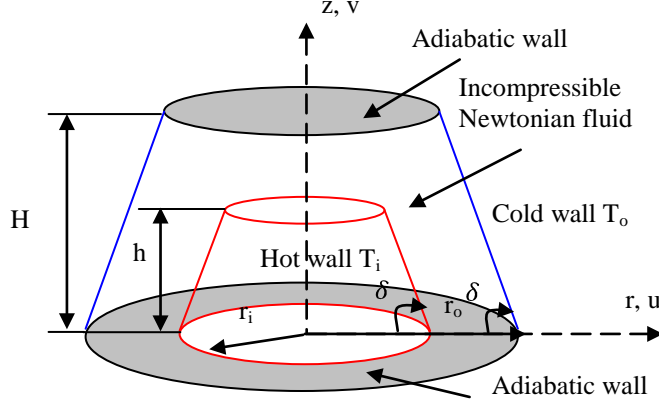


Fig. 1 Physical Model

B. Governing Equations

The problem description and the assumptions application on the fluid properties, the governing differential equations in vector form can be written as:

$$\text{Continuity,} \quad \vec{\nabla} \cdot \vec{V} = 0 \quad (1)$$

$$\text{Momentum,} \quad \rho(\vec{\nabla} \cdot \vec{V})\vec{V} = \mu \nabla^2 \vec{V} - \vec{\nabla} p - \rho \vec{g} \quad (2)$$

$$\text{Energy,} \quad \rho c_p (\vec{\nabla} \cdot \vec{V})T = \lambda (\vec{\nabla} \cdot \vec{\nabla})T \quad (3)$$

In present study can be written as the governing dimensionless equations in cylindrical coordinates in the following forms.

$$\text{Continuity,} \quad \frac{1}{R} \frac{\partial}{\partial R} (RU) + \frac{\partial V}{\partial Z} = 0 \quad (4)$$

$$\text{R momentum,} \quad U \frac{\partial U}{\partial R} + V \frac{\partial U}{\partial Z} = -\frac{\partial P}{\partial R} + Pr \left[\frac{\partial}{\partial R} \left(\frac{1}{R} \frac{\partial}{\partial R} (RU) \right) + \frac{\partial^2 U}{\partial Z^2} \right] \quad (5)$$

Z momentum with the Boussinesq approximation for the buoyancy term,

$$U \frac{\partial V}{\partial R} + V \frac{\partial V}{\partial Z} = -\frac{\partial P}{\partial Z} + Pr \left[\frac{1}{R} \frac{\partial}{\partial R} \left(R \frac{\partial V}{\partial R} \right) + \frac{\partial^2 V}{\partial Z^2} \right] + PrRa(T^* - 0.5) \quad (6)$$

$$\text{Energy} \quad U \frac{\partial T^*}{\partial R} + V \frac{\partial T^*}{\partial Z} = \frac{1}{R} \frac{\partial}{\partial R} \left(R \frac{\partial T^*}{\partial R} \right) + \frac{\partial^2 T^*}{\partial Z^2} \quad (7)$$

Where the dimensionless variables and numbers are defined as follows:

$$U = \frac{uL}{\alpha}; V = \frac{vL}{\alpha}; R = \frac{r}{L}; Z = \frac{z}{L}; Ar = \frac{H}{L}; X = \frac{h}{L} \quad (8)$$

$$T^* = \frac{T - T_o}{T_i - T_o}; P = \frac{pL^2}{\rho \alpha^2}; Pr = \frac{\nu}{\alpha}; Ra = \frac{\beta g \Delta T L^3}{\alpha \nu} \quad (9)$$

C. Boundary Conditions

The corresponding dimensionless boundary conditions for the radial and vertical velocity is equals to zero at all walls. The temperature boundary conditions are as follows.

- At $0 \leq Z \leq \frac{H}{L}$ and $R_o \leq R \leq R_o - \frac{H}{L} \cot \delta$: $U = V = 0$ and $T^* = 0$ for the isothermal cold tilted wall.

- At $0 \leq Z \leq \frac{h}{L}$ and $R_i \leq R \leq R_i - \frac{h}{L} \cot \delta$: $U = V = 0$ and $T^* = 1$ for the isothermal hot tilted wall.

- At $Z = \frac{h}{L}$ and $0 \leq R \leq R_i - \frac{h}{L} \cot \delta$: $U = V = 0$ and $T^* = 1$ for the isothermal hot horizontal wall.

- At $Z = \frac{H}{L}$ and $Z = 0$: $U = V = 0$ and $\frac{\partial T^*}{\partial Z} = 0$ for the adiabatic walls.

III. NUMERICAL METHOD

To solve the governing equations using the finite volume method was used The FLUENT 12.0, CFD code, with first order formulation was solved the segregated implicit. The conservation governing equations was solved independently, by the segregated solver. The first order upwind differencing scheme is used the equations of momentum and energy. The discretization scheme used for pressure was body force weighted to take the density variations in consideration. The pressure-velocity coupling is ensured using the SIMPLE algorithm. The Gambit used for created and meshed the geometrical model with a simple quadrilateral cell. If necessary for correctly resolving the steep gradients in the thin buoyancy-driven boundary layer. A very fine spacing near the walls in conical partially annular grid. All the variables were calculated right up to the walls without using any wall function. on the wall boundary conditions, the radial and vertical velocity values were to zero. The dimensionless temperature of the active walls are set to 0 and 1 respectively. While meshing the domain, it is taken care that the mesh size does not influence the solution.

The residuals of continuity, momentum and energy equations are required to be lower 10^{-7} in order to achieved totally converging solution. The relaxation parameters have been adapted for every simulation in order to speed up convergence.

IV. NUMERICAL SOLUTIONS

A. Nusselt Number

The energy transmitted by the inner cylinder of the annulus are expressed in values to obtain the local and mean Nusselt numbers. The local Nusselt number for the annulus inner cylinder is obtained from temperature gradients by the following relationships:

$$Nu_1 = \left. \frac{\partial T^*}{\partial n} \right|_{l=\frac{x}{\sin \delta}} \quad \text{and} \quad Nu_2 = \left. \frac{\partial T^*}{\partial Z} \right|_{Z=x} \quad (10)$$

The mean Nusselt number is defined by

$$\begin{aligned} \overline{Nu} &= \frac{\int_0^{2\pi} \int_0^{\frac{x}{\sin \delta}} \left(\frac{\partial T^*}{\partial R} \sin \delta + \frac{\partial T^*}{\partial Z} \cos \delta \right) R d\phi dl}{\frac{\pi}{\cos \delta} [R_i^2 - (R_i - X \cot \delta)^2] + \pi (R_i - X \cot \delta)^2} \\ &+ \frac{\int_0^{2\pi} \int_0^{R_i - X \cot \delta} \frac{\partial T^*}{\partial Z} R d\phi dR}{\frac{\pi}{\cos \delta} [R_i^2 - (R_i - X \cot \delta)^2] + \pi (R_i - X \cot \delta)^2} \\ \overline{Nu} &= \frac{2\pi \left[\int_0^x \frac{\partial T^*}{\partial R} (R_i - \tan \delta Z) dZ - \int_{R_i}^{R_i - X \cot \delta} \frac{\partial T^*}{\partial Z} R dR \right]}{\frac{\pi}{\cos \delta} [R_i^2 - (R_i - X \cot \delta)^2] + \pi (R_i - X \cot \delta)^2} \\ &+ \frac{\int_0^{R_i - X \cot \delta} \frac{\partial T^*}{\partial Z} 2\pi R dR}{\frac{\pi}{\cos \delta} [R_i^2 - (R_i - X \cot \delta)^2] + \pi (R_i - X \cot \delta)^2} \quad (11) \end{aligned}$$

B. Validation

Before continuing, it's required to ensure the dependability and the precision of the present numerical model and the FLUENT 12.0 CFD code. The heat transfer data computed for differentially heated of the conical annular, with different parameters which correspond to the cone angle $\delta = 90^\circ$, aspect ratio $Ar = H / L$, radius ratio $K = r_o / r_i$, height ratio $h = X / L$ & Rayleigh number $10^4 \leq Ra \leq 10^5$. The present problem is to numerically investigate the natural convection flow in a vertical cylinder annular space and The average Nusselt number variation is compared with those of reference from the literature data. Table 1 demonstrated the comparison between the current results and Those of [17] and [18]. It is clearly demonstrated in Table 1 that, for several values of Rayleigh number. Was checked and ensured with the present results and those obtained by these authors. There is a satisfactory agreement.

Table 1

Values of the overall Nusselt number at the Isothermal Walls for Annulus Aspect ratio $Ar=10$ and $K=2$, $\delta=90^\circ$

Rayleigh number	[17]	[18]	Present
10^4	2.355	2.33	2.343
510^4	3.718	3.758	3.755
10^5	4.558	4.568	4.564

V. RESULTS AND DISCUSSION

A. Effects of Rayleigh number Number

In this study The results obtained with respect to different parameters being $Ar=1$, $K=2$, $X=0.5$ and $\delta=45^\circ$. Fig.2 shows for Rayleigh number $10^3 \leq Ra \leq 10^4$ that there is a logarithmic temperature distribution in the all-region of the annulus

illustrates that heat from the left wall toward the right wall is transferred by conduction regime for Rayleigh number $Ra=5 \times 10^4$. The temperature gradient become slightly flatter at the core of the annulus which indicates that the conduction dominance is slashed in reason to a small quantity of convection established in the central part. The flow models show where convection promotes the transfer of heat. Fig. 2 shows the Rayleigh number $Ra = 10^5$ A vertical steep temperature gradient formed near the active wall. This confirms the increased in heat transfer rate due the existence of the cells models formed at interior annulus. This regime transition, wherein the boundary layer formed at the left and right active wall attain the central part of the annulus and merges all. Therefore, ago a rotational movement of the fluid, provoking mixing and ameliorate in heat transfer evaluation. However, for Rayleigh number $Ra = 10^6$, the nucleus was considered almost isothermal with the temperature gradient just about equal to zero. This indicate that the heat transfer in the annulus is mainly drawn by the moving boundary layers close by the walls and the fluid flow is in the regime of the laminar boundary layer. The heat transferred through the nucleus is negligible.

Vertical velocity profiles are presented in Fig. 3 for different Rayleigh numbers ranging from $Ra = 10^3$ to $Ra = 10^6$. The profiles are plotted along the horizontal direction. Other geometric parameters were selected as $Ar = 1$, $K = 2$, $X = 0.5$ and $\delta = 45^\circ$. As expected, the velocity is very low across wherever in the annulus at $Ra \leq 10^4$. The fluid move is not effectual confirmed that the conductive regime is predominant effective under this condition. This means that the fluid is virtually stagnant in the annulus at $0 \leq R \leq 0.5$ and $0.9 \leq R \leq 1.1$. But, when the Rayleigh number is in the range of $5 \times 10^4 \leq Ra \leq 10^5$, the fluid entrained by the buoyancy-driven force in annulus is begins to accelerate from the base and forms the primary flow in the vertical direction to up. The velocity increases when the Rayleigh number is large enough $Ra = 10^6$, and the fluid flow is now confined adjacent at a time in the hot wall ($0.37 \leq R \leq 0.67$) and the cold wall ($1.09 \leq R \leq 1.33$).

The Rayleigh number effects on streamlines (left) and isotherms (right) Fig. 4 (a) - (d) Present $Ar = 1$, $K = 2$, $X = 0.5$ and $\delta = 45^\circ$ visualizations are given from $Ra = 10^3$ to $Ra = 10^6$. The single cell is formed, shown from these figures, of all values of the Rayleigh numbers considered, which is in the direction of rotation clockwise. At lower Rayleigh number $Ra \leq 10^4$ such that Fig. 4 a-b the isotherms are almost vertical at the active wall for most of the annulus, illustrating the mechanism of heat transfer flow by conduction dominated. For higher values of the Rayleigh number (i.e. $10^5 \leq Ra \leq 10^6$) as shown in Fig. 4 c-d, due to the increase of the mode of convection heat transfer, two thin boundary layers were formed vicinity of the hot and cold walls for $1 \leq R \leq 2$. The isotherms are deformed and crowded adjacent the bottom left and upper right of the annulus and are stratified horizontally. The flow majority moves to upwardly right and top of the annulus in reason to the presence of the wall partly cooled and heated. because of adiabatic boundaries at the upper and the bottom of the annulus the Flow becomes motionless. However, the increased convection mode of heat transfer

provoked by increasing the Rayleigh number and the virtually parallel distribution to the horizontal walls. It can also be seen from streamlines, the fluid velocity increases and the fluid direction and revolved towards the top right and bottom left of the annulus when the increase of the Rayleigh number.

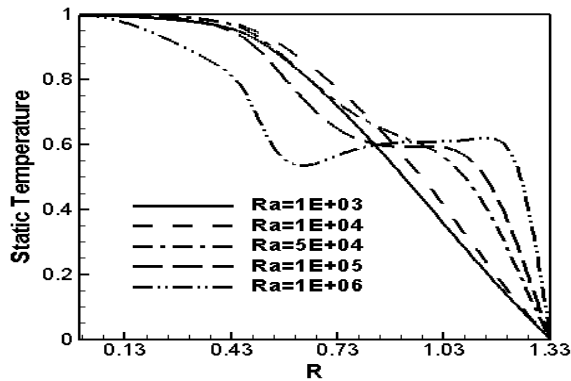


Fig.2 Temperature profiles variation with horizontal distance for annulus Aspect ratio $Ar=1$, $K=2$, $X=0.5$ and $\delta=45^\circ$ at $Z=0.75$.

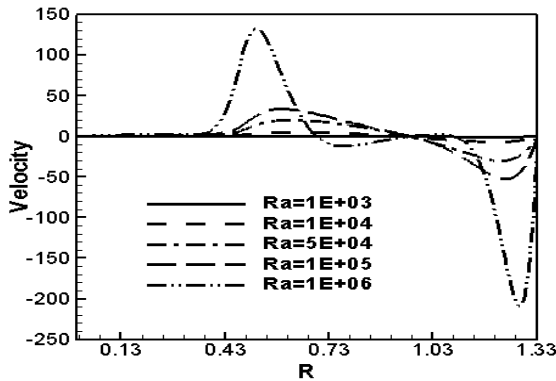
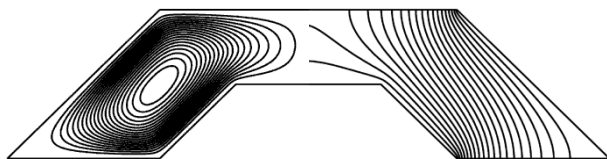
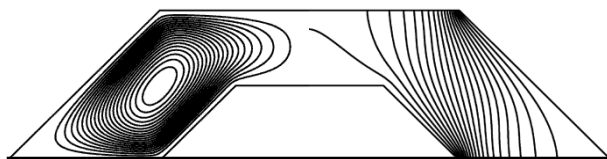


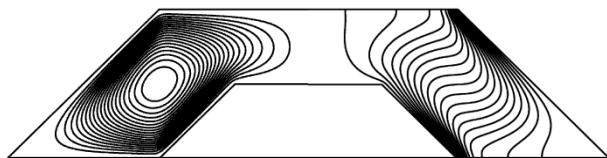
Fig. 3 Axial velocity profiles variation with horizontal distance for annulus Aspect ratio $Ar=1$, $K=2$, $X=0.5$ and $\delta=45^\circ$ at $Z=0.75$.



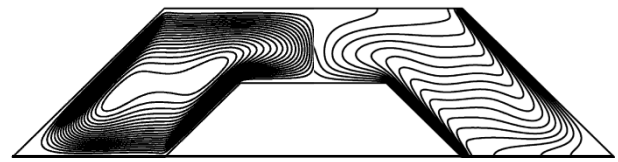
a) $Ra=10^3$



b) $Ra=10^4$



c) $Ra=10^5$



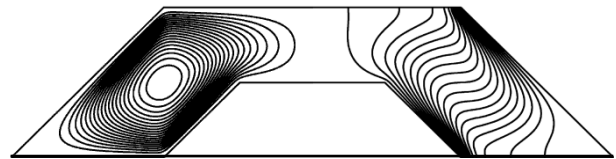
d) $Ra=10^6$

Fig.4 Streamlines and isotherms for annulus Aspect ratio $Ar=1$, $K=2$, $X=0.5$ and $\delta=45^\circ$.

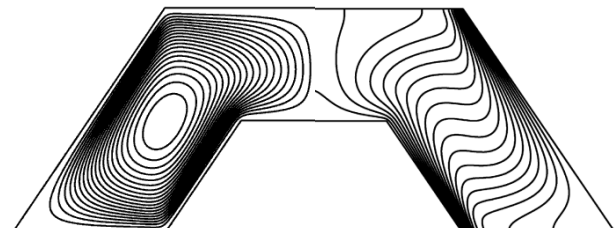
B. Effects of Aspect ratio

The isotherms (on the right) and streamlines (on the left) are depicted variations for aspect ratio Ar as can be seen from Fig. 5. The figure obtained for different aspect ratio values i.e. $Ar=1$, 1.5 & 2 and three different values of title angles $\delta=45^\circ$, 56.31° & 63.44° corresponding to $K=2$, $X=0.5$, 0.75 & 1 and $Ra=10^5$. The form of the isotherms show that increasing the aspect ratio provoked to the isotherms crowding at the bottom left and top right of the annulus. The temperature gradient in the hot wall, there is continuous variations low aspect ratio Fig. 5a indicates that the heat transfer rate continuously varies along the vertical height of the hot wall, which is not the case at higher aspect ratio Fig. 5c. The fluid flow center increased when aspect ratio increases.

The increase in the Nusselt number for different aspect ratio $Ar=1$, 1.5 and 2 , and height ratio $X=0.5$, 0.75 and 1 , and its linear variation with the Rayleigh number on a logarithmic scale are presented in Fig. 6. The other parameters are $K=2$ and $\delta=45^\circ$, 56.31° & 63.44° . For the hot wall, the average heat transfer rate increases as the Rayleigh number is increased by the growing contribution of natural convection. And the heat transfer rate increases with increase in the annulus aspect ratio.



a) $Ar=1$, $\delta=45^\circ$



b) $Ar=1.5$, $\delta=56.31^\circ$

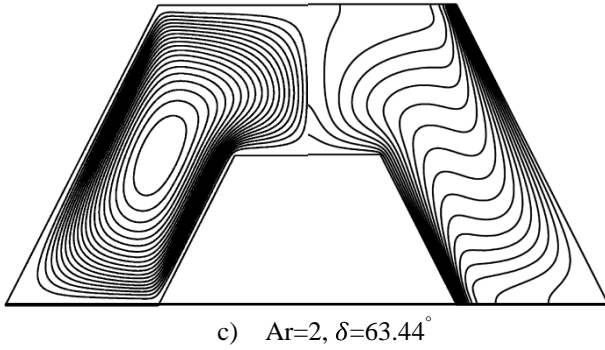


Fig. 5 Streamlines and isotherms for different Annulus Aspect ratio at $Ra=10^5$ and $K=2$.

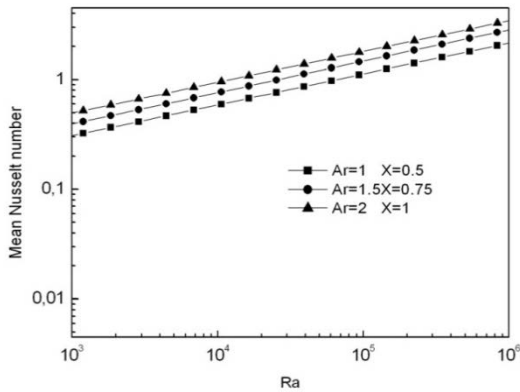


Fig. 6 Nusselt number variation with Rayleigh number and annulus Aspect ratio, Height ratio at $K=2$ and $\delta=45^\circ, 56.31^\circ \& 63.44^\circ$.

C. Effects of Height ratio

The isotherms (on the right) and streamlines (on the left) with different annulus height ratio X as demonstrated in Fig. 7. This figure corresponds to the several values $Ra = 10^5$, $Ar=1$, $K = 2$ and $\delta=45^\circ$. It's clearly noted from this figure that the isotherms move to the hot wall with a ratio of height increasing. This informs that increasing of the annulus height ratio provoked increasing the heat transfer from the hot wall of annulus. The temperature gradient hot wall can also be seen from the isothermal continuous decrease as the decrease in the ratio of the height. (The fluid flow is clearly visualized in the streamlines, The fluid flow is clearly visible in the streamlines). The complete cycle formed through the fluid circulation directed upward toward the hot wall falls then to the cold wall of the annulus . showing that the fluid flow concentrates of the circular cell at the entire annular space of small height ratio, but it moves half of the annular space ($1 \leq R \leq 2$), the height ratio increases. When the ratio of the height increases the orientation of the cell becomes parallel to the vertical inner cone.

The Nusselt number variation with aspect ratio X for several Rayleigh number. The figure corresponds to $Ar = 1$, $K = 2$ and

$\delta=45^\circ$ are plotted in Fig. 8. As expected, the heat transfer rate is greater at the Rayleigh number is greater. It can be inferred from the figure that the growth rate effect is higher than the line for $Ra \leq 10^5$ is stronger at higher Rayleigh number values and the line corresponding to $Ra = 10^6$. The height ratio does not influence the heat transfer rate when $Ra \leq 10^5$, because the fluid move is very slow, and therefore the conductive regime prevails over convection regime, which explains the almost constant value the Nusselt number.

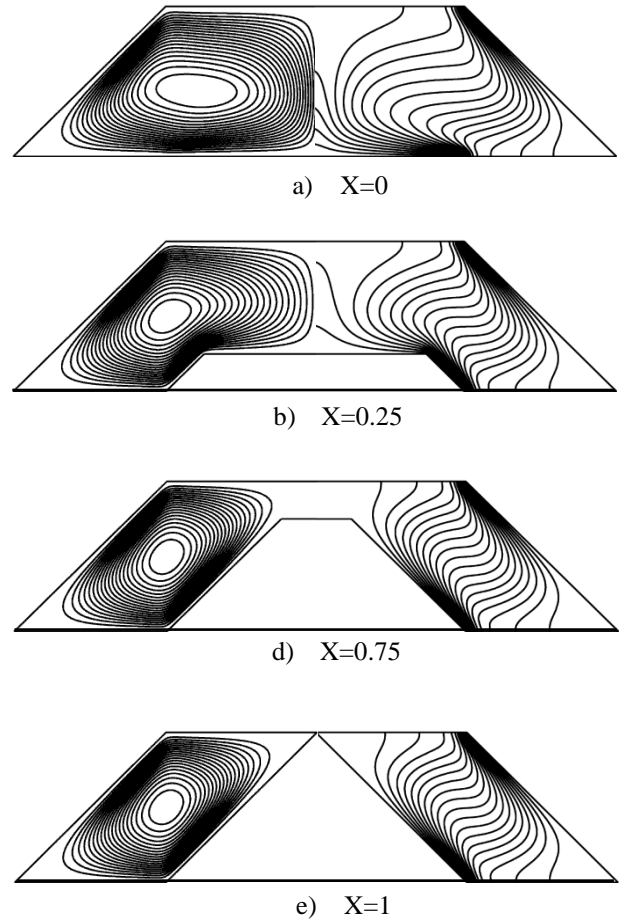


Fig. 7 Streamlines and isotherms for different annulus Height ratio at $Ra=10^5$, $Ar=1$, $K=2$ and $\delta=45^\circ$.

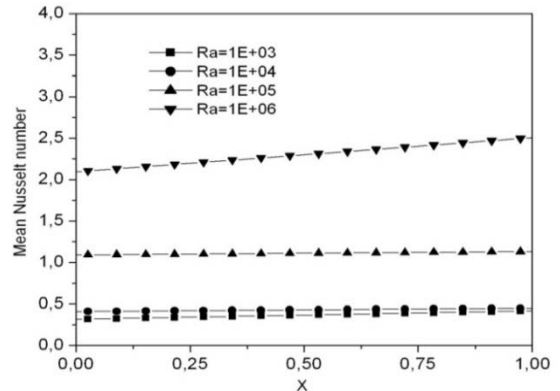


Fig.8 Nusselt number Variation with annulus Height ratio and Rayleigh number at $Ar=1$ and $K=2$, $\delta=45^\circ$.

VI. CONCLUSION

In this paper, the numerical study of natural convection in a Two-Dimensional vertical conical partially annular space for steady-state regime with differentially heated walls has been analyzed. The effect of main parameters as Rayleigh number, Aspect ratio and Height ratio of annulus. Concise summaries of the major results are reported in the following:

-The heat transfer rate increases with increasing Rayleigh number. The heat transfer rate increasing is a function of the annulus Aspect ratio.

-For lower Rayleigh number values we observed a dominance of conduction heat transfer. At higher values of Rayleigh number was observed that heat transfer rate increased and dominated by convection mode.

-The natural convection regime has been bounded by Rayleigh number. When the Rayleigh number is weak, the fluid is practically stagnant. But for higher values of Rayleigh number the fluid entrained and begins to accelerate by the buoyancy-driven force in annulus from the base and forms the primary flow in the vertical direction to up.

-It is found that the annulus height ratio is one of the more important parameters on flow and temperature fields and heat transfer. The Nusselt number increase is a function of the annulus height ratio.

-For high value of the annulus height ratio the cell orientation becomes parallel to the vertical inner cone i.e. The fluid motion is accelerated fully in the $1 \leq R \leq 2$ and they are almost zero in the other side $0 \leq R \leq 1$ at above the inner cone. But when height ratio decreases the fluid motion is accelerated increasingly in the zone $0 \leq R \leq 1$ (the circular cell of the fluid motion is concentrated at the all in this zone).

ACKNOWLEDGMENT

The authors acknowledge the partial support of the work within the BinLaden Research Chair on Quality & Productivity Improvement in the Construction Industry, funded by Saudi BinLaden Group.

References

- [1] A. Sridhar and K.S. Reddy, "Transient analysis of modified cuboid solar integrated-collector-storage system," *Applied Thermal Engineering*, vol. 27, pp.330-346, 2007.
- [2] S.G. Wang and T.Y. Li and P.T. Hsu and Kaohsiung and Taiwan, "Natural convection of micropolar fluid in a partially divided enclosure," *Acta Mechanica*, vol. 136, pp. 41 – 53, 1999.
- [3] Y.L. He and W.W. Yang and W.Q. Tao, "Three-Dimensional Numerical Study of Natural Convective Heat Transfer of Liquid in a Cubic Enclosure," *Numerical Heat Transfer Part A Applications*, vol. 47, pp.917-934, 2005.
- [4] H.N. Dixit and V. Babu, "Simulation of high Rayleigh number natural convection in a square cavity using the lattice Boltzmann method," *International Journal of Heat and Mass Transfer*, vol. 49, pp. 727–739, 2006.
- [5] A.A. Ganguli and A.B. Pandit and J.B. Joshi, "CFD simulation of heat transfer in a two-dimensional vertical enclosure," *Chemical Engineering Research and Design*, vol. 87, pp. 711–727, 2009.
- [6] M. Aounallah and Y. Addad and S. Benhamadouche and O. Imine and L. Adjilout and D. Laurence, "Numerical investigation of turbulent natural convection in an inclined square cavity with a hot wavy wall," *International Journal of Heat and Mass Transfer*, vol. 50, pp. 1683–1693, 2007.
- [7] Y. Varol and H.F. Oztop and I. Pop, "Natural convection in right-angle porous trapezoidal enclosure partially cooled from inclined wall," *International Communications in Heat and Mass Transfer*, vol. 36, pp.6–15, 2009.

- [8] E. Fuad Kent and E. Asmaz and S. Ozerbay, "Laminar natural convection in right triangular enclosures", *Heat and Mass Transfer*, 2007, Vol. 44, pp. 187–200.
- [9] I. Hajri and A. Omri and S. Ben Nasrallah, "A numerical model for the simulation of double-diffusive natural convection in a triangular cavity using equal order and control volume based on the finite element method," *Desalination*, vol. 206, pp. 579–588, 2007.
- [10] Y. Varol and H.F. Oztop and T. Yilmaz, "Natural convection in triangular enclosures with protruding isothermal heater," *International Journal of Heat and Mass Transfer*, vol. 50, pp. 2451–2462, 2007.
- [11] A. Hadjadj and S. Maamir and B. Zeghamati, "A new study of laminar natural convection in two concentric vertical cylinders," *Heat and Mass Transfer*, vol. 35, pp. 113-121, 1999.
- [12] P. Venkata Reddy and G. S.V.L. Narasimham, "Natural convection in a vertical annulus driven by a central heat generating rod," *International Journal of Heat and Mass Transfer*, vol. 51, pp.5024–5032, 2008.
- [13] F. A. Hamad and M. K. Khan, "Natural convection heat transfer in horizontal and inclined annuli of different diameter ratios", *Energy Conversion and Management*, 1998, Vol. 39, pp. 797-807.
- [14] E.L.M. Padilla and A. Silveira-Neto, "Large-eddy simulation of transition to turbulence in natural convection in a horizontal annular cavity," *International Journal of Heat and Mass Transfer*, vol. 51, pp. 3656-3668, 2008.
- [15] M. Habibi Matin and I. Pop, "Natural convection flow and heat transfer in an eccentric annulus filled by Copper nanofluid," *International Journal of Heat and Mass Transfer*, vol. 61, pp. 353–364, 2013.
- [16] N.J.A. Salman and A.B. Irfan and Z.A. Zainal and H.M.T. Khaleed and K. Jeevan, "Heat transfer in a conical cylinder with porous medium," *International Journal of Heat and Mass Transfer*, vol. 52, pp. 3070–3078, 2009.
- [17] G. de Vahl Davis and R.W.Thomas, "Natural Convection Between Concentric Vertical Cylinders High Speed Computing in Fluid Dynamics," *Physics of Fluids*, vol. 2, pp. 198–207, 1969.
- [18] R. Kumar and M.A. Kalam, "Laminar Thermal Convection between Vertical Coaxial Isothermal Cylinders," *International Journal of Heat and Mass Transfer*, vol. 34, pp. 513-524, 1991.

Mathematical Modeling of Leather Fatliquoring

H. Charvátová, D. Janáčová, K. Kolomazník, V. Vašek, R. Drga, P. Mokrejš

Abstract—The contribution deals with mathematical modeling of fatliquoring that is one of the processes in a tannery technology. It is focused on diffusion transport of lubricant into the inner porous structure of the , wherein lubricant is not bound to the structure. Based on the formulated mathematical model, the main parameters influencing the process of fatliquoring are considered.

Keywords—Fatliquoring, leather, mathematical model, diffusion of lubricant.

I. INTRODUCTION

FATLIQUORING is one of the processes in tannery technology. Its purpose is transport of lubricant into internal structures of the leather material in order to slipperiness and achieve ductility, flexibility and resilience finished to mechanical stress. Therefore, it is important to deal with the proposal diffusion model describing the transport of lubricant to the internal structure of the treated leathers.

II. MECHANISM OF LUBRICANT SORPTION INTO THE LEATHER MATERIAL

In this process the leather material binds only fat (lubricant) and the emulsifier acts to disperse of lubricant particles. This process allows the diffusion transport of lubricant into the

This work was supported by the European Regional Development Fund under the project CEBIA-Tech No. CZ.1.05/2.1.00/03.0089 and by the Ministry of Education, Youth and Sports of the Czech Republic under the Research Plan No. MSM.

H. Charvátová, Tomas Bata University in Zlín, Faculty of Applied Informatics, Department of Automation and Control Engineering, nám. T. G. Masaryka 5555, 760 01 Zlín, Czech Republic (e-mail: charvatova@fai.utb.cz)

D. Janáčová, Tomas Bata University in Zlín, Faculty of Applied Informatics, Department of Automation and Control Engineering, nám. T. G. Masaryka 5555, 760 01 Zlín, Czech Republic; phone: +420 576 035 274; fax: +420 576 032 716; (e-mail: janacova@fai.utb.cz)

K. Kolomazník, Tomas Bata University in Zlín, Faculty of Applied Informatics, Department of Automation and Control Engineering, nám. T. G. Masaryka 5555, 760 01 Zlín, Czech Republic (e-mail: kolomaznik@fai.utb.cz)

V. Vašek, Tomas Bata University in Zlín, Faculty of Applied Informatics, Department of Automation and Control Engineering, nám. T. G. Masaryka 5555, 760 01 Zlín, Czech Republic (e-mail: vasek@fai.utb.cz).

R. Drga, Tomas Bata University in Zlín, Faculty of Applied Informatics, Department of Security Engineering, nám. T. G. Masaryka 5555, 760 01 Zlín, Czech Republic (e-mail: rdrga@fai.utb.cz)

P. Mokrejš, Tomas Bata University in Zlín, Faculty of Technology, Department of Polymer Engineering, nám. T. G. Masaryka 5555, 760 01 Zlín,

inner porous structure of the leather, wherein lubricant is not bound to the leather structure.

Suppose diffusion mechanism of the components transport in the internal structure of leather material wherein all deviations from Fick's diffusion are included in the value of the effective diffusion coefficient [1].

It is assumption of the closed system that is most similar to the real case, realized by tanning barrel. Mixing in a barrel will be perfect. Temperature during the entire process is constant.

Due to geometrical properties, the solid material (leather) is considered as a plane plate with isotropic properties with respect to the sorption characteristics of a lubricant. We also suppose that all geometry parameters are constant. Diffusion of lubricant in the leather can be then described by equation (1) [4]:

$$\frac{\partial c(x, \tau)}{\partial \tau} = D \frac{\partial^2 c(x, \tau)}{\partial x^2} - \frac{\partial c_A(x, \tau)}{\partial \tau}, \quad (0 \leq x \leq b, \tau > 0). \quad (1)$$

Limiting case assumes a linear sorption of lubricant:

$$c_A(x, \tau) = Kc(x, \tau). \quad (2)$$

$$\frac{\partial c_A(x, \tau)}{\partial \tau} = K \frac{\partial c(x, \tau)}{\partial \tau}. \quad (3)$$

Substituting of the linear case into equation (1) is:

$$\frac{\partial c(x, \tau)}{\partial \tau} = K \frac{\partial^2 c(x, \tau)}{\partial x^2}, \quad (0 \leq x \leq b, \tau > 0), \quad (4)$$

where

$$K = \frac{D}{1 + A}. \quad (5)$$

Providing isotropic properties can be applied the condition of symmetry (6):

$$\frac{\partial c(0, \tau)}{\partial x} = 0. \quad (6)$$

Czech Republic (e-mail: mokrejs@ft.utb.cz)

If we relate the concentration of lubricant in a leather to the total volume of the leather and the concentration of lubricant

in the bath to the total volume of the bath, then the reminder of perfect mixing bath is given by equation (7):

$$c(b, \tau) = \varepsilon c_0(\tau). \quad (7)$$

At steady-state conditions on the surface of the leather, the loss of lubricant in the bath is equal to the volume increment of lubricant in the leather. Lubricant enters into the internal volume through the leather surface. Increase of mass for a given time is determined by the diffusion flux density J_x multiplied by the size of the total surface. The diffusion flux density is given by is given by Fick's second law. Then the other boundary condition is:

$$V_0 \frac{dc_0(\tau)}{dt} = -SD \frac{\partial c(b, \tau)}{\partial x}. \quad (8)$$

Initial concentration of lubricant in the leather is equal to zero (9):

$$c(x, 0) = 0. \quad (9)$$

Initial concentration of lubricant in the leather is given by equation (10):

$$c_0(0) = c_{0p}. \quad (10)$$

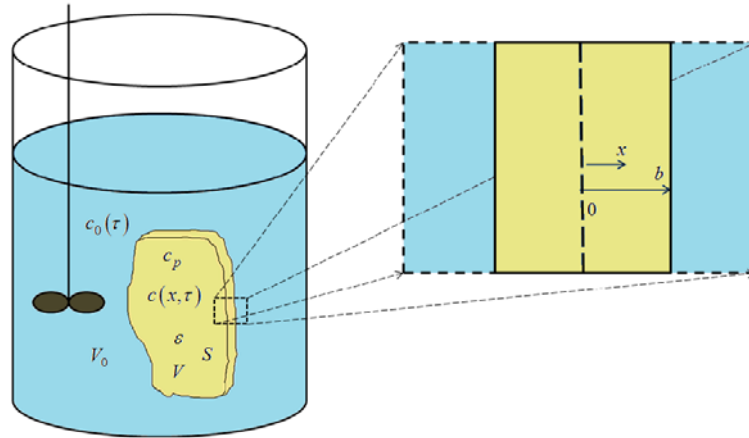


Fig. 1 Sketch of the fatliquoring model

By Laplace transformation we obtained analytical solution of the model, that describes dimensionless concentration fields in the leather $C(X, Fo)$:

$$C(X, Fo) = \frac{\varepsilon(1+A)}{\varepsilon(1+A)+Na} - \frac{-2Na \sum_{n=1}^{\infty} \frac{\cos(q_n X) e^{-q_n^2 Fo}}{\varepsilon(1+A) - \frac{\varepsilon(1+A)}{q_n} \sin(q_n) - Na q_n \sin(q_n)}}{\varepsilon(1+A) - \frac{\varepsilon(1+A)}{q_n} \sin(q_n) - Na q_n \sin(q_n)}, \quad (11)$$

where q are roots of transcendent equation (12):

$$\tan(q) = -\frac{qNa}{\varepsilon(1+A)}. \quad (12)$$

C is dimensionless concentration of lubricant in the leather:

$$C = \frac{c}{c_r}, \quad (13)$$

X is dimensionless space coordinate:

$$X = \frac{x}{b}, \quad (14)$$

Fo is Fourier number (dimensionless time):

$$Fo = \frac{K \cdot \tau}{b^2}, \quad (15)$$

Na is a ratio of volume of liquid in the bath to the volume of the leather:

$$Na = \frac{V_0}{V}. \quad (16)$$

Fig. 2 shows concentration fields in the leather during

fatliquoring. Fig. 3 shows distribution of lubricant in the leather in specific times of the process under the conditions:

- Thickness b of leather 4 mm,
- ratio of volume of liquid in the bath to the volume of the leather 5,
- diffusion coefficient D is $1.10^{-8} \text{ m}^2 \cdot \text{s}^{-1}$,
- sorption coefficient A is 5,
- porosity of the leader ε is 0.5
- initial concentration of lubricant in the bath $0.5 \text{ kg} \cdot \text{m}^{-3}$.

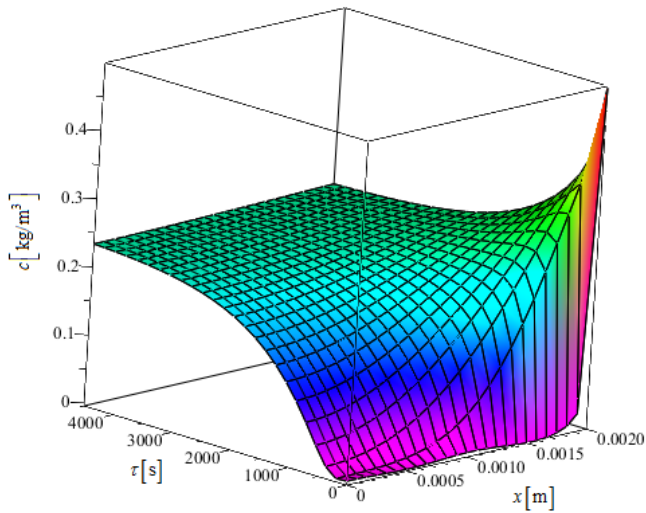


Fig. 2 Concentration field of lubricant in the leather

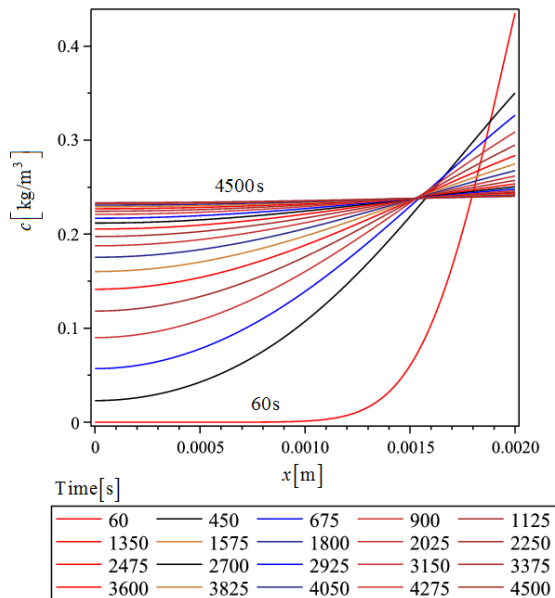


Fig. 3 Concentration of lubricant in the leather in specific times of fatliquoring

III. ASSESSMENT OF PARAMETERS THAT INFLUENCE THE COURSE OF FATLIQUORING

Course of fatliquoring depends on many parameters of both solid and liquid phase. The main parameters of liquid phase are volume of liquid in the bath, initial concentration of lubricant in the bath and concentration of lubricant in the bath during fatliquoring.

The parameters of solid phase which influence process course, are thickness and porosity of the leather, volume of the leather, initial concentration of lubricant in the leather, concentration of lubricant in the leather during fatliquoring. To the main factors depend sorption parameters of lubricant. In the limiting case of linear sorption is it the sorption coefficient A .

The Fig. 4 shows concentration fields in the specific times of fatliquoring for different values of the sorption coefficient A . Solid lines are concentration fields computed for $A = 2$, dashed lines are concentration fields for $A = 4$ and dotted lines are concentration fields for $A = 6$. It is evident that higher value of the sorption coefficient A causes a slowing down the process and also decreases the final concentration of lubricant in the leather.

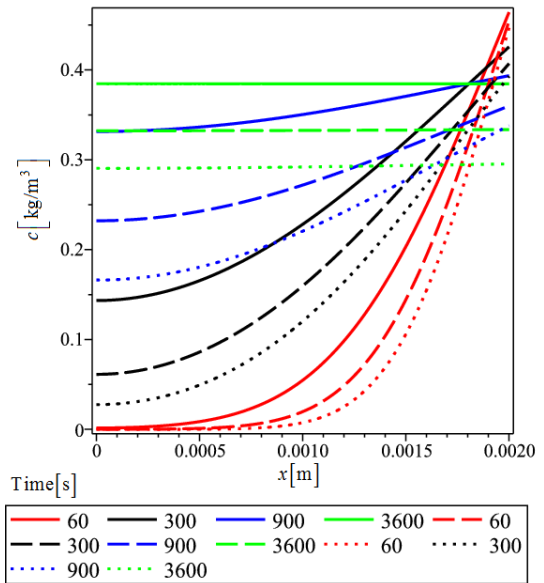


Fig. 4 Assessment of concentration fields of lubricant in the leather for various sorption constants A .

$A = 2$ (solid lines), $A = 4$ (dashed lines), $A = 6$ (dotted lines).

Parameters: thickness of leather 4 mm, ratio of volume of liquid in the bath to the volume of the leather 5, diffusion coefficient $1.10^{-8} \text{ m}^2 \cdot \text{s}^{-1}$, porosity of the leather 0.5, initial concentration of lubricant in the bath $0.5 \text{ kg} \cdot \text{m}^{-3}$.

Also diffusion coefficient is an important parameter influencing the course of fatliquoring. In the Fig. 5 is shown comparison of concentration fields for diffusion coefficient values $1.10^{-8} \text{ m}^2 \cdot \text{s}^{-1}$ (solid lines), $2.10^{-8} \text{ m}^2 \cdot \text{s}^{-1}$ (dashed lines), $3.10^{-8} \text{ m}^2 \cdot \text{s}^{-1}$ (dotted lines) in the specific times of process. With

decreasing value of diffusion coefficient, the rate of lubrication decreases. However, unlike the previous case (dependence of the sorption coefficient A) is achieved for all tested diffusion coefficients the same value concentrations in the leather material at equilibrium (green line in Fig. 5).

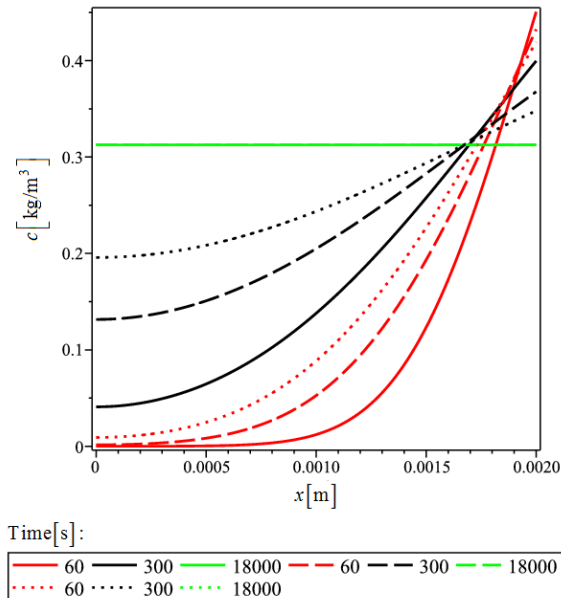


Fig. 5 Assessment of concentration fields of lubricant in the leather for various diffusion coefficients D .

$D = 1.10^{-8} \text{ m}^2 \cdot \text{s}^{-1}$ (solid lines), $D = 2.10^{-8} \text{ m}^2 \cdot \text{s}^{-1}$ (dashed lines),
 $D = 3.10^{-8} \text{ m}^2 \cdot \text{s}^{-1}$ (dotted lines).

Parameters: thickness of leather 4 mm, ratio of volume of liquid in the bath to the volume of the leather 5, sorption coefficient A is 5, porosity of the leather 0.5, initial concentration of lubricant in the bath $0.5 \text{ kg} \cdot \text{m}^{-3}$.

IV. CONCLUSION

Study of diffusion transport of lubricant into the inner porous structure of the leather enabled to formulate mathematical model describing process of lubrication. The mathematical model was used to assess the impact of parameters on the lubrication course.

The main parameters include sorption parameters of lubricant and diffusion coefficient. The obtained results. Knowledge of the mechanism of the studied process will help to propose optimal fatliquoring procedures, which will be achieved by high quality processed.

LIST OF SYMBOLS

- A - sorption coefficient of lubricant to the leather, [1]
 b - half thickness of the leather, [m]
 c - concentration of unbound lubricant in the leather, [$\text{kg} \cdot \text{m}^{-3}$]
 C - dimensionless concentration of unbound lubricant in the leather, [1]
 c_A - concentration of bound lubricant in the leather, [$\text{kg} \cdot \text{m}^{-3}$]

- c_p - initial concentration of lubricant in the leather, [$\text{kg} \cdot \text{m}^{-3}$]
 c_0 - concentration of lubricant in the liquid phase, [$\text{kg} \cdot \text{m}^{-3}$]
 D - diffusion coefficient, [$\text{m}^2 \cdot \text{s}^{-1}$]
 Fo - Fourier number, [1]
 K - modified diffusion coefficient, [$\text{m}^2 \cdot \text{s}^{-1}$]
 Na - ratio V_0/V , [1]
 S - area of the leather, [m^2]
 V - volume of the leather, [m^3]
 V_0 - volume of the liquid phase, [m^3]
 x - space coordinate, [m]
 X - dimensionless space coordinate, [1]
 ε - porosity of the leather, [1]
 τ - time, [s]

REFERENCES

- [1] Crank, J. The Mathematics of Diffusion, Clarendon Press, Oxford, 2nd Ed., 1975
- [2] K. Kolomazník, et al., "Modeling of Raw Hide Soaking", in WSEAS Transactions on Information Science and Applications, Hellenic Naval Academy, Ostrava Poruba, 2005.
- [3] Kaul, S. N., Nandy, T., Szpyrkowitz, L., Gautam, A., Khanna, D. R. (2005). Waste Water Management With Special Reference to Tanneries. Discovery Publishing
- [4] D. Janáčková, H. Charvátová, K. Kolomazník, V. Vašek, Creating software applications for solving diffusion problems in the MAPLE interface, Tomas Bata University in Zlín, Zlín, 2012, ISBN 978-80-7454-133-9 (in Czech)
- [5] Ch. Tocci & S. Adams, Applied Maple for Engineers and Scientists, Boston: Artech House Publishers, 1996.
- [6] F. Garvan, The Maple Book, New York: Chapman & Hall/CRC, 2002.

Hana Charvátová is a research worker at the Department of Automation and Control Engineering, Faculty of Applied Informatics, of Tomas Bata University in Zlín. Her research activities include recycling technology and modeling of natural and synthetic polymers treatment.

Dagmar Janáčková is a Professor in the Department of Automation and Control Engineering, Faculty of Applied Informatics, of Tomas Bata University in Zlín. Her research activities include: modeling of treatment processes of natural polymers, transport processes, recycling of tannery wastes, and optimization and ecological approach of tannery processes. She has received the following honors: Diploma of England, XXIII IULTCS Congress, London, 11–14 September, 1997; Gold Medal - EUREKA EU Brussels 1997; Special Prize, Ministry of Agriculture, Belgium, 1997.

Karel Kolomazník is a Professor in the Department of Automation and Control Engineering, Faculty of Applied Informatics, of Tomas Bata University in Zlín. His research activities include: modeling of biopolymers treatment, chemical engineering transport processes, recycling of proteins, optimization and ecologization of tanning processes, and turning of vegetable and animal fats into biodiesel. He has received the following honors: Germany, American, England Leather Associations, XXIII IULTCS Congress, Friedrichshafen, May 15–20, 1995; England, XXIII IULTCS Congress, London, 11–14 September, 1997; USA, ALCA 1997, Annual Meeting, Regent Resort, NJ; Gold Medal - EUREKA EU Brussels 1997.

Vladimír Vašek is a Professor in the Department of Automation and Control Engineering, Faculty of Applied Informatics, of Tomas Bata University in Zlín. His research activities include: microcomputer applications in technology processes, computer monitoring and control systems, and discrete deterministic controllers approach of tannery processes. He has received the following honors: Diploma of England, XXIII IULTCS Congress, London, 11–14 September, 1997; Gold Medal - EUREKA EU Brussels 1997; Special Prize, Ministry of Agriculture, Belgium, 1997.

Rudolf Drga is an Associate Professor in the Department of Security Engineering, Faculty of Applied Informatics of Tomas Bata University in Zlín. His research activities include electronic security systems.

Pavel Mokrejš is an Associate Professor in the Department of Polymer Engineering, Faculty of Technology of Tomas Bata University in Zlín. His research activities include: treatment of liquid and solid waste from tannery industry, treatment of leather waste from shoe industry, utilization protein hydrolysates, biodegradable casings and films, and isolation of proteins from untraditional sources.

Experimental investigation of nozzle shape effect on wall shear stress beneath impinging round jet

B. Montagné, K. Sodjavi, P. Bragança, A. Meslem and M. Kristiawan

Abstract— This paper reports on measurements of velocities and wall shear rates for an impinging round jet. The test parameter that we consider is the nozzle shape. The Particle Image Velocimetry (PIV) was used to measure the axial and radial velocity components. The limitations of the PIV technique in the vicinity of the target wall are addressed by using the electrodiffusion technique to achieve wall shear rate distribution. A round orifice perforated either on a flat plate (RO/P) or on a hemispherical surface (RO/H), is compared to a reference convergent nozzle (CONV). All the nozzles have the same exit diameter D . The exit volumetric flow rate was also conserved and led to the same Reynolds number based on the exit bulk-velocity, $Re_0 = 5290$. The nozzle-to-wall distance was constant and equal to $2D$. The whole velocity field and wall shear rates in the three impinging round jets having different features are compared. This has improved the understanding of the jet/wall interaction. The wall shear rate is in a close relationship with the near field flow features, themselves affected by nozzle geometry. The orifice nozzles generate narrower exit profiles compared to the convergent nozzle. The *vena contracta* effect in orifice jets, more intense with RO/P than with RO/H, generates an increase of the exit centerline velocity. The hemispherical surface of RO/H nozzle leads to a *vena-stretching* attenuating somewhat the *vena contracta* effect at the jet exit. The instantaneous PIV fields indicated the formation of secondary vortices in the region where a secondary peak in the mean and rms distributions of wall shear rate emerged.

Keywords—Electrodiffusion, hemispherical nozzle, impinging round jet, PIV, wall shear rate.

I. INTRODUCTION

A thorough research, beginning with Gardon et al. contributions [1-3], concerned the heat/mass transfer in impinging jets, and an early observation has been made in [2] about the importance of jet turbulence in heat transfer processes. It was shown that some seemingly anomalous heat-transfer phenomena can be explained as effects of the turbulence occurring in jets. Turbulence is generated by the jet itself and by external disturbances and varies significantly with the nozzle shape, upstream conditions and position within the jet. One decade after the observation of Gardon and Akrifat [2], Popiel and Boguslawski [4] claimed that nozzle exit configuration is the most important factor affecting the heat/mass transfer. Despite these first very significant

indications, there are only a few studies dedicated to heat/mass transfer dependency of nozzle geometry.

Lee et al. [5] compared three round orifice nozzles with an exit jet Reynolds numbers Re_0 in a range of 10000–30000 and nozzle-to-plate spacing H in a range $2D$ – $10D$, where D is the exit nozzle diameter. The orifices were square-edged, standard-edged and sharp-edged, respectively. The square-edged orifice is straight hole with straight-through edges (90° corners at the hole). The standard edged orifice has square edged corners at the entrance, and a bevel edges at the outlet. The sharp-edged orifice is beveled through the entire thickness of the hole (with an angle of 45° relative to the axis normal to the orifice plate). In the stagnation region, the sharp-edged orifice jet yields significantly higher heat transfer rates than either the standard-edged orifice jet or square-edged orifice jet. The effect of nozzle exit configuration on the stagnation point heat transfer is more sensible at shorter nozzle-to-plate spacing.

The literature reveals that for high Reynolds numbers and low nozzle-to-wall distances, two peaks are present on the radial distributions of local Nusselt number, produced by circular impinging jets. The first peak corresponds to the maximum of heat transfer rate and occurs approximately at the nozzle radius. In some investigations [5-8], the location of the first peak is observed from $r = 0.5D$ to $r = 0.7D$ for $H < 4D$. This peak is attributed to the high turbulence intensity at the nozzle edge and to the direct impingement of large toroidal Kelvin-Helmholtz (K-H) vortices originated in the mixing region. The secondary peak occurs at the radial distance from the stagnation point ranging from $1.2D$ to $2.5D$ [5, 7-9]. The second peak is either attributed to the transition from laminar to turbulent boundary layer in the wall jet region [3] or to the unsteady separation of the induced secondary vortices that form near the wall under primary K-H vortices [10]. With the increasing Reynolds number, the location of the secondary peak moves outwards from the stagnation point and the peak height increases [5].

Whereas numerous papers were published on the Nusselt number (Nu) distributions generated by impinging jets, only a few studies have been dedicated to the analysis of the corresponding wall shear rate (γ) distributions [6, 11-13]. Available data of Nu and γ are compared and reveals similarities in their distributions, on the number of peaks and their radial locations. For high Reynolds number ($Re_0 = 41600$)

and $H < 4D$, two peaks are evident in γ (or in wall shear stress $\tau = \mu \cdot \gamma$) distribution [12]. Similarly to Nu -distribution [5-8], the first peak in γ -distribution appears at the distance from the stagnation point ranging from $r = 0.56D$ to $r = 0.74D$, while the second peak is located at $r = 1.9D$ [12, 14]. The fact that peak-locations in γ -distribution are closely matching with those of Nu -distribution, suggests that the wall shear stress and the local heat/mass transfer are closely linked. Also, the connection of the heat/mass transfer phenomena with the large-scale structures which develop in the free jet region or with the subsequent flow dynamics in the stagnation and wall jet regions is now recognized [7, 10, 15, 16]. Therefore, the control of large-scale structures in impinging jets is a key element in the strategy of heat/mass transfer optimization and control. The passive control based on nozzle geometry modifications is particularly attractive because of easy implementation in industrial applications.

The present article is in continuation of our previous study in which a round plate orifice jet is compared to a reference convergent nozzle jet in terms of wall shear rate and local mass transfer at a very low Reynolds number, $Re_0 = 1360$ [17]. It was concluded that the orifice jet enhances significantly transfer phenomenon compared to the reference convergent jet. The orifice jet flow generates larger in size, well-defined and vigorous primary K-H structures with comparison to the convergent nozzle jet. These differences were associated with differences in initial velocity profiles and the resulting flow development. The *vena contracta* in the orifice jet generates a thinner shear layer and an increase of the exit mean velocity relative to exit bulk-velocity.

We consider herein a turbulent case with a Reynolds number $Re_0 = 5290$. We also extend the analysis to an innovative geometry of the nozzle, i.e., a round orifice perforated on a hemispherical surface. The hemispherical nozzle has never been used in the literature for jet generation. The hemispherical surface which is supporting the round orifice considered in the present study is intended to increase the stretching of the shear-layer at the jet exit, supposing to generate a more efficient jet dynamics for wall skin friction enhancement. Contrary to previous investigation where the nozzle-to-wall distance was varied in the range $2D - 5D$, this distance is now kept constant, i. e. $H = 2D$ (with $D = 7.8$ mm for each nozzle). This particular distance was selected by considering that it corresponds approximately to the first half of the potential core length of a round free jet [18], where the K-H toroidal vortices are well formed and are still well defined at the target placed at this distance.

Wall shear stress distribution on the target plate is measured using the electrodiffusion method (ED), the same method as we have used before in [17, 19]. Phares et al. [13] made a critical survey of different techniques used for the measurements of wall shear stress and concluded that the ED method provides the greatest accuracy of any indirect method. To our knowledge, Kataoka et al. [6] have been the first to introduce this technique for the measurement of wall skin friction generated by an impinging jet. This method provides

information on the wall shear rates and the velocity field is captured using Particle Image Velocimetry (PIV). Both techniques (ED and PIV) are complementary as the PIV fails at the vicinity of the wall due to the laser scattering by the solid surface.

The paper is structured within two main Sections. In the Section II we outlined the employed experimental procedures and the Section III is dedicated to results analysis.

II. EXPERIMENTAL PROCEDURES

A. Experimental setup and geometry of nozzles

The experiments are conducted in a liquid-liquid jet impinging orthogonally onto a wall. A schematic diagram of its generation in a reservoir is shown in Figure 1. A gear pump (Ismatec with a GJ-N23 head) draws the liquid from a reservoir and delivers it to a nozzle. The liquid jet issued from the nozzle impinges a circular target disc provided with six electrodes (Figure 2) which serve as the probes for electrodiffusion measurements. The temperature of liquid is controlled by a cooling coil within $\pm 0.2^\circ\text{C}$. The nozzle is screwed to a 200 mm length stainless steel tube with inner and outer diameters of 15 and 20 mm, respectively. A honeycomb manufactured of a 7 mm thick disc by drilling 17 holes with a diameter of 2 mm was fitted in the tube inlet. The nozzle assembly was located in a support which allowed vertical movement for accurate alignment of the nozzle axis with the electrodes centre. The reservoir was placed on a sliding compound table (Proxxon KT 150) which allowed movement in the axial and transverse direction relative to the nozzle with a precision of 0.05 mm.

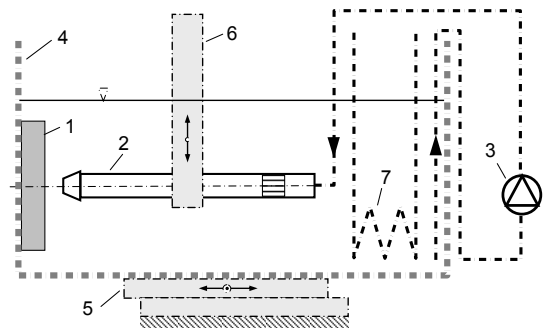


Figure 1: Diagram of apparatus: 1 target disc with electrodes, 2 tube with nozzle and honeycomb, 3 pump, 4 reservoir, 5 compound table, 6 nozzle holder, 7 cooling coil

The target (Figure 2) was manufactured of a Poly(methyl methacrylate) disc with a diameter of 100 mm and a thickness of 17 mm by first drilling holes to insert the electrodes. The platinum foil with a diameter of 50 mm and a thickness of 50 μm was assembled centrally with the disc using Neoprene glue. Holes with a diameter 0.7 mm were drilled through the platinum foil as a continuation of the holes in the disc. The electrodes were manufactured of a 0.5 mm platinum wire

which was coated electrophoretically using a deposit of a polymeric paint. After soldering connecting cables, the electrodes were glued with an epoxy resin into the disc, so that the tops of the platinum wires just projected above the platinum foil. The wires were then rubbed down flush with the surface of the platinum foil using progressively finer grades of emery paper. The last emery paper had a grit size of $10\ \mu\text{m}$. The whole surface was then polished using a fine dental paste. The resulting surface roughness was about $0.11\ \mu\text{m}$ which is much less than the Nernst diffusion layer thickness estimated at $10\ \mu\text{m}$.

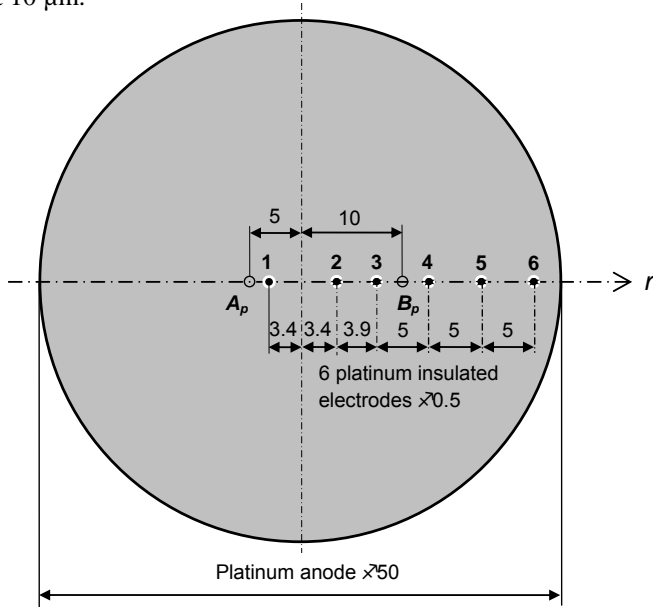


Figure 2: Target disc with electrodes row: 1-6 electrodes ϕ 0.5mm. A_p and B_p are the limits of stagnation point displacement

In this study, three round nozzles (Figure 3) having the same exit diameter $D = 7.8\text{mm}$ are compared: a convergent nozzle (CONV in Figure 3 a), a round orifice on a flat plate (RO/P in Figure 3 b) and a round orifice on a hemisphere (RO/H in Figure 3 c). A convergent nozzle had a conical shape with an area contraction 4:1 on a length of 17 mm. The flat surface orifice nozzle (RO/P) is drilled in a metal plate with a thickness of 0.5 mm, while the curve surface orifice nozzle (RO/H) is made in a hollow sphere with an internal radius of 7.6 mm and a thickness of 1 mm.

The Reynolds number based on the diameter D and the jet bulk-velocity W_b ($W_b = 4Q_0/\pi D^2 = 0.72\text{m/s}$) was $Re_b = 5290$. The distance H between the jet exit and the target wall was kept constant, $H = 2D$, for all the measurements. The coordinate system (r, Y, Z) attached to the nozzle is shown in Figure 4. As sketched in this figure, the flow field may be divided into several regions. In the neighborhood of the stagnation point S , the flow spreads in radial directions parallel to the wall. The development of the impinging jet flow field near the wall is typically divided in two regions: the stagnation region associated with the turning of the mean flow, $r/D < 1$, and the radial wall jet region, $r/D > 1$.

Table 1: Initial conditions of the three studied flows

Nozzle	W_b (m/s)	$Re_b = \frac{W_b D}{\nu}$	W_0 (m/s)	$\frac{W_0}{W_b}$	$\frac{(U_{max})^{Peak}}{W_b}$
CONV	0.72	5290	0.82	1.14	0.99
RO / H			1.07	1.49	1.29
RO / P			1.21	1.68	1.44

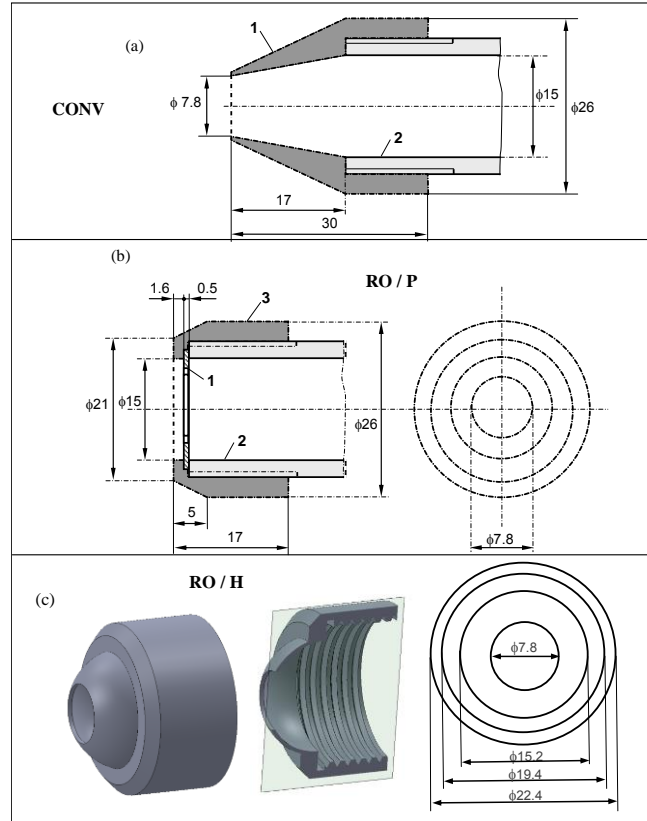


Figure 3: Sketch of nozzles: (a) 1 – Convergent nozzle (CONV), 2 – tube; (b) 1– Round Orifice on Plate (RO/P), 2 – tube, 3 – sleeve nut; (c) Round Orifice on Hemisphere (RO/H) – a plane orifice of $D = 7.8\text{mm}$ is projected onto a spherical surface

B. PIV measurements

Flow analysis has been carried out using PIV measurements. The PIV system includes a Quantel BigSky 200 mJ dual Yag laser and a FlowSense EO (CCD) camera of 2048×2048 pixels resolution with pixel size of $7.4 \times 7.4\ \mu\text{m}^2$. The total view field is about $2D \times 6D$ to cover free and wall jet regions (Figure 4 and Figure 5). The light sheet optics produces a laser sheet of less than 1 mm in thickness. The maximum acquisition frequency of the PIV system is 15 Hz. For each experiment, 500 couples of images are acquired. The recordings are analyzed through two different windows. Firstly, the velocity distribution in the total field of view ($2D \times 6D$) is calculated using an adaptive multi-grid correlation algorithm handling the window distortion and sub-pixel window displacement

the RO/P orifice nozzle generates greater contraction than RO/H orifice nozzle. As shown in Figure 5 a2, b2 and c2, the contracted free jet region leads to a contracted deflection region.

For an axial position Z , the extent of the radial jet expansion in the free jet region is defined by the jet thickness $r_{0.1}$, which is the radial position in the jet where the axial velocity W takes the value $0.1W_c$; W_c is the centerline velocity at the same axial position Z . The streamwise evolution of normalized jet thickness, $r_{0.1}/D$, is plotted in Figure 6 for each jet. As expected, the convergent jet is more expanded than the orifice jets. Comparison of the two orifice jets, confirms that the RO/H nozzle attenuates the *vena contracta* effect, which characterizes orifice jets.

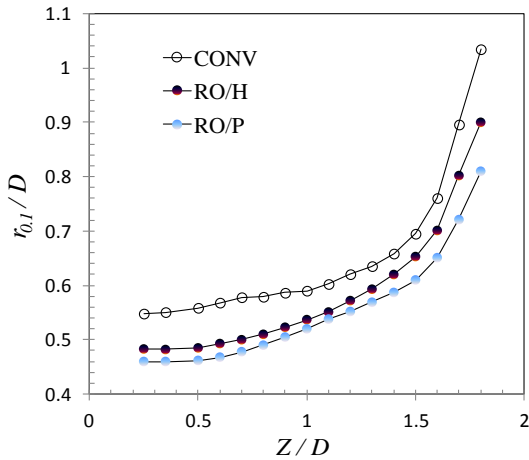


Figure 6: Growth of jet thicknesses in the free jet region

The differences in jet contraction are visible also on the streamwise velocity profiles (Figure 7 a and b), and on transverse velocity profiles as well (Figure 7 c).

In the free jet region, at $Z = 1.7D$ (Figure 7 b), axial velocity profile exhibits an “M shape”, whereas at $Z = 0.5D$ (Figure 7 a) the profile is flat. Hence, flow acceleration in the outer edge of the shear layer is a result of jet/wall interaction. Before impinging the wall, the jet accelerates in the outer edge (Figure 7 b) and decelerates on the axis, as visible on streamwise velocity changes along the jet centerline given in Figure 8. As evidenced by this figure, the axial velocity achieves zero at the stagnation point S . The value of jet bulk velocity W_b reported in this figure highlights when compared to the maximum centerline velocity W_0 , the level of flow acceleration as a function of nozzle geometry. The most accelerated flow is given by RO/P nozzle, followed by RO/H nozzle and then CONV nozzle (see also Table 1 where the values of W_0/W_b are provided). The same trend is found in the wall jet region when one compares the changes of maximum velocity U_{max} along the wall (Figure 9a). Indeed, the peak level of U_{max} is linked to the jet acceleration level (see Table 1). However, the curves have similar shapes and the position of the peak of U_{max} , $r = 0.95D$, seems, to be insensitive to the contraction level of the jet flow (Figure 9a). When U_{max} is normalized by W_0 (Figure 9b), radial distributions of maximum velocity in the wall jet region are self-similar. The comparison of dimensionless distributions

to those of the literature [14, 21, 22] of round jets at the same normalized nozzle-to-plate distance, $H/D = 2$, suggests a possible effect of jet exit Reynolds number Re_0 on the level of U_{max}/W_0 . However, the radial position of the peak value remains almost unchanged with different Re_0 and different round nozzle geometries. In fact, the round nozzle in [14, 22] is a long pipe and a convergent nozzle connected to a short pipe in [21].

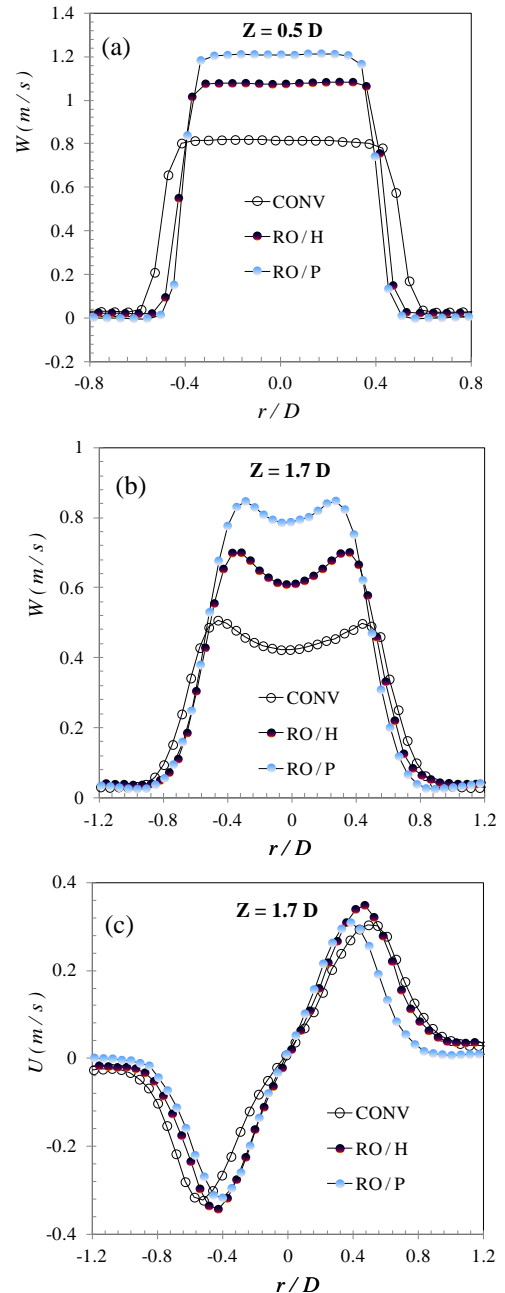


Figure 7: Streamwise velocity (a,b) and transverse velocity (c) profiles in the free jet region

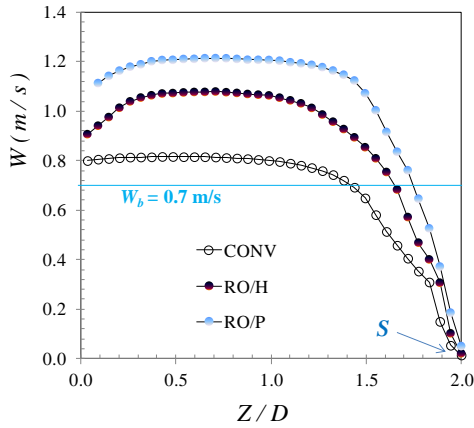


Figure 8: Streamwise mean velocity changes along the jet centerline – comparison to the jet bulk velocity W_b

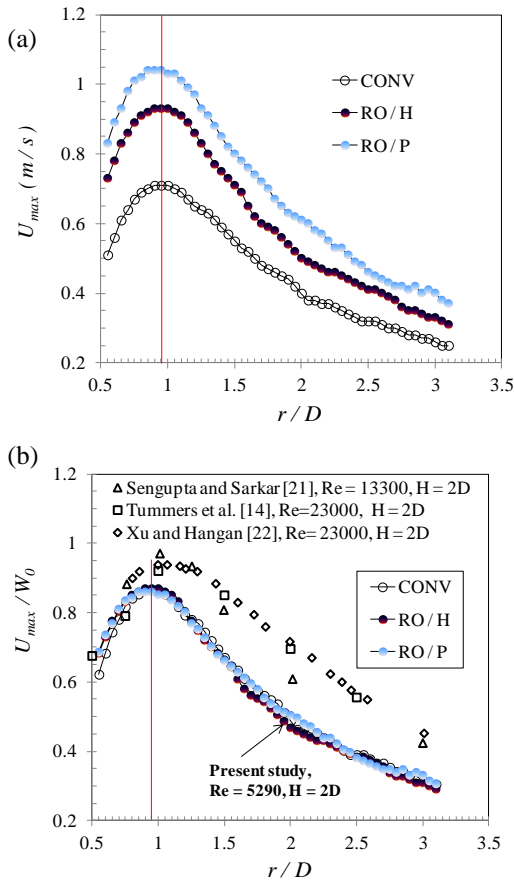


Figure 9: Radial distribution of maximum radial velocity above the wall. (a) dimensional values; (b) dimensionless values and comparison to the literature – the round nozzle in [14, 22] is a pipe and in [21] a convergent connected to a short pipe

B. Wall shear rate

Local and instantaneous wall shear rate was acquired using the electrodiffusion method (ED) described above in paragraph II.C. To measure the mean and the rms values of the wall shear rate, the signals were recorded with a sampling frequency of 500 Hz during a time of 40 sec.

The radial distributions of the wall shear rate were obtained by moving the stagnation point S horizontally in the range limited by the points A_p and B_p on the target shown in Figure 2. Sixteen displacements of the stagnation point with a step of 1mm were performed to well capture the details of wall shear rate profiles. Thereby, several values of the wall shear rate measured by different electrodes at similar radial distances from the stagnation point were obtained. Based on the comparison of the measured values for a given radial position, it was observed that the repeatability is insured with maximum deviation of $\pm 5\%$ of the mean value.

The radial distributions of the mean value of wall shear rate γ and its rms $\sqrt{\gamma'^2}$ are plotted in Figure 10 for CONV, RO/H and RO/P nozzles.

The maximum value of wall shear rate (Figure 10) is equal to 9880 s^{-1} , 15900 s^{-1} and 17000 s^{-1} for the CONV, RO/H and RO/P nozzle jet, respectively. Hence, the maximum of γ is nozzle geometry dependent and is higher for orifice jet than for convergent jet at $Re_0=5290$, as was found earlier for $Re_0=1360$ [17]. The hemispherical orifice nozzle reduces somewhat γ_{max} level, because the curved surface already converge the flow at the exit and so reduces the *vena contracta* effect. This finding is interesting for applications where wall-friction modulation and hence, local heat/mass transfer control is required. The curvature of the plate supporting the exhaust orifice may be modified to achieve a given level of local friction without changing the volumetric flow rate of the injected fluid.

Figure 11 clearly shows the effect of nozzle geometry on the position of the maximum value γ_{max} . The peak is located at $r = 0.7D$ for the CONV nozzle jet, and at $r = 0.6D$ in the RO/H and RO/P nozzle jets. These locations falls in a range of $0.6D$ - $0.74D$ reported in the literature [11-13] for the round impinging jets when $H < 4D$. Thus, the first peak of γ does not coincide with the peak of U_{max} (Figure 9). The first peak of γ is located in the growth region of U_{max} .

Figure 11 also highlights what we might call "*the birth of the second peak*" in the region $r = 1.6D$ - $1.8D$ for both orifice jets. In the convergent jet, this effect is very low suggesting that the second peak is related to the level of U_{max} in the wall jet region (Figure 9 a), itself related to the velocity acceleration at the jet exit (Figure 8).

The radial distributions of the rms(γ) values are given in Figure 12 in their normalized form. Two peaks are present, although the second peak is fairly attenuated in the convergent jet. The second peak in the rms value is clearly linked to the second peak in the mean value (Figure 11). The first peak in rms distribution (Figure 12) is about $0.2D$ farther than the first peak in the mean value distribution (Figure 11).

The instantaneous velocity field (Figure 13 a) shows toroidal K-H vortices along the interface between the jet and the surrounding liquid, which subsequently impinges on the target. For brevity, only CONV and RO/H cases are presented.

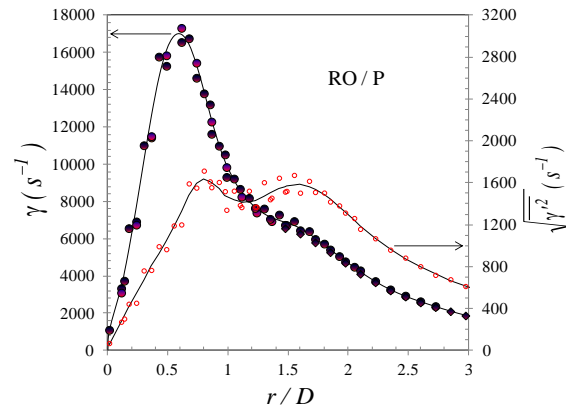
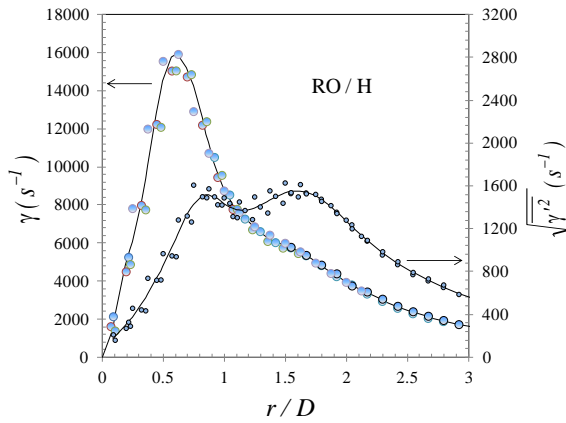
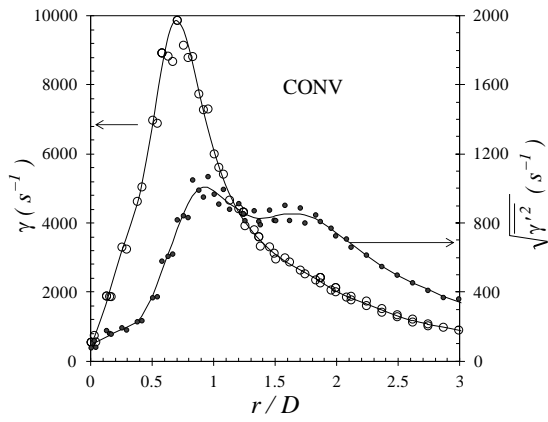


Figure 10: Wall shear rate and its rms values as a function of normalized radial distance from the stagnation point S

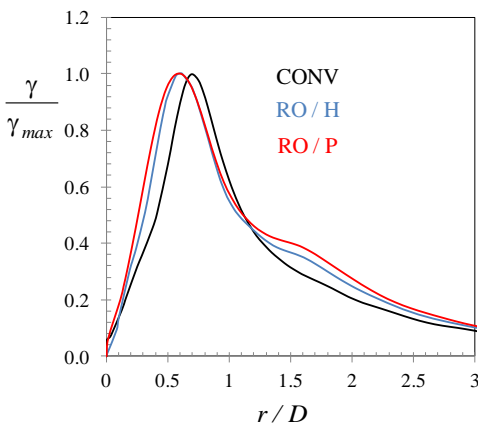


Figure 11: Comparison of normalized wall-shear rate

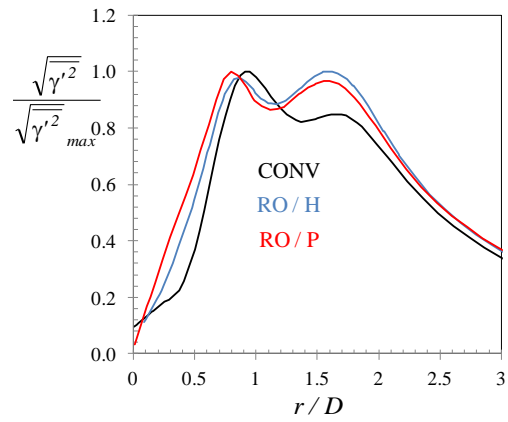


Figure 12: Comparison of normalized values of the rms of wall-shear rate

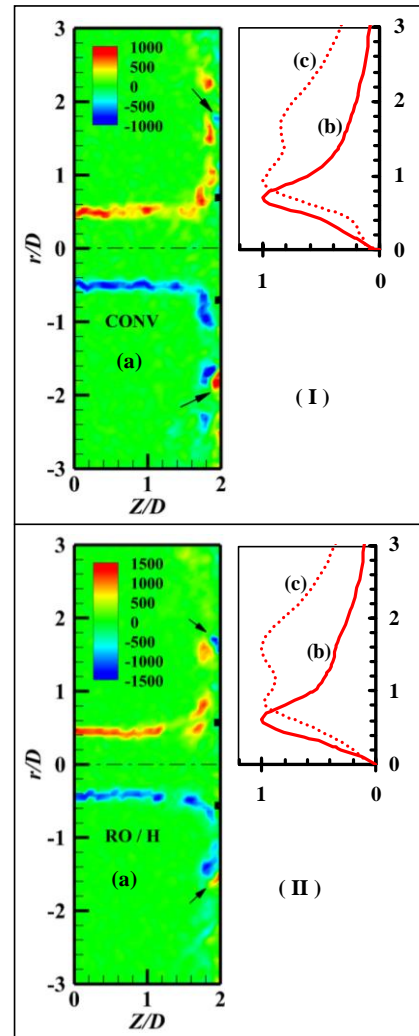


Figure 13: (I) CONV nozzle jet, (II) RO/H nozzle jet: (a) Instantaneous vorticity field $\omega_\gamma = \frac{\partial U}{\partial Z} - \frac{\partial W}{\partial X}$ - Sticks indicate the position of γ_{max} and arrows indicate secondary vortices on the target; (b) γ/γ_{max} ; (c) $\sqrt{\gamma'^2}/\left(\sqrt{\gamma'^2}\right)_{max}$

The first peak in the distribution of the mean value (Figure 13 b) and in the distribution of the rms value (Figure 13 c), appears in the region where the K-H vortices strike the target (Figure 13 a). The second peak (in γ and in its rms distribution) emerges at the position where appear secondary counter-rotating vortices, designated by an arrow in Figure 13 a. The secondary structures are present in both convergent jet (Figure 13, I) and orifice jet (Figure 13, II).

If we advance once again the similarity between the second peak of γ and the second peak of Nu , the observation made above is consistent with that of Hadziabdic and Hanjalic [10]. From their LES simulation of a round impinging jet, the authors observed that the second peak in Nu , (pertinent only for small H/D and high Reynolds Re_0 numbers) is caused by reattachment of the recirculation bubble and associated turbulence production, as well as subsequent strong advection.

IV. Conclusion

Three round impinging jets with a Reynolds number of 5290 and a nozzle-to-wall distance of $2D$, have been compared in the present study. A round orifice perforated either on a flat plate (RO/P) or on a hemispherical surface (RO/H), is compared to a reference convergent nozzle (CONV). In each jet, Particle Image velocimetry (PIV) and Electrodiffusion technique (ED) were used to produce a data set on the flow field and the wall shear rate, respectively.

The instantaneous velocity fields indicated that the formation of small secondary vortices above the impingement plate, under primary Kelvin-Helmholtz, occur in the region $r = 1.6D - 1.8D$. In the same region, mean and rms values of the wall shear rate exhibited a secondary peak in their radial distributions. The appearance of the secondary peak depends on the level of the maximum radial velocity in the wall-jet region. The level of maximum velocity in the wall jet region is as high as the flow is accelerated at the jet exit. The jet acceleration was shown to be more intensive in the orifice jets than in the convergent jet due to the *vena contracta* effect. However, the curved surface supporting the orifice stretches the flow at the exit, and reduces the *vena contracta* effect. This leads to a lower wall-friction than in the case of the flat orifice. This finding is interesting for applications where wall-friction modulation and hence, local heat/mass transfer control, is required without changing the volumetric flow rate of the injected fluid.

ACKNOWLEDGMENT

This work was supported by the Grants of the French National Agency of Research, project "FLUBAT", ANR-12-VBDU-0010 and the Grants of the PRES Limousin Poitou-Charentes

REFERENCES

1. Gardon, R., *Heat Transfer Between a Flat Plate and Jets of Air Impinging on It*. Int. Dev. Heat Transfer (ASME), 1962: p. 454-460.

2. Gardon, R. and J.C. Akfirat, *The role of turbulence in determining the heat-transfer characteristics of impinging jets*. international Journal of Heat and Mass Transfer, 1965. **8**: p. 1261-1272.
3. Gardon, R. and J.C. Akfirat, *Heat Transfer Characteristics of Impinging Two-Dimensional Air Jets*. Journal of Heat Transfer, 1966. **88**(1): p. 101-107.
4. Popiel, C.O. and Boguslawski, L. *Effect of Flow Structure on the heat or mass transfer on a Flat plate in Impinging Round jet*. in *2nd UK National Conf. on Heat Transfer*. 1988.
5. Lee, J. and S.J. Lee, *The effect of nozzle configuration on stagnation region heat transfer enhancement of axisymmetric jet impingement*. international Journal of Heat and Mass Transfer, 2000. **43**: p. 3497-3509.
6. Kataoka, K. and Mizushima, T. *Local enhancement of the rate of heat-transfer in an impinging round jet by free-stream turbulence*. in *Heat transfer 1974; Proceedings of the Fifth International Conference, Tokyo, Volume 2*. 1974. Tokyo.
7. Violato, D., et al., *Three-dimensional vortex dynamics and convective heat transfer in circular and chevron impinging jets*. International Journal of Heat and Fluid Flow, 2012. **37**: p. 22-36.
8. Roux, S., et al., *Experimental investigation of the flow and heat transfer of an impinging jet under acoustic excitation*. international Journal of Heat and Mass Transfer, 2011. **54**: p. 3277-3290.
9. Lytle, D. and B.W. Webb, *Air jet impingement heat transfer at low nozzle-plate spacings*. international Journal of Heat and Mass Transfer, 1994. **37**(12): p. 1687-1697.
10. Hadziabdic, M. and K. Hanjalic, *Vortical structures and heat transfer in a round impinging jet*. Journal of Fluid Mechanics, 2008. **596**: p. 221-260.
11. Kataoka, K., et al., *Mass transfer between a plane surface and an impinging turbulent jet: the influence of surface-pressure fluctuations*. Journal of Fluid Mechanics, 1982. **119**: p. 91-105.
12. Alekseenko, S.V. and D.M. Markovich, *Electrodiffusion diagnostics of wall shear stresses in impinging jet*. Journal of Applied Electrochemistry, 1994. **24**: p. 626-631.
13. Phares, D.J., G.T. Smedley, and R.C. Flagan, *The wall shear stress produced by the normal impingement of a jet on a flat surface*. Journal of Fluid Mechanics, 2000. **418**: p. 351-375.
14. Tummers, M.J., J. Jacobse, and S.G.J. Voorbrood, *Turbulent flow in the near field of a round impinging jet*. international Journal of Heat and Mass Transfer, 2011. **54**: p. 4939-4948.
15. El-Hassan, M., et al., *Experimental investigation of the wall shear stress and the vortex dynamics in a circular impinging jet*. Experiments in Fluids, 2012. **52**(6): p. 1475-1489.
16. Hall, J.W. and D. Ewing, *On the dynamics of the large-scale structures in round impinging jets*. Journal of Fluid Mechanics, 2006. **555**: p. 439-458.
17. Meslem, A., et al., *Flow dynamics and mass transfer in impinging circular jet at low Reynolds number. Comparison of convergent and orifice nozzles*. international Journal of Heat and Mass Transfer, 2013. **67**(0): p. 25-45.
18. Rajaratnam, N., *Turbulent jets*. 1976, Amsterdam, Netherlands: Elsevier Scientific Publishing Company.
19. Kristiawan, M., et al., *Wall shear rates and mass transfer in impinging jets: Comparison of circular convergent and cross-shaped orifice nozzles*. international Journal of Heat and Mass Transfer, 2012. **55**: p. 282-293.
20. Reiss, L.P. and T.J. Hanratty, *Measurement of instantaneous rates of mass transfer to a small sink on a wall*. AIChE Journal, 1962. **8**(2): p. 245-247.
21. Sengupta, A. and P.P. Sarkar, *Experimental measurement and numerical simulation of an impinging jet with application to thunderstorm microburst winds*. Journal of Wind Engineering and Industrial Aerodynamics, 2008. **96**(3): p. 345-365.
22. Xu, Z. and H. Hangan, *Scale, boundary and inlet condition effects on impinging jets*. Journal of Wind Engineering and Industrial Aerodynamics, 2008. **96**(12): p. 2383-2402.

Efficiency evaluation of VHC: a CFD comparison study at constant flow

Ricardo F. Oliveira, Senhorinha F. Teixeira, Helena C. Marques and José C. Teixeira

Abstract—Background: The objective of this work is to numerically evaluate several commercial Valved Holding Chamber (VHC) geometries, in terms of airflow behavior and wall deposition. Also, the Fine Particle Dose (FPD) and Mass Mean Aerodynamic Diameter (MMAD) of the drug dose reaching the lungs were evaluated. Downwards the VHC Mouthpiece, the USP Throat geometry was added. Major detail was included in the VHC components representation.

Methods: Through the use of Computational Fluid Dynamics (CFD), the airflow velocity and turbulence fields were calculated for four geometries (i.e. A2A®, Aerochamber Plus® Flow-Vu®, NebuChamber® and Volumatic®). Using a constant flow of 30 L/min and several realistic spray inputs, the deposition was analyzed for three distinct particle size distributions.

Results: The Volumatic® presents the higher recirculation in comparison to the other small volume VHC devices. Each VHC Valve and Mouthpiece design leads to different flows entering the Throat, where the NebuChamber® exhibits the higher air velocities (i.e. 34 m/s). The higher is the MMAD of the distribution injected, the greater will be the deposition in the upper walls. Therefore, the lower MMAD distribution results in higher dose available for the patient. Volumatic® showed the higher Body deposition, as well as, the NebuChamber® USP Throat. Although the Aerochamber® Valve presents the higher deposition, it provides the greater amount of drug for the patient lungs.

On the other hand, the Volumatic® geometry while yielding the lower MMAD for the patient is far from providing the higher FPD.

Conclusions: Based on the results, the VHC components design lead to very distinct airflow patterns. The sudden changes in particle trajectory result in higher deposition at those locations. The Aerochamber® delivers the higher FDM to the patient lungs, while the Volumatic® delivers the smaller MMAD distribution to the lungs.

The first author would like to express his acknowledgments for the support given by the Portuguese Foundation for Science and Technology (FCT) through the PhD grant SFRH/BD/76458/2011. This work was financed by National Funds-Portuguese Foundation for Science and Technology, under Strategic Project PEst-C/EME/UI4077/2011 and PEst-OE/EME/UI0252/2011.

R. F. Oliveira is with the CT2M R&D center, Department of Mechanical Engineering, University of Minho, Guimarães, 4800-058 Portugal (corresponding author to provide e-mail: ricardo.falcao.oliveira@gmail.com).

S. F. Teixeira is with CGIT R&D center, Department of Production and Systems, University of Minho, Guimarães, 4800-058 Portugal (e-mail: st@dps.uminho.pt).

H. C. Marques is with the iMed.UL R&D center, Faculty of Pharmacy, University of Lisbon, Lisbon, 1649-003 Portugal (e-mail: hcmarques@ff.ul.pt).

J. C. Teixeira is with the CT2M R&D center, Department of Mechanical Engineering, University of Minho, Guimarães, 4800-058 Portugal (e-mail: jt@dem.uminho.pt).

Keywords— Asthma Treatment, Computational Fluid Dynamics (CFD), Deposition Efficiency, pressurized Metered Dose Inhaler (pMDI), Valved Holding Chamber (VHC).

I. INTRODUCTION

SINCE Ancient Egypt, when its use was first recorded[1], the goal of inhalation therapy is to improve breathing and lung function in order to relieve the symptoms of respiratory issues, such as asthma or other chronic obstructive pulmonary disease. Anti-inflammatory and bronchodilator drugs are used to reduce the inflammation of the pulmonary tissue, which causes a decrease of the bronchus diameter.[2] Developed in 1955[1], the pressurized Metered Dose Inhaler (pMDI) became one of the most common oral drug delivery devices used by the medical community in inhalation therapy. The pMDI is a compact, low cost and easy-to-use droplet spray dispenser for multiple-dose treatment.[3] A key component of the device is the actuator spray nozzle, which controls the atomization process and the resulting spray formation in terms of spray angle and droplet size distribution.[4], [5] pMDIs are characterized by high spray velocities which are responsible for the so called “cold-Freon” sensation in the patient’s throat.[6] Plus, the use of this medical device requires coordination between the inspiratory action and pMDI priming. Not all patients have the capacity to use properly a pMDI. In fact, some patients may not be able of such hand-mouth coordination skill.[7], [8]

In order to solve the pMDI drawbacks, spacers were developed. Reports of the first spacer like devices date from 1956 and 1977.[6] They can be classified in three categories: a) simple tube, b) Valved Holding Chamber (VHC) and c) reverse flow.[6], [9] These add-on devices extend the distance between the pMDI and the patient’s mouth and they contribute to the reduction of the high velocity impact of the spray on the throat and the need for inspiratory coordination. The one-way valve makes the normal respiratory cycle possible, by preventing the entrance of the exhalation flux into the VHC.[6], [10]

The VHC geometry influences the airflow pattern inside the device and, therefore, its treatment efficiency. By using Computational Fluid Dynamics (CFD) tools, it was possible to analyze and evaluate different aspects, as the airflow characteristics and drug deposition of the VHC devices. These CFD tools have the advantage to predict different geometric scenarios and evaluate its drug delivery efficiency with low

investment by reducing the need for prototypes. Kleinstreuer and collaborators used CFD to evaluate the drug deposition in the airways with and without spacer.[11] Longest *et al.* also studied the effect of different breathing patterns, with both the pMDI and Dry Powder Inhaler (DPI) devices, on the aerosol delivery using numerical tools.[12] The application of CFD studies in the drug delivery scientific field is not new, although several topics still need to be explored as pointed out in the review of Ruzycki and collaborators.[13]

The CFD modeling of the pMDI spray is very challenging.[13] The physical events start with a multiphase fluid (composed by liquid propellant, excipients and particles of solid Active Pharmaceutical Ingredient - API[14]) stored at 3-5 atm[15], which suffers an initial expansion when dosed, resulting in a flash evaporation[5], [16] inside the plastic actuator. This is followed by a rapid expansion (which leads to high velocities and extreme turbulent multiphase flow assisted with cavitation[17]) running through the actuator nozzle and reaching the exit, becoming in full contact with the ambient air pressure and temperature. Studies show that the pMDI spray size distribution is influenced by the nozzle diameter, length and depth, by the concentration of the components in the mixture and the metered valve volume.[4], [15], [18] Cavitation will also change the droplets size in an unpredictable way, by the detachment of big agglomerates of API and propellant.[5] The ambient and the device temperature is of extreme importance for the spray characteristics, the mixture will rapidly decrease its pressure, absorbing all the energy in its vicinity to evaporate the propellant. The initial spray plume temperature at the nozzle exit is around -60 °C.[19]–[21] Therefore, a higher environment temperature improves the propellant evaporation, resulting in smaller droplets and lower spray velocities. Even the delay between shaking and priming of the pMDI plays a major role in the spray plume characteristics, due to sedimentation by gravity.[22] Also, the spray plume shape is time-dependent, which can be observed by high-speed photography.[3], [9]

It is also known that a pMDI spray produces particles differently charged, due to the materials used in the device and the mixture components.[23] Combining this with the unpredictable wall charge of the VHC devices, makes it a very complex phenomenon to model numerically. The VHC wall charge can change: along the longitudinal position[23], for each type of material, with the detergent used to wash it[24], if it is handled with rubber gloves[25], with the friction during transportation[26], with the type of drying applied[24], also with the type of pMDI spray used[26], even with the number of puffs fired into it[25].

Due to the difficulties associated with the physical phenomena, all the CFD simulations are made by assuming some simplifications.

The main objective of this work is to evaluate four different geometries of commercial VHC devices in terms of velocity magnitude recirculation, and mass deposition in the VHC

Body, Valve and USP Throat. Also, the Fine Particle Dose (FPD) and Mass Mean Aerodynamic Diameter (MMAD) of the drug sample that reaches the lungs are evaluated.

II. MATERIALS AND METHODS

A. Geometry and Grid Generation

This paper reports a numerical fluid simulation in four different VHC geometries, based in commercial models (see Fig. 1): the A2A Spacer[®] from Clement Clarke International (210 mL), Aerochamber Plus[®] Flow-Vu[®] from Trudell Medical International (149 mL), NebuChamber[®] from AstraZeneca (250 mL) and Volumatic[®] from GlaxoSmithKline (750 mL).

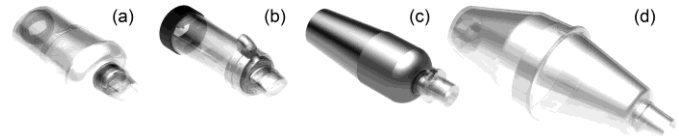


Fig. 1. Geometrical representation of the VHC geometries tested: (a) A2A[®], (b) Aerochamber Plus[®] Flow-Vu[®], (c) NebuChamber[®] and (d) Volumatic[®].

After a computational representation of each VHC geometry, the USP Throat was added at the Mouthpiece of each device. Also a cross-sectional extension of the pMDI mouthpiece was added at the entry of each VHC geometry. Specifically in the Aerochamber[®] case, it was drawn the geometry of the flow warning whistle, close to the VHC pMDI adapter zone. This forced the need for a buffer extension at the VHC entrance for a proper calculation of the flow pressure drop.

The VHC geometries were drawn considering all the details in the Body geometry. Also the Valves were considered to be in the open position at a flow of 30 L/min, for which the devices were connected to a vacuum pump with the calibrated flow. The approximate dimensions and shapes of the Valves were taken into account.

To reduce the computational effort, for each one of the numerical studies, only half of the geometry was simulated via a longitudinal symmetry plane.

The first step in a CFD simulation is the grid generation, for each geometry, taking advantage of the ANSYS Meshing software. The resulting 3D computational grids sizes, composed of tetrahedral elements, were 4.5, 4.8, 4.7, 1.6 (in millions of elements); for the A2A[®], Aerochamber[®], NebuChamber[®] and Volumatic[®] geometries, respectively. For 3D meshing of very complex geometries, the use of tetrahedral elements generally provides a more automatic solution, with the ability to add mesh controls for improving the accuracy in critical sections of the geometry. Thus, a refinement algorithm for proximity was used, in order to improve the solution accuracy. Plus, wall refinements were included to accurately solve the high velocity gradient.

For accuracy and mesh independency, a mesh size study was carried out using three different sizes of mesh elements, in the Volumatic[®] geometry. This study was done accordingly to the methodology proposed by Celik and his collaborators.[27]

The same grid refinements were kept and the value of the velocity was evaluated in a cross-section located at half-length of the VHC Body, where the recirculation is bigger and the grid refinement is most important. Also, the velocity magnitude value for 5 points distributed along the VHC central axis of each geometry was monitored during the numerical iterations.

B. Boundary Conditions

The geometry inlet was defined as a boundary condition at atmospheric pressure with turbulence intensity assumed to be 5 %. A symmetry condition was imposed at the longitudinal symmetry plane. The outflow zone, located at the end of the USP Throat, imposed a constant draw of air flow (i.e. 30 L/min), which was defined by a uniform velocity profile with 2 % of turbulence intensity.

A no-slip condition was set for the geometry walls, which assumes that they have a fixed zero velocity value. These walls were separated in different groups, corresponding to different zones of the geometry for post-processing purposes.

C. Spray Simulation

For the particle calculations, it was considered that all the particles that collided with a wall would be trapped. This simplification does not represent the reality, but it would be the equivalent of having liquid droplets colliding to a dry wall. Although the reality of pMDI spray involves solid API particles trapped inside propellant liquid droplets, this approach seems to be acceptable even without considering evaporation.

For the definition of the pMDI spray, it was necessary to measure the parameters that were not readily available in the literature. Considering in a commercial pMDI HFA-134a device, the parameters considered are detailed in Table I.

TABLE I. PMDI SPRAY CHARACTERISTICS USED IN THE SIMULATIONS

Characteristic	Value
API	Salbutamol
Propellant	HFA-134a
Plume Max. Velocity (m/s)	90
Plume Angle (°)	22
Nozzle Diameter (mm)	0.25
API Mass (µg)	100
Plume Duration (s)	0.1
Salbutamol Density (kg/m ³)	1230
Size Distribution	Log-Normal

In Table II, the three different types of size distribution characteristics simulated for each geometry are reported. The distributions are characterized by their MMAD and Geometric Standard Deviation (GSD). A graphical representation of the sprays can be found in Fig. 2.

TABLE II. SPRAY DISTRIBUTION SIZE CHARACTERISTICS USED IN THE SIMULATIONS

Distribution Number	1	2	3
MMAD (µm)	2.28	5.47	14.0
GSD	1.35	1.50	1.80

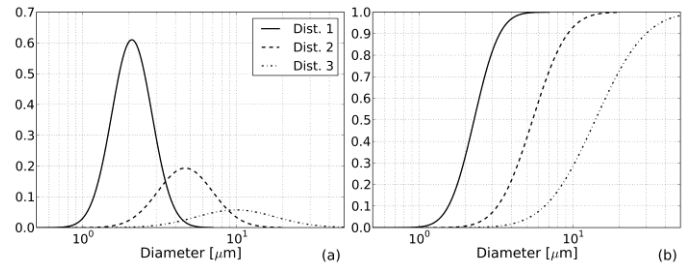


Fig. 2. Representation of the three particle size distributions used in the simulations. Log-Normal forms: (a) distributed and (b) cumulative.

These distributions were selected with the purpose of testing the effect of MMAD increase in the deposition, but keeping the same spray shape and the total mass amount of API (i.e. 100 µg). The simulations did not include the evaporation of the propellant (i.e. the particles are considered to be solid) and the collision with a wall assumes certain retention. Therefore, it was important to consider three distinct scenarios: Dist. 1 – a characteristic distribution of the solid API particles that can be measured in a Cascade Impactor (CI); Dist. 3 – represents the expected size distribution of a pMDI spray before the evaporation of the propellant that can be measured by laser diffraction; and Dist. 2 – represents a distribution that should be an average between the two other cases.

Through the Python language, a script was programmed. It contained mathematical operations for the creation of an injection file using the characteristics reported in Tables I and II. In addition, the spray was considered to have a conical shape, and that the particles exiting the circular section of the nozzle were randomly distributed within it. This injection file is the spray input into the CFD solver. More details regarding the pMDI spray simulation can be found elsewhere.[3], [28]

D. Solver Configuration

The numerical simulations were performed using FLUENT 14.0 from ANSYS® as the solver. FLUENT software uses a control volume technique to solve the conservation equations for mass, momentum and turbulence measurements.[29], [30] Concerning the turbulence calculations, a two-equation model was used, known as the $k-\epsilon$ Standard. Also the Standard algorithm was used for the calculation of the boundary layer.[30] The solution of the partial differential equations for mass and momentum was defined in a sequential process, using the SIMPLE (or Semi-Implicit Method for Pressure-Linked Equations) algorithm. The standard discretization scheme was used to solve the pressure field whereas the momentum, the turbulent kinetic energy and turbulent dissipation rate equations were discretized by applying the second order upwind scheme. Convergence was reached in the simulation by using a criterion value of 1.0E-6 for the

continuity (pressure), velocity, and for k and ϵ turbulence parameters. The simulation was obtained in steady state and the fluid was assumed incompressible and Newtonian. There is no energy exchange and the gravitational acceleration was applied with a magnitude value of 9.81 m/s^2 .

For the particle tracking within the velocity domain, an Euler-Lagrangian approach was used. The tracking was executed after the numerical convergence of the continuous phase has been reached. A drag coefficient law based in the work of Morsi and Alexander[30] was used with a correction for the Cunningham Slip effect for particles under $1 \text{ }\mu\text{m}$ of diameter.[20], [31] A model for statistically simulate the turbulence effect on particle trajectory, known as stochastic tracking, was used. Five stochastic paths were considered for each particle tracking with different random turbulence eddy number. No electrostatic or evaporation effects were taken into account during the particle tracking calculations.

E. Post Processing

The grid computed numerical fields were evaluated in terms of velocity magnitude and pathlines, by using the CFD-Post program suite from ANSYS.

For evaluating the four VHC devices, the mass deposition fraction in the Body, Valve and USP Throat was calculated. Also the fraction that exited the geometry to the lungs, as well as, its MMAD and FPD, were calculated. These metrics were quantified through a Python language script by several mathematical operations, having as input the deposition wall files from the CFD studies.

III. RESULTS

A. Velocity Contours

Fig. 3 presents the CFD results for the velocity magnitude contours, obtained at the symmetry plane of each one of the four geometries. The results are plotted in a logarithmic greyscale and expressed in m/s. The airflow is drawn through the USP Throat exit at 30 L/min.

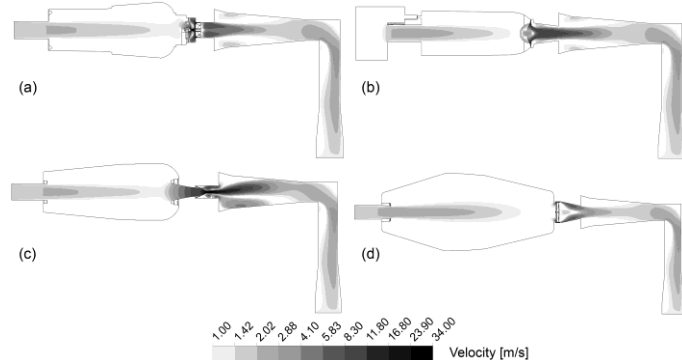


Fig. 3. Velocity magnitude contours for the symmetry plane of each geometry: (a) A2A®, (b) Aerochamber®, (c) NebuChamber® and (d) Volumatic®. Results are represented in m/s in a logarithmic greyscale, for a flow of 30 L/min.

B. Airflow Pathlines

Taking the VHC Body section of the geometry and plotting

the velocity magnitude contours along with the airflow pathlines, the results shown in Fig. 4 were obtained. The pathlines provide a better pattern perception into the level of recirculation created by each geometry, as the airflow is kept at 30 L/min.

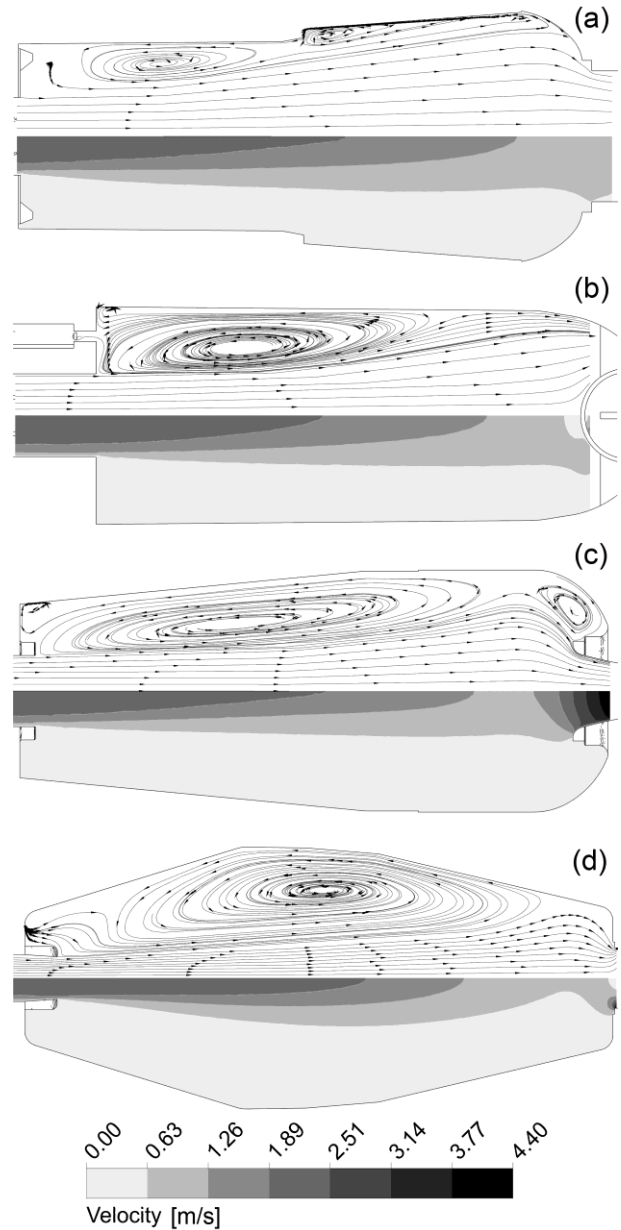


Fig. 4. Representation of the airflow pathlines inside the VHC body, along with the velocity magnitude contour for the following geometries: (a) A2A®, (b) Aerochamber®, (c) NebuChamber® and (d) Volumatic®. Velocity results shown in m/s, for a flow of 30 L/min.

In Fig. 5, some randomly seeded pathlines in a cross-section plane upstream the Valve of each geometry are represented. It is possible to observe the direction of the flow as well as the different designs of each Valve and Mouthpiece simulated.

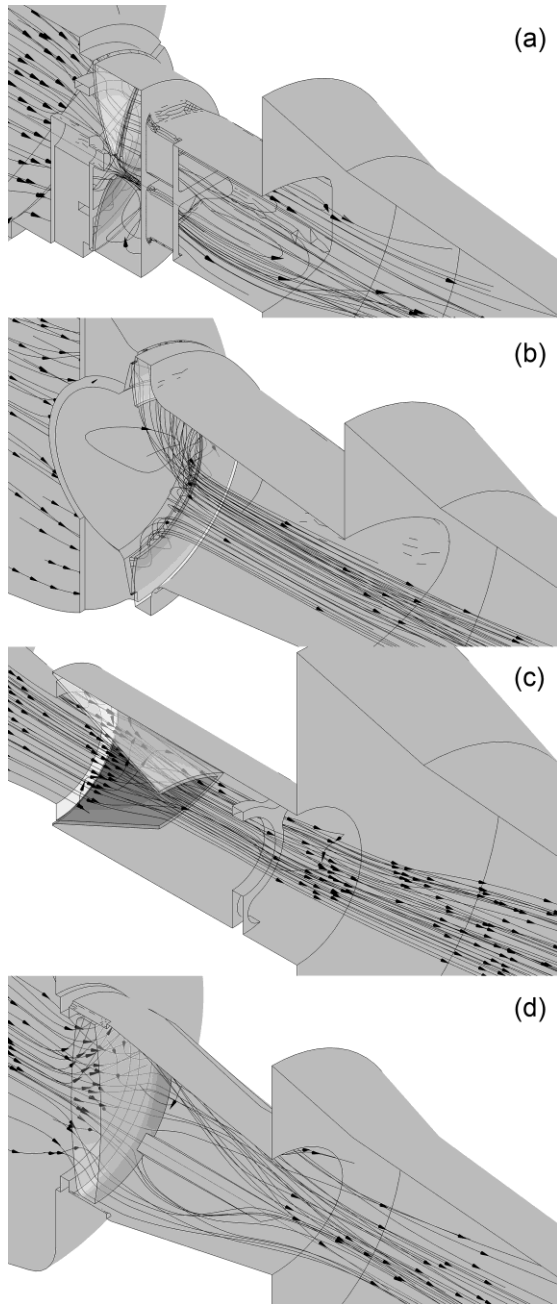


Fig. 5. Detail of the VHC valves flow pathlines for the devices: (a) A2A®, (b) Aerochamber®, (c) NebuChamber® and (d) Volumatic®. The valve surfaces drawn with a 60% of transparency, and the arrows indicate the direction of the flow.

C. Particle Deposition

Fig. 6 reports the mass fraction deposition results in relation to the total mass emitted (i.e. 100 μg), for each zone and geometry. Results are expressed in percentage for a constant flow of 30 L/min. The zone “To Lungs” represents the amount of drug that exits the USP Throat and, therefore, leaves the domain. This amount of drug will be the same entering the CI device. This is represented in this easy way for experimental comparison and better understanding of the drug delivery effectiveness to the patient lungs.

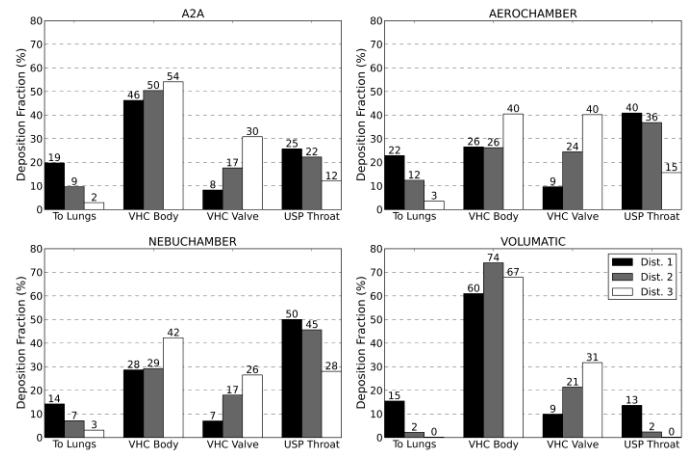


Fig. 6. Representation of the deposition fraction for the three distributions at the four zones, in four VHC geometries. Results shown in percentage at 30 L/min.

In Fig. 7 (a), the MMAD and GSD (in vertical alignment inside the bars) of the amount of drug dose that reaches the lungs are shown. The effective fraction of the emitted dose (i.e. FPD) that reaches the lungs is also represented in Fig. 7 (b). Both are characterized for a constant flow of 30 L/min, for each distribution and VHC geometry.

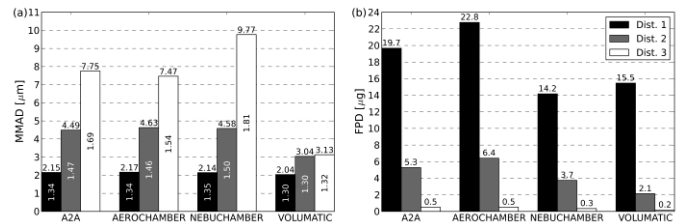


Fig. 7. (a) Values of MMAD and GSD and (b) FPD drug amount, both obtained for each VHC geometry and for three different size distributions. The values were taken from the dose reaching the lungs at a flow of 30 L/min.

IV. DISCUSSION

A. Velocity

It can be observed, in Fig. 3, that the (c) NebuChamber® geometry shows higher velocities downwards the Valve, at a value of around 34 m/s. This can be explained by the small cross-section area of the NebuChamber® Valve (see Fig. 5 (c)), which results in a higher drug deposition in the USP Throat walls (see Fig. 6).

The (b) Aerochamber® and (d) Volumatic® geometries show lower velocity values, around 13 m/s. Their Valve and Mouthpiece design is simpler and include less obstacles, having a higher cross-section area (see Fig. 5 (b) and (d)) that results in lower velocities.

For the USP Throat velocity contours a similarity is found for Fig. 3 (a), (b) and (d) geometries, due to their air jet being aligned with the USP Throat centerline. On the other hand, the (c) NebuChamber® shows a distinct behavior, where the jet appears to be aiming towards the wall.

B. Recirculation

Observing Fig. 4, it can be concluded that different VHC Body geometries lead to different airflows and therefore distinct recirculation patterns. The (d) Volumatic[®] has the widest recirculation area, as expected, due to its high volume in comparison to the other geometries considered in this study. Such large recirculation zone can be the reason of the high deposition in the VHC Body when compared with the other devices, see Fig. 6.

The (a) A2A[®] geometry presents multiple small area recirculation zones. For the (c) NebuChamber[®] geometry, it is visible a major recirculation zone plus two other smaller ones, formed in the vicinity of wall recesses.

In the (b) Aerochamber[®] geometry, it is visible a single recirculation area located downstream the VHC entrance, caused for sudden expansion. Even the whistle entrance modeled did not provide a meaningful influence in this recirculation zone.

C. Deposition

By observing the results in Fig. 6, it can be concluded that the deposition is greater in the Volumatic[®] Body than in the other VHC's bodies. On the other hand, the Aerochamber[®] Valve yields the largest Valve deposition. The NebuChamber[®] geometry results in a greater USP Throat deposition than the other VHCs. Also the Aerochamber[®] VHC leads to the greatest amount of delivered drug that reaches the lungs.

Analyzing the different distributions, it can be noticed that Dist. 1 presents a higher amount of drug reaching the lungs in comparison to the other distributions. This is an expected result since the Dist. 1 has the lower MMAD, and as it is well known, particles with lower diameter are most likely to follow the flow stream and not collide with solid obstacles. On the other hand, Dist. 3 presents the highest deposition in the VHC walls (i.e. Body and Valve) and therefore the lowest amount of drug delivered to the lungs. As explained before, because Dist. 3 exhibits the highest emitted MMAD, this results in higher deposition.

Due to the fact that no evaporation has been considered and that a 100% probability of retention is assumed in case of a particle-wall collision, the results may be an over prediction of the reality. On the other hand, the fact that no electrostatic effects have been considered, the deposition for low diameter particles may be under predicted.

D. MMAD and GSD

From Fig. 7 (a) it can be concluded that injected spray distributions with higher MMAD results in higher MMAD delivered to the lungs, although there is a general reduction of its original MMAD value, as well as, the GSD value. This is expected due to the fact that the coarse fraction of the distribution has higher probability to get trapped in the domain walls, resulting in a lowering of the MMAD and GSD values.

Comparatively between all the VHCs, the Volumatic[®] shows the highest reduction of MMAD from the initial injected distribution. This is a great reduction in comparison to

the other geometries, and surely is related to the fact that Volumatic[®] is a higher volume VHC than the other three, which are of similar volume. NebuChamber[®] presents the lowest reduction in the MMAD value from the initial distribution, making it the less attractive for patient treatment. Nonetheless, it must be kept in mind that this VHC device is the only one made of metal, the results are less likely to be affected by the electrostatic forces on the deposition. Aerochamber[®] and A2A[®] present similar distributions delivered to the lungs.

E. Fine Particle Dose

Fig. 7 (b) provides an insight from the clinical point of view into the amount of dose that reaches the lung, by evaluating the fraction with diameter lower than 4.7 μm . The results show that the lower MMAD emitted distribution (i.e. Dist. 1) results in higher FPD reaching the lungs, independently of the geometry.

For all the distributions, the Aerochamber[®] presents the highest FPD values, which for the conditions considered in the simulation appears to provide the best option for treatment, followed by the A2A[®]. Conversely, the NebuChamber[®] shows the lowest value of FPD.

The combination of the several results shows that despite the fact that the Volumatic[®] geometry presents the lower MMAD for the patient, it does not guarantee the higher FPD. As well as, the fact of the NebuChamber[®] has the lower Body and Valve deposition is far from having the higher FPD and lower MMAD, but has the higher USP Throat deposition.

REFERENCES

- [1] M. Sanders, "Inhalation therapy: an historical review," *Prim. care Respir. J.*, vol. 16, no. 2, pp. 71–81, Apr. 2007.
- [2] Global Initiative for Asthma, "Global strategy for asthma management and prevention," GINA, 2012.
- [3] R. F. Oliveira, S. F. C. F. Teixeira, J. C. Teixeira, L. F. Silva, and H. Antunes, "pMDI Sprays: Theory, Experiment and Numerical Simulation," in *Advances in Modeling of Fluid Dynamics*, C. Liu, Ed. Rijeka, Croatia: Intech, 2012, p. 300.
- [4] H. Smyth, A. J. Hickey, G. Brace, T. Barbour, J. Gallion, and J. Grove, "Spray pattern analysis for metered dose inhalers I: Orifice size, particle size, and droplet motion correlations," *Drug Dev. Ind. Pharm.*, vol. 32, no. 9, pp. 1033–1041, Oct. 2006.
- [5] C. A. Dunbar, "Atomization mechanisms of the pressurized metered dose inhaler," *Part. Sci. Technol.*, vol. 15, no. 3–4, pp. 253–271, Jul. 1997.
- [6] S. P. Newman, "Spacer devices for metered dose inhalers," *Clin. Pharmacokinet.*, vol. 43, no. 6, pp. 349–360, Jan. 2004.
- [7] M. B. Dolovich and R. Dhand, "Aerosol drug delivery: developments in device design and clinical use," *Lancet*, vol. 377, no. 9770, pp. 1032–1045, Mar. 2011.
- [8] J. B. Fink, "Metered-dose inhalers, dry powder inhalers, and transitions," *Respir. Care*, vol. 45, no. 6, pp. 623–635, Jun. 2000.
- [9] C. Terzano, "Pressurized metered dose inhalers and add-on devices," *Pulm. Pharmacol. Ther.*, vol. 14, no. 5, pp. 351–66, Jan. 2001.
- [10] M. B. Dolovich and J. B. Fink, "Aerosols and devices," *Respir. Care Clin. N. Am.*, vol. 7, no. 2, pp. 131–173, Jun. 2001.
- [11] C. Kleinstreuer, H. Shi, and Z. Zhang, "Computational analyses of a pressurized metered dose inhaler and a new drug-aerosol targeting methodology," *J. aerosol Med.*, vol. 20, no. 3, pp. 294–309, Jan. 2007.
- [12] P. W. Longest, G. Tian, R. L. Walenga, and M. Hindle, "Comparing MDI and DPI aerosol deposition using in vitro experiments and a new

- stochastic individual path (SIP) model of the conducting airways,” *Pharm. Res.*, vol. 29, no. 6, pp. 1670–88, Jun. 2012.
- [13] C. A. Ruzycski, E. Javaheri, and W. H. Finlay, “The use of computational fluid dynamics in inhaler design,” *Expert Opin. Drug Deliv.*, vol. 10, no. 3, pp. 307–23, Mar. 2013.
- [14] S. W. Stein, P. Sheth, and P. B. Myrdal, “A model for predicting size distributions delivered from pMDIs with suspended drug,” *Int. J. Pharm.*, vol. 422, no. 1–2, pp. 101–15, Jan. 2012.
- [15] S. P. Newman, “Principles of metered-dose inhaler design,” *Respir. Care*, vol. 50, no. 9, pp. 1177–1190, Sep. 2005.
- [16] A. Q. Shaik, “Numerical modeling of two-phase flashing propellant flow inside the twin-orifice system of pressurized metered dose inhalers,” Loughborough University, 2010.
- [17] C. A. Dunbar, A. P. Watkins, and J. F. Miller, “An experimental investigation of the spray issued from a pMDI using laser diagnostic techniques,” *J. Aerosol Med.*, vol. 10, no. 4, pp. 351–68, Jan. 1997.
- [18] S. W. Stein, “Estimating the number of droplets and drug particles emitted from MDIs,” *AAPS PharmSciTech*, vol. 9, no. 1, pp. 112–5, Jan. 2008.
- [19] S. W. Stein and P. B. Myrdal, “The Relative Influence of Atomization and Evaporation on Metered Dose Inhaler Drug Delivery Efficiency,” *Aerosol Sci. Technol.*, vol. 40, no. 5, pp. 335–347, Jun. 2006.
- [20] W. H. Finlay, *The mechanics of inhaled pharmaceutical aerosols: an introduction*. Academic Press, 2001, p. 306.
- [21] B. J. Gabrio, S. W. Stein, and D. J. Velasquez, “A new method to evaluate plume characteristics of hydrofluoroalkane and chlorofluorocarbon metered dose inhalers,” *Int. J. Pharm.*, vol. 186, no. 1, pp. 3–12, Sep. 1999.
- [22] E. Berg, “In vitro properties of pressurized metered dose inhalers with and without spacer devices,” *J. Aerosol Med.*, vol. 8, no. Supplement 3, pp. S3–S11, Sep. 1995.
- [23] P. C. L. Kwok, R. Collins, and H.-K. Chan, “Effect of spacers on the electrostatic charge properties of metered dose inhaler aerosols,” *J. Aerosol Sci.*, vol. 37, no. 12, pp. 1671–1682, Dec. 2006.
- [24] J. H. Wildhaber, S. G. Devadason, M. J. Hayden, R. James, A. P. Dufty, R. A. Fox, Q. A. Summers, and P. N. LeSouëf, “Electrostatic charge on a plastic spacer device influences the delivery of salbutamol,” *Eur. Respir. J.*, vol. 9, no. 9, pp. 1943–1946, Sep. 1996.
- [25] N. J. Dewsbury, C. J. Kenyon, and S. P. Newman, “The effect of handling techniques on electrostatic charge on spacer devices: A correlation with in vitro particle size analysis,” *Int. J. Pharm.*, vol. 137, no. 2, pp. 261–264, Jun. 1996.
- [26] P. C. L. Kwok, “Electrostatics of Aerosols for Inhalation,” University of Sydney, 2007.
- [27] I. B. Celik, U. Ghia, P. J. Roache, C. J. Freitas, H. Coleman, and P. E. Raad, “Procedure for Estimation and Reporting of Uncertainty Due to Discretization in CFD Applications,” *J. Fluids Eng.*, vol. 130, no. 7, pp. 1–4, 2008.
- [28] R. F. Oliveira, A. C. M. Ferreira, S. F. C. F. Teixeira, J. C. Teixeira, and H. M. C. Marques, “pMDI Spray Plume Analysis: A CFD Study,” in *Lecture Notes in Engineering and Computer Science: Proceedings of The World Congress on Engineering 2013, WCE 2013*, 2013, vol. 3, pp. 1883–1888.
- [29] H. K. Versteeg and W. Malalasekera, *An introduction to computational fluid dynamics: the finite volume method*. Harlow, England: Longman, 1995, p. 257.
- [30] ANSYS, *ANSYS FLUENT Theory Guide*. Canonsburg, PA, USA: ANSYS Inc, 2011, p. 794.
- [31] P. W. Longest and J. Xi, “Effectiveness of Direct Lagrangian Tracking Models for Simulating Nanoparticle Deposition in the Upper Airways,” *Aerosol Sci. Technol.*, vol. 41, no. 4, pp. 380–397, Mar. 2007.

An investigation on development of cooling dual discharge fan module

Joo-Han Kim, Jung-Moo Seo and In Soung Jung

Abstract—There is representative part among convenience items which increase convenience of driver while part that driver contacts most and recognizes easily sensuously among this convenience function drives into vehicles seat part. On high-reliability, high-tech of vehicles, convenience function in seat part is expanded greatly. Air conditioning ventilation system that can keep temperature comfortable environment on deluxe car among them is raised by important convenience function. This paper deals with a design of the seat cooling fan for vehicle, especially brushless DC (BLDC) motor and blade for cooling dual discharge fan module. We achieved blade flow analysis about high effectiveness and low commutation torque ripple motor design. We have used the 2D Finite Element Method for calculating the characteristics of brushless DC (BLDC) motor, computing fluid mechanics (CFD) as numerical analysis for blade design.

Keyword — BLDC motor; Cooling fan; Fan blade; Technical development

I. INTRODUCTION

A lot of research and developments are achieved in automotive safety security through electronic controller, convenience function enlargement to meet on development of various electronic driver technologies, safety reinforcement of vehicles and various functional request of vehicles driver. Also, it is real condition that is inclining a lot of efforts in reinforcement of these vehicles function for automotive addend value enlargement. There is representative part among convenience items which increase convenience of driver while part that driver contacts most and recognizes easily sensuously among this convenience function drives into vehicles seat part. On high-reliability, high-tech of vehicles, convenience function in seat part is expanded greatly.

Air conditioning ventilation system that can keep temperature comfortable environment on deluxe car among them is raised by important convenience function. These

products have already developed in universal cooling system company and apply to various vehicles.

We are analyzing that is expanded by the various model of a car in early time. Also, the development of vehicles seat part is preceded at the fastest speed.

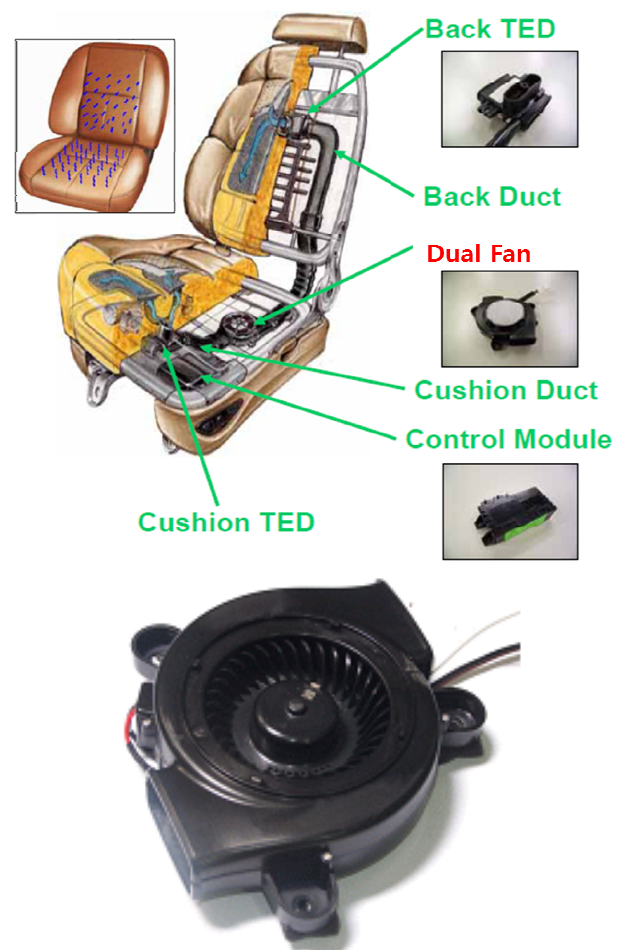


Fig. 1 Cooling seat system and fan module

This paper deals with a design of the seat cooling fan for vehicle, especially brushless DC (BLDC) motor and blade for cooling fan module. We achieved blade flow analysis about high effectiveness and low commutation torque ripple motor design. We have used the 2D Finite Element Method for calculating the characteristics of brushless DC (BLDC) motor, computing fluid mechanics (CFD) as numerical analysis for blade design.

This work was supported by the Energy Efficiency & Resources of the Korea Institute of Energy Technology Evaluation and Planning (KETEP) grant funded by the Korea government Ministry of Knowledge Economy

F. A. Joo-Han Kim is with the Korea Electronics Technology Institute (KETI), 203-101 B/D 192 Yakdae-Dong, Wonmi-Gu Puchon-Si, Kyunggi-Do, 420-140, South Korea (e-mail: kimjh@keti.re.kr).

S. B. Jung-Moo Seo is with the Korea Electronics Technology Institute (KETI), 203-101 B/D 192 Yakdae-Dong, Wonmi-Gu Puchon-Si, Kyunggi-Do, 420-140, South Korea.

T. C. In Soung Jung is with the Korea Electronics Technology Institute (KETI), 203-101 B/D 192 Yakdae-Dong, Wonmi-Gu Puchon-Si, Kyunggi-Do, 420-140, South Korea.

II. BRUSHLESS DC (BLDC) MOTOR DEVELOPMENT

In the basic design, the basic shape and the motor specification are decided by magnetic load distribution method and characteristic analysis is performed by finite element method (FEM) and by equivalent magnetic circuit method (EMCM). The simulated results are presented in following Table 1. Among the items, the Slot opening and pole angle of permanent magnet are designed in consideration of analyzed cogging torque. The specifications of the proposed BLDC motor for cooling fan are shown in table 1.

Table 1. Specification of designed BLDC motor

Parameter	Value	Unit
Phase number	3	
Pole/slot number	6/9	
Coil turns per phase	180	
Coil diameter	0.3	mm
Stator core outer diameter	24.5	mm
Air gap	0.5	mm
Axial length of core	10	mm
Permanent magnet	Rubber (Br:0.25T)	

The governing equation of 2D FE analysis model is equation (1).

$$\frac{1}{\mu} \left(\frac{\partial^2 A_z}{\partial x^2} + \frac{\partial^2 A_z}{\partial y^2} \right) = -J - \frac{1}{\mu_r} \left(\frac{\partial M_{ry}}{\partial x} + \frac{\partial M_{rx}}{\partial y} \right) \quad (1)$$

Here, A is magnetic vector potential and J is current density of coil. If the analysis model is infinite to z axis direction, A and J are existed only to z axis direction. Also, M_r is residual magnetization.

Fig. 2 shows flux line distribution and cogging torque of the designed motor at no load condition. Through the results, flux line distribution and cogging torque characteristics could be estimated and validity of designed model would be confirmed.

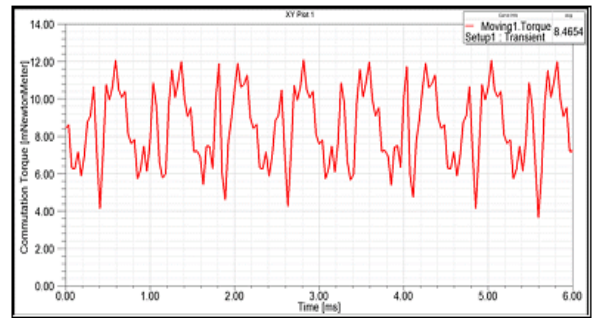


Fig. 2 Flux line distribution and cogging torque at no load condition (FEM analysis results)

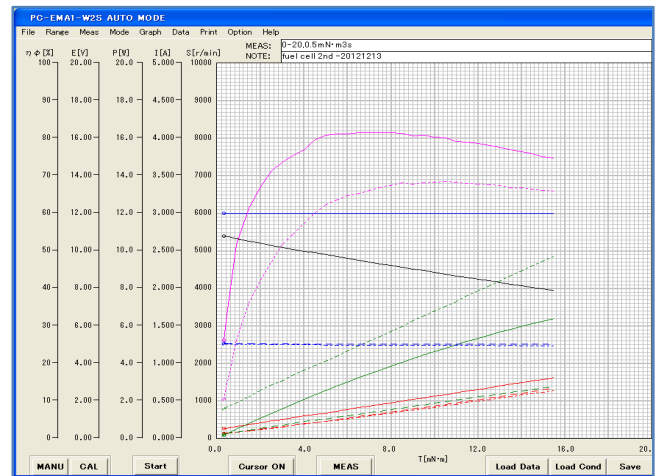
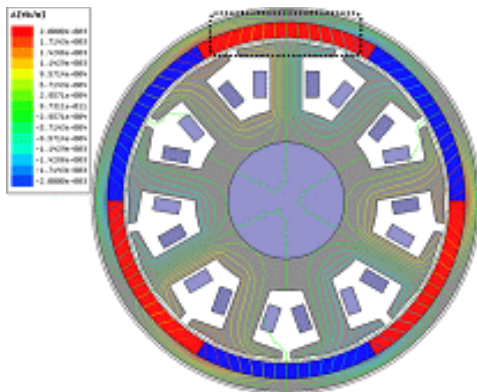


Fig. 3 BLDC motor prototype / Measured performance curves of BLDC motor



The BLDC motor was tested extensively with dynamometer load and evaluated its performance over various tests. The prototype motor was tested extensively with dynamometer load and evaluated its performance over wide speed at various loads using the Toque Meter.

The features of Speed-Torque-Current (N-T-I) in case of supplying 12V rated voltage are shown in Fig. 3. We confirmed generating power of 4.1W that have torque of 8mNm in speed of 4,620 rpm, in the case of approving voltage of 12 V this experiment. In this load point, input current is about 497m A, efficiency was evaluated about 81.5 %.

III. FAN BLADE DEVELOPMENT

We executed numerical analysis to improve dual discharge sirocco fan blade's performance that is applied on seat cooling. The blade's performance in design step can achieve Computational Fluid Dynamics (CFD) as numerical analysis. We modeled imagination wind tunnel for this, achieved numerical analysis locating third dimension data of blade shape in imagination wind tunnel. And, we applied Sliding Mesh Interface(SMI) method to consider blade's turning effect by numerical analysis method. The sliding mesh Interface method is used to predict the time dependent flow through a two-dimensional rotor-stator blade row. The time-varying rotor-stator interaction is modeled by allowing the mesh associated with the moving rotor to translate (slide) relative to the stationary mesh associated with the stator blade.

No.	Factor	Level	
		1	2
1	Blade Diameter	85 mm	89 mm
2	Hub Diameter	32 mm	35 mm
3	Inclined Angle	5 °	20 °

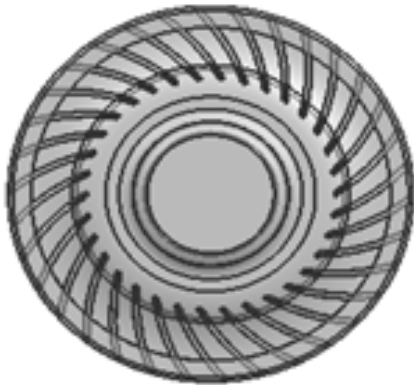


Fig. 4 Fan design parameters and blade geometry

Solver setup and computation

The results are obtained with the solution of the continuity, N-S equations along with the equations for the selected turbulence model. After the boundary conditions are specified and the solution models are selected, the iterations are performed in SC/Tetra (commercial CFD simulation software).

Solving condition

- Differencing scheme : LUD
- Pressure correction method : SIMPLE
- Turbulence model : Realizable k-ε turbulence model
- Wall treatment : Wall function

NO.	D _o [mm]	D _H [mm]	B _t [°]
L1	85	32	5
L2	85	35	20
L3	89	32	20
L4	89	35	5

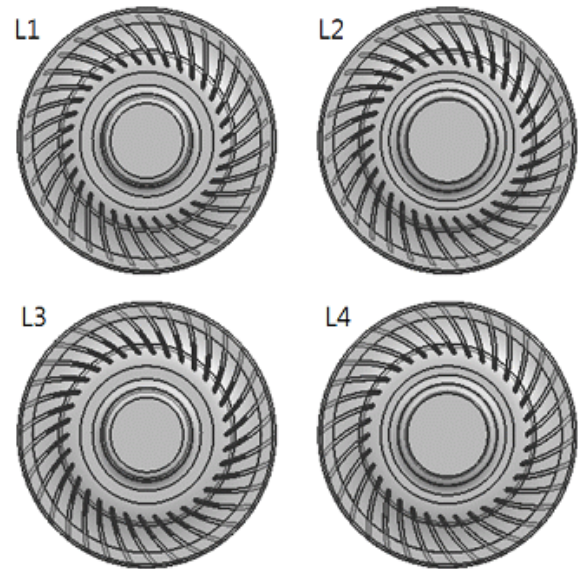
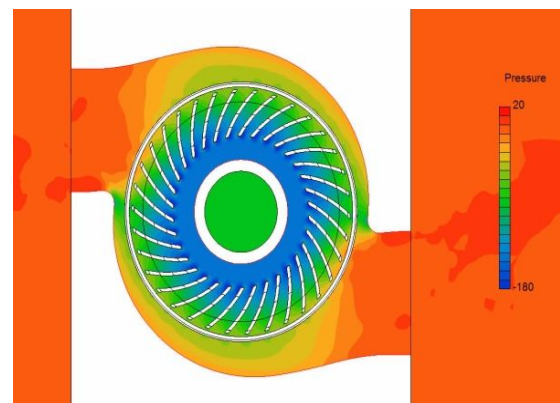


Fig. 5 Fan blade optimization models

Final Fan Blade Design Specs (L4)

- Blade Diameter : 89mm
- Hub Diameter: 35mm
- Inclined Angel : 20 degree
-



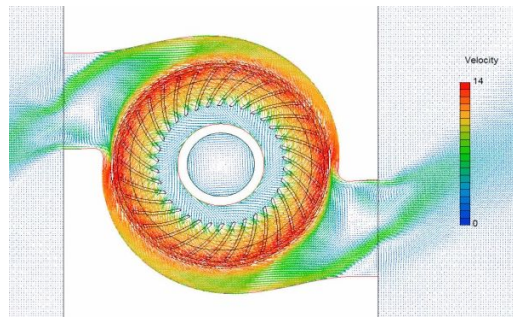


Fig. 6 Blade surface pressure distribution / Velocity of flow distribution of L4 (CFD analysis results)

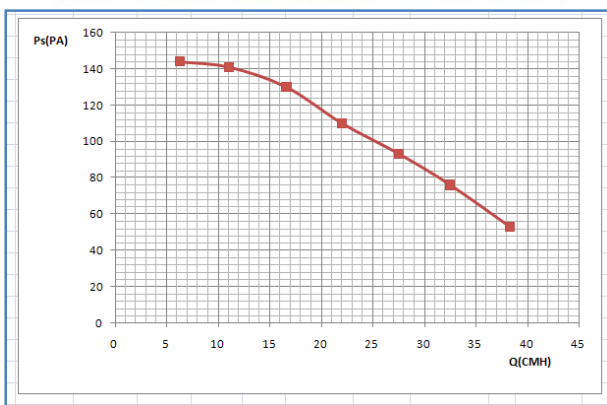


Fig. 7 Measured performance curves of Fan blade

Finally, the designed motor is connected with a fan blade, and output characteristics of the overall fan system with respect to pressure and flow condition changes are measured in Fig. 7. As can be seen in Fig. 7, the required output value of system, air pressure of 120 pa and air flow of 19.5CMH, is gained at an input voltage of 12V.

IV. CONCLUSION

This study presents a design of seat cooling dual discharge sirocco fan module for vehicle. For the designing of high efficiency and high power fan BLDC motor, it is proposed optimized design by finite element method. And we executed numerical analysis to improve seat cooling dual discharge

sirocco fan's performance that is applied on vehicle. The dual discharge sirocco fan blade's performance in design step could achieve computing fluid dynamics (CFD) as numerical analysis. We confirmed BLDC motor generating power of 4.1W that have torque of 8mNm in speed of 4,620 rpm, in the case of approving voltage of 12 V. In this load point, input current is about 497m A, efficiency was evaluated about 81.5 %. The dual output value of discharge fan module, air pressure of 120 pa and air flow of 19.5CMH, is gained at an input voltage of 12V.

REFERENCES

- [1] Eck, B., Fans design and operation of centrifugal, axial-flow and cross-flow fan, Oxford Pergamon Press, New York, USA, 1973.
- [2] Lee, K. Y., Choi, Y. S., Kim, Y. L. and Yun, J. H., "Design of axial fan using inverse design method," Journal of Mechanical Science and Technology, 22, 2008, 1883-1888.
- [3] Lee, K. S., Kim, K. Y. and Samad, A., "Design optimization of low-speed axial flow fan blade with three-dimensional RANS analysis," Journal of Mechanical Science and Technology, 22, 2008, 1864-1869.
- [4] Kim, K., Choi, J., "Numerical Optimization for Design of an Automotive Cooling Fan, SAE Technical Paper 970935, 1999
- [5] J. G. Kassakian, "Automotive electrical systems the power electronics market of the future," in Proc. 15 IEEE Applied Power Electronics conf., New Orleans, Feb. 2000, pp. 3-9.
- [6] Lee, S. H. & Hur, N., 2008, "Analysis of an Underhood Thermal; Management by using a Semi-Microscopic Heat Exchange Method for the Radiator Heat Transfer," Proceedings of the Fifth International Conference on Computational Fluid Dynamics, pp.241-242, Seoul, Korea.
- [7] Christophel, J.R., Thole, K.A., Cunha F.J., "Cooling the Tip of a Turbine Blade Using Pressure Side Holes- Part1: Adiabatic Effectiveness Measurements", Proceedings of ASME Turbo Expo 2004, Power for Land, Sea, and Air, June 2004.
- [8] AMCA Standard 210-99: Laboratory Methods of Testing Fans for Aerodynamic Performance Rating, AMCA, 1999.

First A. Joo-Han Kim, research scientist; b. Yechon, Gyeongsangbuk-do, Republic of Korea, Nov. 30, 1971; PhD, Sogang University, Seoul, 2012. Mr. rschr. Korea Electronics Tech Inst., Puchon-Si, Kyunggi-Do, Republic of Korea, 1999 - . Achievement include development of actuator, fluid machinery, automation system, gear head, mechatronics

Laminar and Turbulent Simulations of Several TVD Schemes in Two-Dimensions – Part I – Results II

Edisson S. G. Maciel

Abstract—This work, first part of this study, describes five numerical tools to perform perfect gas simulations of the laminar and turbulent viscous flow in two-dimensions. The Van Leer, Harten, Frink, Parikh and Pirzadeh, Liou and Steffen Jr. and Radespiel and Kroll schemes, in their first- and second-order versions, are implemented to accomplish the numerical simulations. The Navier-Stokes equations, on a finite volume context and employing structured spatial discretization, are applied to solve the supersonic flow along a ramp in two-dimensions. Three turbulence models are applied to close the system, namely: Cebeci and Smith, Baldwin and Lomax and Sparlat and Allmaras. On the one hand, the second-order version of the Van Leer, Frink, Parikh and Pirzadeh, Liou and Steffen Jr., and Radespiel and Kroll schemes is obtained from a “MUSCL” extrapolation procedure, whereas on the other hand, the second order version of the Harten scheme is obtained from the modified flux function approach. The convergence process is accelerated to the steady state condition through a spatially variable time step procedure, which has proved effective gains in terms of computational acceleration (see Maciel). The results have shown that, with the exception of the Harten scheme, all other schemes have yielded the best result in terms of the prediction of the shock angle at the ramp. Moreover, the wall pressure distribution is also better predicted by the Van Leer scheme. This work treats the Baldwin and Lomax, and the Sparlat and Allmaras second-order results obtained by the five schemes.

Keywords—Laminar and turbulent flows, TVD algorithms, Cebeci and Smith turbulence model, Baldwin and Lomax turbulence model, Sparlat and Allmaras turbulence model.

I. INTRODUCTION

CONVENTIONAL non-upwind algorithms have been used extensively to solve a wide variety of problems ([1]). Conventional algorithms are somewhat unreliable in the sense that for every different problem (and sometimes, every different case in the same class of problems) artificial dissipation terms must be specially tuned and judiciously chosen for convergence. Also, complex problems with shocks and steep compression and expansion gradients may defy solution altogether.

Edisson S. G. Maciel is with the Federal University of Great Dourados, Rodovia Dourados – Itahum, km 12 – Caixa Postal 364 – Dourados, MS, Brazil – 79804-970 (corresponding author to provide phone: +55 012 99174-3844; e-mail: edisavio@edissonsavio.eng.br).

Upwind schemes are in general more robust but are also more involved in their derivation and application. Some upwind schemes that have been applied to the Euler equations are, for example, [2-6]. To comments about these methods and to the motivation of this study the reader is encouraged to read the first part of this study, THEORY, in [7].

This work, first part of this study, describes five numerical tools to perform perfect gas simulations of the laminar and turbulent viscous flow in two-dimensions. The [2-6] schemes, in its first- and second-order versions, are implemented to accomplish the numerical simulations. The Navier-Stokes equations, on a finite volume context and employing structured spatial discretization, are applied to solve the supersonic flow along a ramp in two-dimensions. Three turbulence models are applied to close the system, namely: [8-10]. On the one hand, the second-order version of the [2-6] schemes are obtained from a “MUSCL” extrapolation procedure, whereas on the other hand, the modified flux function approach is applied in the Harten (1983) scheme for the same accuracy. The convergence process is accelerated to the steady state condition through a spatially variable time step procedure, which has proved effective gains in terms of computational acceleration (see [11-12]). The results have shown that the [2,4-6] schemes have yielded the best results in terms of the prediction of the shock angle at the ramp. Moreover, the wall pressure distribution is also better predicted by the [2] scheme. This work treats the [9-10] second-order results obtained by the five schemes.

II. RESULTS

A. Turbulent Viscous Results

Baldwin and Lomax Results/TVD. In this case, only the [2-4] schemes have presented converged results. Figures 1 to 3 exhibit the pressure contours obtained by the [2-4] schemes, respectively, as using the [9] turbulence model. A weak shock wave is formed ahead of the ramp corner in all solutions. It is important to remember that such weak shock wave is due to the boundary layer detachment which induces a false thick geometry at the ramp and the flow only see this thick geometry, originating the oblique shock wave. So, it is possible to distinguish that the effect of increasing boundary

layer thickness is more pronounced in the [4] solution than in the other solutions. It also induces the expected behavior of a larger circulation bubble formed in the [4] solution. In terms of the pressure field, the [2] scheme presents the most severe pressure field, characterizing this algorithm as more conservative.

by the [2-4] algorithms. The [4] scheme presents a bigger circulation bubble in extent and size than the others.

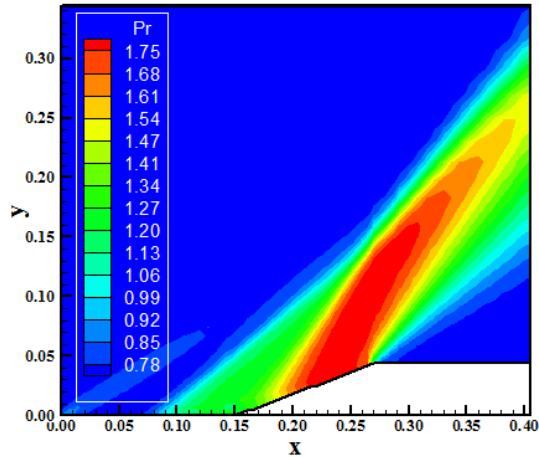


Figure 1. Pressure contours (VL-BL).

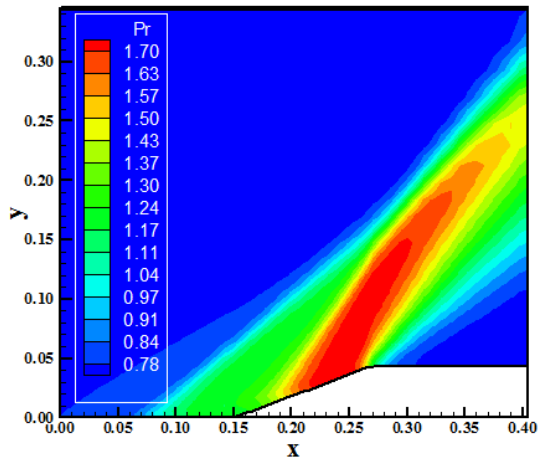


Figure 2. Pressure contours (H-BL).

Figures 4 to 6 show the Mach number contours obtained by the [2-4] numerical algorithms, respectively, as using the [9] turbulence model. It is possible to observe that the boundary layer detachment is bigger in the [4] solution, with the consequent formation of a bigger circulation bubble than the other solutions. The Mach number field of all solutions is the same in quantitative terms, although in qualitative terms they are different.

Figure 7 presents the wall pressure distributions generated by all algorithms. As noted, all solutions capture the circulation bubble formation close to the ramp corner, but all solutions differs from the theoretical solution (all underpredict the shock plateau). Figures 8 to 10 exhibit the circulation bubble formed close to the ramp corner generated

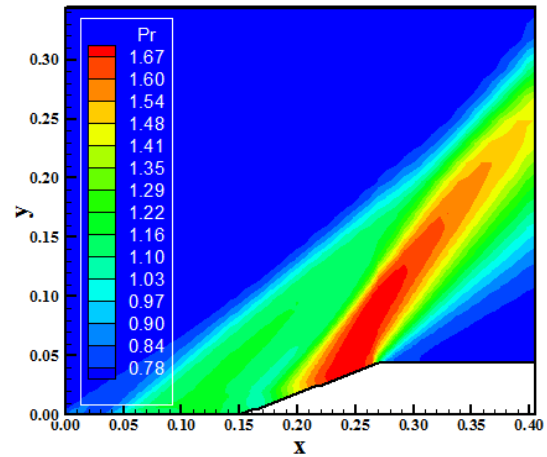


Figure 3. Pressure contours (FPP-BL).

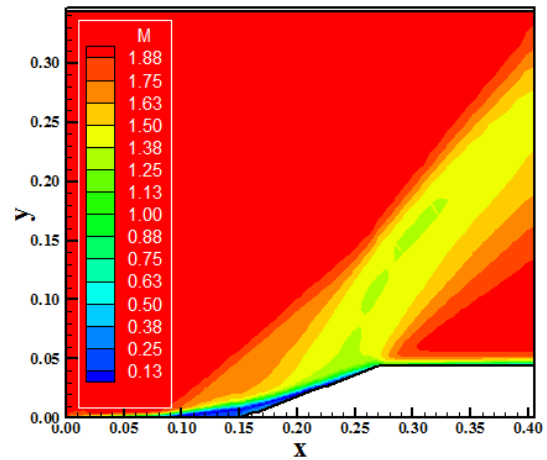


Figure 4. Mach number contours (VL-BL).

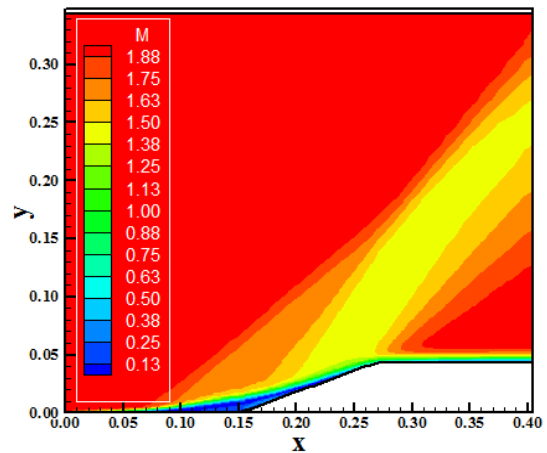


Figure 5. Mach number contours (H-BL).

In resume, the [9] turbulence model predicts a great extent region of boundary layer detachment and, consequently,

bigger bubble size. The [9] model predicts bigger separation than the [8] model.

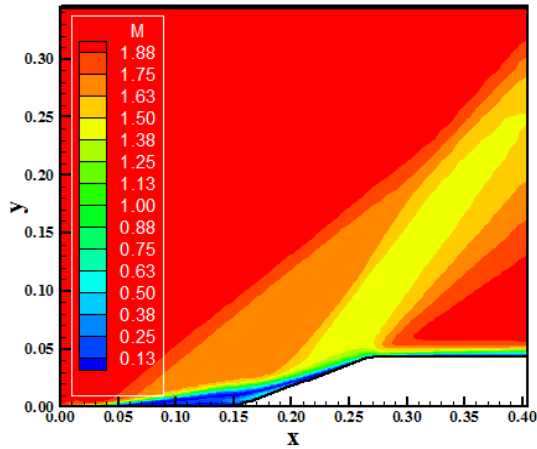


Figure 6. Mach number contours (FPP-BL).

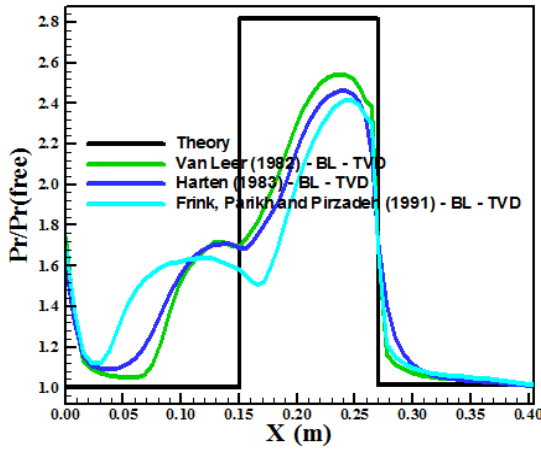


Figure 7. Wall pressure distributions.

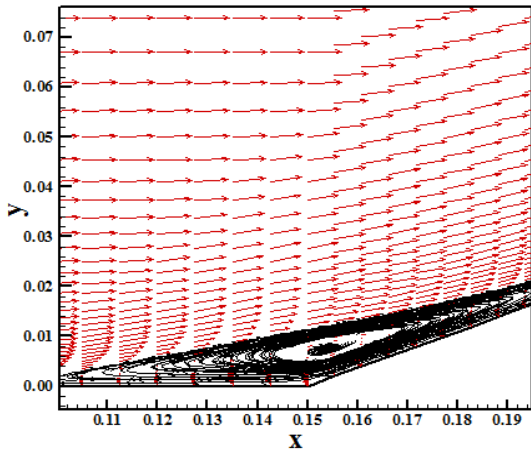


Figure 8. Circulation bubble (VL-BL).

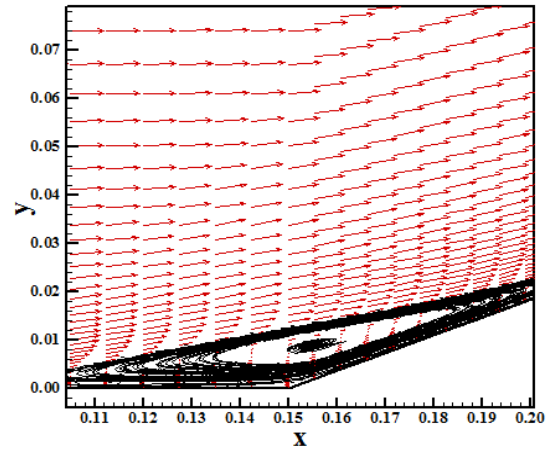


Figure 9. Circulation bubble (H-BL).

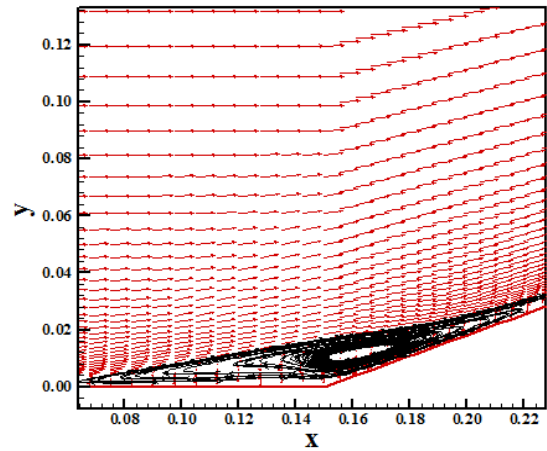


Figure 10. Circulation bubble (FPP-BL).

Sparlat and Allmaras Results/TVD. Only the [5] scheme did not present converged results. Figures 11 to 14 present the pressure contours obtained by the [2-4,6] schemes, respectively, as using the [10] turbulence model. The [2] solution captures a small boundary layer detachment, which results in a less intense weak shock wave. The [4] solution captures the biggest boundary layer detachment, which results in a more intense weak shock wave. The pressure field generated by the [2] scheme is again the most severe in relation to those generated by the others schemes.

Figures 15 to 18 show the Mach number contours obtained by the [2-4,6] numerical schemes, respectively. The [4] solution again captures a bigger circulation bubble than the other solutions. In quantitative terms the solutions are the same, the difference existing in qualitative terms.

Figure 19 shows the wall pressure distributions obtained by the [2-4,6] algorithms. All solutions capture the circulation bubble at the ramp corner. Moreover, the [2] pressure peak is close to the theoretical pressure plateau.

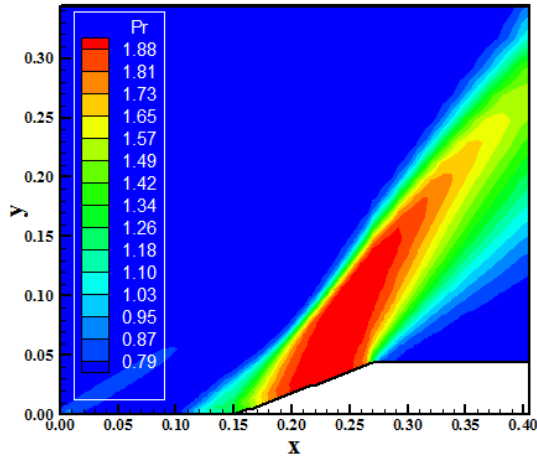


Figure 11. Pressure contours (VL-SA).

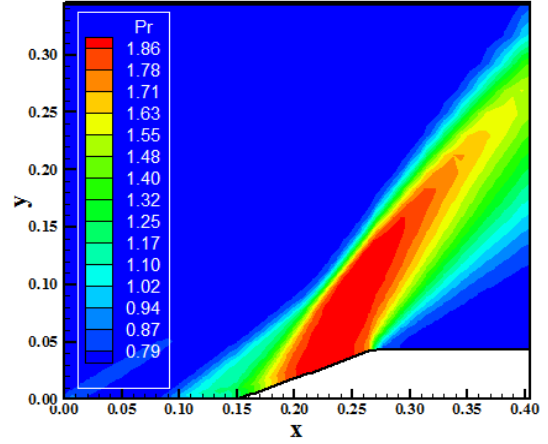


Figure 14. Pressure contours (RK-SA).

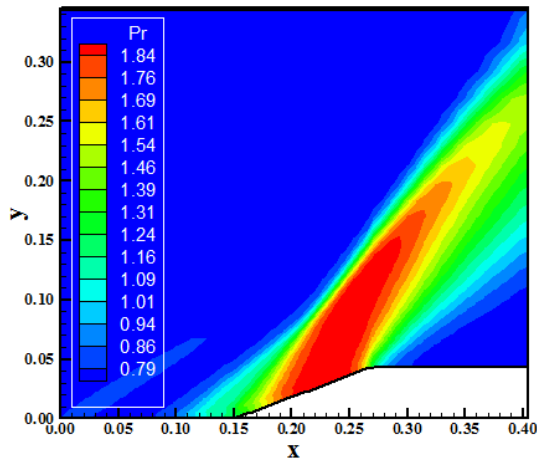


Figure 12. Pressure contours (H-SA).

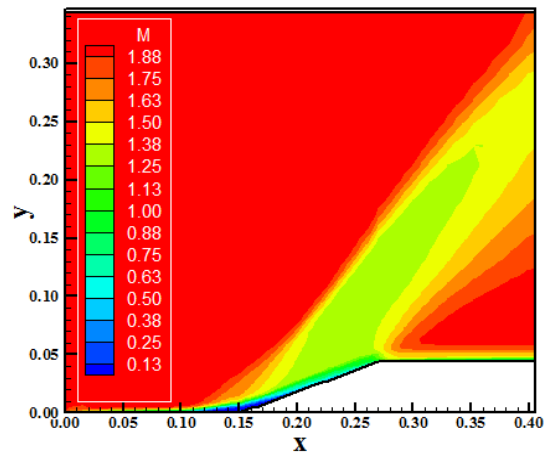


Figure 15. Mach number contours (VL-SA).

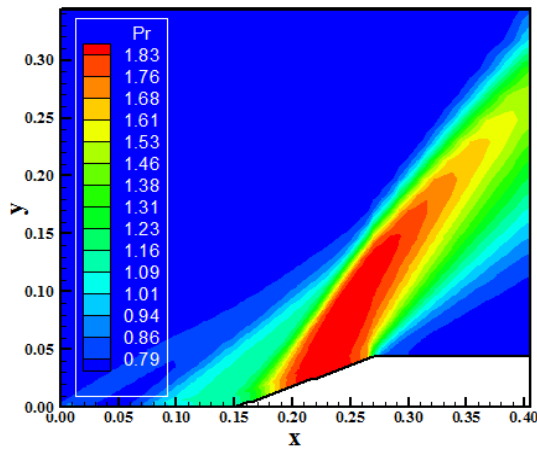


Figure 13. Pressure contours (FPP-SA).

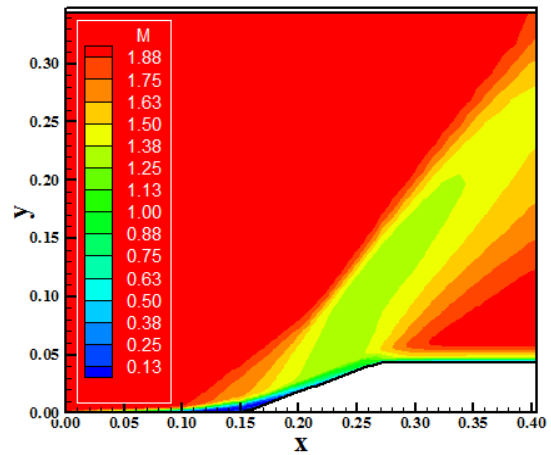


Figure 16. Mach number contours (H-SA).

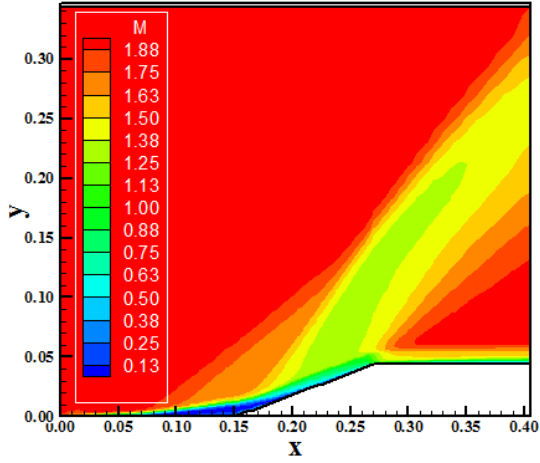


Figure 17. Mach number contours (FPP-SA).

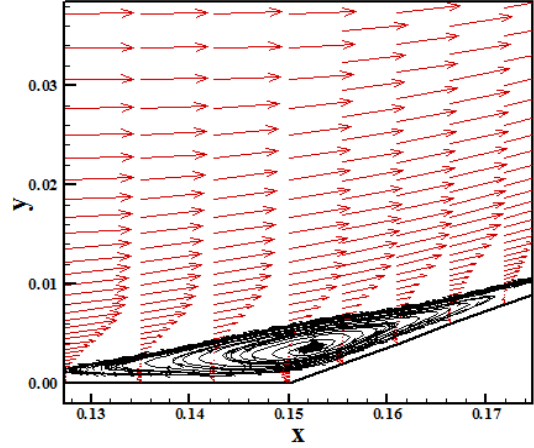


Figure 20. Circulation bubble (VL-SA).

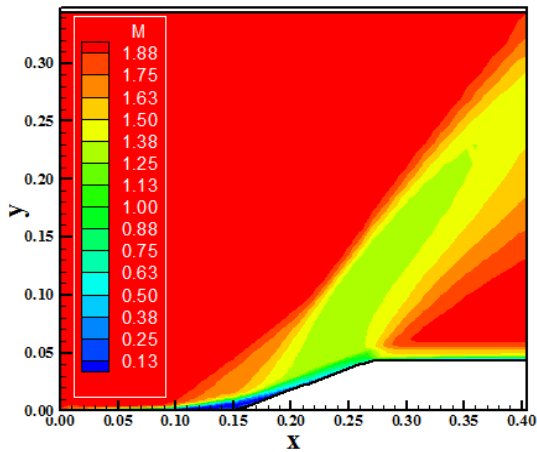


Figure 18. Mach number contours (RK-SA).

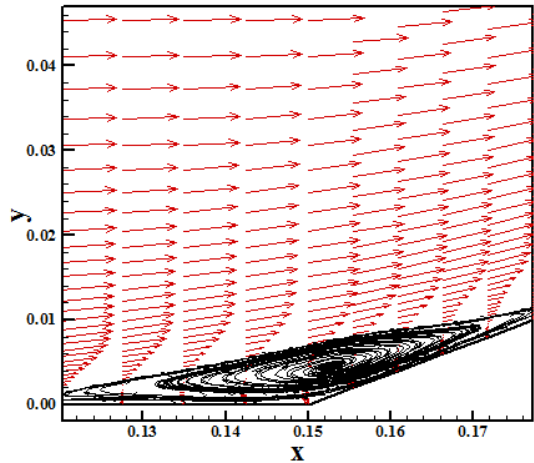


Figure 21. Circulation bubble (H-SA).

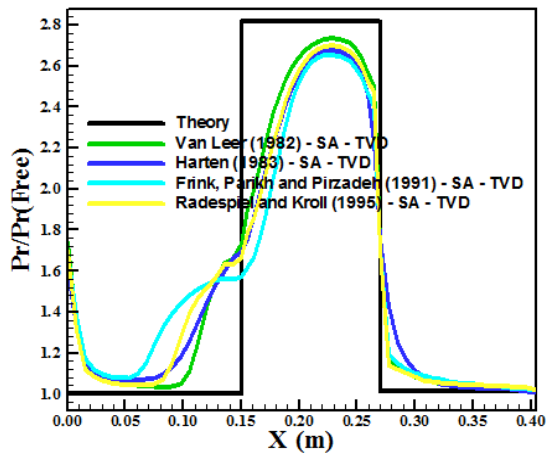


Figure 19. Wall pressure distributions.

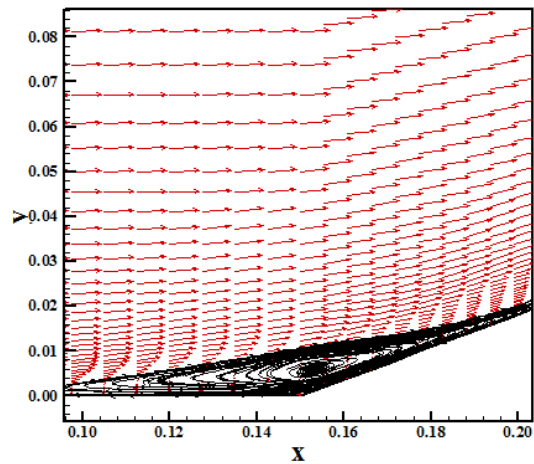


Figure 22. Circulation bubble (FPP-SA).

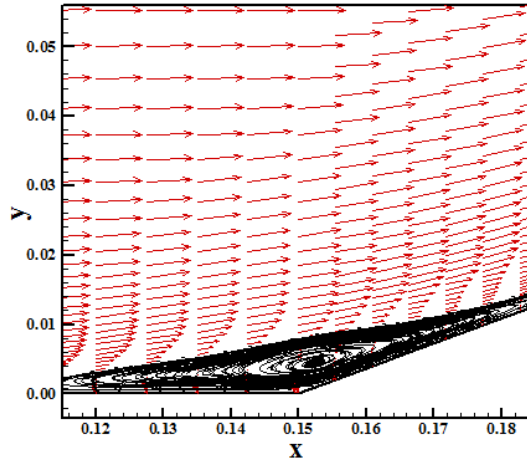


Figure 23. Circulation bubble (RK-SA).

It is important to be mentioned here that the best behavior to the pressure plateau was obtained by the [8] turbulence model in spite of the loss of physical meaning of the flow (loss of the circulation bubble formation).

Figures 20 to 23 exhibit the circulation bubble captured by the [2-4,6] schemes, respectively, as using the [10] turbulence model. As can be seen, the [4] solution generates the largest bubble region than the other solutions.

In resume, the [10] turbulence model predicts a less extent region of boundary layer detachment and, consequently, minor bubble size. The [10] model, an one-equation model, predicts less severe separation than the [9] model.

B. Quantitative Analysis

One way to quantitatively verify if the solutions generated by each scheme are satisfactory consists in determining the shock angle of the oblique shock wave, β , measured in relation to the initial direction of the flow field. [13] (pages 352 and 353) presents a diagram with values of the shock angle, β , to oblique shock waves. The value of this angle is determined as function of the freestream Mach number and of the deflection angle of the flow after the shock wave, ϕ . To $\phi = 20^\circ$ (ramp inclination angle) and to a freestream Mach number equals to 2.0, it is possible to obtain from this diagram a value to β equals to 53.0° . Considering [14] work and using a transfer in Figures 4 to 8 (laminar, first order), Figs. 20 to 22 (laminar, second order), and Figs. 30 to 34 (CS), as also, considering this work and using a transfer in Figs. 1 to 3 (BL), and Figs. 11 to 14 (SA), it is possible to obtain the values of β to each scheme and to each studied case, as well the respective errors, shown in Tab. 1.

It is possible to distinguish that only the [3] scheme did not capture the exact value of the oblique shock wave angle. All other schemes capture this exact value in a particular case. The [9] turbulence model was the most exact because allows the [2] and [4] schemes to capture accurately the shock angle.

Table 1. Values of the oblique shock wave angle and percentage errors.

Case	Lam., 1 st	Lam., 2 nd	CS, TVD	BL, TVD	SA, TVD
VL	51.0	56.4	51.0	53.0	51.6
Error (%)	3.77	6.42	3.77	0.00	2.64
H	49.3	55.0	52.5	55.0	51.7
Error (%)	6.98	3.77	0.94	3.77	2.45
FPP	52.4	51.6	51.4	53.0	55.0
Error (%)	1.13	2.64	3.02	0.00	3.77
LS	53.0	-	52.0	-	-
Error (%)	0.00	-	1.89	-	-
RK	51.0	-	51.2	-	53.0
Error (%)	3.77	-	3.40	-	0.00

Table 2. Computational data.

Case	Lam., 1 st	Lam., 2 nd	CS, TVD	BL, TVD	SA, TVD
VL	0.7 ⁽¹⁾ 3,872	0.1 32,138	0.1 12,318	0.1 32,144	0.1 19,961
H	0.9 ⁽¹⁾ 2,909	0.9 3,880	0.9 1,100	0.9 3,880	0.9 2,376
FPP	0.9 ⁽¹⁾ 6,326	0.1 48,378	0.1 22,374	0.1 48,378	0.1 34,615
LS	0.9 ⁽¹⁾ 6,484	-	0.1 22,593	-	-
RK	0.9 ⁽¹⁾ 3,904	-	0.1 13,614	-	0.1 33,091

⁽¹⁾: Convergence in 4 orders.

Table 2 presents the computational data of the simulations. With exception of the first order results, all others results converged in three (3) orders. All second order solutions of the [2,4-6] schemes converged with a CFL number of 0.1. On the other hand, all second order solutions of the [3] scheme converged with a CFL Number of 0.9. It is important to highlight the excellent convergence of the [3] scheme, converging in all cases with a CFL number of 0.9.

III. CONCLUSIONS

This work, first part, describes five numerical tools to perform perfect gas simulations of the laminar and turbulent viscous flow in two-dimensions. The [2-6] schemes, in its first- and second-order versions, are implemented to accomplish the numerical simulations. The Navier-Stokes equations, on a finite volume context and employing structured spatial discretization, are applied to solve the supersonic flow along a ramp in two-dimensions. Three turbulence models are applied to close the system, namely: [8-10]. On the one hand, the second-order version of the [2,4-6] schemes are obtained from a "MUSCL" extrapolation procedure, whereas on the other hand, the modified flux function approach is applied in the [3] scheme for the same

accuracy. The convergence process is accelerated to the steady state condition through a spatially variable time step procedure, which has proved effective gains in terms of computational acceleration (see [11-12]). The results have shown that the [2,4-6] schemes have yielded the best results in terms of the prediction of the shock angle at the ramp. Moreover, the wall pressure distribution is also better predicted by the [2] scheme. This work treats the [9], and the [10] second-order results obtained by the five schemes.

Maciel, E. S. G., and Pimenta, A. P., "Thermochemical Non-Equilibrium Reentry Flows in Two-Dimensions – Part I", *WSEAS Transactions on Mathematics*, Vol. 11, Issue 6, June, pp. 520-545, 2012; Maciel, E. S. G., and Pimenta, A. P., "Thermochemical Non-Equilibrium Entry Flows in Mars in Two-Dimensions – Part I", *WSEAS Transactions on Applied and Theoretical Mechanics*, Vol. 8, Issue 1, January, pp. 26-54, 2013; Maciel, E. S. G., "Aplicações de Algoritmos Predictor-Corretor e TVD na Solução das Equações de Euler e de Navier-Stokes em Duas Dimensões", Recife, PE, Editor UFPE, 2013. He is interested in the Magnetogasdynamics field with applications to fluid dynamics and in the use of ENO algorithms.

REFERENCES

- [1] P. Kutler, "Computation of Three-Dimensional, Inviscid Supersonic Flows", *Lecture Notes in Physics*, Vol. 41, pp. 287-374, 1975.
- [2] B. Van Leer, "Flux-Vector Splitting for the Euler Equations", Proceedings of the 8th International Conference on Numerical Methods in Fluid Dynamics, E. Krause, Editor, *Lecture Notes in Physics*, Vol. 170, pp. 507-512, Springer-Verlag, Berlin, 1982.
- [3] A. Harten, "High Resolution Schemes for Hyperbolic Conservation Laws", *Journal of Computational Physics*, Vol. 49, pp. 357-393, 1983.
- [4] N. T. Frink, P. Parikh, and S. Pirzadeh, "Aerodynamic Analysis of Complex Configurations Using Unstructured Grids", *AIAA 91-3292-CP*, 1991.
- [5] M. Liou, and C. J. Steffen Jr., "A New Flux Splitting Scheme", *Journal of Computational Physics*, Vol. 107, pp. 23-39, 1993.
- [6] R. Radespiel, and N. Kroll, "Accurate Flux Vector Splitting for Shocks and Shear Layers", *Journal of Computational Physics*, Vol. 121, pp. 66-78, 1995.
- [7] E. S. G. Maciel, "Laminar and Turbulent Simulations of Several TVD Schemes in Two-Dimensions – Part I – Theory", Submitted to the *VIII National Congress of Mechanical Engineering (VIII CONEM)*, Brazil, 2014 (under revision).
- [8] T. Cebeci, and A. M. O. Smith, "A Finite-Difference Method for Calculating Compressible Laminar and Turbulent Boundary Layers", *Journal of Basic Engineering*, Trans. ASME, Series B, Vol. 92, No. 3, pp. 523-535, 1970.
- [9] B. D. Baldwin, and H. Lomax, "Thin Layer Approximation and Algebraic Model for Separated Turbulent Flows", *AIAA Paper 78-257*, 1978.
- [10] P. R. Sparlat, and S. R. Allmaras, "A One-Equation Turbulence Model for Aerodynamic Flows", *AIAA Paper 92-0439*, 1992.
- [11] E. S. G. Maciel, "Analysis of Convergence Acceleration Techniques Used in Unstructured Algorithms in the Solution of Aeronautical Problems – Part I", *Proceedings of the XVIII International Congress of Mechanical Engineering (XVIII COBEM)*, Ouro Preto, MG, Brazil, 2005. [available in CD-ROM]
- [12] E. S. G. Maciel, "Analysis of Convergence Acceleration Techniques Used in Unstructured Algorithms in the Solution of Aerospace Problems – Part II", *Proceedings of the XII Brazilian Congress of Thermal Engineering and Sciences (XII ENCIT)*, Belo Horizonte, MG, Brazil, 2008. [available in CD-ROM]
- [13] J. D. Anderson Jr., "Fundamentals of Aerodynamics", McGraw-Hill, Inc., EUA, 563p, 1984.
- [14] E. S. G. Maciel, "Laminar and Turbulent Simulations of Several TVD Schemes in Two-Dimensions – Part I – Results I", Submitted to the International Conference on Mechanics, Fluid Mechanics, Heat and Mass Transfer (MFMHMT 2014), Interlaken, Switzerland, 2014 (under revision).

Edisson S. G. Maciel (F'14), born in 1969, february, 25, in Recife, Pernambuco. He is a Mechanical Engineering undergraduated by UFPE in 1992, in Recife, PE, Brazil; Mester degree in Thermal Engineering by UFPE in 1995, in Recife, PE, Brazil; Doctor degree in Aeronautical Engineering by ITA in 2002, in São José dos Campos, SP, Brazil; and Post-Doctor degree in Aeronautical Engineering by ITA in 2009, in São José dos Campos, SP, Brazil.

He is Professor at the Federal University of Great Dourados. The last researches are based on thermochemical reentry non-equilibrium simulations in Earth and thermochemical entry non-equilibrium simulations in Mars. They are:

Thermodynamic performances of the turbojet combustion chambers – numerical evaluation

Constantin Rotaru, Mihai Mihaila-Andres, Pericle Gabriel Matei and Raluca Ioana Edu

Abstract—This paper presents the results of a study on the thermodynamic performances of a typical turbojet combustion chamber using a chemical reactor network. Several approaches of the aerodynamic shapes of the combustion chamber were considered to choose the methodology that better predicts the temperature field in front of the turbine. In order to find the optimal characteristics of the burned process, the modelling and simulation of the combustion in the turbojet engine were made with Fluent and Maple software.

Keywords—Aircraft engine, CFD, Combustion chamber, Turbojet.

I. INTRODUCTION

THE thrust of the present aircraft engine is developed by compressing air in the inlet and compressor, mixing the air with fuel, burning the mixture in the combustor and expanding the gas stream through the turbine and nozzle. The expansion of gas through the turbine supplies the power to turn the compressor and the net thrust delivered by the engine is the result of converting internal energy to kinetic energy.

The combustion chamber of the turbojet engines is one of the most important components which assures the chemical energy transformation of the fuel in caloric energy and transmits this energy to the working fluid with a high level efficiency.

The modeling of the combustion systems in energy conversion equipment, such as the turbojet combustion chambers, has many challenges especially concerning the limitations of the predictive capacity of the models based on the computational fluid dynamics and their associated computational cost. A complete description of the combustion processes needs a simultaneous solution of the laws that govern the fluid mechanics and reaction kinetics, and its complexity increases as grows the number of species and reactions of the kinetics mechanism.

Constantin Rotaru is with the Aviation Integrated Systems and Mechanics Department, Military Technical Academy, Bucharest, Romania (tel: +40745974488; fax: +4021 335 57 63; e-mail: rotaruconstantin@yahoo.com).

Mihai Mihaila-Andres is with the Aviation Integrated Systems and Mechanics Department, Military Technical Academy, Bucharest, Romania (e-mail: mihailmi@rdslink.ro)

Pericle Gabriel Matei is with the Aviation Integrated Systems and Mechanics Department, Military Technical Academy, Bucharest, Romania (e-mail: pgmatei@yahoo.com).

Raluca Ioana Edu is with the Aviation Integrated Systems and Mechanics Department, Military Technical Academy, Bucharest, Romania (e-mail: edu_ioana_raluca@yahoo.com).

A first approach that aims the attenuation of the computational effort in the simulation of practical combustion systems such as the turbojet combustors, consists in the simplification of the chemical kinetics description while retaining the fluid mechanics description. This simplification involves a set of reduced elementary reactions and chemical species. However, the reduced schemes are valid only within a narrow range of pressure, temperature and composition in which the reduced mechanism is capable to simulate, not being able to represent in detail the chemical process.

The chemical reactor network is an alternative to the simulation of air-breathing engine combustors because it simplifies the fluid mechanics descriptions while keeping the details of the chemical kinetic description. This approach consists in the resolution of simplified transport equations to describe the operation of trivial combustion models such as well stirred reactor (WSR) and plug flow reactor (PFR), which are systematically arranged into a structured scheme with the purpose to represent the combustion process occurring within combustion equipment. These models are very useful in the prediction of relevant thermochemical properties such as temperature and pollutants emissions, which are the most significant parameters in the aircraft engines operation. While the PFR model assumes that the confined fluid moves through plugs, as a result of the absence of axial diffusion, the WSR model considers the mixing among reactants and products as being homogenous and instantaneous [1].

The principal advantage in the simulation of gas turbine combustors by mean of the chemical reactor network approach is the relatively low computational cost, when compared with the CFD approach. However, this benefit appears as detriment to a detailed description of the flow within the domain under analysis. To develop a model that simulates the operation of a gas turbine combustor, several hypotheses must be made, which aim to reduce the complexity of the governing equations related to the fluid mechanics. Thus, with the usage of the chemical reactor network approach, it is possible to obtain an accurate description of the combustion process in confined regions of a gas turbine combustor. For this purpose it is required the use of WSR and PFR models, which must be linked in a systematic and structured arrangement. The WSR models are used in the description of the combustion process occurring in the flame or primary zone of the combustion, whereas PFR models simulate the combustion in the intermediate and dilution zones.

Combustion stability, intensity and efficiency depend on the

fluid flow and turbulence distribution within the combustor. To create the high turbulence necessary for intense combustion, there must be considerable pressure drop across the small holes in the chamber liner through which most of the air enters the combustion zone. Other causes of pressure drop in combustors include the bulk acceleration of the hot gas as its density decreases because of combustion and friction on the channels walls. For best engine performance the sum of these pressure losses should not be greater than a few percentage points of the combustor inlet pressure. A typical turbojet combustion chamber is presented in Fig. 1.

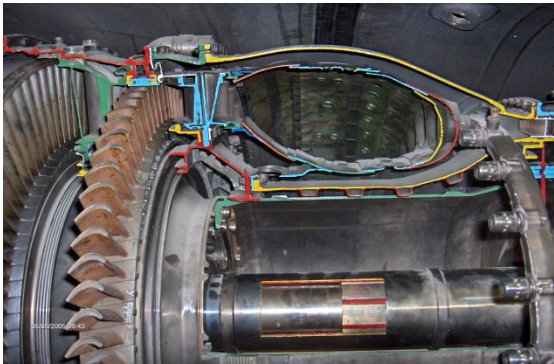


Fig. 1 Combustion chamber

The performances of a turbojet engine are strongly dependent on the mass flow rate per unit cross-sectional area of the engine. A large area for a given flow rate implies not only large engine mass per unit thrust but also large nacelle drag for an externally mounted engine (civilian aircrafts) or large volume for an engine placed inside the fuselage (military aircrafts). For this reason it is desirable for the velocity of the working fluid to be as high as possible, without incurring excessive losses due to wall friction and viscous mixing. A limitation is imposed by the combustors since it is necessary to maintain a stationary flame within a moving air stream [2].

The thermal energy of the air/fuel mixture flowing through an air-breathing engine is increased by the combustion process. The fuel must be vaporized and mixed with the air before this chemical reaction can occur. Once this is done, the combustion process can occur and thus increase the thermal energy of the mixture.

The design of the main burner of an air-breathing engine differs in many ways from that of conventional combustion devices because the following properties of the combustion chamber are desired: complete combustion; low total pressure lost; stability of combustion process; short length and small cross section; operation over a wide range of mass flow rates, pressures and temperatures.

The theoretical heat of reaction of the fuels assumes a complete combustion with no unburned hydrocarbon fuel and no dissociation of the products of combustion. The actual heat release is affected by the quality of fuel atomization, vaporization, mixing, ignition, chemical kinetics, flame stabilization, intermediate air flow, liner cooling and the aerodynamics of the combustor. Here a variety of timescales

as in residence time, chemical reaction rate timescales, spontaneous ignition delay time that includes vaporization timescale among other time constants enter the real combustion problem.

II. COMBUSTION CHAMBER MODEL

A self-stabilized, steady flow combustion system requires two distinct regions: a primary zone (well stirred reactor) in which the flow stream is recirculated in order to promote gross mixing of products, reactants and reaction intermediates (being governed by a coupled set of nonlinear equations) and a secondary zone (Fig. 2) which has the main function to allow sufficient convective residence time for the primary zone effluent to burn out before exiting the combustor (plug flow reactor).

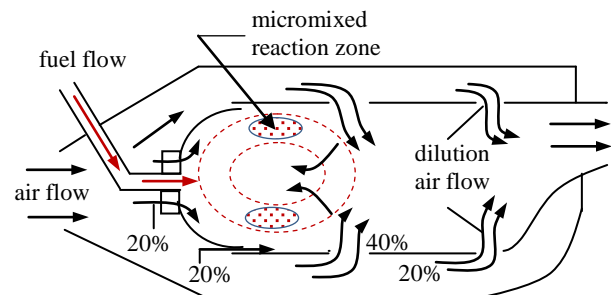
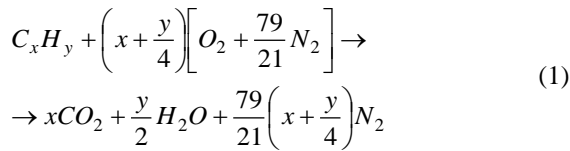


Fig. 2 Combustion chamber flow pattern

A typical distribution of airflow into a can-contained combustion zone is presented in Fig. 2 where about 20% of the intake air passes through swirling vanes that surround the central fuel spray nozzle. The primary zone in which the fuel-air ratio is nearly stoichiometric, is fed by other airflow (about 80%) [3]. These flows are designed to interact in such a way that a large and steady swirl is established in the primary combustion zone.

The rates of reaction in a turbojet combustion chamber are affected by both chemical kinetics and mixture turbulence which controls the rate of mixing of fuel and air, and also the instantaneous geometry of the flame surface. The flame travels into a mixture of reactants at a rate that is dependent on the state of the reactants and is limited either by mixture turbulence or by chemical kinetics. A flame remains stationary in a traveling mixture of reactants if the speed of the flame relative to the reactants is just equal to the reactants mixture velocity. Turbulence can rise the burning velocity, so, the flame tube must have the zones of low velocity in which the flames can propagate into an unburned mixture.

The maximum combustion temperature occurs when hydrocarbon fuel molecules are mixed with just enough air, so that, all of the oxygen atoms are consumed, all of the hydrogen atoms form water vapor and all of the carbon atoms form carbon dioxide CO_2 . This ideal mixture of fuel and air is represented by a general atom balance equation, called the stoichiometric equation, given by

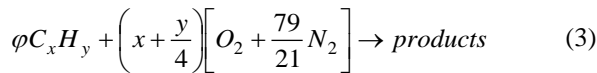


The stoichiometric mass-basis fuel/air ratio is

$$f_{st} = \frac{36x + y}{103(4x + y)} \quad (2)$$

Although the stoichiometric ratio for most fuels is typically 0.06 to 0.07 and the fuel-to-air ratio for the engine is 0.015 to 0.03, in the primary burning zone of the combustion chamber, the mixture is fuel rich and this ratio is typically 0.08. Because the overall performance of an engine and the life of the turbine, are strongly dependent on burner exit temperature, predicting this temperature is extremely important. All jet fuels are hydrocarbons and most of them have characteristics similar to those of kerosene.

The fuel/air equivalence ratio is defined as the ratio of the actual fuel/air ratio to the stoichiometric fuel/air ratio $\phi = f / f_{st}$ and it permits representation of either fuel-rich or fuel-lean mixtures by multiplying the fuel term in the atom-balance equation by ϕ



Ignition of a fuel/air mixture in a turbojet combustion system requires inlet air and fuel conditions within flammability limits, sufficient residence time of a combustible mixture and location of an effective ignition source in the vicinity of the combustible mixture. When the temperature in the combustion system is below the spontaneous ignition temperature, an ignition source is required to bring the local temperature above the spontaneous ignition temperature [4, 5].

The problem of lean mixture in a burner can be overcome by mixing and burning a rich fuel/air mixture in a small region where the local equivalence ratio is near unity. By using only a portion of the total air in a region, a locally rich mixture can be efficiently burned and then the products of combustion diluted and cooled to an acceptable turbine inlet temperature by the remaining air. At usual pressure and temperature, hydrocarbon/air mixture will react for ϕ from approximately 0.5 to 3 and not at all below 0.2 *atm* at standard temperature. A limitation is imposed by the combustion because it is necessary to maintain a stationary flame within a high velocity airstream. Provided stable combustion is attained, complete combustion in the case of lean mixture is virtually ensured since, with excess oxygen, local fuel-rich areas are unlikely.

On the other hand, combustion of a near-stoichiometric mixture requires an essentially uniform distribution of constituents to avoid wasting some fuel in local fuel rich regions.

A fuel air mixture of equivalence ratio leaner than 0.6 and richer 3.0 will not react in room temperature and pressure. With the increase in temperature, the flammability limit boundary widens to $0.3 < \phi < 4.0$ in the spontaneous ignition

temperature range ($T > 225\text{ C}$) for a kerosene-air mixture (Fig. 3).

At high altitude, where the pressure is reduced, chemical reaction rates may be much slower than turbulent mixing rates. The probability of chemical combination of atoms and molecules depends on the frequency of molecular collisions and on the energy of the colliding molecules. Combustion proceeds as a chain reaction in which energy released from one combination is sufficient to raise neighboring atoms above the threshold energy, so, raising the temperature decreases the energy that, on average, must be added to a particle before the reaction threshold is reached. For a given temperature, high pressure corresponds to high density and this means greater frequency of collision of fuel and oxidant atoms.

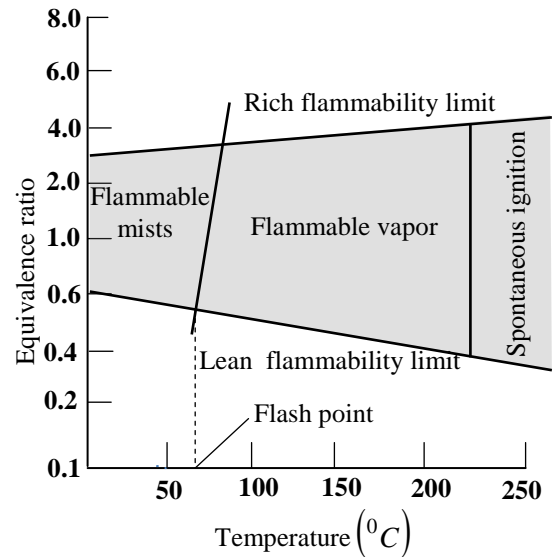
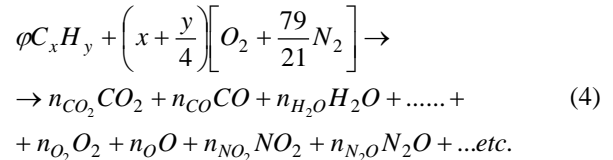


Fig. 3 Flammability limits

Off-stoichiometric fuel/air ratios, as characterized by the equivalence ratio $\phi \neq 1$, affect the type and distribution of combustion products, as well as the temperature. For off-stoichiometric mixtures, and also for possibly incomplete combustion, the atom-balance equation can be generalized as



where *etc.* indicates that the list of possible product gases may be as many combinations of O, H, C and N atoms as exist in nature [1,3].

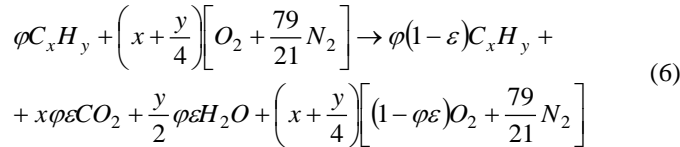
Assuming that combustion occurs at constant pressure, without either heat or work transfer with surroundings, then the total enthalpy of the products will be the same as the reactants. The static enthalpy of a mixture of gases is given by

$$H = \sum_{k=1}^{NS} n_k h_k \quad (5)$$

where *NS* is the number of product species, n_k is the mole

numbers and h_k is the static enthalpy of the k^{th} product species. If the reactants are ignited and allowed to burn to the final equilibrium state without heat being added or removed during the process, the final equilibrium temperature is called the adiabatic flame temperature and it is found by solving the algebraically equation $H_P = H_R$, where the indices P and R represent the products and reactants. Both the adiabatic flame temperature and heat of reaction are end-state quantities calculated on the basis of static change from the given reactant mol numbers $\{n_i\}_R$ to the set of product mole number $\{n_i\}_P$. The product mole numbers can be calculated either from assumed complete combustion or chemical equilibrium. However, neither result considers the instantaneous rates of change mole numbers nor the integrated values of mole numbers that may exist at specific moments. Because fluid particle residence times in any subcomponent of a turbojet engine are less than a millisecond (10^{-3} s), it is very often the case that insufficient time is available for the exothermic combustion reactions to reach chemical equilibrium. For purpose of mathematical modeling finite-rate chemical kinetics for homogeneous gas-phase chemical reaction, it is assumed that very many individual, reversible, elementary physical-chemical collision reactions of the form $CO + OH \rightarrow CO_2 + H$ can occur.

For incomplete combustion, the atom-balanced equation may be generalized as



where ε is the combustion reaction progress variable. When $\varepsilon = 1$, the maximum value of T_{aft} (the adiabatic flame temperature) is realized and may be very well approximated by the linear equation

$$T_{\text{aft}} \approx T_i + \frac{\varphi_{st} h_{PR}}{c_p} \quad (7)$$

where T_i is the air inlet temperature in the combustion chamber, h_{PR} is the heat of reaction and c_p is the specific heat at constant pressure.

The volumetric mass rate of consumption of the fuel can be expressed by a modified Arrhenius equation for the overall combustion reaction

$$\begin{aligned} \dot{\omega}_f = M_f \left(x + \frac{y}{4}\right) \varphi A e^{-T_{act}/T} \times \\ \times \left(\frac{p}{RT \sum N_P}\right)^2 (1 - \varepsilon)(1 - \varepsilon \varphi) \end{aligned} \quad (8)$$

where $M_f = 12x + y$ is the molecular weight of the fuel, A is the pre-exponential factor, T_{act} is the activation temperature,

p is the pressure in the combustion chamber, R is the universal gas constant and $\sum N_P$ has the expression

$$\sum N_P = \frac{100}{21} \left(x + \frac{y}{4}\right) + \varphi \left[1 + \left(\frac{y}{4} - 1\right) \varepsilon\right] \quad (9)$$

The static temperature T is represented by the linear equation

$$T = T_i + \varepsilon \left(\frac{\varphi_{st} h_{PR}}{c_p}\right) \quad (10)$$

The equation (8) could give the optimal value of ε for which $\dot{\omega}_f$ is a maximum. A design goal for combustor primary zone is to achieve as nearly as possible this maximum value of $\dot{\omega}_f$ at some location in the combustion device.

Stable and efficient combustion can be upset by the fuel/air mixture becoming too lean or too rich such that the temperature and reaction rates drop below the level necessary to effectively heat and vaporize the incoming fuel and air. The effects of mass flow rate, combustion volume and pressure on the stability of the combustion process are combined into the combustor loading parameter.

The residence time, t_{res} , in the burner is given by

$$t_{res} = \frac{L}{V_{av}} \approx \frac{L}{V_{ref}} = \frac{\rho_{i3} A_{ref} L}{\dot{m}_3} \quad (11)$$

where V_{ref} is based on the air mass flow rate entering the combustor, A_{ref} is the cross-sectional area normal to the airflow of combustion chamber, L is the length of the burner and ρ_{i3} is the density of the air entering the combustion chamber [6].

The minimum external energy needed to initiate a reaction is a function of the equivalence ratio as well as the type of fuel for vaporized fuel-air mixture. Figure 4 shows the level of ignition energy of various vaporized fuel-air mixtures as a function of equivalence ratio [7, 8]. The minimum ignition energy corresponds to a particular equivalence ratio.

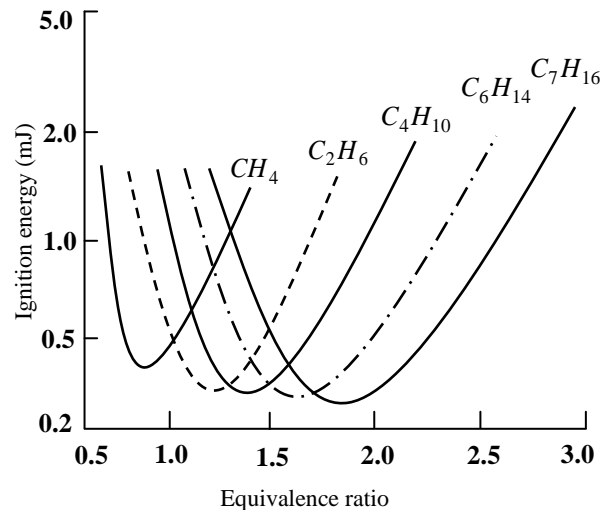


Fig. 4 Minimum ignition energy

Assuming an isentropic compression process, the total density at state 3 (the station behind the compressor) is proportional to the total pressure at this state, $\rho_{t3} \propto (p_{t3})^{1/\gamma_c}$ and the residence time, t_{res} , is proportional to the reaction time, so, the length of burner could be estimated by

$$L \approx \frac{A_4}{A_{ref} \sqrt{T_{t4}}} (p_{t4})^{\left[n \frac{\gamma_c - 1}{\gamma_c} \right]} \quad (12)$$

where station 4 is the high pressure turbine stator inlet and γ_c is the ratio of specific heats.

The reaction timescale, t_{re} , is inversely proportional to reaction rate, which may be written as

$$t_{re} \approx p^{-n} T^{-m} e^{\frac{E_a}{RT}} \quad (13)$$

The pressure and temperature exponents in a turbojet combustor have values around 1-2 for n and 1.5-2.5 for m [3].

III. RESULTS

The combustion chamber geometrical model of a turbojet engine is presented in Fig. 5 and it is similar to a real model with 24 injectors.

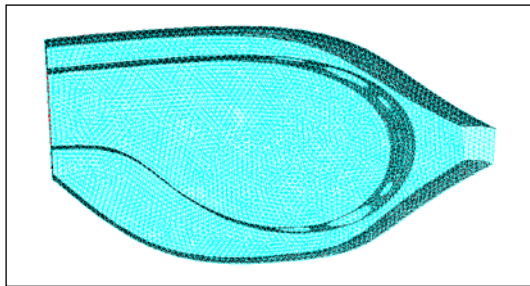


Fig. 5 Combustion chamber geometrical model

The faces were meshed with elements Tri, type Pave and the volume was meshed with elements Tet/Hybrid, type TGrid with an interval size 0.8.

The boundary conditions were: pressure inlet; pressure outlet; wall; - periodic.

The length of combustion chamber is 37 cm and the flame tube has the shape presented in Fig. 6.

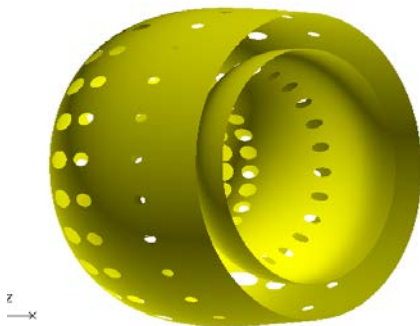


Fig. 6 Flame tube

The combustion was modeled using the mixture-fraction/PDF approach with the equilibrium mixture consisting of 10 chemical species: C_5H_{12} (fuel), CH_4 , CO , CO_2 , H_2 , H_2O , $H_2O(l)$, O_2 , OH , $C(s)$, N_2 .

In the first step was calculated the adiabatic system chemistry for settings Adiabatic, Equilibrium Chemistry and Beta PDF with 0,7 Fuel Rich Flamability Limit [9, 10].

In the second step was calculated the Nonadiabatic System Chemistry with 0,3 Fuel Rich Flamability Limit.

The simulations were made in Fluent software [11]

- Segregated implicit solver;
- K-epsilon viscous model;
- Injection Type: group;
- Number of Particle Steam: 10;
- Particle Type: Droplet;
- Diameter Distribution: linear;
- Stochastic tracking Model: 10 Number of Tries.

Some results are presented in the following pictures (Figs. 7-9).

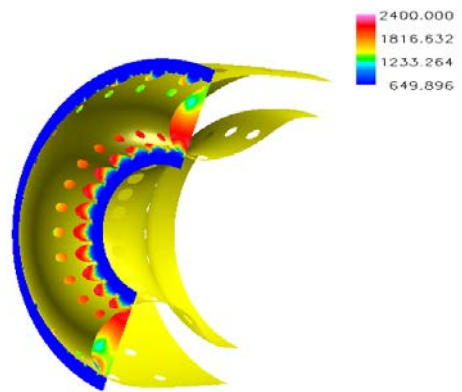


Fig. 7 Temperature

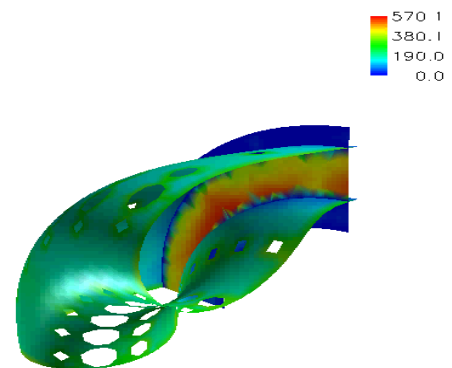


Fig. 8 Velocity magnitude

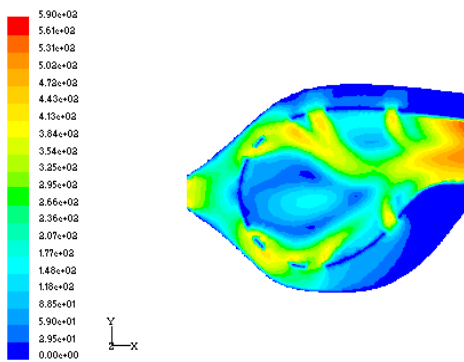


Fig. 9 Contours of velocity magnitude

IV. CONCLUSION

A low turbulence intensity environment in a fuel-air mixture flow of 50-100 m/s results in a root mean square of the turbulence fluctuation speed of 2.5-5 m/s. In a high turbulence intensity in a flow with a mean speed of 100 m/s, the turbulence contribution to flame propagation speed may be as high as 30 m/s.

In order to approach new constructive solutions for complex systems like the aircraft engines, it is necessary to use software codes to study the behavior or performances of these systems. For an aircraft engine the experimental validation is expensive, so the first step in this study is the simulation of the virtual model of constructive elements, like combustion chamber. In this study are obtained some results regarding the shape of the combustion chamber, the optimal type of fuel from the class $C_n H_{2n+2}$ and also the percent of the addition parts of alkanes ($C_2 H_{2n}$) and aromatic hydrocarbons.

It is important to emphasize the inherent limitation in the use of the chemical reactor network approach in the simulation of combustion as the result of the simplification on the fluid mechanics equations, in contrast to the more elaborate description of the kinetic of combustion and the lower computational burden. A good alternative in the modeling and simulation of turbojet combustion systems could be the adoption of sophisticated approaches, such as the CFD, to get a better prediction of the thermodynamic performances of the turbojet combustion chambers.

REFERENCES

- [1] J. D. Mattingly, "Elements of Propulsion. Gas Turbines and Rockets", AIAA, Reston Virginia, USA, 2006.
- [2] L. C. Jaw, J. D. Mattingly, "Aircraft Engine Controls – Design, System Analysis and Health Monitoring", AIAA, Reston Virginia, USA, 2009.
- [3] S. Farokhi, "Aircraft Propulsion", John Wiley & Sons Inc., USA, 2009.
- [4] Rotaru Constantin, Arghiropol Adrian, "Numerical Computation of Internal Flow for Turbojet Engine Combustion Chamber", 16th International Conference The Knowledge-Based_Organization: Applied Technical Sciences and Advanced Military Technologies, Proceedings 3, pag. 117-122, Romania, 2010.
- [5] Rotaru, C., Safta, D., Barbu, C., "Aspects regarding internal flow in combustion chamber of turbojet engines", Proceedings of the 5th IASME/WSEAS International Conference on Fluid Dynamics and Aerodynamics, Greece, 2007.

- [6] R. F. Huang, H. F. Yang, C. M. Hsu, "Flame Behavior and Thermal Structure of Combusting Nonpulsating and Pulsating Plane Jets", Journal of Propulsion and Power, Volume 29, number 1, 2013, pag. 114-124.
- [7] Ronald D. Flack, "Fundamentals of Jet Propulsion with Applications", Cambridge University Press, 2005.
- [8] Rotaru Constantin, "Aspects Regarding Combustion Chamber Dynamics for Turbojet Engines", ICMT'09 International Conference on Military Technologies, Brno, Czech Republic, Proceedings, pag. 342-349, 2010.
- [9] J. D. Mattingly, W. H. Heiser, D. T. Pratt, "Aircraft Engine Design", second edition, AIAA, Reston Virginia, USA, 2002.
- [10] Rotaru, C., Arghiropol, A., Barbu, C., "Some aspects regarding possible improvements in the performances of the aircraft engines", Proceedings of the 6th IASME/WSEAS International Conference on Fluid Dynamics and Aerodynamics, Greece, 2008.
- [11] FLUENT Documentation.

Strength Verification of the Planetary Gear System

Jae-hwan Shim, Sung Gil Han, Yoo In Shin

Department of Mechanical and Aerospace engineering,
Graduate School, Gyeongsang National University, 501,
Jinju-daero, Jinju, Gyeongnam, 660-701, Korea

Chan Heon Yoon

Youngdong Tech Co., Changwon, Gyeongnam, 641-847,
Korea

Jeong Se Suh, Chul Ki Song

Department of Mechanical Engineering, ERI
Gyeongsang National University, 501, Jinju-daero, Jinju,
Gyeongnam, 660-701, Korea
cksong@gnu.ac.kr

Abstract— Planetary gear systems are used in the driving system of excavators as a reduction gear and they are widely used in industrial areas such as transmission in automobile, machine tools, semiconductor equipment, and so on. Planetary gear systems have the advantages of high power density, large reduction in a small volume, multiple kinematic combinations, and axial direction of power path. Gears in planetary gear systems sometimes get short life due to wear and breakage by repetitive load during operation time.

In this paper, a strength design evaluation for the planetary gear system was performed to ensure the gears' stability and durability during operation time.

Keywords—Strength design verification, Planetary gear system, Reduction gear, Stability, Durability

I. INTRODUCTION

PLANETARY gear systems normally consist of a centrally pivoted sun gear, a ring gear, and several planet gears found between the sun gear and ring gear. Compared to traditional gear boxes, the planetary gear systems have some advantages.

Planetary gear systems possess larger efficiency in small volumes because of the compact combination of gears in the planetary gear system. They also have an outstanding efficiency of just 3% for power transmission tantamount to the power loss that occurs on each of the shift stages. Through this aspect, we can figure out that the rate of transmissible input energy in the planetary gear system is smaller than the mechanical loss which comes from a gear box. Based on the advantages mentioned above, the planetary gear system has been designed. [1]-[6]

The driving system of excavators consists of two parts which are a planetary gear system and a hydraulic motor as shown in Figure 1.

There are numerous researches to verify strength of gears in planetary gear systems. However, most of the researches have been performed focusing on gears with only one kind of material without any comparison with other materials. In addition, researches for comparison with modified gears by changing shape of the gears are not enough to verify strength of

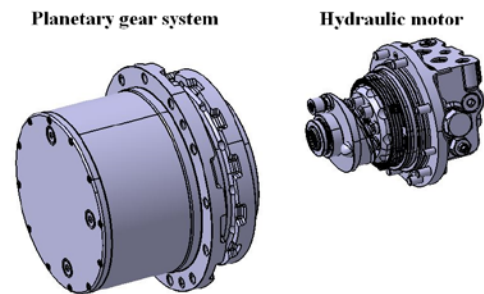


Fig. 1 Driving system for excavators

gears in planetary gear systems. [7]-[9]

Therefore, in this paper, strength design verification for a planetary gear system that is used in the driving system of excavators has been performed.

II. MODELING OF PLANETARY GEAR SYSTEM FOR ANALYSIS

Optimum modeling for analysis is needed to carry out a more precise analysis result. Therefore, the modeling for strength and durability analysis is focused on gear train part. [10]

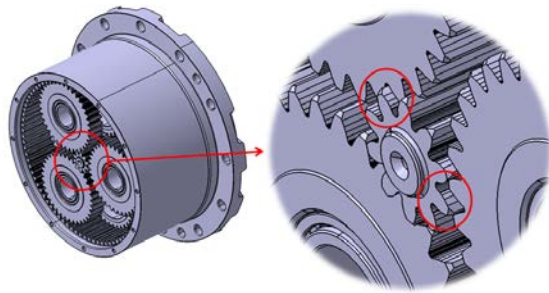
In order to perform the research for comparing gears with two kind of different materials for each, the same modeling is used.

In order to perform the research for comparing two shapes of gears, the width of the planetary gears is extended to 1mm as shown in Figure 2. We have assumed that the contact face between the sun gear and the planetary gears can be wider than in the previous model of planetary gears by extending the widths of the gears. The occurring stress can be smaller than the previous model as well. Therefore, the modified model of the planetary gears has been also used for the research.

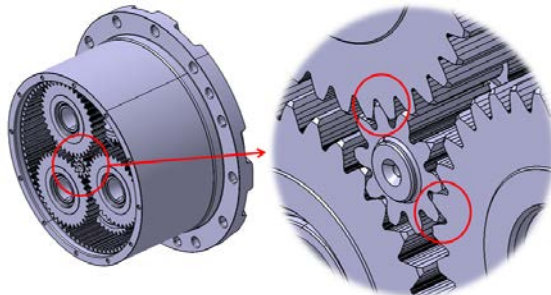
III. STRENGTH ANALYSIS OF PLANETARY GEAR SYSTEM

A. Boundary Conditions and Load Conditions

In this research, SCM420H and SCM822H are applied to the planetary gear system as its materials. SCM420H and



(a) The space of sun gear to extend width of planetary gears



(b) The modeling after extending width of 1 mm for planetary gears

Fig. 2 The modified modeling for planetary gears

SCM822H are applied to perform the research for two kind of different materials, and SCM420H is also applied to perform the research for two shapes of gears.

SCM420H is widely used as a component material of industrial reduction gear, and SCM822H is widely known as a typical alloy steel for machine structural use. SCM822H has many advantages such as excellent mechanical attributes, increase of corrosion-resistance and wear-resisting quality, protection from decline in mechanical attributes if subject to high temperature, improvement of quenching efficiency, and so on. The material properties are shown in Table 1. [11]

Power to drive the planetary gear system is generated from the hydraulic motor of the driving system. The maximum output of hydraulic motor is 210.5 Nm and 1,294.5 rpm. Analysis for stability and durability of the planetary gear system design should be performed under extreme load conditions. Thus, outputs in maximum torque are applied as input conditions for analysis. The average temperature in the planetary gear system is established at 60°C, and the lubricant is established SAE 80W grade which is generally used for planetary gear systems as well. [12]-[13]

In addition, according to evaluation standards for the lifetime of RS B 0095, the standard of track drive units for small excavators [14], input conditions are established to verify durability for driving over 1,000 hours. The input conditions are arranged in Table 2 and applied to the three researches.

B. The Results of Strength Analysis for Gears

Strength analysis is performed to evaluate the durability and stability of gears in the planetary gear system. Boundary

Table 1 Material properties

Material	Tensile strength (MPa)	Yield strength (MPa)	Heat treatment	Surface hardness (Hv)
SCM420H	932	792	annealing, carburizing	800
SCM822H	1030	1030	annealing, carburizing	670

Table 2 Input conditions

Precondition	Test load case
Temperature (° C)	60
Speed (rpm)	1,294.5
Torque (Nm)	210.5
Lubricant	SAE 80W

conditions, load conditions, and material properties are established to perform this research.

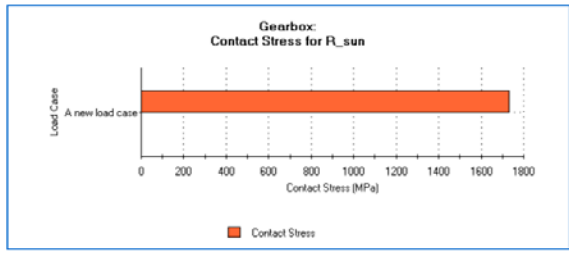
The results of the strength analysis for the two materials and the modified model are shown in Figure 3 to Figure 8. The stress on planetary gears occurs in two parts. The two parts are internal contact part which contacts the sun gear, and external contact part which contacts the ring gear. Further, the substances for the divided stress form two parts and are shown in Figures 4, 6, and 8.

According to the analysis results, the first maximum bending stress occurs on the sun gear, and the second maximum bending stress occurs on the planetary gear by power transmission route.

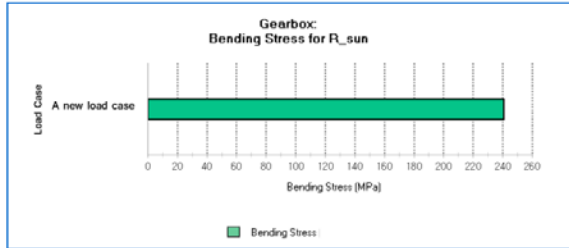
In the case of applying on SCM420H, the measurement of first stress is 204.5 MPa, and the measurement of second stress is 182.6 MPa. The maximum contact stress on the sun gear and planetary gear occurs at the same measurement of 1733.2 MPa. In the case of applying on SCM822H, the maximum bending stress occurs at 240.5 MPa on sun gear and occurs at 182.6 MPa on planetary gear. The maximum contact stress occurs at the same measurement of 1703.6 MPa on sun gear and planetary gear.

In the case of the modified model with SCM420H, the maximum bending stress occurs at 212.8 MPa on sun gear and occurs at 161.5 MPa on planetary gear. The maximum contact stress occurs at the same measurement of 1630.3 MPa on sun gear and planetary gear.

By comparing the analysis results for SCM420H with the analysis results for SCM822H, the bending stress for two materials occurs with similar measurements. However, we could find that the measurement for SCM822H is larger than SCM420H at about 30 MPa in the case of the contact stress.



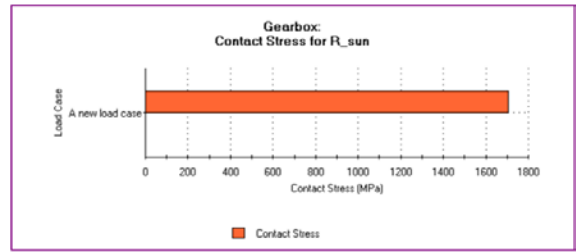
(a)



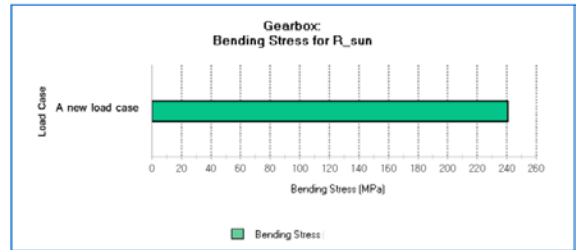
(b)

Fig. 3 Stress of the sun gear for SCM420H
(a) contact stress : 1733.2 MPa
(b) bending stress : 240.5 MPa

Planetary gear	182.6	182.6	161.5	1733.2	1703.6	1630.2
-----------------------	-------	-------	-------	--------	--------	--------

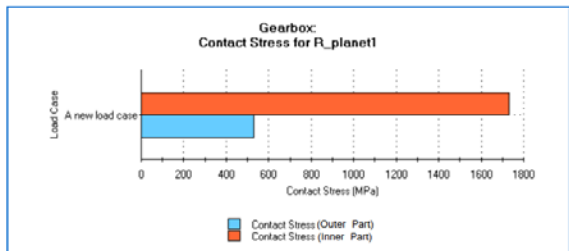


(a)

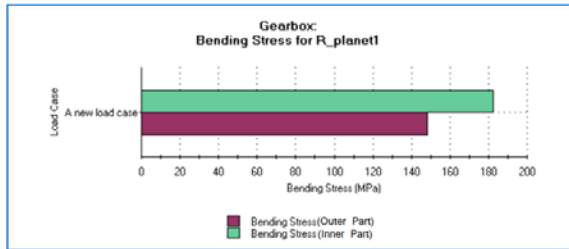


(b)

Fig. 5 Stress of the sun gear for SCM822H
(a) contact stress : 1703.6 MPa
(b) bending stress : 240.5 MPa

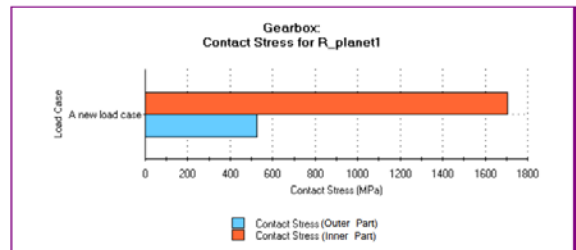


(a)

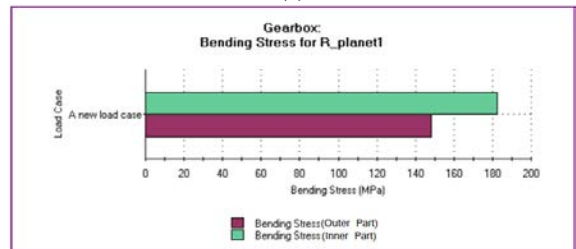


(b)

Fig. 4 Stress of the planetary gear for SCM420H
(a) contact stress : 1733.2 MPa
(b) bending stress : 182.6 MPa



(a)



(b)

Fig. 6 Stress of the planetary gear for SCM822H
(a) contact stress : 1703.6 MPa
(b) bending stress : 182.6 MPa

Table 3 The results of gear strength analysis

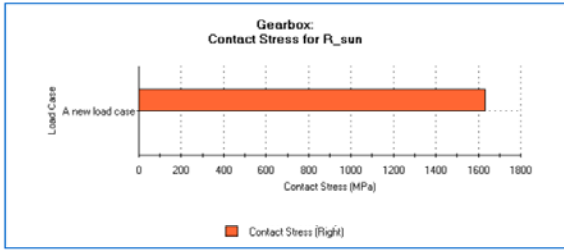
	Bending stress (MPa)			Contact stress (MPa)		
	SCM 420H	SCM 822H	Modified model (420H)	SCM 420H	SCM 822H	Modified model (420H)
Sun gear	240.5	240.5	212.8	1733.2	1703.6	1630.2

Above all things, the analysis results for the modified model are definitely remarkable. Although the maximum bending stress that occurs on sun gear is larger than the maximum bending stress of SCM420H, the other results of stress except the above case are small by at least over 20 MPa.

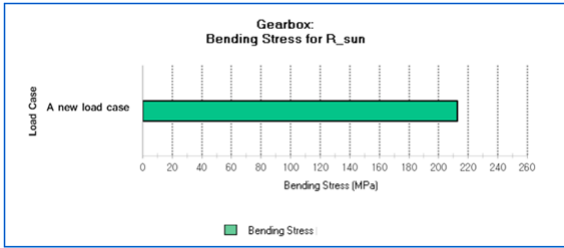
The results of the strength analysis for three cases are shown in Table 3.

C. Safety Factor of Gears

Safety factor is the result applied at JIS 4 grade, the result of safety factors for SCM420H and SCM822H, with the modified

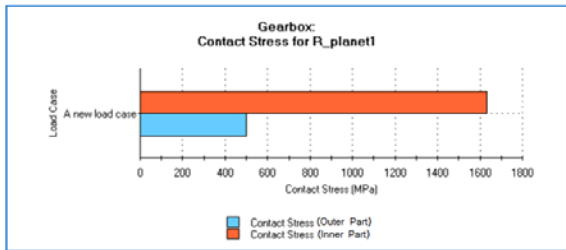


(a)

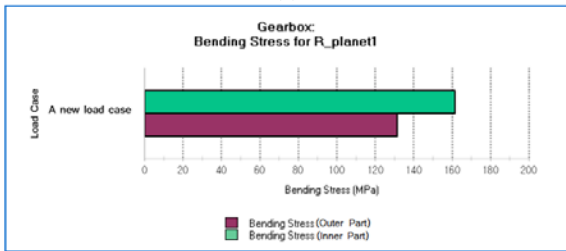


(b)

Fig. 7 Stress of the sun gear for the modified model
 (a) contact stress : 1630.2 MPa
 (b) bending stress : 212.8 MPa



(a)



(b)

Fig. 8 Stress of the planetary gear for the modified model
 (a) contact stress : 1630.2 MPa
 (b) bending stress : 161.5 MPa

Table 4 The results of safety factor

	SCM420H		SCM822H		Modified model with SCM420H	
	contact	bending	contact	bending	contact	bending
Sun gear	0.995	2.038	1.012	2.038	1.058	2.304

Planetary gear	1.069	1.959	1.087	1.959	1.136	2.214
----------------	-------	-------	-------	-------	-------	-------

Table 5 Contact life cycle of gears

	SCM 420H	SCM 822H	Modified model (420H)
Sun gear	456 h / Fail	1240 h / Pass	1360 h / Pass
Planetary gear	3284 h / Pass	4464 h / Pass	9796 h / Pass

model arranged in Table 4.

According to the result of the strength analysis, in the case of applying SCM420H properties, safety factor for contact stress at the planetary gear is more than 1.0; however, the safety factor at the sun gear is less than 1.0 as in Table 4. In the cases of applying SCM822H and the modified model, the safety factors for contact stress at the sun and planetary gear are more than 1.0. Therefore, it is possible to design gears which have high strength in cases of applying SCM822H and the modified model.

IV. DURABILITY ANALYSIS OF PLANETARY GEAR SYSTEM

A. Durability Evaluation of Gears

Durability analysis for driving over 1,000 hours is performed by the standard of RS B 0095. The results are arranged in Table 5.

As a result of the durability analysis, all cases are satisfied with the evaluation standard for a life of RS B 0095 except in the case of the sun gear where SCM420H is applied.

V. CONCLUSION

In this research, strength and durability analysis for SCM420H, SCM822H, and the modified model have been performed to analyze the durability and stability of a planetary gear system which is used in the driving system of excavators, the result of the analysis obtained by dimensional analysis. The analysis results for the three cases are compared and analyzed.

The case where SCM420H is applied as material of the gears lacks stability and durability because the safety factor for contact stress is less than 1.0.

On the other hand, if SCM822H is applied as material of gears, any problems for stability and durability will not occur because the safety factor for contact and bending stress is over 1.0. The case using the modified model is also stable and durable. Therefore, the application of SCM822H as material of the planetary gear system is appropriate to use.

ACKNOWLEDGMENT

This research was financially supported by the Ministry of Education and Korea Institute for Advancement of Technology (KIAT) through the Human Resource Training Project for Regional Innovation and is partially supported by the "Brain

Korea 21 Plus” project.

REFERENCES

- [1] I. H. An, M. J. An, Z. Xu, S. K. Lyu, “A Study on the Effect of the Honing in SCM420H Planetary Gear”, Journal of the KSMPE, Vol.10, No. 3, pp. 13-18, 2011
- [2] F. Chaari, T. Fakhfakh, and Haddar, “Dynamic Analysis of a Planetary Gear Failure Caused by Tooth Pitting and Cracking”, Journal of Failure Analysis and Prevention, Vol. 6 No. 2, pp. 73~78, 2006
- [3] Milosav Ognjanovic', Miloš Ristic', Predrag Živkovic, “Reliability for design of planetary gear drive units”, An International Journal of Theoretical and Applied Mechanics, 2013
- [4] Nicholas, P.C., Gear Design and Application, Mcgraw Hill, New York, pp.94~121.
- [5] Brownlee, K. A, Hodges, J. L, Rosenblatt. M, “Evaluation of fatigue strength”, Journal of America stat. Assn, Vol. 48, pp. 29~35, 1953
- [6] J. H. Yang, H. O. Kim, H. D. Lee, “An Experimental Study on Improvement of Contact Stress of Bevel Gear, Conference of the KSPE, pp. 873, 2011
- [7] Tesfahunegn YA, Rosa F, “The effects of the shape of tooth profile modification on the transmission error, bending, and contact stress of spur gears”, International Journal of Mechanical Engineering, Sci. 224, pp.1749–1758, 2010
- [8] Shanmugasundaram Sankar, Muthusamy Nataraj, “Profile Modification-a design approach for increasing the tooth strength in spur gear”, The International Journal of Advanced Manufacturing Technology, Vol. 55, Issue 1-4, pp. 1~10, 2011
- [9] Tea Hyoung Chong, Young Ju Kim, Seung Hyun Park, “Reliability Evaluation of Multi-Stage Gear Drive”, Transactions of the Korean Society of Machine Tool Engineers, Vol. 15 No. 2, pp. 16-23, 2006
- [10] S. G. Han, Y. I. Shin, H. C. Kim, H. C. Kim, H. C. An and C. K. Song, “ Strength Design Evaluation of the Double Planetary Gears”, Conference of the Eighth International Symposium on Mechanics, Aerospace and Informatics Engineering 2013, pp. 62-63, 2013
- [11] M. G. Kong, C. K. Song and Y. D. Kim, “Strength Design Evaluation of the Multi-range Transmission”, Journal of the KSPSE, Vol. 15, No. 3, pp. 12-17, 2013
- [12] A. Kahraman, “Load Sharing Characteristics of Planetary Transmissions,” Mech. Mach. Theory, 29, pp. 1151-65, 1994.
- [13] S, G, Lyu, and K. M. Kim, “A Study on the Bending Fatigue Strength of Sintering Spur Gear., the Korea Institute of Industrial Safety, Vol. 9, No. 3, pp. 28-33
- [14] Korea Agency for Technology and Standard, “RS B 0095”, 2005

Instability and interaction of the tourbillonner macrostructure with the boundary layer in a cavity differentially heated

^ATALOUB Djedid and ^BBEGHIDJA Abdelhadi

Abstract— The study of the interaction of boundary layer with the flow and the influence of heat exchange in cavity for strong numbers of Rayleigh $Ra=2.5 \cdot 10^{10}$ is the subject of the various numerical simulations. The resulting field velocity can be dividing up into two fields: The flow of the average field in the cavity, and the field velocity fluctuating of this flow in the cavity. The cavity is the seat of instability generating or modulating the swirling structure.

This work is in the continuity of in experiments undertaken former studies. It also fits in the more general prospect for the dynamics of the fluids, turbulence and the heat transfers. It contributes to the development of the methods allowing the comparison between the digital simulations and the experiment in the case of the turbulent flows comprising of the non stationary macrostructures. From this point of view the method of Large Eddy Simulation (known as LES) east considers beside that of RANS. Our objective consists in confronting our resulting with those from experimental on the one hand and those establish by other numerical studies. It is noted that a purely thermal approach on the fluctuations is to be developed and to treat.

Finely this work presents a numerical validation of LES-WALE model using the results of the *K-epsilon* model, this study is based on 3D numerical simulation using FLUENT code calculates to determine the longitudinal velocity, the thermal fields for the configuration the and velocity vectors (U, V, W) for configuration in the plane of the recirculation zones for the cases. Therefore, the results have good agreement with those of *k-epsilon* model, as they show the difference between the cases of flows.

Keywords— Natural convection, finite volume, parallelepiped, *k-epsilon*, LES.

I. INTRODUCTION

TO define the state of a fluid moving, four unknown functions must be given: three components of the vector velocity and pressure. These functions must be given in each point of the space field and at any moment. For that one has recourse to the Navier-Stokes equations which connect these parameters and which are deduced starting from the physical

A. Faculty of Science M'sila University y, M'sila 28000, Algeria (corresponding author to provide phone: +213779290730; fax: +21331818781; e-mail: djtaloub@yahoo.fr).

B. Mechanical department of engineering, Constantine1University,, Constantine 25000, Algeria(e-mail: abeghidja1@yahoo.fr).

A.B. Laboratory of Renewable Energy and Sustainable Development (LRESD) Constantine1University, Constantine 25000, Algeria

laws from conservation and the Newtonian laws from the movement.

So that these equations are applicable to the flows of fluid, it should be supposed that the fluid in question is a continuous medium.

The large swirling structures are very anisotropic and are conditioned inter alia by the specific geometrical configuration of the flow considered. Recently and since the means of calculation allow it, a novel method is essential more and more even in the field of the industrial applications. On the basis of noted preceding, the idea is to separate the scales from turbulence to solve numerically only the large swirling structure and to replace the effect of smallest by models under mesh. The motivation comes owing to the fact that the large structures are anisotropic and are responsible for all those mechanisms of exchange. The calculation direct as of these swirls gives to the results more credibility without making the cost very prohibitory. In addition more the small scales which are isotropic have as a main role the dissipation of energy. This characteristic makes easier the construction of a model universal to model their interaction with the calculated structures. By adopting this technique, one can only be gaining since in addition to their isotropic natures, these swirls are all the more small as the Reynolds number is high. While introducing, the model one avoids effort of calculation enormously compared to calculation DNS while keeping the deterministic aspect of the solution. This technique called Large Eddy Simulation is recognized currently more and more like a technique complementary to experimental measurements for comprehension, the prediction and it control turbulent flows. It makes it possible in particular to visualize the dynamics of the swirling structures with large scales.

This work is based on many previous studies both experimental and numerical, including Mergui [1]-[2], Salat [3]-[4] Lankhorst [5], Tian [6] Ampofo [7] examined numerically flows turbulent natural convection in a parallelepiped cavity. Many numerical investigations have also been conducted with cavities of modest size or $Ra < 10^9$ [8]-[9]. Beyond ($Ra > 10^{10}$).

We consider here a configuration of the normal convection in a fluid of cavity of parallelepiped, where a gradient in temperature is imposed between the walls.

There are examples off such applications has configuration in

the solar systems, double glazed Windows, gold the description off the air flow within has room.

The aim of this work is to compare the results of fluent code to those proposed references.

A. Description of the problem

The physical model considered is schematized on the fig. 1. It is about a three-dimensional parallelepiped cavity of great dimension ($H=2.46$ m height, $L= 0.385$ m of width, $D=0.72$ m of depth), filled of air, whose walls are differential heated at a constant temperature according to table 1. We study eight different configurations. The flow in this cavity is turbulent with a number $Ra = 2.5 \cdot 10^{10}$.

T_c : wall heat
 T_f : wall cold
 L_D : side wall right
 L_G : side wall left
 P_d : ceiling
 P_c : floor

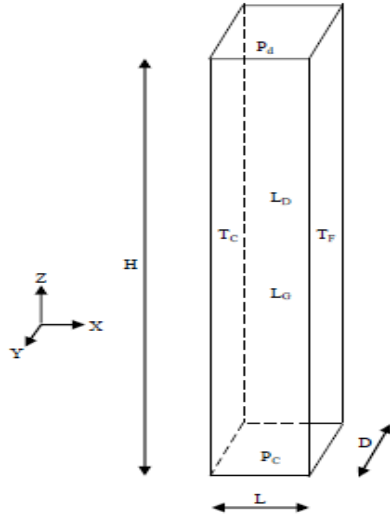


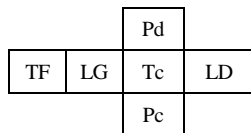
Fig. 1 Geometric configuration of the 3D model

Table 1. Various studied configurations and their mode of representation

Configurations	C1	C2	C3	C4
	F	F	C	F
modes	F C C C	F F C F	F C C C	F M C M
	C	C	C	F

C5	C6	C7	C8
F	C	C	F
F F C F	F C C C	F M C M	F F C F
F	F	TF	TF

C : hot
 F : cold
 M : middle
 TF : very cold



B. Simplifying assumptions

In order to obtain a simple mathematical model, one adopts the following assumptions:

- The flow is three-dimensional
- The fluid is Newtonian and incompressible
- The generated flow is turbulent
- the transfer of heat per radiation is negligible
- The physical properties of the fluid are constant except the density which obeys the approximation of Boussinesq in the term of pushed of Archimedes.

II. NUMERICAL SIMULATION OF TURBULENCE

Numerical simulation of turbulent and concepts related to the turbulence and that can provide adapted and effective modeling flows. We introduced the same equations governing our flows through this article and after posing problems of closing LES.

A. Basic Equations

The equations of evolution are used to describe the flow of an incompressible fluid in its movement. firstly reflects the conservation of mass locally, the other is conservation of movement quantity, and the third equation takes to reflect the heat transfer in the case of isothermal flow: energy equation.

The forms of these equations are different depending on the assumptions about the type of flow and fluid considered. In this study, we assume an incompressible fluid with constant thermodynamic properties ($\mu = \text{const}$, $\rho = \text{constant}$, $\lambda = \text{constant}$, $C_p = \text{constant}$).

By applying a low-pass filter to results equations and the above assumptions, the system of equations to be solved in a filtered LES approach [10] we obtain:

$$\frac{\partial \bar{u}_i}{\partial x_i} = 0 \quad (1)$$

$$\frac{\partial \bar{u}_i}{\partial t} + \frac{\partial}{\partial x_j} (\overline{u_j u_i}) = -\frac{1}{\rho} \frac{\partial \bar{p}}{\partial x_i} + \frac{\partial}{\partial x_j} (2\nu \bar{S}_{ij} + \tau_{ij}) \quad (2)$$

$$\frac{\partial \bar{T}}{\partial t} + \frac{\partial}{\partial x_j} (\overline{u_j T}) = \frac{\partial}{\partial x_j} \left(\alpha_f \frac{\partial \bar{T}}{\partial x_j} + \Theta_i \right) \quad (3)$$

\bar{S}_{ij} : Corresponds to the rate tensor of resolved deformation given by:

$$\bar{S}_{ij} = \frac{1}{2} \left(\frac{\partial \bar{u}_i}{\partial x_j} + \frac{\partial \bar{u}_j}{\partial x_i} \right) \quad (4)$$

The new terms $\bar{\tau}_{ij}$ and $\bar{\Theta}_i$ from the filter respectively represent the tensor sub-mesh stress (or Reynolds stress) and heat flux sub-mesh and are defined by:

$$\bar{\tau}_{ij} = \overline{u_i u_j} - \bar{u}_i \bar{u}_j \quad (5)$$

$$\bar{\Theta}_i = \overline{T u_i} - \bar{T} \bar{u}_i \quad (6)$$

Modeling constraints sub-mesh $\bar{\tau}_{ij}$ is based on an assumption of sub-mesh viscosity (Boussinesq hypothesis) linking constraints in the mesh deformation rate tensor resolved \bar{S}_{ij} [10]:

$$\overline{\tau_{ij}} - \frac{1}{3} \delta_{ij} \overline{\tau_{kk}} = 2\nu_t \overline{S_{ij}} \quad (7)$$

“Eq. (2)” can be written as:

$$\frac{\partial u_i}{\partial t} + \frac{\partial}{\partial x_j} (\overline{u_j u_i}) = -\frac{1}{\rho} \frac{\partial p}{\partial x_i} + \frac{\partial}{\partial x_j} (2(\nu + \nu_t) \overline{S_{ij}}) \quad (8)$$

The Smagorinsky model is based on an assumption of mixing length in which it is considered that the viscosity is proportional to the mesh length scale (here associated with the filtering equations, namely the characteristic mesh size) denoted Δ and a velocity scale determined by the product $\Delta \|\overline{s}\|$, where $\|\overline{s}\|$ is the norm of the strain rate defined tensor and resolved by Ref. [10]:

$$\|\overline{s}\| = \sqrt{2\overline{S_{ij}S_{ij}}} \quad (9)$$

Finally, writing the Smagorinsky model is as follows:

$$\nu_t = (C_s)^2 \|\overline{s}\| \quad (10)$$

The constant C_s is determined from the assumption of local equilibrium between production and dissipation of turbulent kinetic energy.

B. Numerical Schemes

We use the following calculation:

- The power-law schema: this one is best placed to capture the physical phenomena of heat transfer;
- The discretization scheme of pressure velocity coupling is SIMPLE;
- The convergence criterion used is the under-relaxation.

C. Mesh

The influence of the size and the number of the nodes on the solution expressed by the heat transfer to the “heated” active part is illustrated by the temperature, for the configuration 1 in the plan medium by Fig. 2.

An irregular distribution “geometrical continuation” of the nodes is used to solve more precisely the physical phenomena present in particular in mode of boundary layer characterized by the existence of strong gradients in the parietal zones. Profiles vertical velocity becomes insensitive with the number of nodes starting from the grid $150 \times 75 \times 75$.

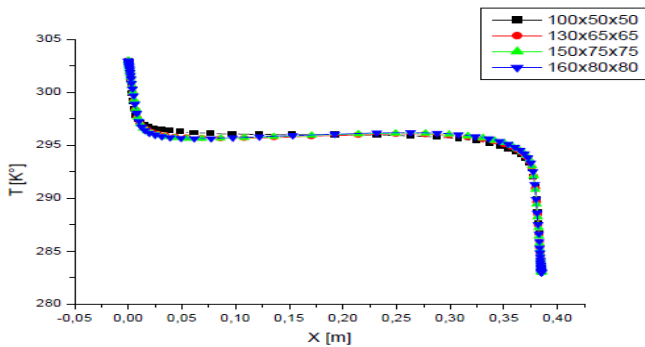


Fig. 2. Convergence of the profile of temperature for C1 in the $y=D/2=0.36m$ plan and $z=H/2=1.23m$.

D. Validation

In order to verify the accuracy of the numerical results obtained in the present work, a validation of the numerical code was made taking into account some numerical studies available in the literature. Ampofo results [11] obtained in the case of a square cavity containing air, were used to test our simulation by Fluent. The comparison was made by considering the Rayleigh number 1.58×10^9 . Comparison of velocity profiles along the plane medium shows excellent agreement.

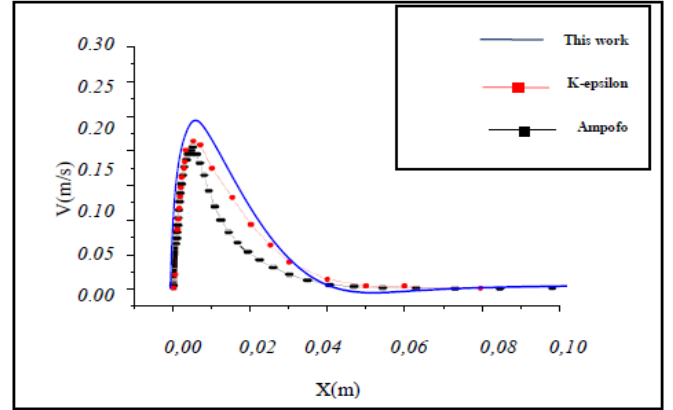


Fig. 3 Comparison of velocity profile V along the $y = 0.36m$ for the configuration C1.

III. RESULTS AND DISCUSSION

The results are represented in this work for a number of Rayleigh fixed at $2,5 \cdot 10^{10}$ and the variation in temperature $\Delta T = 20^\circ C$, we go fixed the number of Prandtl $Pr = 0,71$.

The thermal fields are represented in fig. 4 for various configurations as represented in Table. 1

The recovered heat of the hot wall is transported by convection towards the cold wall and upwards, it is what explains the relatively high temperature near to the ceiling. One can notice that the temperature of the air raised in the case of the two hot side walls (configuration C1, C3 and C6), whereas in the other configurations the temperature of the air is less hot, and one notices the presence of the effect of the gradient in vertical temperature expressed by the push of Archimedes in the phenomenon of convection. Indeed the effect of the configuration C1 and C2 tends to amplify the transfer on revenge in the configurations C6, C7 and C8 it is less present.

Fig. 9 represents the profiles of temperature in the plan medium and for a height equalizes $1,23m$, we notice that each configuration at a temperature means of the air in the heart of the cavity.

One can notice the thermal boundary layer near to the hot and cold wall with a thermal thickness of boundary layer approximately $0,02m$.

The velocity vectors are represented in fig. 5. The flow is mono cellular to priority with the ascending fluid along the hot wall and goes down along the cold wall. However one notes a disturbance as well as the appearance of several zones of

recirculation indicating a greater complexity and a higher degree of turbulence.

In fig. 6 we represent the field vertical velocity we clearly observe the rise of the fluid near to the hot wall and descend it near to the cold wall.

Fig. 7 presents the horizontal field velocity we observe near to the floor, the fluid flow of the cold wall towards the hot wall on the other hand near to the floor it is the reverse. The flow is mono cellular, as it appears in fig. 5 in addition it comprises first dominant swirling structure, located at a height varying from one configuration to another.

For fig. 8 we represent the profile vertical velocity. In this graph one can see the dynamic boundary layer near to the wall hot and cold, the thickness of this layer is equal approximately $0,1m$.

In this study one saw the influence of the walls (the temperature imposed on each walls table. 1) on the flows for various configurations with high number of Rayleigh, thereafter. We established initially, the phenomenon of interaction of the swirling structures of the flow with the boundary layer.

We notice the effects on the profiles of temperature given in fig. 9 and those velocities fig. 8.

It appears clearly for certain configurations C1, C3 and C6, a strong imbalance of the stratification (not perfectly horizontal).

With the same height $Z = H/2 = 1,23m$ the side faces has a direct influence on the velocity vector respectively with dimensions heat C2 and with dimensions cold C1 and intensity velocity $0,2m/s$ and $0,3m/s$ (see fig. 6 C1 and C2).

In fig. 5, we note the appearance of the nodes of recirculation, which one could allot to zones and places of interaction swirling structure/boundary layer.

Indeed, it is possible that it is the place also of release of turbulence.

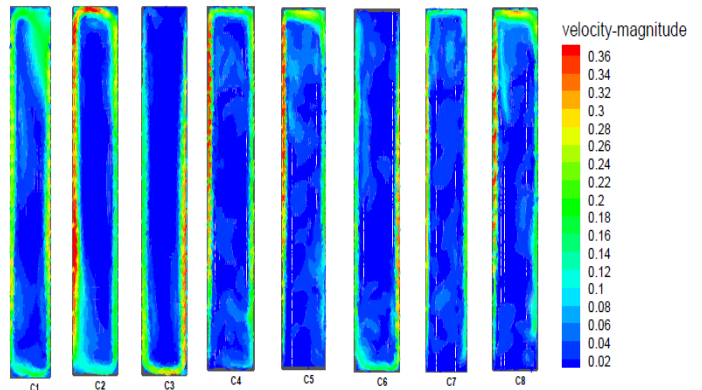


Fig. 5 Velocity vectors (U-W) for the eight configurations in the $y=D/2=0.36m$ plan.

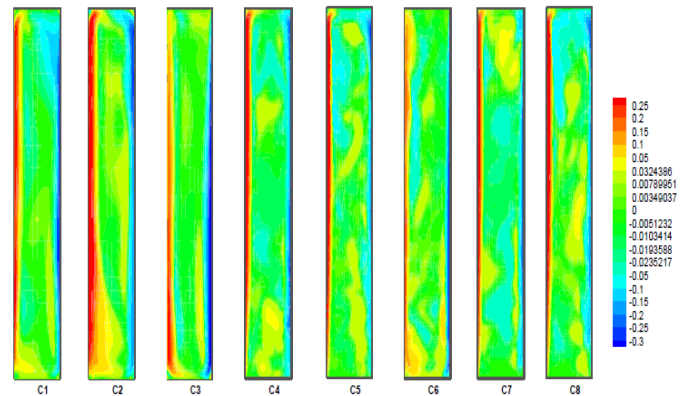


Fig. 6 Fields velocity vertical for the eight configurations in the $y=D/2=0.36m$ plan.

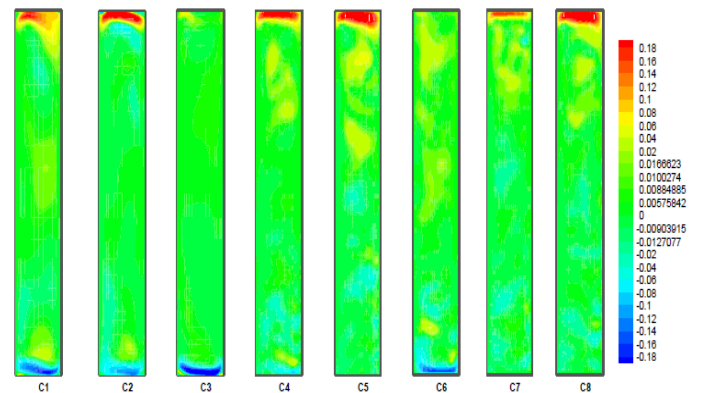


Fig. 7 Fields horizontal velocity for the eight configurations in the plan $y=D/2=0.36m$

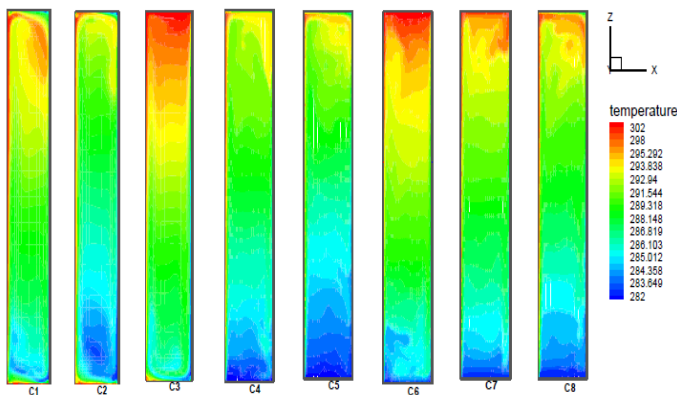


Fig. 4 Thermal fields for the eight configurations in the $y=D/2=0.36m$ plan

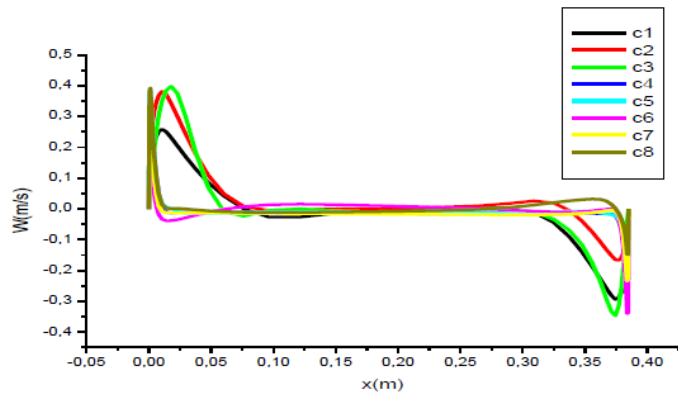


Fig. 8 Profile vertical velocity for the eight configurations in the $y=D/2=0.36\text{m}$ plan and $z=H/2=1.23\text{m}$.

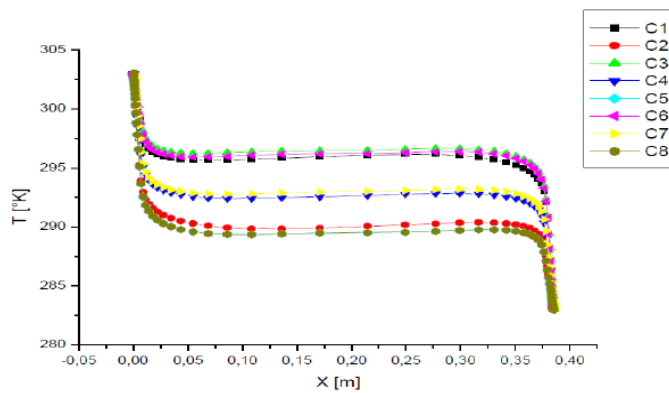


Fig. 9 Profile of temperature for the eight configurations in the $y=D/2=0.36\text{m}$ plan and $z=H/2=1.23\text{m}$.

IV. CONCLUSION

In conclusion, we can confirm through this study the direct influence of side walls on the nature of the air flow in cavity. This influence results in the stratification of the mass of air which changes according to the configurations i.e. boundary conditions. Of other by, we highlighted the influence of number of Rayleigh thus of the ΔT (since the characteristics of the fluid remain unchanged), on the phenomena of convection and consequently on the zone of release of turbulent instability.

Taking into account the coherence of our results with those established numerically and in experiments, by others we succeeded in validating code Fluent the computer for the configurations studied with LES, and finished volumes.

REFERENCES

[1] S. Mergui, F. Penot, Analyzes speeds and temperature of the air in natural convection in a cavity differentially heated with $Ra=1.69 \cdot 10^9$, *Int. J. Heat Mass Transfer* 40 (14) (1991) 3427-3441.
 [2] S. Mergui, Experimental characterization of the flows of air of natural and mixed convection in a closed cavity, Thesis Doctorate, University of Poitiers 1993.
 [3] J. Salat, F. Penot, Experimental approach of the natural convection of turbulent transition in a cubic cavity differentially heated VI Inter-

University conference Frensh-Quebec Thermics of the Systems, (26-28 mai 2003, Quebec).

[4] J. Salat, Contribution to the study of the three-dimensional natural convection in cavity differentially heated. Thesis of Doctorate of the Poitiers University, 2004.
 [5] A.M. Lankhorst, D. Angirasa, C.J. Hoogendoorn, LDV measurements of buoyancy induced flows in an enclosure at high Rayleigh numbers, *Exp. Thermal and Fluid Science* 6 (1993) 74-79.
 [6] Y.S. Tian, T.G. Karayiannis, Low turbulence natural convection in an air filled square cavity: Part 1. The Thermal and Fluid Flow Fields, *IJHMT* 43 (2000) 849-866.
 [7] F. Ampofo, T.G. Karayiannis, Experimental benchmark data for turbulent natural convection in an air filled square cavity, *IJHMT* 46 (19) (2003) 3551-3572.
 [8] G. De Vahl Davis, Laminar natural convection in an enclosed rectangular cavity, *In. J. Heat and Mass Transfer* 11 (1968) 675-1693.
 [9] S. Xin, P. Le Quéré, Direct numerical simulation of two dimensional chaotic natural convection in a differentially heated cavity of aspect ratio 4, *J. Fluid Mech.* 304 (1995) 87-118.
 [10] A. Chatelan, Large eddy Simulation of the turbulent flows with heat transfers, Thesis Doctorate prepared at the Laboratory of Modeling and Development of Software (CEA Grenoble).
 [11] F. Ampofo, Turbulent natural convection of air in a non-partitioned or partitioned cavity with differentially heated vertical and conducting horizontal walls, *Exp. Thermal and Fluid Science* 29 (2005) 137-157.
 [12] F.X. Trias, A. Gorobets, M. Soria, A. Oliva D. Direct numerical simulation of a differentially heated cavity of aspect ratio 4 with Rayleigh numbers up to 1011: Part I. Numerical methods and time-averaged flow, *Int. J. Heat and Mass Transfer* 53 (2010) 665-673.
 [13] P.L. Betts, A.A. Dafa'Alla, Turbulent buoyant air flow in a tall rectangular cavity, UMIST?, Manchester, England.
 [14] A. Dafa'Alla, P. Betts, Experimental study of turbulent natural convection in a tall air cavity, *Exp. Heat Transfer* 9 (1996) 165-194.
 [15] A. Beghidja, Dj. Taloub, Effect of Rayleigh number on the turbulent structures with boundary layer in a differentially heated, *In. J. Mechanics and Energy (IJME)* Vol. 1, Issue 2, 2013, ISSN: 2286-5845
 [16] A. Beghidja, M. Bouafia, J.J. Vullierme, F. Yguel, A. Zammit, Modeling of the exchanges convective on the front verticals of cavities to great numbers of Rayleigh, *General review of thermics* Tom 34 (405) (1995) 515-526..
 [17] F. Ampofo, Turbulent natural convection of air in a non-partitioned or partitioned cavity with differentially heated vertical and conducting horizontal walls, *Exp. Thermal and Fluid Science* 29 (2005) 137-157.

On spectral relaxation method for an MHD flow and heat transfer of a Maxwell fluid

Stanford Shateyi, University of Venda, South Africa

Abstract—The present study investigates magnetohydrodynamic flow and heat transfer of a Maxwell fluid using a spectral relaxation method. The method is based on simple iteration schemes formed by reduction of the order of the momentum equation followed by a rearrangement of the resulting governing nonlinear equation systems which are then solved using spectral methods. The effect of the flow parameters on the velocity and temperature of the flow were investigated. The results were validated using the `bvp4c` where the spectral relaxation method was found to be accurate and rapidly convergent to the numerical results.

Keywords—MHD flow, Maxwell fluid, spectral relaxation method, spectral method

I. INTRODUCTION

The study of non-Newtonian fluid flows over a stretching sheet find applications in numerous manufacturing processes. These include wire and fibre coating, extrusion of molten polymers through a slit die for the production of plastic sheets, and foodstuff processing amongst others. In a characteristic sheet production process, the extrudate starts to solidify as soon as it exits from the die. The quality of the final product depends on the rate of heat transfer and hence the need for the cooling process to be controlled effectively (Motsa et al. 2012 ; Mukhopadhyay 2012).

Non-Newtonian fluids are mainly classified into three types namely differential, rate and integral Hayat et al (2012). The Maxwell model is the simplest subclass of the rate type fluids. This fluid model has become the most popular as it can predict stress relaxation and also excludes the complicating effects of shear-dependent viscosity, Mukhopadhyay and Gorla 2012. In view of the Maxwell model, several researchers have analyzed the MHD flow of a Maxwell fluid under various aspects of rotation, thermal radiation, heat and mass transfer, chemical reaction, suction/injection, thermophoresis and heat source/sink (Bataller 2011; Zheng et al. 2013; Noor 2012; Vajravelu 2012).

S. Shateyi is with the Department of Mathematics and Applied Mathematics, University of Venda, , X5050, 0950 South Africa e-mail: stanford.shateyi@univen.ac.za.

Manuscript received December, 2013

In this study we aim at investigating magnetohydrodynamic flow and heat transfer of a Maxwell fluid over a stretching sheet in a Darcian porous medium. The study will be carried out using the spectral relaxation method. It is a newly proposed numerical scheme used to solve nonlinear systems of boundary value problems. It is based on simple iteration schemes formed by reduction of the order of the momentum equation followed by a rearrangement of the resulting governing nonlinear equation systems which are then solved using the Chebyshev spectral collocation method Motsa and Makukula (2013) and Shateyi and Makinde (2013).

II. PROBLEM FORMULATION

We consider a steady MHD flow of a Maxwell fluid over stretching sheet in a Darcian porous medium. A uniform magnetic field B_0 is applied normal to the flow direction and there is no applied electric field. The boundary layer approximations for the flow under consideration are

$$\frac{\partial u}{\partial x} + \frac{\partial v}{\partial y} = 0, \quad (1)$$

$$u \frac{\partial u}{\partial x} + v \frac{\partial u}{\partial y} + \lambda_1 \left[u^2 \frac{\partial^2 u}{\partial x^2} + v^2 \frac{\partial^2 u}{\partial y^2} + 2uv \frac{\partial^2 u}{\partial x \partial y} \right] = \nu \frac{\partial^2 u}{\partial y^2} - \frac{\sigma B_0^2}{\rho} \left(u + \lambda_1 v \frac{\partial u}{\partial y} \right) - \frac{\nu}{K} u, \quad (2)$$

$$u \frac{\partial T}{\partial x} + v \frac{\partial T}{\partial y} - \frac{\sigma B_0^2}{\rho c_p} u^2 = \frac{k}{\rho c_p} \frac{\partial^2 T}{\partial y^2} + \frac{\mu}{\rho c_p} \left(\frac{\partial u}{\partial y} \right)^2 + \frac{Q}{\rho c_p} (T - T_\infty). \quad (3)$$

The suitable boundary conditions are

$$u = u_0(x) = \lambda x, \quad v = 0, \quad T = T_w(x) = \frac{Ax^2}{l^2} + T_\infty \quad \text{at } y = 0, \quad (4)$$

$$u \rightarrow 0, \quad \frac{\partial u}{\partial y} \rightarrow 0 \quad T \rightarrow T_\infty, \quad \text{as } y \rightarrow \infty, \quad (5)$$

A. Similarity transformation

The governing equations (2) - (5) can be transformed to a set of nonlinear ordinary differential equations by

introducing the following non-dimensional variables:

$$\eta = \sqrt{\frac{\lambda}{\nu}} y, \quad \psi = \sqrt{\lambda \nu x} f(\eta), \quad \theta(\eta) = \frac{T - T_\infty}{T_w - T_\infty}, \quad (6)$$

where ψ is the stream function that satisfies the continuity equation (1) with

$$u = \frac{\partial \psi}{\partial y} = \lambda x f'(\eta), \quad v = -\frac{\partial \psi}{\partial x} = \sqrt{\lambda \nu} f(\eta) \quad (7)$$

Using equations (6) and (7) in the governing equations we obtain the following set of non-linear ordinary differential equations.

$$f'''' + (1 + MDe)ff'' - (f')^2 - (\gamma + M)f' + De(2ff'f'' - f^2f''') = 0, \quad (8)$$

$$\frac{1}{Pr}\theta'' + f\theta' + (\Lambda - 2f')\theta + Ec[M(f')^2 + (f'')^2] = 0, \quad (9)$$

where $De = \lambda_1 \lambda$ is the Deborah number, $M = \frac{\sigma B_0^2}{\lambda \rho}$ is the magnetic parameter, $\gamma = \frac{\nu}{\lambda K}$ is the porosity parameter, $\Lambda = \frac{Q}{\lambda \rho c_p}$ is the heat source/sink parameter, $Pr = \frac{\rho c_p}{k}$ is the Prandtl number, $Ec = \frac{\lambda}{c_p A}$ is the Eckert number.

The boundary conditions become:

$$f = 0, \quad f' = 1, \quad \theta = 1, \quad \text{at } \eta = 0, \quad (10)$$

$$f' \rightarrow 0, \quad \theta \rightarrow 0, \quad \text{as } \eta \rightarrow \infty. \quad (11)$$

III. METHOD OF SOLUTION

In this section we present the development of the spectral relaxation method (SRM) for the solution of the governing equations and its implementation on the governing equations (8 - 9). Before applying the SRM, it is convenient to reduce the order of the momentum equation by introducing the transformation $f'(\eta) = g(\eta)$. The transformed equations become

$$g'' + (1 + MDe)fg' - g^2 + De(2fgg' - f^2g'') - (\gamma + M)g = 0 \quad (12)$$

$$f' = g, \quad (13)$$

$$\frac{1}{Pr}\theta'' + f\theta' - 2g\theta + \Omega\theta + Ec[Mg^2 + (g')^2] = 0, \quad (14)$$

and the boundary conditions are

$$f = 0; \quad g = 1; \quad \theta = 1; \quad \text{at } \eta = 0, \quad (15)$$

$$g \rightarrow 0; \quad \theta \rightarrow 0 \quad \text{as } \eta \rightarrow \infty \quad (16)$$

To develop the SRM algorithm, we consider equations (12 - 14) in the order in which they are listed and label them as equations for g , f and θ respectively. The labelling strategy is guided by the highest order derivatives in each particular equation. In the equations for g , at a particular iteration level (denoted by $r + 1$), the functions f and θ are assumed to be known from the previous iteration level (denoted by r). It is also assumed that all nonlinear terms in g are evaluated at the previous iteration. In addition, it is also assumed that all derivative terms in g which appear as factors of g are to be evaluated at the previous iteration. The equation for g is then solved to obtain an updated solution g_{r+1} which is then used in the next equation. The resulting iteration algorithm can be expressed as follows:

$$(1 - De f_r^2)g_{r+1}'' + (1 + MDe)f_r g_{r+1}' + 2De f_r g_r' g_{r+1} - (\gamma + M)g_{r+1} = g_r^2, \quad (17)$$

$$f_{r+1}' = g_{r+1}, \quad (18)$$

$$\frac{1}{Pr}\theta_{r+1}'' + f_{r+1}\theta_{r+1}' + (\Omega - 2g_{r+1})\theta_{r+1} - Ec[Mg_{r+1}^2 + (g_{r+1}')^2] = 0. \quad (19)$$

The boundary conditions are the same as (15) and (16) but are now evaluated at the current iteration ($r+1$).

The equations for the algorithm (17 - 19) form a system of decoupled linear differential equations with variable coefficients which can be solved using standard numerical methods for solving differential equations. In this work, we use the Chebyshev spectral collocation method. It is for this reason that the solution method is referred to as the *spectral relaxation method*. For brevity, we omit the details of the spectral methods, and refer interested readers to (Canuto 1988; Fornberg 1996; Trefethen 2000).

IV. RESULTS AND DISCUSSION

The magnetohydrodynamic flow and heat transfer in a Maxwell fluid over a stretching sheet in a porous medium has been solved numerically using a spectral relaxation method (SRM). The results are displayed in this section showing a comparison between the SRM solutions with those generated using the `bvp4c` and effects of selected flow parameters on the velocity and temperature. The comparison was made to validate the accuracy of the SRM solutions. The `bvp4c` is an in-built MATLAB solver for boundary value problems based on the fourth order Runge-Kutta schemes. The tolerance level for both methods was set to be 10^{-10} . The figures were generated using $N = 100$ and $\eta_\infty = 20$ unless specified.

A plot of the error of the norm against the number of

iterations has been used in Figure 1 to illustrate how the SRM error reduces with increased number of iterations. The plot has been generated for different values of the magnetic parameter. A steep decrease of the error is being observed for all values of M . The decrease in the error is an indication that the method is convergent and gives stable solutions. The convergence rate is taken to be the number of iterations the solution takes to reach a specified accuracy level. For example, in the figure it shows that when $M = 4$ the solution will converge after fourteen iterations for the given accuracy level compared to sixteen when $M = 2$. In Table I is a

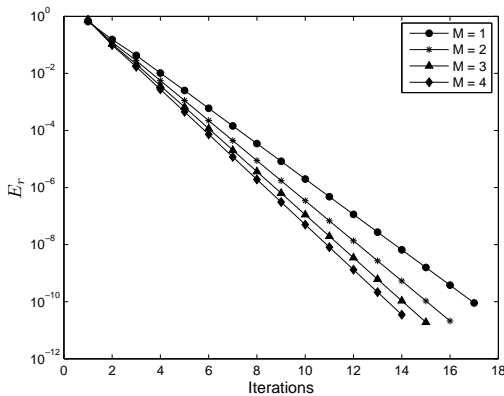


Fig. 1. The SRM error curve illustrating the convergence criteria of the method.

TABLE I
COMPARISON OF SRM SOLUTIONS FOR $-f''(0)$ AGAINST THOSE OF THE **bvp4c** FOR DIFFERENT VALUES OF M , De AND γ WHEN $N = 60$ OBTAINED AT DIFFERENT VALUES OF η_∞ .

M	De	γ	Basic SRM		SRM with SOR (ω)		bvp4c
			iter.	ω	iter.	$-f''(0)$	
1	1	1	18	0.90	12	1.96971626	1.96971626
2	1	1	17	0.90	12	2.28778217	2.28778217
3	1	1	16	0.95	10	2.56666187	2.56666187
1	0.5	1	17	0.90	12	1.85307105	1.85307105
1	1	1	18	0.90	12	1.96971626	1.96971626
1	2	1	22	0.95	17	2.18931579	2.18931579
1	1	0.5	21	0.90	12	1.84034071	1.84034071
1	1	1	18	0.90	12	1.96971626	1.96971626
1	1	2	16	0.95	11	2.20681301	2.20681301

comparison of the SRM solutions of the shear stress $-f''(0)$ against those of the **bvp4c** generated at selected values of the magnetic parameter, the Deborah number and the porosity parameter. The Table also displays the advantage of accelerating the convergence rate. An improvement in the convergence rate is observed for all cases. The effect of the magnetic parameter, Deborah

number and porosity parameter is to increase the shear stress. A very good agreement between the two solutions for up to eight decimal places is being observed. The heat transfer rate $-\theta'(0)$ for selected values of the Prandtl number, Eckert number and the magnetic parameter is shown in Table II. The comparison between the SRM and **bvp4c** results shows a very good agreement for up to eight decimal places. Heat transfer rate increases with increase in Pr while decreases with increase in Ec and M . In the Table the advantage of accelerating the convergence is again shown. The convergence rates improve for all cases with relaxation.

TABLE II
COMPARISON OF SRM SOLUTIONS FOR $-\theta'(0)$ AGAINST THOSE OF THE **bvp4c** FOR DIFFERENT VALUES OF Pr , Ec AND M WHEN $N = 60$ OBTAINED AT DIFFERENT VALUES OF η_∞ .

Pr	Ec	M	Basic SRM		SRM with SOR (ω)		bvp4c
			iter.	ω	iter.	$-\theta'(0)$	
3	0.2	1	18	0.90	12	2.09594309	2.09594309
5	0.2	1	18	0.90	12	2.72342818	2.72342818
7	0.2	1	18	0.90	12	3.21999625	3.21999625
5	0.5	1	18	0.90	12	1.59114632	1.59114632
5	1	1	18	0.90	12	-0.29599013	-0.29599013
5	1.5	1	18	0.90	12	-2.18312657	-2.18312657
5	0.2	1	18	0.90	12	2.72342818	2.72342818
5	0.2	2	17	0.90	12	2.38301961	2.38301961
5	0.2	3	16	0.95	10	2.08191143	2.08191143

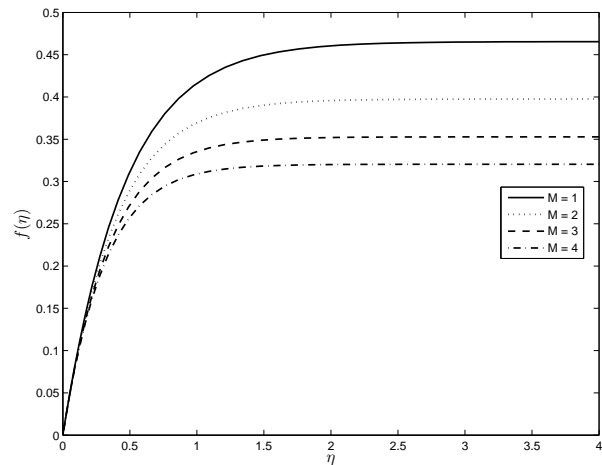


Fig. 2. Effect of the magnetic parameter on the transverse velocity ($De = 1$ and $\gamma = 1$).

The variation of the transverse velocity $f(\eta)$ for different values of the magnetic parameter M is shown in Fig. 2. For any M , $f(\eta)$ increases with η asymptotically. Applying a magnetic field decreases the momentum boundary layer thickness and increase the power required

to stretch the sheet. This in turn decreases $f(\eta)$ with increase in the magnetic parameter. While $f(\eta)$ increases asymptotically with η , the longitudinal velocity, $f'(\eta)$ is seen to decrease with η in Fig. 3. For the same justification as in Fig. 2 the longitudinal velocity is seen to decrease with increase in the magnetic parameter. In

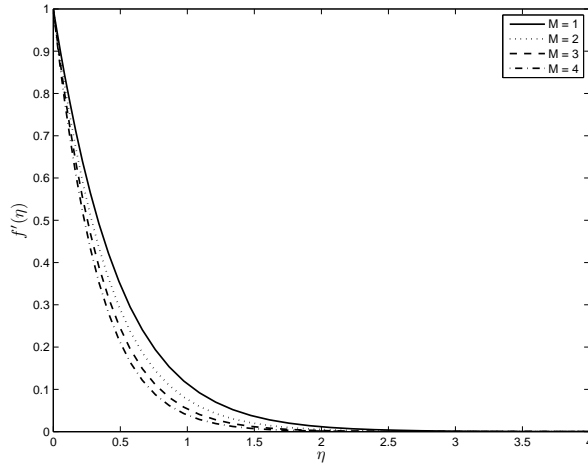


Fig. 3. Effect of the magnetic parameter on the longitudinal velocity ($De = 1$ and $\gamma = 1$).

Fig. 4 the longitudinal velocity $f'(\eta)$ is seen to also decrease with increase in the Deborah number.

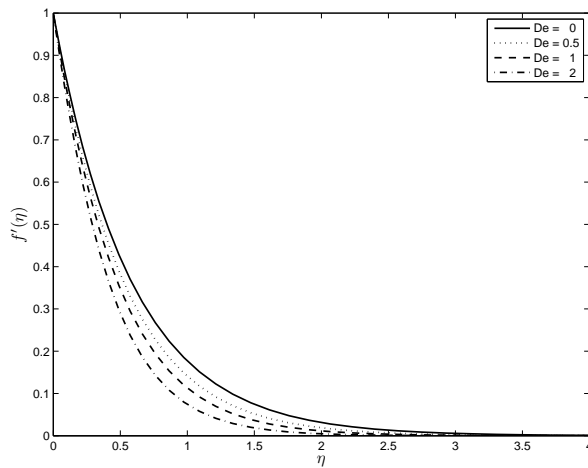


Fig. 4. Effect of the Deborah number on the longitudinal velocity ($M = 1$ and $\gamma = 1$).

In Fig. 5 is the effect of the porosity parameter on the velocity of the flow. Increasing the porosity of the surface tends to decrease the velocity of the flow.

The temperature profiles for different values of the magnetic parameter are shown in Fig. 6. Thermal bound-

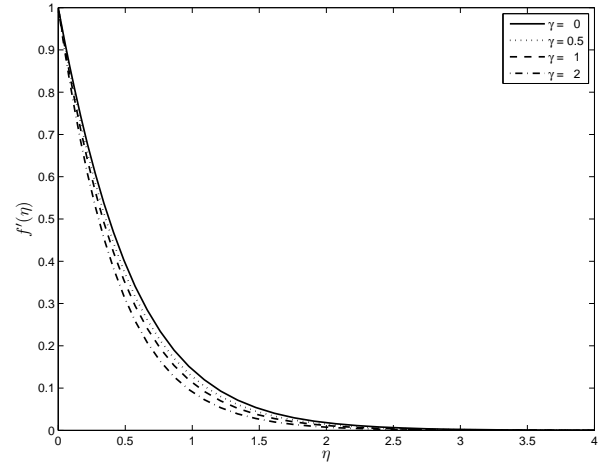


Fig. 5. Effect of the porosity parameter on the longitudinal velocity ($M = 1$ and $De = 1$).

ary layer increases in the presence of a magnetic field, thus increasing the magnetic parameter results in an increase of the temperature.

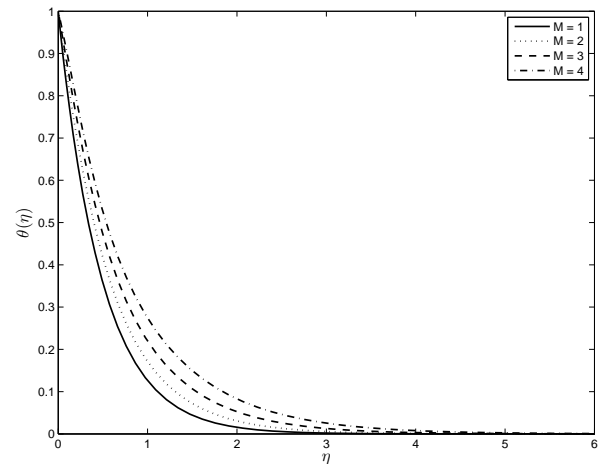


Fig. 6. Effect of the magnetic parameter on the temperature ($Ec = 0.2$, $Pr = 3$, $\Lambda = 0.1$).

Figure 7 shows the effect of the Eckert number on the temperature profile. High Ec numbers implies high heat levels produced by friction hence increased temperatures on the system.

V. CONCLUSION

A spectral relaxation method (SRM) has been successfully used to solve numerically the magnetohydrodynamic flow and heat transfer in a Maxwell fluid over a

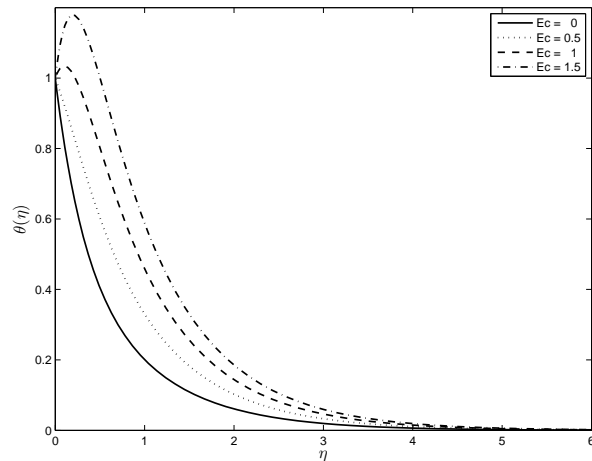


Fig. 7. Effect of the Eckert number on the temperature ($Pr = 3$, $M = 1$, $\Lambda = 0.1$).

stretching surface in a porous medium. The entropy generation number was computed using numeric expressions of the velocity and temperature. Discussed was the effect of the Deborah number, the magnetic parameter and the porosity parameter on the velocity of the flow and that of the Prandtl number, Eckert number, magnetic parameter and heat source/sink parameter on the temperature of the flow. It was found that velocities depend strongly on the magnetic and the viscoelastic parameters while the temperature varied significantly with the Prandtl number, the magnetic parameter, the Eckert number and the heat source parameter. The spectral relaxation method was found to be accurate and rapidly convergent to the numerical results.

ACKNOWLEDGMENT

The author would like to thank the University of Venda for financial support.

REFERENCES

- [1] Motsa, S. S., Hayat, T., and O. M. Aldossary, MHD flow of upper-convected Maxwell fluid over porous stretching sheet using successive Taylor series linearization method, *Appl. Math. Mech. -Engl. Ed.*, vol. 33, no. 8, pp. 975–990, 2012.
- [2] Mukhopadhyay, S., Heat transfer analysis of the unsteady flow of a Maxwell fluid over a stretching surface in the presence of a heat source/sink, *CHIN. PHYS. LETT.*, vol. 29, no. 5 pp. 054703, 2012.
- [3] Hayat T, M. Farooq, Z. Iqbal and A. Alsaedi, Mixed convection Falkner-Skan flow of a Maxwell fluid, *Journal of Heat Transfer*, vol. 134, pp.114504, 2012.
- [4] Mukhopadhyay S. and R. S. R. Gorla, Unsteady MHD boundary layer flow of an upper convected Maxwell fluid past a stretching sheet with first order constructive/destructive chemical reaction, *Journal of Naval Architecture and Marine Engineering*, vol. 9, pp. 123–133, 2012.

- [5] Bataller, R. C. Magnetohydrodynamic flow and heat transfer of an upper-convected Maxwell fluid due to a stretching sheet, *FDMP*, vol.7, no.2, pp.153–173, 2011.
- [6] Zheng, L., Liu, L., and Zhang, X., Maxwell fluids unsteady mixed flow and radiation heat transfer over a stretching permeable plate with boundary slip and nonuniform heat source/sink, *Journal of Heat Transfer*, vol. 135, pp. 031705, 2013.
- [7] Noor, N. F. M., Analysis for MHD flow of a Maxwell fluid past a vertical stretching sheet in the presence of thermophoresis and chemical reaction, *World Academy of Science, Engineering and Technology*, vol. 64, pp. 1019–1023, 2012.
- [8] Vajravelu, K., Prasad, K. V., Sujatha, A., and C.-O. NG, MHD flow and mass transfer of chemically reactive upper convected Maxwell fluid past porous surface, *Appl. Math. Mech. -Engl. Ed.*, vol. 33, no. 7, pp. 899–910, 2012.
- [9] Motsa S.S., Khan Y., Shateyi S., A New Numerical Solution of Maxwell Fluid over a Shrinking Sheet in the Region of a Stagnation Point, *Mathematical Problems in Engineering* .Volume 2012, 1-11, doi:10.1155/2012/290615.
- [10] Nadeem, S., Hussain, M., Naz, M., MHD stagnation flow of a micropolar fluid through a porous medium. *Meccanica*, 45, (2010), 869-880.
- [11] Motsa S. S ., Dlamini P.G., M. Khumalo, Solving Hyperchaotic Systems Using the Spectral Relaxation Method, *Abstract and Applied Analysis*, Volume 2012, 1- 18, doi:10.1155/2012/203461.
- [12] Shateyi, S. and Makinde, O. D., Hydromagnetic Stagnation-Point Flow towards a Radially Stretching Convectively Heated Disk, *Mathematical Problems in Engineering*, Volume 2013, Article ID 616947, 8 pages <http://dx.doi.org/10.1155/2013/616947>.
- [13] Canuto, C., M. Y. Hussaini, A. Quarteroni, and T. A. Zang. (1988). *Spectral Methods in Fluid Dynamics*, Springer-Verlag, Berlin.
- [14] Fornberg, B., *A Practical Guide to Pseudospectral Methods*, Cambridge Univ. Press, New York, 1996. Trefethen, L. N., *Spectral Methods in MATLAB*, SIAM, 2000.
- [15] Trefethen, L. N. (2000). *Spectral Methods in MATLAB*, SIAM, Philadelphia.

Specific Heat and Volumetric Heat Capacity of Some Saudian Soils as affected by Moisture and Density

Nidal H. Abu-Hamdeh

Mechanical Engineering Department, King Abdulaziz University, Jeddah, Saudi Arabia, nabuhamdeh@kau.edu.sa

Abstract— The ability to monitor soil heat capacity is an important mean in managing the soil temperature regime, which in turn, affects its ability to store heat. The effect of water content and bulk density on the specific heat and volumetric heat capacity of two Saudian soils (sand and loam) was investigated through laboratory studies. These laboratory experiments used the calorimetric method to determine specific heat of soils. For the type of soils studied, specific heat increased with increased moisture content. Also, volumetric heat capacity increased with increased moisture content and soil density. Volumetric heat capacity ranged from 1.55 to 3.50 for loam and from 1.06 to 3.00 MJ/m³/°C for sand at moisture contents from 0 to 0.20 (kg/kg) and densities from 1200 to 1400 kg/m³. Specific heat ranged from 1140 to 2090 for loam and from 800 to 1530 J/kg/°C for sand at moisture contents from 0.01 to 0.20 (kg/kg) and soil density of 1200 kg/m³. The volumetric heat capacity and specific heat of soils observed in this study under varying moisture content and soil density were compared with independent estimates made using derived theoretical relations. The differences between the observed and predicted results were very small. Loam soil generally had higher specific heat and volumetric heat capacity than sandy soil for the same moisture content and soil density.

Keywords— *Volumetric heat capacity; specific heat; moisture; density*

I. INTRODUCTION

Since the early growth and development of a crop may be determined to a large extent by microclimate, the practical significance of knowing the soil temperature is most important as it plays a significant role in influencing soil microclimate. Changes in soil temperature are governed by its thermal properties. Heat capacity of soil is the one of these properties that controls temperature variations to a larger extent and refers to its ability to store thermal energy. This property is determined by evaluating the amount of energy required to increase the temperature of a unit mass or volume of a material by one degree. Reference [1] defines the specific heat capacity as the material property that determines the amount of energy absorbed or released, or the enthalpy change in a body before its temperature will change.

Heat transfer through geomaterials is encountered in many engineering fields dealing with high level nuclear waste isolation, energy piles, thermal ground improvement techniques, waste containment facilities, etc. ([2],[3]). In recent years, much effort has been made into developing techniques to

model heat storage and transfer through soils in order to determine their thermal properties ([4]-[8]). Predicting the transport of water, heat, and solute in soil would help manage soil and water resources in irrigated agriculture. Since the propagation and storage of heat in a soil is governed by its thermal characteristics, thermal properties are necessary for modeling the transport of heat in soil ([9],[10]). The heat capacity of a soil depends on several factors. These factors can be arranged into two broad groups, those which are inherent to the soil itself, and those which can be managed or controlled to a certain extent. Those factors or properties that are inherent to the soil include the mineralogical composition and the organic component of the soil [11]. Factors influencing soil heat capacity that can be managed externally include water content and soil density ([11]-[13]). Water content plays a major role in soil heat capacity but is the most difficult factor to manage. Soil management affects heat capacity because practices that cause soil compaction will increase the bulk density and decrease the porosity of a soil. This in turn will have a significant effect on heat capacity.

References [10] and [13] developed models that allow estimation of thermal conductivity and volumetric heat capacity of soils from the volume fractions of their constituents and the shape of the soil particles. The dual-probe heat-pulse technique ([14]-[17]) Kluitenberg et al, 1993) has been used to measure soil thermal properties.

For Saudian soils, however, information on thermal properties has been lacking. These data could be useful in constructing models to predict the thermal regime of soils. Such information assumes greater importance with increasing concerns and intentions in developing the agricultural industry in Saudia Arabia. Because the growth and development of a crop may be determined to a large extent by rates of soil warming and cooling, the practical significance of knowing the soil thermal capacity is most important as it is one of the most important factors controlling rates of soil warming and cooling. In this study, the first objective was to study the effect of moisture content and bulk density on specific heat and volumetric heat capacity of two different soil types; sand and loam. For Saudi Arabia this point is of great concern, since sandy and loam soils are the most common types of soil in the country. The second objective was to compare the predicted and observed specific heat and volumetric heat capacity values under varying water content and soil density.

II. PREDICTION EQUATIONS

Independent estimates of the soil heat capacity and specific heat were obtained using relations derived based on ([9],[10],[18]) for comparison with the laboratory measurements obtained in this study. The following is a summary of the procedure on which the derivation of these relations is based. Heat capacity H of a soil is calculated as the sum of the heat capacities of its different constituents ([9],[10],[18]). Thus if m_s and m_w are masses in kg of soil particles and soil water, respectively, then.

$$H = m_s c_s + m_w c_w \quad (1)$$

where: H is heat capacity of the soil in J/°C, c_s and c_w , are the specific heats in J/kg/°C of dry soil particles and soil water, respectively. Usually, the contribution of air can be neglected ($m_a c_a$) because of negligible mass of gaseous phase. Also, the contribution of organic matter ($m_o c_o$) is ignored because the organic matter contents of the soils under test are small [9].

Using (1), the specific heat c of a moist soil can be given by the relation

$$(m_s + m_w) c = m_s c_s + m_w c_w \quad (2)$$

Equation (2), when divided by the total volume of the soil sample V_T , yields

$$\rho c = \rho_d c_s + \rho_d w c_w \quad (3)$$

where: $w = m_w / m_s$ is the gravimetric moisture content in kg/kg; ρ and ρ_d are the wet bulk density and dry bulk density in kg/m³, respectively, and given by:

$$\rho = (m_s + m_w) / V_T \quad (4)$$

$$\rho_d = m_s / V_T \quad (5)$$

Since the volumetric heat capacity C_v of a moist soil is given by $C_v = \rho c$, (3) can be rewritten in the form

$$C_v = \rho_d c_s + \rho_d w c_w$$

or

$$C_v = \rho_d (c_s + w c_w) \quad (6)$$

where: C_v is the volumetric heat capacity of moist soil in J/m³/°C; and $\rho_d c_s$ is the volumetric heat capacity of dry soil in J/m³/°C. Eqn (6) was used to predict the volumetric heat capacity C_v of a moist soil using an average value for c_s of 950 J/kg/°C for loam and 870 J/kg/°C for sand as measured in this study.

To derive the prediction equation for the specific heat c of a moist soil, (3) can also be rewritten in the following form

$$c = \rho_d (c_s + w c_w) / \rho \quad (7)$$

Since $\rho_d = \rho / (1+w)$, then the specific heat c of a moist soil is given by

$$c = (c_s + w c_w) / (1 + w) \quad (8)$$

Equation (8) was used to predict the specific heat c of a moist soil using the same value for c_s loam and sand as above.

III. SOIL SPECIFIC HEAT AND VOLUMETRIC HEAT CAPACITY

Specific heat is used to calculate the energy change associated with a temperature change. Most reported soil specific heat capacities were determined by the calorimetric method [19]. Briefly, this method consists of heating a substance to a particular temperature and quickly mixing it into a liquid medium of known temperature and known specific heat. From the law of conservation of energy, the heat lost by the substance must equal the heat gained by the liquid. By knowing the masses involved, the changes in temperatures, and the specific heat of the liquid, the unknown specific heat may be easily computed. The specific heat of dry soil particles c_s was determined from the equilibrium temperature when mixing equal quantities of dry soil and water at different initial temperatures according to:

$$c_s = (T_w - T_e) * c_w * W_w / (T_e - T_s) * W_s \quad (9)$$

where: T_w initial temperature of water in calorimeter (°C), T_s initial temperature of dry soil (°C), T_e equilibrium temperature of mixed water and dry soil in calorimeter (°C), c_w specific heat of water J/kg/°C, W_w mass of water in calorimeter (kg), and W_s mass of dry soil (kg).

The specific heat of moist soil was similarly measured but by mixing the moist soil with dry soil rather than water. The specific heat of the moist soil c can be calculated from the equilibrium temperature provided the specific heat of the dry soil c_s is known according to:

$$c = (T_s - T_e) * c_s * W_s / (T_e - T_{ds}) * W_{ds} \quad (10)$$

where: T_s initial temperature of dry soil in calorimeter (°C), T_{ds} initial temperature of moist soil in calorimeter (°C), T_e equilibrium temperature in calorimeter (°C), W_s mass of dry soil in calorimeter (kg), W_{ds} mass of moist soil in calorimeter (kg).

Combining (6) and (7) and since $\rho_d = \rho / (1+w)$, C_v the volumetric heat capacity of moist soil can be calculated from the following equation provided the specific heat of the moist soil c is known:

$$C_v = \rho_d (1 + w) c \quad (11)$$

IV. MATERIALS AND METHODS

Measurements of heat capacity were made on two soils: sand (91% sand, 6% silt, and 3% clay) with a soil organic matter content of 1.34% and loam soil (41% sand, 36% silt, 23% clay) with a soil organic matter content of 2.18%. Soils were air-dried and screened through a 2-mm sieve. For the determination of specific heat and volumetric heat capacity of soil at different moisture contents and compaction, the calorimetric method was followed. A small cylindrical capsule of copper of diameter 10 mm and length 35 mm was prepared. Its one end was closed and there was a removable cap at the other end. The thickness of the wall of the capsule was approximately 1 mm. The capsule was then pushed into the soil with certain moisture content till it was just filled up. By this technique, small soil samples at any desired density could be conveniently obtained. The soil sample was heated in a double-

walled steam chamber. The sample could thus be heated without coming in contact with steam. Specific heat of the soil sample was then determined in usual way by the calorimetric method explained in previous section. The temperatures were recorded at an interval of 0.5 s by using a 0.2 mm copper-constantan thermocouple. The samples were weighed prior to each test on a balance reading to 0.001 g. The experiment was repeated with soils at different moisture contents and packed into the container to same density. To investigate the effect of density, the soil of known weight at given moisture content was packed to different known volumes marked on the container. Various levels of moisture contents and bulk density were used for the two soils. The moisture levels used ranged from 0 to 0.2 kg/kg. Moisture contents throughout this study were measured by drying at 105 °C for approximately 24 h. The bulk densities of soils ranged from 1200 to 1400 kg/m³. The experiment was replicated three times for each treatment. Independent estimates of volumetric heat capacity and specific heat and under varying water content and soil density were also made using (6) and (8), respectively.

V. RESULTS AND DISCUSSION

A statistical analysis was performed to test the null hypothesis that “replicate” had no effect on the results obtained. Means were separated by the LSD procedure at alpha level α of 5% to compare means between replicates for each treatment. The analysis indicated that the replicate effect was not significant. Thus, the results were combined over the three replicates for each treatment in this study.

Specific heat of two sieved and repacked Saudian soils as a function of water content is shown in Figs 1 and 2. The two figures show both predicted and observed specific heat of the loam and sandy soils as a function of water content at a given bulk density using (8) and (10), respectively. At various water contents and at a given bulk density, specific heat increased with increasing soil water content for both soils. It is observed that the specific heat of both the soils, exhibit a nearly linear relationship up to certain moisture content. For higher values of moisture content, specific heat increased less rapidly in case of sandy and more rapidly in case of loam soil. In general, the loam soil had higher specific heat than the sandy soil. The differences in mineralogy and sand, silt, and clay fractions could be the primary reasons that loam soils often have a

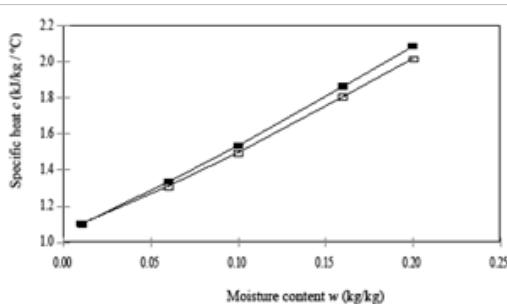


Fig. 1. Measured (■) and predicted (□) specific heat (c : error range 0-0.26 kJ/kg/°C) as a function of moisture content for a loam soil at a bulk density of 1200 kg/m³.

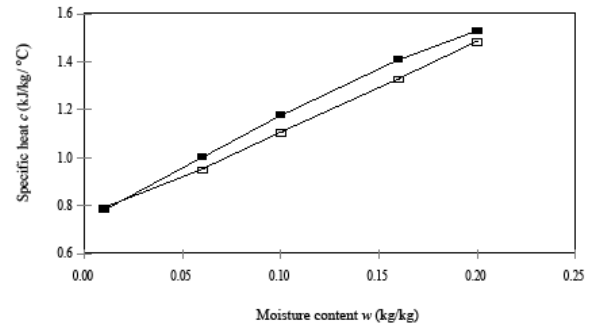


Fig. 2. Measured (■) and predicted (□) specific heat (c : error range 0-0.26 kJ/kg/°C) as a function of moisture content for a sandy soil at a bulk density of 1200 kg/m³.

higher specific heat than sandy soils. The sandy soils often contain more quartz. Similar results were reported by ([12],[20]). Reference [9] reported that the clay soil had higher specific heat than the sandy soil and that for higher values of moisture content, specific heat increased less rapidly in case of sandy and more rapidly in case of clay soil. Rapid increase in the specific heat of loam soil with increasing moisture content is probably due to adsorption of water forming thick hulls around loam particles, which greatly enhanced its effective specific heat compared with sandy soil. It is expected that this type of relation between specific heat and water content holds up to saturation point beyond which specific heat of soil tends to approach the specific heat of water quite rapidly. Comparisons of the specific heat values predicted using (8) with the values measured by the capsule method using (10) are shown in Figs 1 and 2. The differences between the observed and predicted results were small.

Variations of volumetric heat capacity predicted using (6) with the volumetric heat capacity measured by the capsule method using (11) for the two soils are shown in Figs 3 and 4. They show the observed and predicted volumetric heat capacity of the loam and sandy soils as a function of moisture content and bulk density. At various moisture contents and at a given bulk density, measured volumetric heat capacity increased with increasing soil moisture content for both soils. For sandy soil, measured C_v varies linearly with moisture content (Fig 4) and the linearity was equally good for loam soil (Fig 3). In addition, measured volumetric heat capacity increased with increasing bulk density for the two soils. Measured volumetric heat capacity increased with increasing bulk density for the two soils as a result of particle contact enhancement as porosity is decreased, and because of greater mass of solids per unit volume. For the loam soil, measured volumetric heat capacity did not increase uniformly with increasing bulk density at various water contents (Fig 3). Initially, it increased rapidly with an increase in bulk density for loam soil. However, further increases in bulk density increased the measured volumetric heat capacity only slightly (Fig 5). Such a phenomenon was absent in the sand soil. It appears that higher values of bulk density of sand did improve contact between the relatively larger sand particles, and produced relatively more homogenous soil samples.

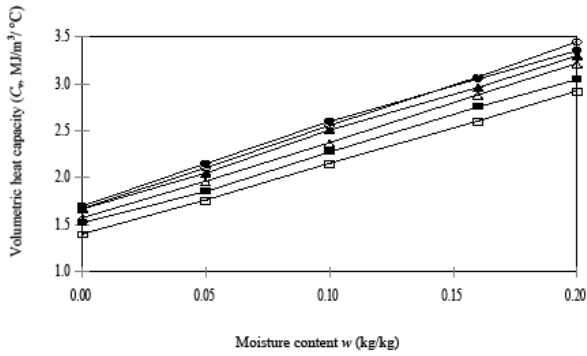


Fig. 3. Measured (■) and predicted (□) volumetric heat capacity (C_v : error range 0-0.38 MJ/m³/°C) as a function of moisture content for a loam soil at the bulk densities: ■ and □, 1200 kg/m³; ▲ and Δ, 1300 kg/m³; ● and ○, 1400 kg/m³.

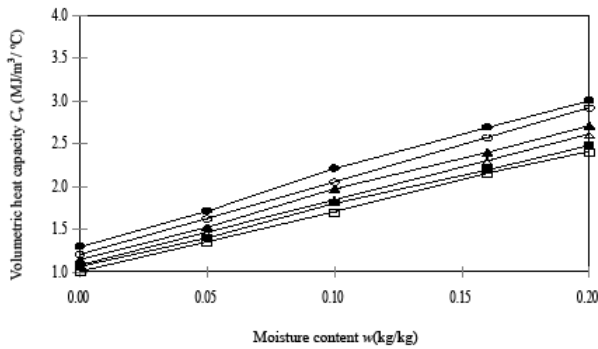


Fig. 4. Measured (■) and predicted (□) volumetric heat capacity (C_v : error range 0-0.38 MJ/m³/°C) as a function of moisture content for a sandy soil at the bulk densities: ■ and □, 1200 kg/m³; ▲ and Δ, 1300 kg/m³; ● and ○, 1400 kg/m³.

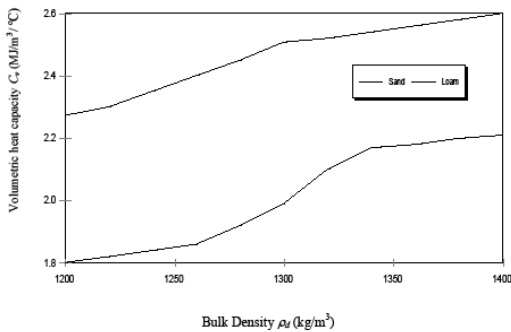


Fig. 5. Measured volumetric heat capacity as a function of bulk density at a moisture content of 0.1 kg/kg for both soils.

Comparisons of the volumetric heat capacity values measured by the capsule method using (11) with the values predicted using (6) for the loam soil (Fig 3) and the sandy soil (Fig 4) show that C_v predicted agreed closely for both soils with C_v measured by the calorimeter method. The differences between the measured and predicted volumetric heat capacity values were small, and were constant over the full moisture content range used in this study. The slopes of the lines for the two soils shown in Figs 3 and 4 are practically the same. The results, therefore, clearly reveal that the calorimeter method yielded C_v values very close to those generated from (6) for both soils. In general, the loam soil had higher volumetric heat capacity than the sandy soil. As shown in Table 1, similar results were reported by other researchers ([9],[12],[18],[21]).

TABLE 1. COMPARISON OF THERMAL PROPERTIES OBTAINED IN THIS STUDY WITH VALUES OBTAINED BY OTHER RESEARCHERS

Source	Specific heat, J/kg °C		Volumetric heat capacity, × 10 ⁶ J/m ³ °C	
	Sand	Loam	Sand	Loam
This study	800-1530	1140-2090	1.06-3.01	1.52-3.50
Ghuman and Lal, (1985)	910	1450	1.52	1.54
Yadav and Saxena, (1973)	820-1610	1100-1990	1.14-3.14	1.56-3.55
Bristow, (1998)	—	—	1.10-3.00	—
Abu-Hamdeh (2003)	830-1670	—	1.09-3.04	—

* Dashes indicate that property was not investigated.

VI. CONCLUSIONS

The effect of water content and bulk density on the specific heat and volumetric heat capacity of some sieved and repacked soils was investigated through laboratory studies. For the type of soils studied, specific heat increased with increased moisture content. Also, volumetric heat capacity increased with increased moisture content and soil density. The differences between the observed and predicted results of the volumetric heat capacity and specific heat were very small. Loam soil generally had higher specific heat and volumetric heat capacity than sandy soil for the same water content and soil density. Moisture content values and bulk densities were chosen to represent actual values that can be found in natural soils. Additional studies are now needed to test the effect of the above parameters on thermal conductivity of undisturbed Saudian soils.

REFERENCES

- [1] D.A. Gunn, L.D. Jones, M.G. Raines, D.C. Entwisle, and P.R.N. Hobbs, "Laboratory measurement and correction of thermal properties for application to the rock mass," *Geotech. Geol. Eng.*, vol. 23, 773-791, 2005.
- [2] H.M. Abuel-Naga, D.T. Bergado, and A. Bouazza, "Thermal conductivity evolution of saturated clay under consolidation process," *International Journal of Geomechanics ASCE*, vol. 8 (2), 114-122, 2008.
- [3] H.M. Abuel-Naga, D.T. Bergado, A. Bouazza, and M.J. Pender, "Thermal conductivity of soft Bangkok clay from laboratory and field measurements," *Engineering Geology*, vol. 105, 211-219, 2009.

- [4] Z.H. Wang, E. Bou-Zeid, and J.A. Smith, "A spatially-analytical scheme for surface temperatures and conductive heat fluxes in urban canopy models," *Boundary-Layer Meteorol*, vol. 138, 171–193, 2011.
- [5] W. Chen and W. Liu, "Numerical and experimental analysis of heat and moisture content transfer in a lean-to greenhouse," *Energy and Buildings*, vol. 38 (2), 99–104, 2006.
- [6] L. Lloret and M.V. Villar, "Advances on the knowledge of the thermo-hydronechanical behaviour of heavily compacted FEBEX bentonite," *Physics and Chemistry of the Earth*, vol. 32 (8–14), 701–715, 2007.
- [7] T.E. Ochsner, R. Horton, and T. Ren, "A new perspective on soil thermal properties," *Soil Science Society of America Journal*, vol. 65, 1641-1647, 2001.
- [8] H.K. Ahn, T.J. Sauer, T.L. Richard, and T.D. Glanville, "Determination of thermal properties of composting bulking materials," *Bioresource Technology*, vol. 100, 3974–3981, 2009.
- [9] N.H. Abu-Hamdeh, "Thermal Properties of Soils as affected by Density and Water Content," *Biosystems Engineering*, vol. 86(1), 97-102, 2003.
- [10] D.A. De Vries, "Thermal properties of soils," in *Physics of Plant Environment*, W.R. Van Wijk, Ed. North-Holland, Amsterdam, 1963, pp. 210-235.
- [11] P.J. Wierenga, D.R. Nielsen, and R.M. Hagan, "Thermal properties of soil based upon field and laboratory measurements," *Soil Science Society of America Proceedings*, vol. 33, 354-360, 1969.
- [12] M.R. Yadav and G.S. Saxena, "Effect of compaction and moisture content on specific heat and thermal capacity of soils," *Journal of Indian Society of Soil Science*, vol. 21, 129-132, 1973.
- [13] D.A. De Vries, *The thermal conductivity of soil*. Meded. Landbouwhogeschool, Wageningen, 1952.
- [14] G.S. Campbell, C. Callissendorff, and J.H. Williams, "Probe for measuring soil specific heat using a heat pulse method," *Soil Science Society of America Journal*, vol. 55, 291-293, 1991.
- [15] K.L. Bristow, G.S. Campbell, and C. Callissendorff, "Test of a heat-pulse probe for measuring changes in soil water content," *Soil Science Society of America Journal*, vol. 57, 930-934, 1993.
- [16] K.L. Bristow, R.D. White, and G.J. Kluitenberg, "Comparison of single and dual-probes for measuring soil thermal properties with transient heating," *Australian Journal of Soil Research*, 32, 447-464, 1994.
- [17] G.J. Kluitenberg, M. Ham, and K.L. Bristow, "Error analysis of the heat-pulse method for measuring the volumetric heat capacity of soil," *Soil Science Society of America Journal*, vol. 57, 1444-1451, 1993.
- [18] K.L. Bristow, "Measurement of thermal properties and water content of unsaturated sandy soil using dual-probe heat-pulse probes," *Agricultural and Forest Meteorology*, vol. 89, 75-84, 1998.
- [19] S.A. Taylor and R.D. Jackson, "Heat capacity and specific heat," *Agronomy*, vol. 9, 345-348, 1965.
- [20] B.S. Ghuman and R. Lal "Thermal conductivity, thermal diffusivity, and thermal capacity of some Nigerian soils," *Soil Science*, vol. 139, 74-80, 1985.
- [21] N.H. Abu-Hamdeh and R.C. Reeder, "Soil thermal conductivity: effects of density, moisture, salt concentration, and organic matter," *Soil Science Society of America Journal*, vol. 64, 1285-1290, 2000.

Effect of stent porosity on hemodynamics within cerebral aneurysm models: Numerical study

Dai Thanh Phan, Minh Tuan Nguyen, and Sang-Wook Lee

Abstract—In this study, numerical simulations have been carried out to investigate the effects of stent porosity on blood flow characteristics inside stented saccular aneurysm models on variously curved vessels, i.e., vessels with constant and realistic curvatures. Four different stent porosities of 100%, 80%, 74% and 64% were considered. A finite element method (FEM) solver was employed on unsteady incompressible Navier–Stokes equations of laminar flow. Results were presented in terms of the flow velocity vector fields, the volume inflow rates into the aneurysm, and the wall shear stress (WSS) in the aneurysm sac. It was shown that a stent with porosity of 80%, which is highest in the present study, was found effectively reducing flow into the aneurysm and that stents with lower porosities have only small increase of flow reducing effect. The geometry of aneurysm also has significant effects on stent performance. Further extensive simulations with patient-specific geometry will be necessary.

Keywords—cerebral aneurysm, hemodynamics, stent, porosity, velocity reduction ratio, computational fluid dynamics

I. INTRODUCTION

CEREBRAL aneurysm is an abnormal widening or bulging of a portion of an intracranial artery due to weakness in the wall of the blood vessel. When the size of an aneurysm increases, there is a significant risk of rupture, resulting in subarachnoid hemorrhage (SAH), other complications or death. SAH is a common and frequently devastating condition, accounting for 5% of all strokes and affecting as many as 30,000 Americans each year [1].

In order to treat aneurysm, endovascular techniques using stents have been more popular. A stent is a flexible cylindrical tube made of a mesh of stainless steel or alloys. Due to its limited permeability, the stent modifies the blood flow into the aneurysm. The resulting stagnant flow normally promotes the formation of a stable thrombus (coagulation) in the aneurysm sac leading to its eventual occlusion [2]. The performance of stent in the respect of hemodynamics depends on its dimension and shape and many studies have been carried out to investigate the effect of stent design on the intra-aneurysmal flow structure. Lieber et al. [3] investigated the effect of the stent strut size on

This work was supported by the Ministry of Science, ICT and Future Planning under Grant 10044910

D. T. Phan is with the School of Mechanical Engineering, University of Ulsan, Ulsan, Korea (e-mail: daihanhbkc@gmail.com).

M. T. Nguyen is with the School of Mechanical Engineering, University of Ulsan, Ulsan, Korea (e-mail: minh Tuan710@gmail.com).

S.-W. Lee is with the School of Mechanical Engineering, University of Ulsan, Ulsan, Korea (phone: 82-52-259-2765 fax: 82-52-259-1680 e-mail: leesw@ulsan.ac.kr).

the intra-aneurysmal flow in a sidewall aneurysm model using particle image velocimetry. Liou et al. [4] investigated the effect of stent shapes (helix stent vs. mesh stent) on intra-aneurysmal flow using particle tracking velocimetry measurements and flow visualization. It is expected that the porosity of a stent is the most important parameter that affects its ability to impede or modify the aneurysmal flow [5], [6]. A lower porosity results in more flow blockage, but if the porosity is too low, the stent might inadvertently block perforating vessels or become too rigid for deployment [7], [8]. Because of these constraints, the neurovascular stents currently in use are high-porosity stents. However, there is a lack of study of realistic stent for cerebral aneurysm in scientific literature. In this paper, we will systematically evaluate the influence of the relatively thin strut and high porosity stents.

Recently, computational fluid dynamics (CFD) becomes a valuable tool to investigate blood flow dynamics implicated in vascular disease in non-invasive manner. In this article, we present a study on the use of CFD to examine changes in local hemodynamic inside aneurysm models with virtual implantation of stent. The finite element method was employed under incompressible, unsteady, Newtonian conditions. Stents with four different porosities ($C_\alpha = 100\%$, 80%, 74%, and 64%) are considered for comparing the effect of stent porosity. This study demonstrates the capability of CFD tools for evaluating flow characteristics by stenting in aneurysm and understanding hemodynamic phenomena.

II. METHOD

A. Model Geometry

The idealized cerebral aneurysm model was constructed with

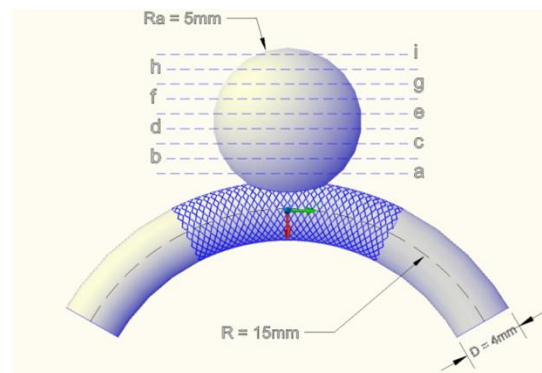


Fig. 1 Cerebral aneurysm model with constant curvature

Table 1 The dimension of three stent samples

Stent	H (mm)	B (mm)	t (mm)	C_α (%)
w/o	-	-	-	100
1	0.64	0.36	0.038	80
2	0.65	0.27	0.038	74
3	0.54	0.16	0.038	64

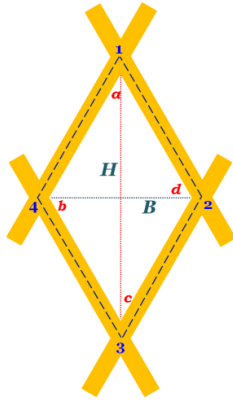


Fig. 2 A schematic geometry of a rhombus stent

15 mm curvature of radius vessel and a sphere attached to center of the baseline as shown in Fig. 1. The diameters of the aneurysm and parent vessel are 10 mm and 4 mm respectively. Four rhombus shaped-stents with porosities of 100% (no stent), 80%, 74%, and 64% [9] were examined in unsteady pulsatile inflow condition. Stent was deformed to fit into the curved parent vessel.

Detailed shape of the stent design and dimensions are described in Fig. 2 and Table 1, respectively.

Porosity, one of the most important parameters of stent design, is defined as the proportion of open area to total area of the stent as follows:

$$C_\alpha = A_{abcd}/A_{1234} \quad (1)$$

B. Computational Fluid Dynamics (CFD)

Three-dimensional unsteady incompressible momentum and mass conservation equations for Newtonian fluid flow were solved as

$$\rho \frac{\partial \mathbf{u}}{\partial t} + \rho \mathbf{u} \cdot \nabla \mathbf{u} = -\nabla p + \mu \nabla^2 \mathbf{u} \quad (2)$$

$$\nabla \cdot \mathbf{u} = 0 \quad (3)$$

where, \mathbf{u} and p is fluid velocity vector and pressure, respectively. CFD simulations were carried out using a well-validated, in-house finite-element-based solver employing a sufficient density of quadratic tetrahedral elements. Rigid walls and Newtonian rheology were assumed. Pulsatile inflow boundary conditions were prescribed based on representative waveform shapes in basilar artery. Each simulation was run for

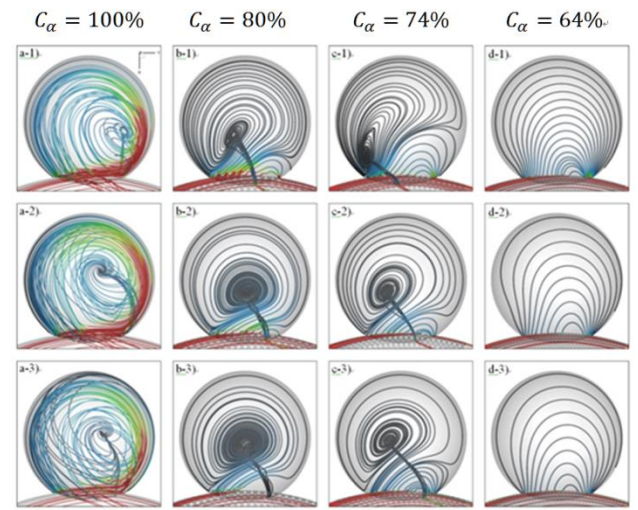


Fig. 3 Comparison of intra-aneurysmal flow structures

four cardiac cycles to damp initial transients; the data from simulation of the fourth cardiac cycle were used for analysis.

III. RESULTS AND DISCUSSION

A. Intra-aneurysmal flow structure

Fig. 3 shows comparison of intra-aneurysmal flow patterns by stent porosity. Stents produce significant flow modifications. The inflow into the aneurysm sac is shifted from the distal side of the neck in the unstented model to the proximal side in the stented model. The flow reversal adjacent to the bottom wall of the parent vessel is also greatly reduced after stenting.

For the unstented case, there is a counter-clockwise vortex inside the aneurysm sac which is driven directly by the flow in the parent vessel. After stenting, the vortex is reduced due to the blockage effect of the stents. In the case of $C_\alpha = 64\%$, counter-clockwise rotating vortex was disappeared, but only weak clockwise rotating vortex present. This is similar observations made by Yu et al. [9], Liou et al. [10], and Kim et al. [11] in numerical and experimental studies.

B. Velocity Reduction Ratio

The mean velocity in the midplane in the unstented case is much larger than stented model. The mean velocity lowered

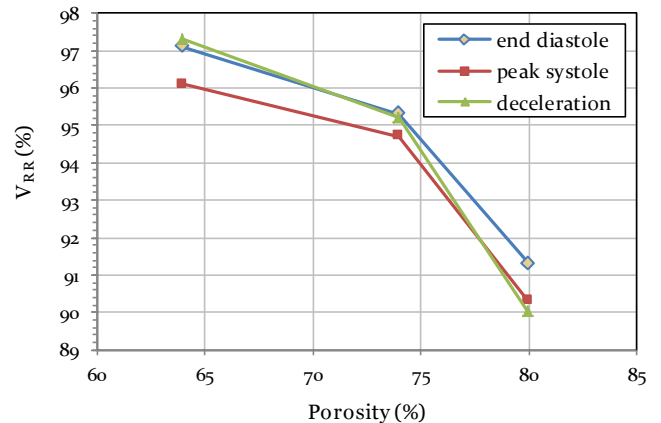


Fig. 5 Comparison of velocity reduction ratio

with decrement of stent porosity. In order to assess a quantitative comparison on the flow reduction rate related to the stent efficiency, the variation of the flow pattern in the stented aneurysm was investigated. A global measure of the effect of the stent, i.e., mean velocity reduction [9], [12] is defined as

$$V_{RR} = (\bar{V}_{ns} - \bar{V}_{st}) / \bar{V}_{ns} \quad (4)$$

where, \bar{V}_{ns} and \bar{V}_{st} are the mean unstented and stented velocities in the aneurysm sac, respectively. The reduction of the mean velocity can be interpreted as the increase of the respective flow characteristics due to the effects of stent strut porosity.

Fig. 5 shows the velocity reduction rate within aneurysm sac for different porosity of stents. As expected, the lower stent porosity has a higher velocity reduction rate. At peak systolic phase, the velocity reduction rate for $C_\alpha = 80\%$, 74% and 64% is approximately 90%, 95% and 96% respectively. We may expect this reduction of mean velocity promotes the occurrence of the hemostasis inside the aneurysm which lower the risk of the growth or possible rupture.

C. Wall shear stress

The WSS is known as an important factor that influences aneurysm growth and rupture. The effect of WSS in vascular biology had been studied intensively earlier in the literature. According to the experimental and the CFD study, a high WSS (> 40.0 Pa) is regarded as a major factor in initiation of cerebral aneurysm [13], [14] while a low WSS (< 2.0 Pa) might be a major factor for its growth and rupture [15].

Fig. 6 shows the WSS distribution in both unstented and stented aneurysms. The stents reduced significantly the WSS on the aneurysm wall. Even $C_\alpha = 80\%$ case decrease WSS up to ten times lower than unstented model. In particular, around the dome of aneurysm the magnitude of WSS value is considerably

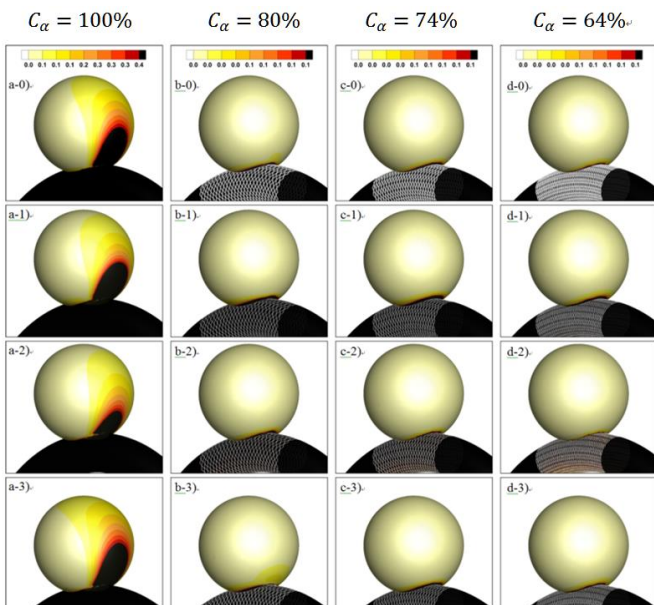


Fig. 6 Comparison of WSS distribution by stent porosity

low, which may associated with the risk of rupture.[15]

D. Cerebral Aneurysm model with realistic curvature

We may expect the curvature of the parent vessel has great effect on the effectiveness of stent. Thus, an elliptic shaped aneurysm on a parent vessel with more realistic curvature which mimics in vivo arterial morphology [16] was considered. Two different porosities of stent, i.e., $C_\alpha = 100\%$ (no stent) and $C_\alpha = 80\%$ were applied, but with the same rhombus shaped mesh design.

Fig. 7 compares the streamtraces within the aneurysm sac. Evidently, the vortex strength in the stented aneurysm is lower compared to the unstented aneurysm model. However, the reduction of velocity is much lower than the case of constant curvature vessel by the stent with the same porosity.

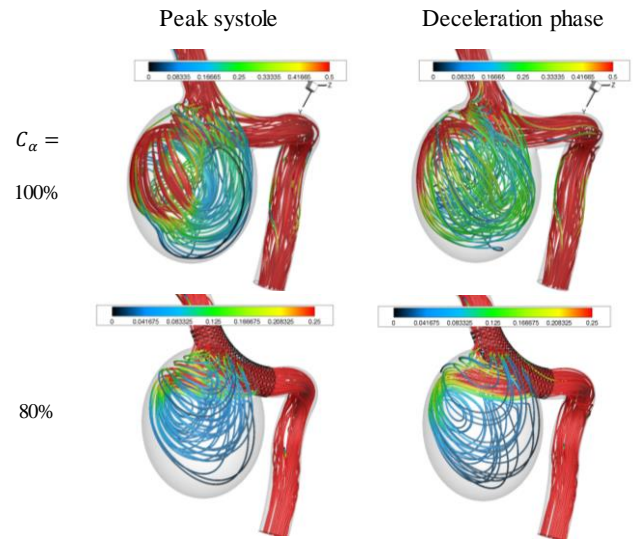


Fig. 7 Comparison of intra-aneurysmal flow structures (streamtraces)

This indicates the effectiveness of stent for an aneurysm is greatly dependent on the parent vessel morphology, not only stent design parameters such as porosity, which imply the requirement of extensive parametric study with varying parent geometry for optimal stent design.

IV. CONCLUSION

We demonstrated the CFD simulations of stented aneurysm flow by various stent porosity and parent vessel geometry.

The results showed the stent porosity affects the intra-aneurysmal flow patterns. The implantation of stents reduced the strength of vortex and velocity in the aneurysm sac. A stent with porosity of 80%, which is highest in the present study, was found effectively reducing flow into the aneurysm and stents with lower porosities have only small increase of flow reducing effect.

The vorticity and velocity reduction rates are strongly correlated to the blood clotting, according to the clotting fraction prediction [17], [18]. The characteristics of flow are also affected by aneurysm and parent vessel geometry. When the geometry changes from an ideal model to a realistic model,

the performance of stent was reduced significantly.

In conclusion, the present numerical study helps better understand about effect of stent porosity on hemodynamics in cerebral aneurysm. Although rather simple rigid models have been used, we could observe fundamental characteristics of stented cerebral aneurysm flow. However, to understand more detailed and accurate performance of stent, more extensive studies with patient-specific geometry based on medical images will be necessary.

ACKNOWLEDGMENT

We would like to thank to B. R. Park and W. S. Nam for their great help in graphic works.

REFERENCES

- [1] J. T. King Jr., "Epidemiology of aneurysmal subarachnoid hemorrhage," *Neuroimaging Clin. N. Am.*, vol. 7, pp. 659-668, 1997.
- [2] B. B. Lieber, A. P. Stancampiano, and K. Wakhloo, "Alteration of hemodynamics in aneurism models by stenting: in fluence on stent porosity," *Ann. Biomed. Eng.*, vol. 25, no. 3, pp. 460-469, 1997.
- [3] B. B. Lieber, V. Livescu, L. N. Hopkins, and A. K. Wakhloo, "Particle image velocimetry assessment of stent design influence on intra-aneurysmal flow," *Ann. Biomed. Eng.*, vol. 30, pp. 768-777, 2002.
- [4] T. M. Liou, S. N. Liou, and K. L. Chu, "Intra-aneurysmal flow with helix and mesh stent placement across side-wall aneurysm pore of a straight parent vessel," *J. Biomech. Eng.*, vol. 126, pp. 36-43, 2004.
- [5] S. A. Berger, W. Goldsmith, and E. R. Lewis (eds.), *Introduction to Bioengineering*, Oxford: Oxford University Press, UK, 2000
- [6] M. E. Kim, I. Levy, H. Meng, and L. N. Hopkins, "Quantification of hemodynamic changes induced by virtual placement of multiple stents across a wide-necked basilar trunk aneurysm," *Neurosurgery*, vol. 61, pp. 1305-1312, 2007
- [7] M. A. Burbelko, L. A. Dzyak, N. A. Zorin, S. P. Grigoruk, and V. A. Golyk, "Stent-graft placement for wide neck aneurysm of the vertebrobasilar junction," *AJNR Am. J. Neuroradiol.*, vol. 25, pp. 608-610, 2004.
- [8] S. Rudin, Z. Wang, I. Kyprianou, K. R. Hoffmann, Y. Wu, and H. Meng, *et al.*, "Measurement of flow modification in phantom aneurysm model: comparison of coils and a longitudinally and axially asymmetric stent -initial findings," *Radiology*, vol. 231, pp. 272-276, 2004.
- [9] C. H. Yu, K. Matsumoto, S. Shida, D. J. Kim and M. Ohta, "Steady flow analysis on a cerebral aneurysm model with several stents for new stent design using PIV," *J. Mech. Sci. Tech.*, vol. 26, no. 5, pp. 1333-1340, 2012.
- [10] T. M. Liou and Y. C. Li, "Effects of stent porosity on hemodynamics in a sidewall aneurysm model," *J. Biomech.*, vol. 41, pp. 1174-1183, 2008.
- [11] Y. H. Kim, X. F. Xu and J. S. Lee, "The effect of stent porosity and strut shape on saccular aneurysm and its numerical analysis with lattice Boltzmann method," *Ann. Biomed. Eng.*, vol. 38, no. 7, pp. 2274-2292, 2010.
- [12] M. Hirabayashi, M. Ohta, K. Barath, D. A. Rufenacht, and B. Chopard, "Numerical analysis of the flow pattern in stented aneurysms and its relation to velocity reduction and stent efficiency," *Math. Comp. Simulation*, vol. 72, pp. 128-133, 2006.
- [13] L. Bousset, V. Rayz, C. McCulloch, A. Martin, G. Acevedo-Bolton, and M. Lawton, *et al.*, "Aneurysm growth occurs at region of low wall shear stress: patient-specific correlation of hemodynamics and growth in a longitudinal study," *Stroke*, vol. 39, pp. 2997-3002, 2008.
- [14] S. Kondo, N. Hashimoto, H. Kikuchi, F. Hazama, I. Agata, H. Kataoka, "Cerebral aneurysms arising at on branching sites. An experimental study," *Stroke*, vol. 28, pp. 398-403; discussion 403-404, 1997.
- [15] M. Shojima, M. Oshima, K. Takagi, R. Torii, M. Hayakawa, and K. Katada, *et al.*, "Magnitude and role of wall shear stress on cerebral aneurysm computational fluid dynamic study of 20 middle cerebral artery aneurysm," *Stroke*, vol. 35, pp. 2500-2505, 2004.
- [16] D. A. Steinman, J. S. Milner, C. J. Norley, S. Lownie, and D. W. Holdsworth, "Image-Based Computational Simulation of Flow Dynamics in a Giant Intracranial Aneurysm," *AJNR Am. J. Neuroradiol.* vol. 24, pp. 559-566, 2003.
- [17] R. Ouared, and B. Chopard, "Lattice Boltzmann simulations of blood flow: non-Newtonian rheology and clotting processes," *J. Stat. Phys.*, vol. 121, pp. 209-221, 2005.
- [18] M. Hirabayashi, M. Ohta, K. Barath, D. A. Rufenacht, and B. Chopard, "Numerical analysis of the flow pattern in stented aneurysms and its relation to velocity reduction and stent efficiency," *Math. Comp. Simulation*, vol. 72, pp. 128-133, 2006.

Investigation of turbulence characteristics of burning process of the solid fuel in BKZ 420 combustion chamber

¹Askarova A.S., ²Bekmukhamet A., ³Bolegenova S.A., ⁴Beketaeva M.T., ⁵Maximov Yu.V., ⁶Ospanova Sh.

^{1,2,3,4,5,6} Al-Farabi Kazakh National University, Almaty

Abstract— In this paper the results obtained by the numerical method modeling of Ekibastuz coal burning in BKZ-420 combustion chamber of Kazakhstan Power Plant. There are devoted to the numerical simulation of the furnace boiler BKZ-420, its steam generating capacity equal 420 T/h. Boiler (Fig. 2) has six vortical pulverized coal burners arranged in two levels with three burners on the front wall of the boiler. Burned in the furnace high ash, low-grade coal from Ekibastuz, Its ash content 40%, volatile 24%, humidity 5%, highest calorific value 16750 kJ/kg. Milling dispersity of coal was equal to $R_{90} = 15\%$.

Keywords— Combustion, Heat and mass transfer, BKZ-420, turbulence, pulverized coal, two-phase flows, Ekibastuz coal.

I. INTRODUCTION

At the moment the world energy in the foreseeable future based on the use of fossil fuels, mainly low-grade coal. It should be noted that the deterioration of steam coal is widespread, and not only in the CIS countries, but also in the developed capitalist countries. Today the world's thermal power plants (TPP) produce more than 40% of electricity and heat. Although generally coal had several 'ups and downs' during its utilisation history, it is still one of the most important fuels for the generation of primary energy, especially of electric energy (Fig.1). According to IEA statistics issued in 2003, coal supplies around 24% of primary energy needs and generates some 40% of produced global electricity, while further increase in utilisation of coal is expected in the

A.S. Askarova¹. Al-Farabi Kazakh National University, Almaty, 050038 Kazakhstan (e-mail: Aliya.Askarova@kaznu.kz).

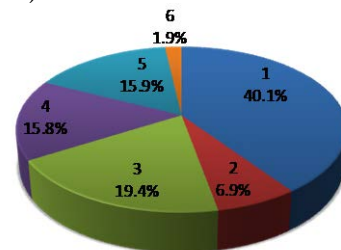
A. Bekmukhamet², He is now 3rd course PhD student of the Department of Thermal Physics and Technical physics, Al-Farabi Kazakh National University, 050038 Kazakhstan (corresponding author to provide phone:+7-707-878-43-14 ; fax: no ; e-mail: Kazsat2006@gmail.com).

S.A. Bolegenova³, PhD of the Department of Thermal Physics and Technical physics, Al-Farabi Kazakh National University, 050038 Kazakhstan (e-mail: Symbat.80@mail.ru).

M.T. Beketaeva⁴, She is now 2nd course PhD student of the Department of Thermal Physics and Technical physics, Al-Farabi Kazakh National University, 050038 Kazakhstan. (e-mail: mika.1986_86@mail.ru).

Yu.V. Maximov⁵, PhD of the Department of Thermal Physics and Technical physics, Al-Farabi Kazakh National University, 050038 Kazakhstan. (e-mail: maximov.v@mail.ru).

future (IEA, 2003a) .



1 - coal, 2 - liquid fuel (fuel oil, diesel fuel), 3 - gas 4 - nuclear energy, 5 - hydro, 6 - other (solar, wind, geothermal, waste, including vegetable origin)

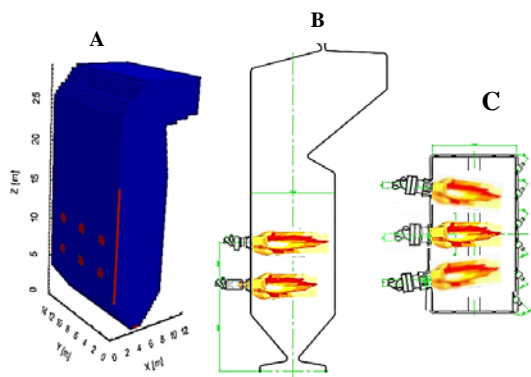
Figure 1. Total world electricity generation by fuel

Solution of many technical tasks impossible without using of CFD software packages, allows modeling of difficult particular process in practice. In this article investigated numerical study of physical characteristics and aerodynamic properties of pulverized flue combustion in thermal power plant with Florean [1-3] program complex.

Investigation of problems of convective heat and turbulent flows in the presence of chemical reactions is an actual problem of thermo-physics and hydro aerodynamics, because such flows are widely distributed in nature and take importance in many technical devices. Knowledge of laws of such flows important when constructing combustion physics theory, at creation new physico-chemical technologies, and also at the decision of problems of power system. In researches difficult combustion process should be analyzed according to the influence of physical and chemical parameters of the combustion reaction.

There are devoted to the numerical simulation of BKZ-420 combustion chamber. Its steam capacity equal 420 T/h. Boiler equipped with six vortex dust burner, arranged in two levels with three burners on the front wall of the boiler as shown in figure 1. In the boiler has burnt dust low-grade high-ash coal from Ekibastuz, with ash content 40 %, volatile 24 %, moisture content 5 % and the highest calorific value 16700 kJ / kg. The fineness of coal milling is equal to $R_{90} = 15\%$. All numerical calculations were performed on above methodology.

On the front wall of the combustion chamber six double-flow vortex of dust and gas burners in two stages (three per stage) are established. The last burner turned to the center of burner by 8 degrees. The capacity of each burner is 12 T/h (Fig.2).



A -3D view of BKZ 420 boiler and its breakdown into control volumes

B- Burners establish arranged on two levels

C – Top view on the cross section (h = 10.75m)

Figure 2 - General view of the industrial boiler BKZ-420 of the Almaty TPP-2

Industrial implementation of any new technology is not possible without preliminary analysis of advantages and disadvantages suggested method. The rapid development in computer sciences gives the advance to computational techniques to be used for simulation of complex combustion processes in industrial furnaces.

Products of combustion contain different harmful substances and the emission of this components grows in to a great problem. Industrial development causes an increase in hydro carbonaceous fuels' consumption. These fuels contain harmful and poisonous components such as carbonic oxide (CO), nitric oxide (NO), sulphur dioxide, acid sulphate, lead combinations and different hydrocarbons etc (Table-1).

To decrease emissions of harmful substances various methods are applied, including special fire regimes (organization of combustion process), which suppresses the formation of harmful substances in flame and two-stage burning, when the burners work with low air surplus. In this way numerical experiments became one of the most effective and suitable means for detail analysis and in-depth study of physical and chemical phenomena.

In this paper software package FLOREAN [2] for 3-D modeling of coal-dust combustion in furnaces of real-sized boilers was used. This program enables to calculate velocity components u , v , w , temperature T , pressure P , concentration of combustion products and other turbulence characteristics of combustion process all over the combustion space and at its exit. Pressure is determined through the connection between the continuity equation and the equation of motion by means of Patankar's Simple-method [3].

Complex physical and chemical processes include the conservation equations of mass, conservation of angular momentum and energy for the gas and solid phases. The gas flow is considered in the Euler system, the dynamics of a solid phase is considered in the Lagrangian system. The turbulent structure of the flow is described by a two-parameter model of turbulence. The radiation heat transfer is transfer six stream model. The mathematical description of the physical and

chemical processes are based on the solution of the equation balance. In general, all of these equations contain four components: changes in the value of time, component describing convective transport, component describing diffusive transport, component describing the source or flow.

Table 1 - Source data of coal and BKZ-420 combustion chamber for numerical calculation

Characteristic	Quantity
Coal type	Ekibastuz
Density of particles	1300 kg/m ³
C _{daf} , %	82.0
H _{daf} , %	5.0
N _{daf} , %	1.5
O _{daf} , %	11.5
Ash, %	40.0
Humidity, %	5.0
Volatile content, %	24-28
Coal consumption in the boiler	72 000.00 kg/h
Consumption of coal to the burner through two channels	12 000.00 kg/h
Primary air flow to the boiler	107 035 kg/h
Secondary air flow rate to the boiler	402 656 kg/h
The temperature the secondary air	280 °C
Temperature of aeromixture	88.85 °C
The average particle size of coal	64 мкм
The lower heating value of coal	16 750 kJ / kg
The amount of computation (control volumes)	671113

II. MATHEMATICAL MODEL

Program FLOREAN is based on the numerical solution of the Reynolds averaged balance equations for mass, species, energy and momentum [1,2, 3, 4]. It predicts gas flows, species concentrations, temperature fields due to combustion, radiation and convective heat transfer and the pollutant formation and destruction in furnace chambers. The mean flow equations are closed by the k- ϵ turbulence model.

The changes of the concentrations of the flue gas components and the fuel due to the combustion are taken into account in the source/sink terms by appropriate sub models.

In addition, in the source/sink term the heat balance takes into account the energy release due to the combustion reactions and the significant heat transfer due to radiation using a six flux radiation model. Equation for conservation of thermal energy is written in terms of the enthalpy h . Radiation heat transfer is determined by 6 flux radiation model by Lockwood etc [5].

Pulverised coal flames are turbulent reacting two-phase flows. Particle presence is approximated as continuum and the

mean particle velocity is assumed to be approximately equal to the gas phase velocity.

In the standard k-ε model written basic transport equation of turbulent kinetic energy k:

$$\frac{\partial(\bar{\rho}k)}{\partial t} = -\frac{\partial(\bar{\rho}u_j k)}{\partial x_j} + \frac{\partial}{\partial x_j} \left[\frac{\mu_{eff}}{\sigma_k} \frac{\partial k}{\partial x_j} \right] + P - \bar{\rho} \cdot \varepsilon, \quad (1)$$

where P - production of turbulent kinetic energy, which is defined the following equation:

$$P = \left[\mu_{turb} \cdot \left(\frac{\partial \bar{u}_i}{\partial x_j} + \frac{\partial \bar{u}_j}{\partial x_i} \right) - \frac{2}{3} \cdot \bar{\rho} \cdot k \cdot \delta_{ij} \right] \cdot \frac{\partial \bar{u}_i}{\partial x_j}; \quad (2)$$

The equation for the turbulent kinetic energy dissipation ε:

$$\frac{\partial(\bar{\rho}\varepsilon)}{\partial t} = -\frac{\partial(\bar{\rho}u_j \varepsilon)}{\partial x_j} + \frac{\partial}{\partial x_j} \left[\frac{\mu_{eff}}{\sigma_\varepsilon} \frac{\partial \varepsilon}{\partial x_j} \right] + C_{\varepsilon,1} \cdot \frac{\varepsilon}{k} \cdot P - C_{\varepsilon,2} \cdot \frac{\varepsilon^2}{k} \cdot \bar{\rho} \quad (3)$$

The turbulent viscosity is determined by the equation Prandtl - Kolmogorov:

$$\mu_t = C_\mu \cdot \bar{\rho} \cdot \frac{k^2}{\varepsilon} \quad \text{where } C_\mu \text{ - empirical constant.}$$

$$C_\mu = 0.09; \quad \sigma_k = 1.00; \quad \sigma_\varepsilon = 1.30; \quad C_{1\varepsilon} = 1.44; \quad C_{2\varepsilon} = 1.92.$$

The boundary conditions for the turbulence model are defined as follows:

$$k_{in} = 1.5 \cdot (u_{i,in} Tu)^2 \quad \text{- kinetic energy of turbulence at the inlet.}$$

It should be noted that the modeling of flows in the presence of turbulence, which are taken as a basis for solving the equations for the turbulent characteristics (kinetic energy of turbulence and its dissipation), allows to obtain the desired accuracy of the solution, while excluding non-useful machine costs associated with obtaining it.

III. RESULTS OF CFD RESEARCH

Florea solves a number of transport equations depending on the user's specific problem setup. It's given the (general) continuity, momentum, energy species and turbulence equations. In Figure 3-7 are the vector field full speed $V = \sqrt{u^2 + v^2 + w^2}$ throughout the volume of the combustion chamber by means of which one can characterize the behavior of pulverized coal flow within the combustion chamber. One can clearly see the area of the fuel mixture through the burner[5].

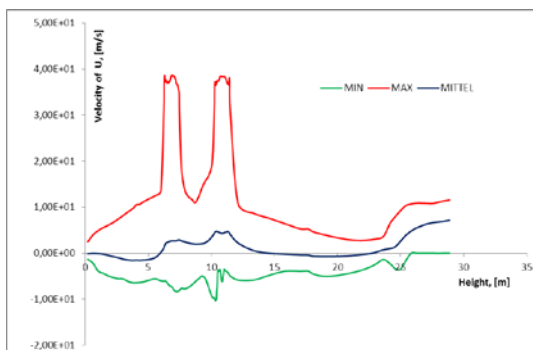


Figure 3- Distribution of the vector velocity direction of the x axis height of the combustion chamber of the boiler BKZ-420

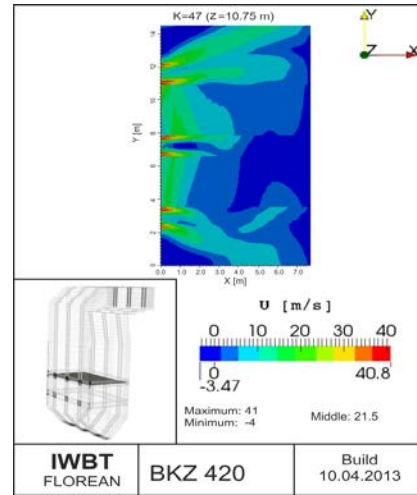


Figure 4- Velocity profile on the cross section of the combustion chamber of the boiler BKZ-420 (K=47, Z = 10.75m)

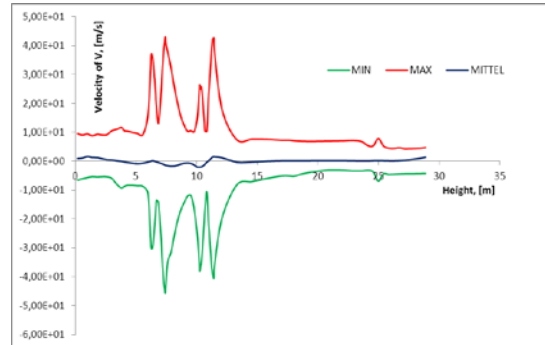


Figure 5- Distribution of the vector velocity direction of the y axis height of the combustion chamber of the boiler BKZ-420

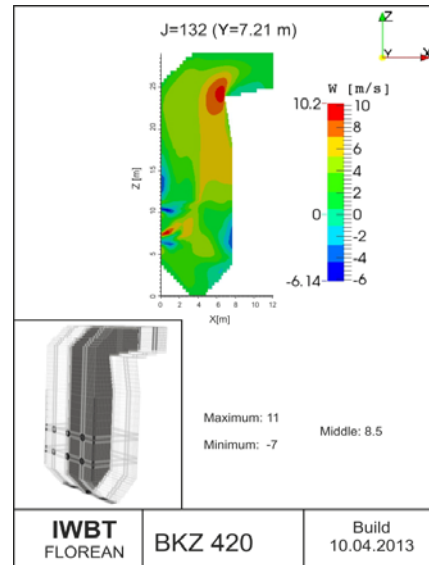


Figure 6- Velocity profile on the cross section of the combustion chamber of the boiler BKZ-420 (J=132, Y = 10.75m)

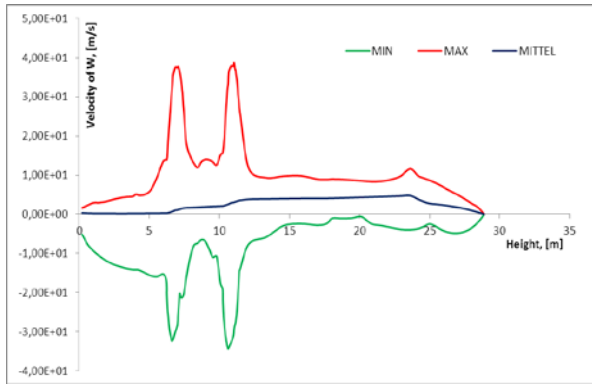


Figure 7- Distribution of the vector velocity direction of the Z axis height of the combustion chamber of the boiler BKZ-420.

Figure 4 - in the cross section, which accounts for the lower tier of burners ($K=47$, $h = 10.75m$) has max speed on the inlet, it equal 40 m/s, Figure 5- distribution of the vector velocity direction of the y axis height of the combustion chamber of the boiler BKZ-420, there are we can see two pics , its mean is speed on the inlet of burner.

Figure 6-7 Velocity profile on the cross section of the combustion chamber of the boiler BKZ-420 ($J=132$, $Y = 7.2 m$) by Z axis. There are max speed equal to $W=11 m/s$.

Speed vector Fields in the figures are shown as arrows vectors of length gives a value of full speed, their direction connected with the direction of the full-speed at the selected point of the combustion chamber. Presented on Figures-8 able to obtain whole velocity profile in the BKZ-420 chamber include three different level by Y axis: $Y_1 = 2.85 m$, $Y_2 = 7.2 m$, $Y_3 = 11.69 m$.

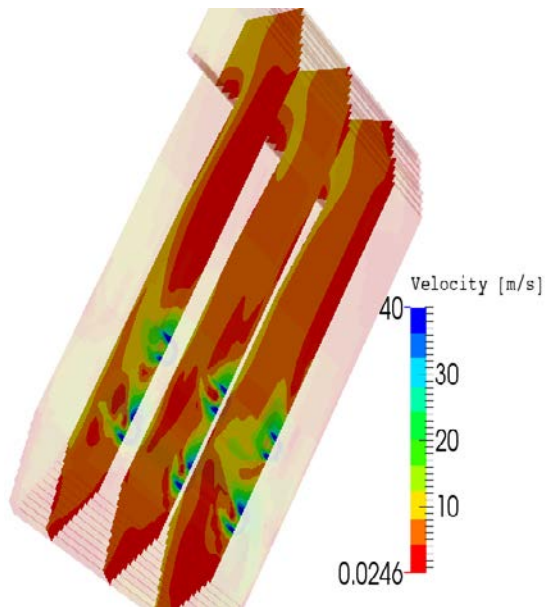
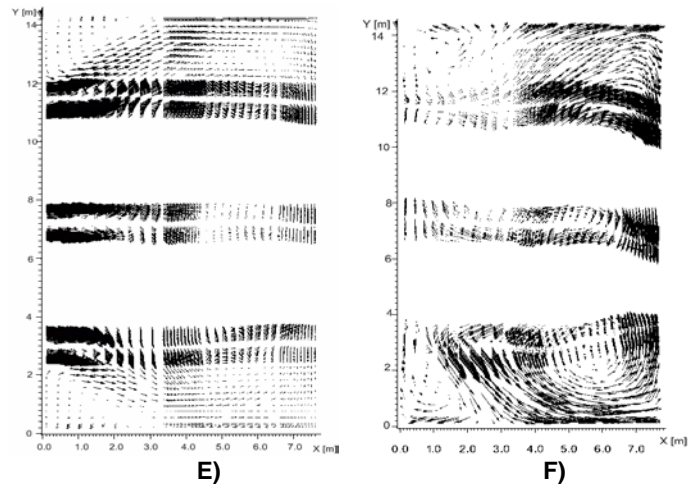


Figure 8- Velocity profile on the different levels of the combustion chamber $Y_1 = 2.85 m$, $Y_2 = 7.2 m$, $Y_3 = 11.69 m$ on the Y axis for two longlines ($z_1 = 6.2 m$) and ($z_2 = 10.75 m$).



E- ($Z_1=10.75 m$), F- ($Z_2=6.2 m$), H- ($Y=7.2 m$)

Figure 9 – Velocity vector profile by the combustion chamber height

The Figure 9 illustrates the picture of the velocity distribution in the combustion chamber by means of which one can characterize the behavior of pulverized coal flow within the combustion chamber. One can clearly see the area of the fuel mixture through the burner. According above all of the figure we can see max velocity on the inlet of burner, also on the cross section by Z axis F- ($Z_2=6.2 m$), Right and left side of burner exist turbulence flow of combustion.

On the basis of mathematical models and 3D computer modeling had conducted the study of complex of heat exchange processes taking place during combustion of low-grade coal fuel (Ekibastuz caol) on real energetic facility of the Republic of Kazakhstan (the combustion chamber of the boiler BKZ-420 of TPP-2). It is shown that the most intense burning is observed in the central part of the chamber where the flow temperature reaches about 980 °C. Due to the fact that coal particles in this area have a more intense radiation and have higher concentration and the total surface, it is seen that the temperature reaches a peak in the cross sections of the location of the burners. This is an area combustion reaction occurs more intensively. As you approach the exit from the combustion

chamber temperature profile is stabilized, and the differences between the minimum and maximum values decreases. Pressure field on the Fig.10 that max pressure on the below opposite side burner.

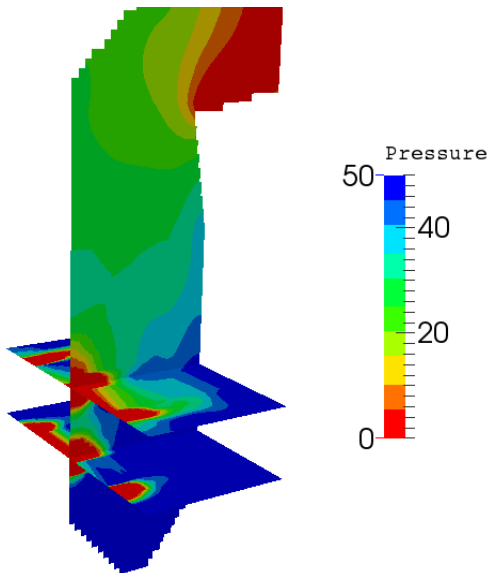


Figure 10 – Pressure profile by the height of combustion chamber

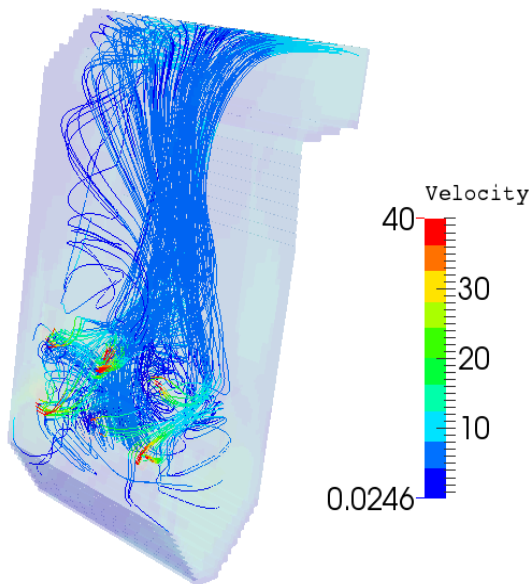


Figure 11 –3D view of turbulence combustion profile by the by the height of combustion chamber

Results obtained by means of computer modeling of gas flows behavior, velocity fields due to combustion, radiation and convective heat transfer and the pollutant formation and destruction in furnace of real boiler BKZ-420 can be used to predict main characteristic of combustion process and to provide recommendations for effective boiler performance. Results from CFD simulation can be useful for engineers to choose an

appropriate boiler performance for successful furnace and overall combustion process optimization[6].

REFERENCES

- [1] Leithner, R., Müller, H. CFD studies for boilers// *Second M.I.T. Conference on computational Fluid and Solid Mechanics*, Cambridge, 2003.
- [2] Askarova A., Heierle Y., Leithner R., Müller H. CFD Code Florean for Industrial Boilers Simulations // *Wseas transactions on heat and mass transfer*, Issue 4, Volume 4, 2009, ISSN: 1790-5044, pp.98-107.
- [3] Leithner, R., Müller, H. CFD studies for boilers // *Second M.I.T. Conference on computational Fluid and Solid Mechanics*, Cambridge, 2003.
- [4] Askarova A.S., Bolegenova S.A., Maximov V.Yu., Bekmuhamet A., Ospanova Sh.S. Numerical research of aerodynamic characteristics of combustion chamber BKZ-75 mining thermal power station // *Journal Procedia Engineering*. - 2012. – V. 42, №389 (162). - P. 1365-1374.
- [5] A. Askarova, S. Bolegenova, V. Maximov, A. Bekmuhamet, M. Beketayeva Numerical experimenting of burning high-ash content Ekibastuz coal in the real boiler of CHP // *Recent Advances in Fluid Mechanics and Heat & Mass Transfer*, Greece, 2013.- pp. 138-147.
- [6] Aliyarov B.K., *Mastering Ekibastuz coal combustion in thermal power plants*. Almaty: 1996. - 272.

Atmospheric boundary layer effects on aerodynamics of NREL Phase VI wind turbine in parked condition

Mohammad Moshfeghi, Nahmkeon Hur

Abstract—In a natural condition, the wind is affected by the groundcover and the type of terrains which impose vertical velocity profile to the wind. This wind profile, which is also called atmospheric boundary layer (ABL), dramatically influences the aerodynamic behaviors and loadings of horizontal axis wind turbines. However, for the sake of simplicity, many numerical simulations only deal with the uniform wind speed. To consider the effects of the ABL, numerical simulations of the two-bladed NREL Phase VI wind turbines aerodynamic at the parked condition are conducted under both uniform and ABL. The Deaves-Harris (DH) model is applied to the ABL. The wind turbine blades are kept at the six o'clock position and are considered at two different pitch angles. The aerodynamic forces and moments of the uniform the DH model are compared. The results show that the pitch angle at which the HAWT is parked plays an important role on the blade loading. Also it is observed that for the fully separated conditions, the Down-blade and the blade in the uniform wind are under approximately similar aerodynamic loadings, while the Up-blade encounters more aerodynamic loads, which is even noticeable value for this small wind turbine. This in turn means that for an appropriate and exact design, effects of ABL should be considered with more care.

Keywords— Aerodynamic loading, Atmospheric boundary layer, Horizontal axis wind turbine, Parked condition.

I. INTRODUCTION

WHEN a horizontal axis wind turbine (HAWT) is kept parked or in the standstill condition, the blades might be at different pitch angles, which in turn, cause different aerodynamic loading over the blades. The investigation of the effects of pitch angle on the aerodynamic loads of parked HAWTs has been already conducted for the some HAWT including the NREL Phase VI under uniform wind profile [1], [2]. However, the assumption of the uniform wind is an ideal consideration. In a real case, the local terrain and groundcover have a strong impact on the wind and apply a shear effect to the wind. Hence, the real wind profile is called planetary boundary

This work was supported by the National Research Foundation of Korea (NRF) grant funded by the Korea Government (MSIP): Multi-phenomena CFD Research Center (ERC) in Sogang University (No. 2009-0093128).

Mohammad Moshfeghi is with Multi-phenomena CFD Engineering Research Center (ERC), Sogang University, Seoul, South Korea (email: mmoshfeghi@sogang.ac.kr).

Nahmkeon Hur is with Multi-phenomena CFD Engineering Research Center (ERC)/ Department of Mechanical Engineering, Sogang University, Seoul, South Korea (corresponding author: e-mail : Nhur@sogang.ac.kr; phone: +82-2-705-8637; fax:+82-2-7138637).

layer (PBL) or atmospheric boundary layer (ABL). Under the assumption of the ABL the wind profile needs to be characterized based on the height and the density of the vegetation and surface-covering objects and also the land elevation, slope, and orientation [3]-[5]. Even for a more detailed study one may assume the wind in a more complex framework, and the stochastic fluctuations in the wind direction and wind speed and day-night cycle also must be taken as the influential parameters to the wind profile [6]. Regardless of the details of the assumption for the ABL, the vertical wind profile is the common effect. Hence, the investigation of the impact of the ABL has attracted more aerodynamicists. For example, the large eddy simulations (LES) of large wind-turbine arrays in the ABL condition is simulated by Johan Meyers [7] to investigate the impact of different choices in modeling of the wind turbine array. Also, Shen and colleagues [8] have studied the flap-wise and edge-wise moment fluctuations as important sources of the fatigue damage in wind turbine blades by a lifting surface method to investigate the periodic unsteady nature in the wind shear. Moreover, the ABL is also investigated as a crucial parameter from the point of view of the energy production [9].

To take into account the effects of the wind shear in the present study, the NREL Phase VI HAWT is simulated at two pitch angles with both uniform wind speed of 20 (m/s) and the Deaves-Harris (DH) ABL model with the same wind speed at the hub height.

II. WIND PROFILE MODELS

Just a few hundred meters above the Earth surface and within the ABL profile, the wind speed increases from zero at the ground surface and reaches its nominal velocity. Flow near the surface encounters obstacles that reduce the wind speed, and introduce random vertical and horizontal velocity components at right angles to the main direction of flow. Generally, the reduction in velocity near the earth surface is considered as a function of surface roughness. Therefore, the wind velocity profile differs from one terrain type to another. The ABL is usually simulated by three theoretical and empirical methods, i.e., Power law, Log law and Deaves and Harris model (DH).

A. Power law

This formulation is preferred for the calculation of wind loadings on the wind turbine blade. The main advantage of this

method is its simplicity in calculations.

$$U(z) = U(z_{ref}) \times \left(\frac{z}{z_0}\right)^\alpha \quad (1)$$

where z_{ref} is the reference height; z_0 is the surface roughness length which is the representative of the terrain and ground surface covering and is defined as the extrapolated height at which the mean wind speed becomes zero if the vertical wind profile has a logarithmic variation with the height; $U(z_{ref})$ denotes the mean wind speed at z_{ref} and α is called the ground roughness exponent.

Despite the advantage of simplicity, the Power law was proposed based on empirical field tests and ignores the physics of the atmospheric boundary layer.

B. Log law

Due to the asymptotic approximation for the neutral atmospheric boundary layer, Davenport formulated the wind profile as:

$$U(z) = \left(\frac{U_0^*}{\kappa}\right) \times \ln\left(\frac{z}{z_0}\right) \quad (2)$$

where $U(z)$ is the mean wind speed at the height z ; U_0^* is surface friction velocity; and κ is the Von Karman constant ($\kappa=0.4$).

Moreover for the dense surface-covering objects such as buildings and trees, the log law has been modified, in which the z is replaced by $(z-d)$. Here, parameter d is called zero-plane displacement height and is defined as the height above the ground at which zero wind speed is achieved as a result of obstacles such as trees or buildings. Based on the micro-meteorological data, the Log law is more accurate than the Power law, meets the lowest boundary condition and also provides acceptable wind speed prediction up to the height of 100 (m) [6]. However, for an elevation higher than 200 (m) the model deviates from the field measurements.

C. Deaves-Harris Model

This model was first proposed in 1978 by Deaves [10]. The model takes into account three additional parameters and therefore is more precise than the Power law and the Log law. The DH model equation is proposed in such a way that it is applicable to the entire atmospheric boundary layer. In fact, in the DH model, the second term in the right-hand-side of the (2) is modified by adding a quartic (fourth order) polynomial. The DH model is explained as:

$$U(z) = \left(\frac{U_0^*}{\kappa}\right) \times \left[\ln\left(\frac{z}{z_0}\right) + 5.75\left(\frac{z}{h}\right) - 1.88\left(\frac{z}{h}\right)^2 - 1.33\left(\frac{z}{h}\right)^3 + 0.25\left(\frac{z}{h}\right)^4 \right] \quad (3)$$

where h is defined as the atmospheric boundary layer height ($h = U_0^* / Bf$); B is an empirical constant based on the wind profile ($B=6$); and f is the Coriolis parameter ($f=9.375 \times 10^{-5}$ (1/s)). More detailed information about the DH model can be

found in Cook's research [11].

III. WIND PROFILE PARAMETERS

For the DH model in the present simulations the value of surface roughness, z_0 , is chosen as 0.1, which in an appropriate guess for a field with few trees [12]-[13]. Moreover, the wind turbine hub height is assumed to be 12 (m) above the ground surface i.e., $z_{ref}=12$ (m) and the nominal wind speed at the hub height is 20 (m/s) as depicted in Fig. 1.

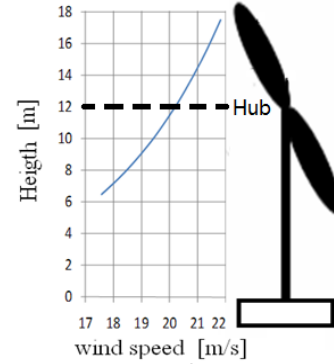


Fig. 1 DH wind profile for the NREL Phase VI

IV. WIND TURBULENCE INTENSITY

Wind turbulence intensity ($T.I.$) is one of the most complicated parameters in wind turbine performance investigation. This is because an exact value (or range of value) for $T.I.$ plays an important role in CFD simulations of wind turbines. The value of $T.I.$ together with the type of terrain, month, and even day-night time effect become very influential for power curves and the energy production of a wind turbine. [5]-[6], [14]-[17]. The sample for the field measurements about the effects of month and day-night time are presented in Figs. 2 and 3, respectively.

Based on many investigations, a realistic average value for the $T.I.$ can be considered between 0.08 and 0.12 [17]. Therefore, for the present CFD simulations, the $T.I.$ value is chosen as 0.1 ($T.I.=10\%$).

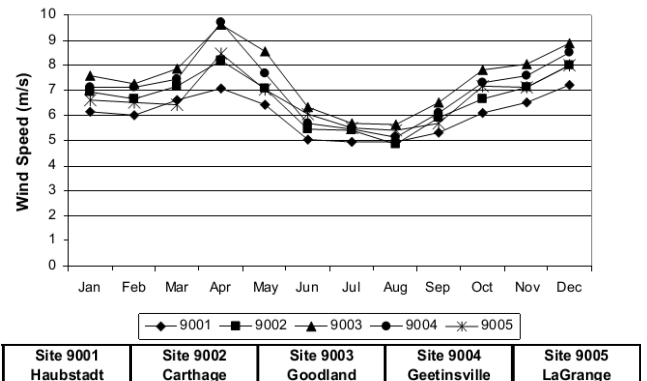


Fig.2 Monthly distribution of the wind speed at different sites [17]

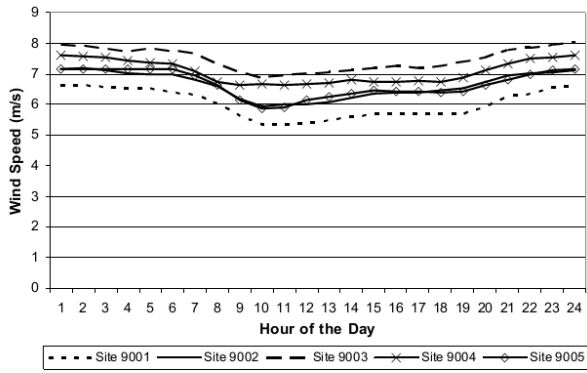


Fig 3 Diurnal wind speed distribution at different sites [17]

V. NREL PHASE VI GEOMETRY AND CFD MODEL

The NREL Phase VI is a two bladed turbine. The blade’s radius is $R=5.03$ (m) with the S809 airfoil, which is an insensitive airfoil to the blade roughness and is especially designed for large HAWTs [18]. The thickness of the S809 airfoil is 21% with the sharp trailing edge (T.E.). Fig.4 shows the blade twist angle and the S809 profile.

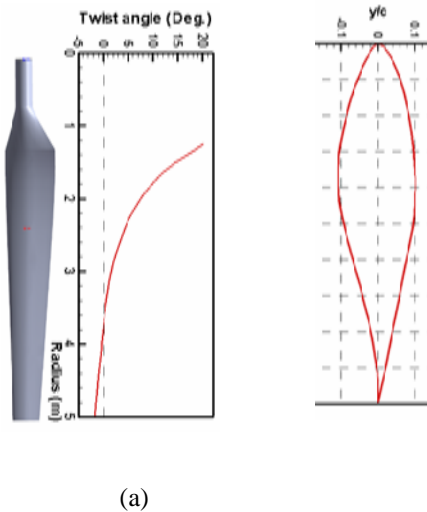


Fig. 4 NREL Phase VI blade twist angle (left); S809 airfoil (right)

The CFD domains consist of three million nodes. The domain and its dimension are shown in Fig. 5. The hexahedral mesh system is created in ANSYS-ICEM 13 and then solved with CFX software. After generating a mesh with proper first grid spacing values, the k-ε turbulence model is applied to the model and the model is solved under steady-state situation.

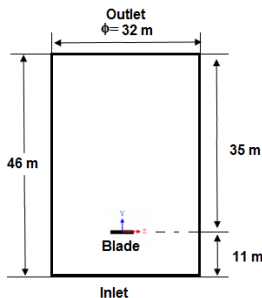


Fig. 5 CFD Domain and dimension

Figures 6, 7 present the distribution of axial velocity at the inlet and slightly upstream the rotor plane for the uniform wind and the ABL profile simulations. It is assumed that the wind speed at the hub is 20 (m/s).

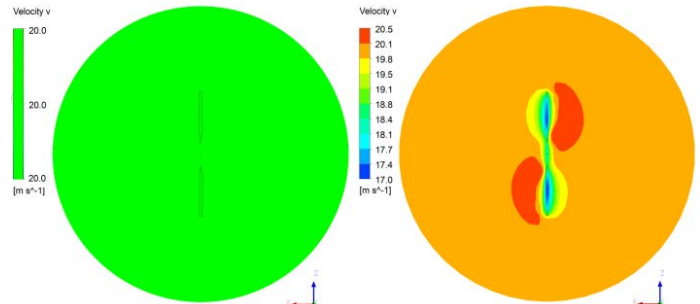


Fig. 6 Axial velocity distribution for the model with uniform wind at inlet (left); $y=0.5$ m upstream the rotor plane (right)

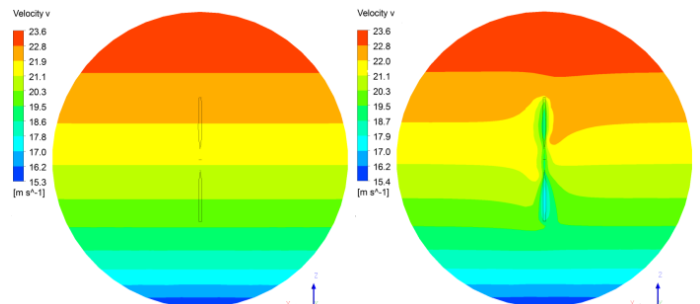


Fig. 7 Axial velocity distribution for the model with DH ABL profile wind at inlet (left); $y=0.5$ m upstream the rotor plane (right)

VI. RESULTS AND DISCUSSIONS

A. Aerodynamic loadings

The NREL Phase VI is solved under two pitch angle values and similar to [2], the angle between the chord line at the radial position of $r/R=47\%$ and the domain longitudinal axis is taken as the measuring parameter (α_{47}). Two cases are studied; one with $\alpha_{47}=-1.48^\circ$ and the other with $\alpha_{47}=23.94^\circ$. Table I shows the value of α_{47} and the corresponding sectional angles at different radial positions of $r/R=30\%$, 63% and 95% , with respect to the domain longitudinal axis. Aerodynamically, this angle is the local geometric angle of attack (AOA) for each section.

As previously shown, the velocity distributions of the uniform and DH profile are different. Hence, the aerodynamic loading on the upper and lower blades are different from each other and from the uniform case. The values of forces in the rotor plane (F_x), axial direction (F_y) and the moment around the axial axis (M_y) are presented in Tables II and III for the $\alpha_{47}=-1.48^\circ$ and $\alpha_{47}=23.49^\circ$, respectively. It can easily be read from the Tables II and III that the values of results for Up-blade and Down-blade for the uniform wind are approximately the same and the differences are related to the numerical errors. On the other hand, the same results are noticeably different for the DH wind profile.

Table I Sectional angle information

Case	α_{30}	α_{47}	α_{63}	α_{95}	α_{tip}
I	-11.08°	-1.48°	2.07°	4.69°	5.03°
II	13.90°	23.49°	27.05°	29.67°	30.02°

 Table II Aerodynamic loading for $\alpha_{47} = -1.48^\circ$

	Fx (N) (Up-blade/Down-blade)	Fy (N) (Up-blade/Down-blade)	Moment (N.m) (Up-blade/Down-blade)
Uniform	7.6 / -5.3	38.6 / 38.2	-159 / -163
DH Profile	1.5 / -12.3	44.6 / 42	-149 / -210

 Table III Aerodynamic loading for $\alpha_{47} = 23.49^\circ$

	Fx (N) (Up-blade/Down-blade)	Fy (N) (Up-blade/Down-blade)	Moment (N.m) (Up-blade/Down-blade)
Uniform	-326.2 / 324.0	176.5 / 176.7	-945 / -937.7
DH Profile	-394.5 / 332.7	212.2 / 183.5	-1142.7 / -963.3

B. Pressure coefficients

The pressure coefficients for models with $\alpha_{47} = -1.48^\circ$ and $\alpha_{47} = 23.49^\circ$ are plotted in Figs.8 and 9 at three different radial positions of $r/R=30\%$ ($r=1.510$ m), $r/R=63\%$ ($r=3.172$ m) and $r/R=95\%$ ($r=4.780$ m). All pressure coefficients are non-dimensionalized with respect to the wind speed of 20 (m/s). As the result show the Up-blade, the Down-blade and the blade in the uniform wind behave differently.

For Case I, as Table I shows, all AOAs are smaller than the separation AOA of S809 airfoil, which is about 10° [18], [19]. Therefore, as it can be observed form Fig. 8(a)-(c), the flow is fully attached. Also, it can be seen that the DH velocity profile affects the pressure distribution, especially at the outer radii.

In Case II, however, the geometrical AOA at $r/R=30\%$ is $\alpha_{30}=13.9^\circ$, which is higher that the separation angle. Nevertheless, the shapes of the pressure coefficient graphs show that for none of blades the flow is separated (Fig.9(a)). This can be interpreted as the result of a radial flow which causes separation delay on the blades. Further away from the root, the blade sections at $r/R=63\%$ and 95% have AOAs much higher than the separation angle. Therefore, one may expect a fully separated flow at these two radial section. Figs. 9(b)-(c) are in complete agreement with the above explanation and show that for these two sections the separation points are almost at the airfoil leading edge.

Finally, it is important to notice that the NREL Phase VI HAWT belongs to the small-size wind turbines and even for such a small wind turbine, with the blade radius of 5.03 (m), the wind profile noticeably influences the pressure values. This issue shows the importance of the effects of wind profile consideration on the modern large-size HAWTs with the blade radius in the range of 70 meters.

C. Streamlines

To investigate the effects of the ABL on the flow pattern, the

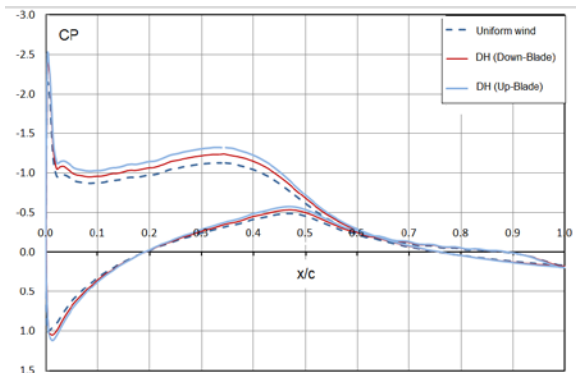
sectional (2D) streamlines for the case $\alpha_{47} = -23.49^\circ$ are shown in Figs.10 at different radial sections. As shown, at $r/R=30\%$ all blades present attached flows, which is in consistence with the Fig. 9(a). However, moving towards the tip, the local AOA increases and the flow separates from the suction surface. Also it can be read from the velocity values that the higher wind speed at the Up-blades creates a larger area of separated zone. Moreover, at a certain position at the Up-blade, compared to the Down-blade or uniform wind, the velocity filed reveals a larger absolute values in both axial (forward) and reversed (backward) zones.

VII. CONCLUSIONS

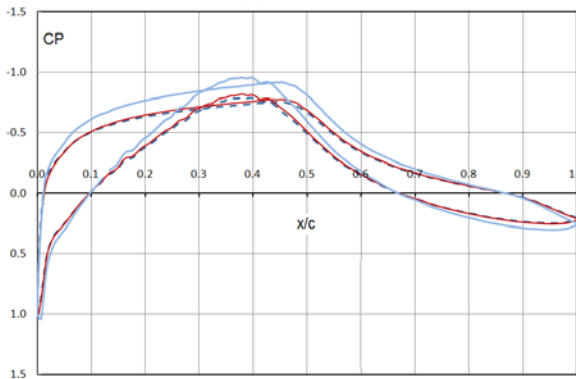
To investigate the influences of the atmospheric boundary layer on the blade loading of horizontal axis wind turbine in parked condition, the results of numerical simulations of NREL Phase VI wind turbines are compared with the uniform wind profile. The Deaves-Harris velocity profile model is applied to the wind. The wind turbine blades are considered to be at six o'clock position and two different pitch angles are simulated. The results indicate the importance of the pitch angle at which the HAWT is parked. It is also observed that when the flow is fully separated, the Down-blade and the blade in the uniform wind are approximately under similar aerodynamic loadings. However, the Up-blade undergoes a higher load value. This is noteworthy that this difference in the aerodynamic loads is happening for a small wind turbine and consequently means that for the exact design of an industrial wind turbine the effects of atmospheric boundary layer must be carefully considered.

The streamlines also show at the inner part of the blade ($r/R=30\%$) the flow is attached. However, by going towards the blade tip the local angle of attack increases and the tendency of the flow for the separation from suction surface increases. In addition, at a certain radial position at the Up-blade and the Down-blade, the absolute velocity in the Up-blade of ABL simulation is generally higher than Down-blade or uniform

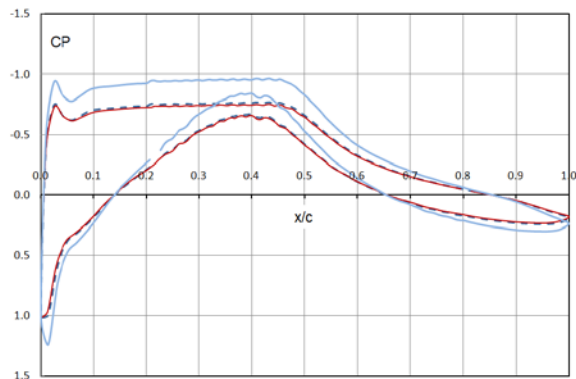
wind both forward and reversed flows.



(a) $r/R=30\%$

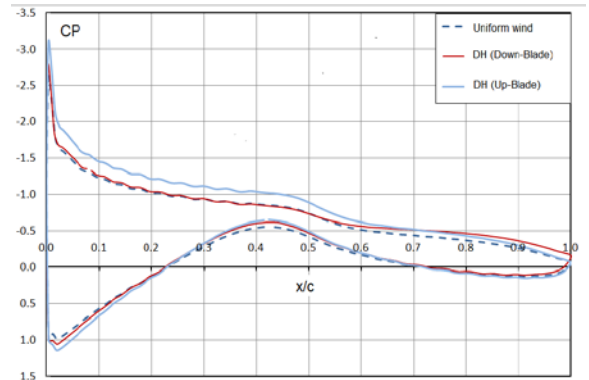


(b) $r/R=63\%$

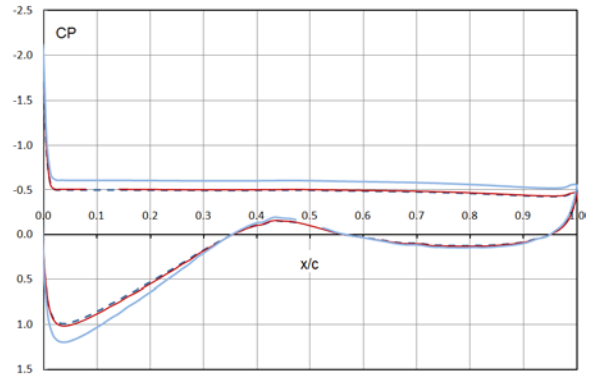


(c) $r/R=95\%$

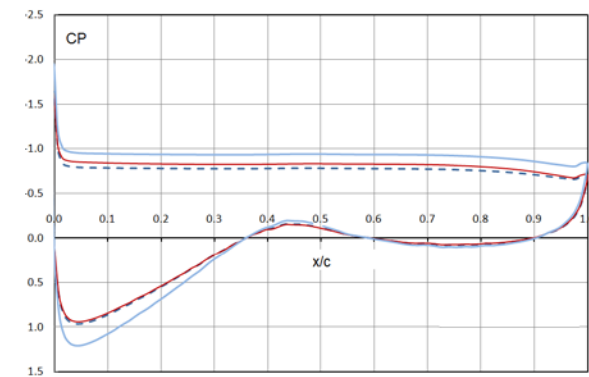
Fig. 8 Pressure coefficient for the model $\alpha_{47}=-1.48^\circ$



(a) $r/R=30\%$

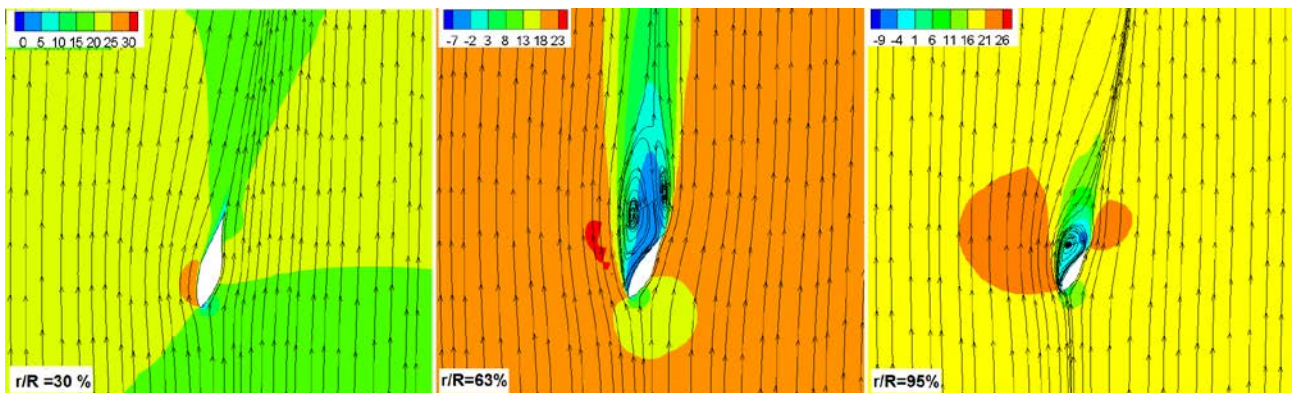


(b) $r/R=63\%$



(c) $r/R=95\%$

Fig. 9 Pressure coefficient for the model $\alpha_{47}=23.49^\circ$.



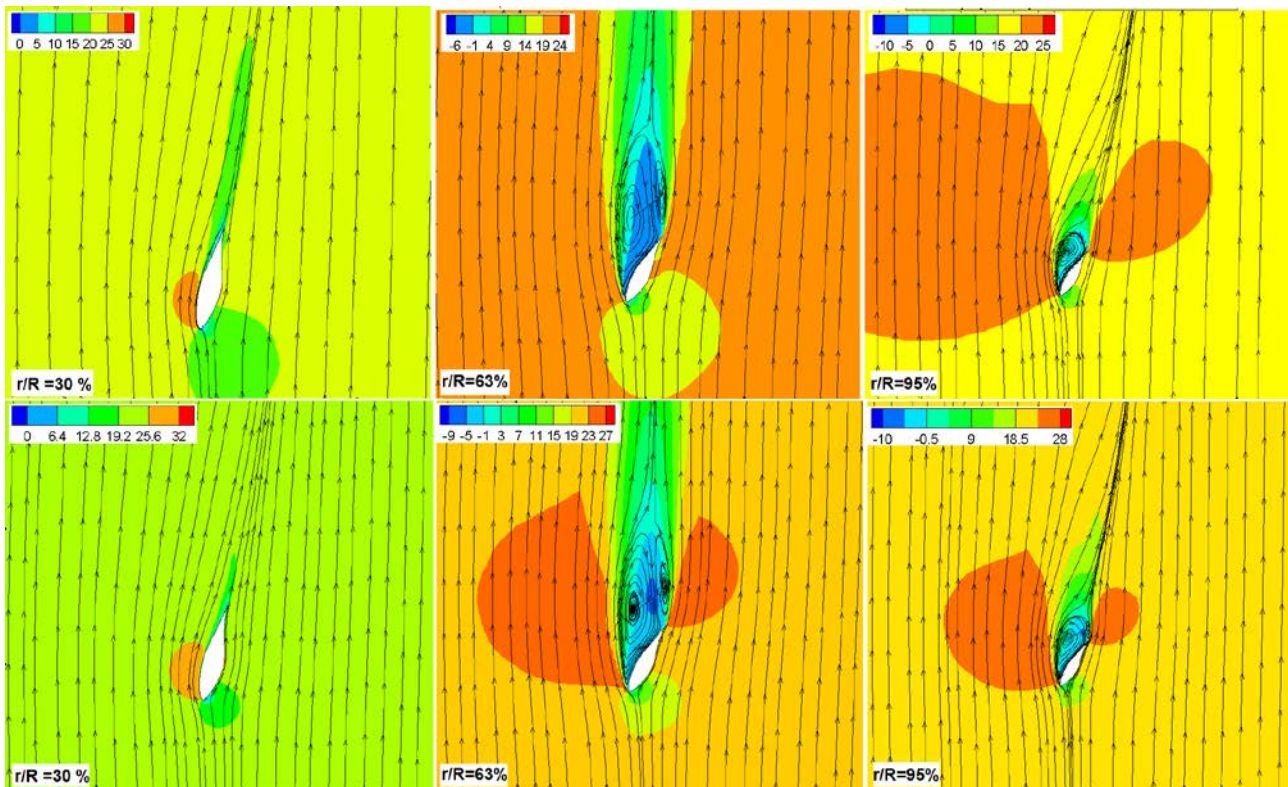


Fig. 10 Streamlines at different radial sections; Uniform wind (Top); ABL(Down-blade) ABL(Up-blade)

REFERENCES

- [1] N. N. Sørensen, J. Johansen, and S. Conway, "CFD computations of wind turbine blade loads during standstill operation KNOW-BLADE", Task 3.1 report, Risø National Laboratory, Roskilde, Denmark, 2004.
- [2] S. Schmitz and J. J. Chattot, "Characterization of three-dimensional effects for the rotating and parked NREL Phase VI wind turbine", Transactions-American society of mechanical engineering, J. Solar energy engineering, vol. 128(4), pp.445-454, 2006.
- [3] J. Horstmann and H. Dankert, "Estimation of friction velocity using tower based marine radars, Geoscience and Remote Sensing Symposium", IEEE International Conference on, IEEE, pp.1323-1326, 2006.
- [4] V. Khnykina, "Business case analysis for deployment of renewable power generation for Western Scotland industrial sites", Glasgow, University of Stathclyde, Dept. of Mechanical Engineering, 2011. Guidelines for design of wind turbines, DNV-Riso, Second Edition, ISBN 87-550-2870-5, 2009.
- [5] Q. S. Li, L. Zhi and F. Hu, "Boundary layer wind structure from observations on a 325m tower", J. Wind engineering and industrial aerodynamics, vol. 98(12), pp.818-832, 2010.
- [6] J. Meyers, and C. Meneveau, "Large eddy simulations of large wind-turbine arrays in the atmospheric boundary layer", 48th AIAA Aerospace Sciences Meeting Including the New Horizons Forum and Aerospace Exposition, Orlando, Florida, January 2010.
- [7] X. Shen, X. Zhu and Z. Du, "Wind turbine aerodynamics and loads control in wind shear flow", J. Energy, vol. 36(3), pp.1424-1434, 2011.
- [8] M. Wachter et al., "The Turbulent Nature of the Atmospheric Boundary Layer and its Impact on the Wind Energy Conversion Process", J. Turbulence, vol. 13, 2012.
- [9] D. M. Deaves and R. I. Harris, "A mathematical model of the structure of strong winds". Report No. 76. United Kingdom Construction industry research and information association, 1978. N. J. Cook, "The Deaves and Harris ABL model applied to heterogeneous terrain", J. Wind engineering and industrial aerodynamics, vol. 66(3), pp.197-214, 1997.
- [10] M. L. Ray, A. L. Rogers, and J. G. McGowan, "Analysis of wind shear models and trends in different terrains, University of Massachusetts", Department of Mechanical and Industrial Engineering, Renewable Energy Research Laboratory, 2006.
- [11] B. S. Sharratt and G. Feng, "Windblown dust influenced by conventional and undercutter tillage within the Columbia Plateau, USA", Earth surface processes and landforms, vol. 34(10), pp.1323-1332, 2009.
- [12] Y. Tamura et al., "Profiles of mean wind speeds and vertical turbulence intensities measured at seashore and two inland sites using Doppler sodars", J. Wind engineering and industrial aerodynamics, vol. 95(6), pp.411-427, 2007.
- [13] C. A. Martins, O. L. Moraes, O. C. Acevedo, and G. A. Degrazia, "Turbulence intensity parameters over a very complex terrain", J. Boundary-layer meteorology, vol. 133(1), pp.35-45, 2009.
- [14] A. Perez, M. A. Garcia, M. L. Sanchez, B. de Torre, "Analysis and parameterisation of wind profiles in the low atmosphere", J. Solar Energy 78 (6) 809-821, 2005.
- [15] Indiana Energy Group Report, Tall Towers Wind Study Final Project Report, October 2005.
- [16] P. Giguère, and M. S. Selig, "Design of a tapered and twisted blade for the NREL combined experiment rotor", National renewable energy, NREL/SR-500-26173, 1999.
- [17] M. Moshfeghi, Y. H. Xie, "CFD investigation of effects of wind tunnels walls on flow properties over S809 airfoil", 7th International Symposium on Multiphase Flow, Heat Mass Transfer and Energy Conversion, China, October 2012.

Dynamics of shock oscillation across second throat of a supersonic diffuser under geometry variation

Jintu K James, Muruganandam T M

Abstract— The experimental study on the effect of geometry variation on shock oscillation across second throat of a supersonic wind tunnel is investigated. Experiments were carried out by changing the curvature of the diffuser, from zero curvature to 15mm radius of curvature at the throat and divergence angle of diffuser from 4 degree to 7 degrees.. The stagnation pressure remains constant in all the experiments. The time variation of shock location and pressure downstream of second throat are analyzed. The FFT plots shows that the behavior of shock oscillation is not periodic in all the profiles. The mechanism of this unsteady shock wave dynamics is studied and presented in the form of variation in shock location and pressure amplitude.

Keywords— Schlieren, second throat, shock wave oscillation, supersonic diffuser

I. INTRODUCTION

In supersonic diffusers, depending on the disturbances present upstream or downstream of the diffuser there can be shock waves oscillations in the channel and the position of the normal shock wave decides the start or unstart of the diffuser flow. Therefore it has practical importance to understand the origin and consequence of these oscillations. There are several factors which affect the oscillation such as shock wave-boundary layer interaction, Mach number of the flow, geometry of the section, etc.

The earlier attempts to investigate the shock wave oscillations and its interaction with turbulent boundary layer in two-dimensional transonic flow show that the flow is either attached or undergoes shock induced separation, depending on shock strength [1]. It is observed that in attached flow, due to acoustic waves, the natural frequency of shock oscillation vary inversely with channel length. Analytical work on this behaviour [2] had emphasized mainly on acoustic field and this analysis was based on solving the unsteady Rankine-hugoniot equation, simultaneously considering the shock

motion. This work did not consider the area variation but emphasis is given to the influence of acoustic disturbances from downstream. Kim et al. [3] showed that shock oscillations still appear even if the shock strengths are significantly below the limit of shock induced separation. To investigate the effects of downstream pressure perturbations on shock oscillations in the diverging portion of the diffuser, several experimental and numerical studies have been carried out [4],[5],[6],[7],[8]. They were using a variable geometry second throat and all have reported that the amplitude of the shock oscillation decreases with increasing perturbation frequency. The work done by Ott et al. [6] investigates the behaviour of an oscillating normal shock in a transonic flow. This paper studied the correlation between an oscillating normal shock wave and side wall pressure response in a nozzle and shows that there is no phase shift present.

The study of shock oscillation in diffuser model [9] showed that separation bubble due to post-shock expansion may be the reason for shock oscillation. This study matched well with Sajbens experimental data. The experimental and analytical work [7] on self-excited shock wave oscillations show that the oscillations are governed by the geometrical shape of the diffuser and Mack number in front of the shock wave. Recently, Bruce and Babinsky [10] studied the complex phenomena of shock oscillation in a parallel walled duct. The mechanism by which the shock responds to back pressure variations is to change their relative strength by moving so that their relative mach number matches the pressure jump.

There are some situations where shock oscillations occur across the second throat depending on the operating conditions of the wind tunnel or intake. In such cases it is required to study the behavior of these oscillations. Almost all works mentioned above constrains the shock oscillation either in a diverging duct or in a constant area passage. But very few tried to analyze the shock oscillation across the convergent divergent portion (across the second throat) of the diffuser, [11]. There are several parameters that influence the characteristics of the shock oscillations such as throat radius, throat height, divergence angle of the diffuser etc. This study mainly aims to analyze the effect of change of these

Jintu K James, Research scholar, Dept of Aerospace Engg. IIT Madras, Chennai 600036, India.(e-mail: jintukjames@gmail.com).

Muruganandam T M, Associate professor, Dept of Aerospace Engg. IIT Madras, Chennai 600036, India. (e-mail: tmmuruganandam@gmail.com)

geometrical parameters on the behavior of shock oscillations and looking for what is the statistics of shock location/oscillation and frequency in diffuser flow.

II. EXPERIMENTAL DETAILS

A. Details of wind tunnel facility used

A high pressure operated blow down wind tunnel facility was used for the experiments as shown in Fig1. The flow inlet is connected to the external reservoir and the flow was controlled by adjusting the opening of a precisely adjustable valve. The settling chamber was designed to reduce the fluctuations of stagnation pressure and allow a uniform flow to enter the nozzle geometry, [12]. The settling chamber was provided with a conical flow spreader and three sets of wire meshes of increasing fineness ratio to reduce the disturbances going to the test section.

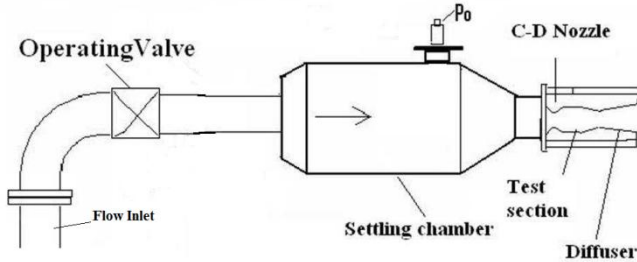


Fig1: The schematic of the experimental facility used and P0 is the piezoresistive transducer.

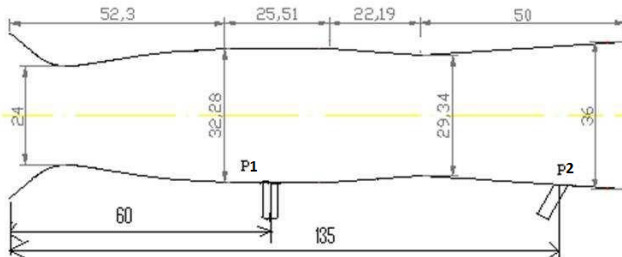


Fig2: Nozzle-diffuser assembly and location of piezoelectric transducers P1 and P2. All dimensions are in mm

The geometry used in the experiments consists of convergent-divergent(c-d) nozzle followed by a c-d diffuser. The nozzle section was designed using MOC to get a Mach number of 1.7 while the diffuser was a simple straight line section as shown in Fig2. The nozzle followed by test section and diffuser were made as an integral piece from an MS block for each of top and bottom wall where as the side walls were made of polycarbonate sheet for optical access. The geometry has a width of 40mm and total length of 150mm including nozzle and diffuser sections.

B. Methodology

The upstream stagnation pressure in the settling chamber is initially increased to a value such that the normal shock is present near the second throat and this pressure is kept constant during the short duration of experiments.

The diffuser flow was visualized by means of Schlieren technique. High speed schlieren images and pressure data were taken simultaneously. A piezoresistive transducer, P0 (GE DRUCK PMP-4110) was used to measure the stagnation pressure in the settling chamber while piezoelectric transducers P1 and P2 (PCB113B27) were mounted on the test section and divergent section were used for transient pressure measurements. The signals from the transducers were acquired by a 16 bit data acquisition system as simultaneous analog input. For the schlieren visualization, a 150 W halogen lamp and a vertical slit were used as a constant point light source. The knife edge was oriented vertically. Instantaneous images were acquired, with a high-speed CMOS camera (RedlakeN4), at sampling rates in the range 2000 FPS to 3500 FPS. The camera frame sync signal was also recorded in the data acquisition to locate the pressure data concurrent with each frame.

III. RESULTS AND DISCUSSION

The experiments were carried out by keeping the stagnation pressure constant and the shock waves made to oscillate across the second throat at that particular pressure. The geometry variation is done by changing the divergence angle and radius of curvature of the second throat of the diffuser, while the area at throat remains the same. Geometries having radius of curvatures zero, 8mm, 12mm and divergence angles of 4, 5, 6, and 7 degrees were analyzed. The geometry which is having zero ROC is the base model and it has a divergence angle of 5 degrees. The stagnation pressure in the settling chamber is increased to 180kPa absolute, to position the shock near the diffuser throat. Since the nozzle area ratio is constant in all the cases, the Mach no in the test section could keep as a constant in all profiles.

The different locations of the normal shock inside the diffuser are shown in Fig3. The vertical lines on the images indicate the location of second throat. The shock is indicated as bright lines on the images and the first image has normal shock positioned upstream of the throat across which the flow is subsonic. While another curved bright region post second throat in the same image shows the existence of another supersonic zone inside the diffuser due to geometric and/or frictional choking of the flow. The normal shock moves downwards and reaches near throat in image 2 and moves further past the throat in image3 and becomes highly oblique in nature. After reaching the maximum downstream position it

moves upstream direction and this oscillation behavior continues.

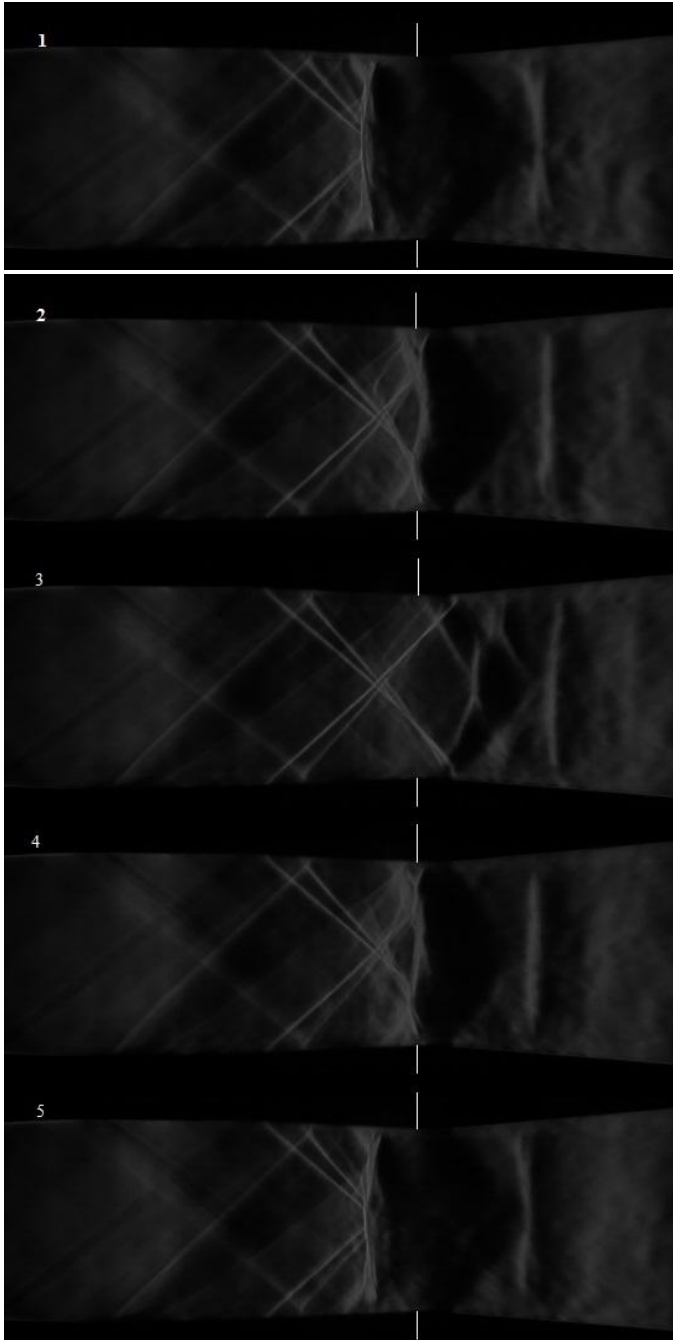


Figure Fig3: Schlieren images of the flow field indicating different locations of shock. The vertical lines marked on the images indicate the location of second throat and the direction of flow is from left to right.

The flow separation occurs at the downstream of the shock and this separation point moves along with the shock in all geometries and the shock train patterns are formed when the starting normal shock wave is in the diverging section.

Time variation of instantaneous shock location across second throat for different geometries is plotted in Fig4. Since the transducer P2 in the diverging section experiences every pressure change due to shock oscillation, pressure data from this transducer was used to plot the FFT and this is shown in Fig5. The geometry which is having 8mm radius of curvature only shows a dominant frequency of 350Hz and having maximum amplitude of oscillation. The data obtained were repeatable and only 8mm ROC profile shows this particular frequency. The disturbances from the exit can propagate to reach the shock and can trigger the shock to oscillate. The separation point can oscillates due to boundary layer instability and hence the shock. But the exact mechanism causing the shock to oscillate periodically in a single geometry of 8mm ROC is not understood completely. The duct resonant frequencies are not matching with the frequency of shock oscillation for this particular case.

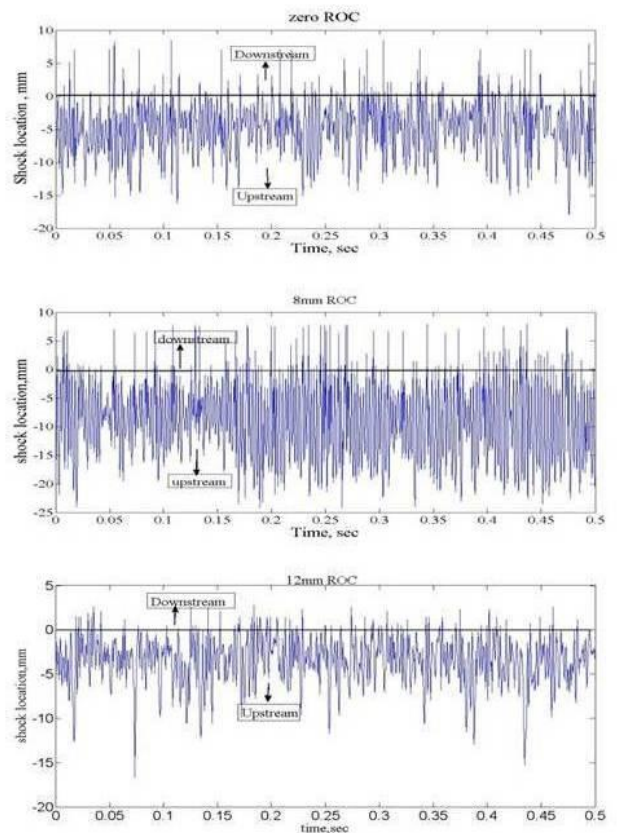


Fig4: Time variation of shock location for different profiles. The horizontal line on shock location curve indicates the location of throat.

There is one possibility exists that the upstream stagnation

pressure fluctuations can cause the shock to oscillate along with the downstream disturbances.

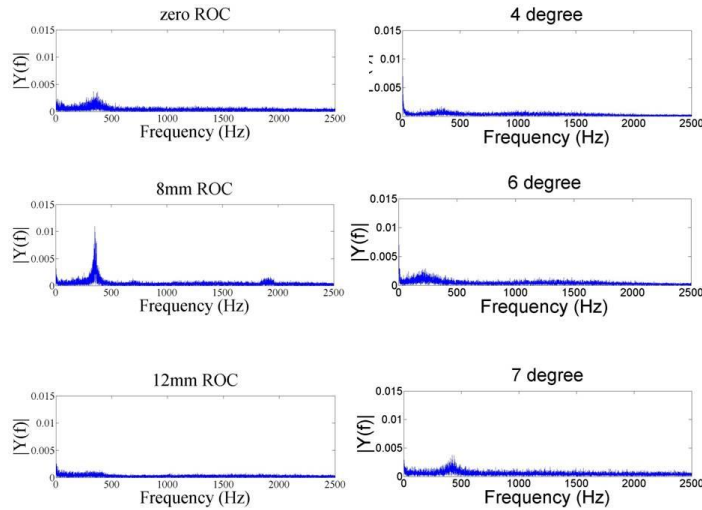


Fig 5: The FFT plots for different geometries. ROC variations and angle variations are represented

To understand the mechanism causing the oscillation, a low disturbance settling chamber was made to analyze the effect of downstream disturbances only. The stagnation pressure data shown in Fig 6 indicates that the settling chamber minimizes the fluctuations reasonably.

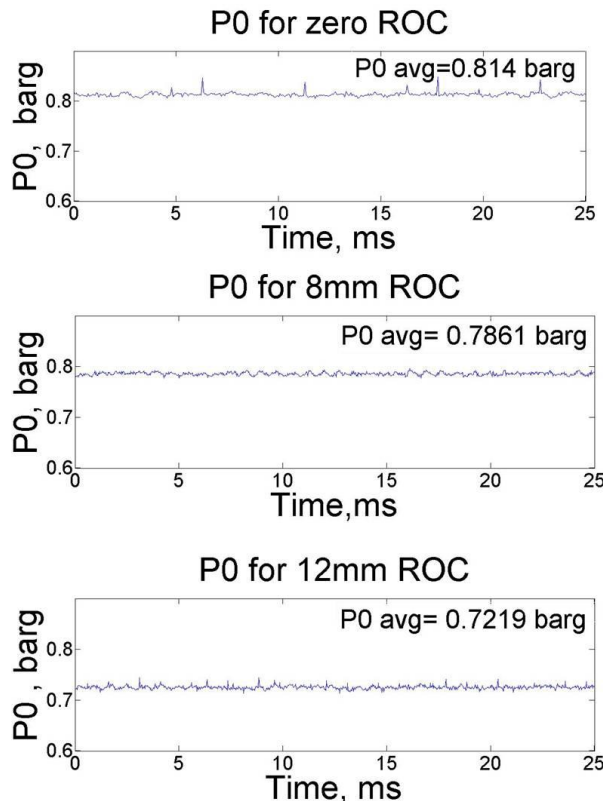


Fig6: Variation stagnation pressure for different profile

The P0 values for different profiles analyzed and it shows that there is no dominant frequency of oscillation and has a very minute fluctuation. So we can assume that the stagnation pressure as constant of having a value P0 avg. The average value of P0 decreases as the radius of curvature increases. The shock experiences less resistance from geometry to push it to divergent section as the ROC increases. Lower values of P0 average indicate that the power required to run the tunnel can be reduced if the ROC is increased.

CONCLUSION

The oscillation characteristics of a normal shock wave in the vicinity of second throat under geometry variation are experimentally investigated. The time variation of shock and the fft of the pressure signals are analyzed from schlieren images and pressure data. The results show that the oscillation characteristics are not periodic in all geometries except 8mm ROC which shows a dominant frequency and the oscillation characteristics are influenced by the geometry variation of diffuser section. The exact mechanism for this particular frequency of oscillation is not understood completely yet it can be due to the boundary layer instability. The average value of stagnation pressure decreases with increase in ROC of diffuser throat.

REFERENCE

- [1] Bogar, T.J., Sajben, M., Kroutil, J. C., 1983. Characteristic frequencies of transonic diffuser flow oscillations. *AIAA Journal* (21)1232-1240.
- [2] Culick, F. E. C. , Rogers, T., 1983. The response of normal shocks in diffusers. *AIAA Journal*. (21)1382–1390.
- [3] Kim, H.D, Matsuo K, Kawagoe S, Kinoshita T, 1991. Flow unsteadiness by weak normal shock wave/turbulent boundary layer interaction in internal flow. *JSME International Journal Series II* 34(4) 457-465
- [4] Sajben, M., Kroutil, J. C., 1981. Effects of initial boundary layer thickness on transonic diffuser flows. *AIAA Journal* (19) 1386–1393.
- [5] Edwards, J. A., Squire, L. C., 1993. An experimental study of the interaction of an unsteady shock with a turbulent boundary layer at mach numbers of 1.3 and 1.5. *Aeronautical Journal* (97) 337–348.
- [6] Ott, P., Bolcs, A., Fransson, T. H., 1995 Experimental and numerical study of the time-dependent pressure response of a

shock wave oscillating in a nozzle. *Journal of Turbomachinery* (117) 106–114.

[8] Bur, R., Benay, R., Galli, A., Berthouze, P., 2005. Experimental and numerical study of forced shock-wave oscillations in a transonic channel. *Journal of Aerospace science and technology* (10) 265-278.

[9] Robinet.J.C. Casalis G., 1999. Shock oscillations in diffuser modeled by selective noise amplification. *AIAA Journal* (37) 453-459

[10] Bruce, P.J.K., Babinsky, H., 2008. Unsteady shock wave dynamics. *Journal of Fluid Mechanics*. (603) 463-473

[11] Abhishek Pateria, Muruganandam, T.M., Shock movement in a supersonic tunnel with increment in pressure. Proceedings of 5th International conference on theoretical applied computational and experimental mechanics (ICTACEM), Dec 27-29, 2010, IIT-Kharagpur, India.

[12] Pope, A., Goin, K.L., 1978. High Speed Wind tunnel Testing, Krieger Pub. Co.

A Study of the Pressure and Potential Distribution by Two Model From Micro Fluidic Devices

Maryam Ghelichkhani

Abstract— Fluid flow in microfluidic channels can be driven by an electric field or pressure gradient or a combined of these "forces". In this paper, the pressure and potential distribution in microfluidic channels of a particular integrated micro fluidic device is investigated and The results obtained by numerical simulation were compared with results obtained by circuit modeling. Circuit modeling can be alternative for numerical.

Keywords- *pressure, potential, full simulation, circuit modelling*

I. INTRODUCTION

Integrated micro fluidic systems with a complex network of fluidic channels are used for chemical and biochemical analysis [1], [2]. These devices offer unique advantages in, reagent mixing, chemical reaction, separation and detection [3]. Micro fluidic devices can reduce reagent consumption, dispersion effects and analysis time. Fluid flow in micro channels can be controlled by applying an electric field and pressure gradient. Important issues that micro fluidic device designers would like to understand are flow rate and pressure distribution and potential distribution within any micro fluidic network [4]. Electro-osmotic flow is driven by electrical field. A typical approach to understand the pressure and potential distribution in the micro channels is to perform two or three dimensional numerical simulations using the partial differential equations which describe micro fluidic transport. Simulation is vastly used in research and industry to develop an accurate design and to reduce time to market period. But circuit models who would like to a useful to micro fluidic designers quickly evaluate new design concepts as they are simplified models, very fast compared to detailed numerical simulators, and yet they are accurate enough to capture the basic physical characteristics and circuit methods are very cheap. A circuit model can be easily integrated into readily available circuit design software; circuit models for micro fluidic devices enable rapid integration of micro fluidic devices with micro mechanical, micro electronic and other components on chip. In this paper, we have compared the pressure and potential distribution in an integrated micro fluidic channel using numerical simulation as well as equivalent circuit modelling. This paper is organized as flows in section 2 electro osmotic flow is described. Circuits models are considered in section 3.

II. ELECTRO OSMOTIC FLOW

When a polar liquid is brought into contact with a glass channel, electric charges are induced in the channel surface. This is due to ionization, ion adsorption or ion dissolution. The surface charges attract charges within liquid near the wall. Ions in the liquid are drawn toward the solid surface thus an Electrical Double Layer (EDL) is formed near the walls. When

electrical potential is applied across the fluid adjacent to the charged surface liquid moves in the direction of the electrical field. This type of flow is known, electro osmotic flow (Fig1).

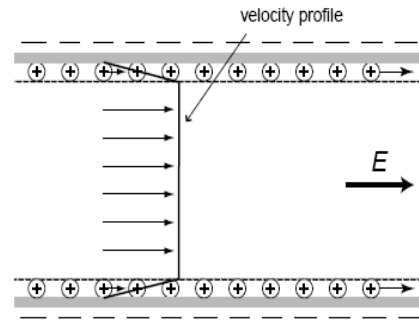


Fig. 1. Velocity profile in electroosmotic flow.

Electro-osmotic flow can be modeled by the Navier-Stokes equations. Forcing term in these equations acts on the ions by the electrical field. The governing equations are the continuity equation (1) and the steady-state momentum equation (2). [4]:

$$\nabla \cdot u = 0 \quad (1)$$

$$(u \cdot \nabla) u = \frac{\mu}{\rho} \nabla^2 u - \frac{1}{\rho} \nabla p + \frac{1}{\rho} F \quad (2)$$

Where u is the velocity vector, μ is the dynamic viscosity, ρ is the density, P is the pressure of the fluid and F is body force vector.

The body force term, F in momentum equation (2) for flow which driven by electro osmotic, is obtained by solving the Poisson-Boltzmann equation [4]:

$$\nabla^2 \psi = \frac{1}{\lambda_D^2} \frac{RT}{F} \sinh\left(\frac{F\psi}{RT}\right) \quad (3)$$

$$F = \varepsilon \nabla \phi \nabla^2 \psi \quad (4)$$

In the Poisson-Boltzmann equation (3), the ψ field induced by the potential on the channel wall (zeta potential) and in equation (4) is obtained the body force term. In equation (3) Here R is the gas constant, T is the temperature and λ_D is the Debye length.

The Debye length is obtained by follow equation [4]:

$$\lambda_D = \left(\frac{\varepsilon RT}{2F^2 c_0} \right)^{\frac{1}{2}} \quad (5)$$

Where ε is the permittivity of the fluid and c_0 is the intrinsic ionic concentration of the fluid when external potential is did not apply to it. If we assume that: the fluid flow is fully developed in the micro fluidic channels and EDL thickness is very small in comparison diameter of channel thus electro kinetic force effect can be induced by a slip velocity in the channel walls. This slip velocity demonstrated by the Helmholtz-Smolochowski equation [5]:

$$u_{slip} = -\frac{\varepsilon \zeta}{\mu} \nabla \phi \quad (6)$$

Where ζ is the zeta potential on the surface of the fluidic channel and $\nabla \phi$ is the potential gradient in the channel. The velocity profile across a capillary slit is defined by follow equation [4]:

$$u_{streamwise} = -\frac{1}{2\mu} \frac{dp}{dx} \left(y^2 - \frac{h^2}{4} \right) + u_{slip} \quad (7)$$

Where x denotes the stream direction of the channel y denotes the transverse direction of the channel and h is the channel depth. By taking the divergence of the momentum equation and applying the continuity condition, obtain the follow equation [4, 5]:

$$\nabla^2 p = \nabla \cdot F - \nabla \cdot (\rho(u \cdot \nabla)u) \quad (8)$$

For regions of channels where fluid flow is fully developed the pressure compute from follow Laplace equation [4]:

$$\nabla^2 P = 0 \quad (9)$$

For regions where the ζ -potential changes on the channel wall, the source term on the right-hand side of equation (8) is not zero. If we assume that the flow is fully developed everywhere except in the regions where the ζ -potential is not uniform, the right-hand side source in equation (8) can estimate by the mass conservation.

III. CIRCUIT MODEL

We used a circuit model for describe the for a two dimensional electro osmotic flow in this section. These models can be used when the flow is driven by a pressure gradient or an electrical field or combined these forces. The circuit model is composed the electrical part and the fluidic part. In electrical part for electro osmotic flow, the potential field due to an applied external potential is computed by solving the Laplace equation [4-6]:

$$\nabla^2 \phi = 0 \quad (10)$$

Where ϕ is potential.

Equation (10) demonstrates, potential dropt linear in simple straight channels (shown in Fig2), thus potential variation can be modeled by linear electrical resistances [4].

This electrical resistance for a simple straight channel is filled by solution is given by the following expression [5]:

$$R = \rho_{sol} \frac{L}{W} \quad (11)$$

Where ρ_{sol} is electrical solution resistivity in the channel, L is the length of the channel, W is the channel width or cross-sectional area of the channel for three dimensional analysis of the channel and R is the electrical resistance of the channel.

For micro fluid device in Figure (2), potential field and pressure in the network is obtained by using the circuit model (Fig3, 4). Circuit model for areas that ζ -potential change from ζ_1 to ζ_2 can be represented by pressure source(Fig2). Pressure source for area E that ζ -potential change from ζ_1 to ζ_2 can be represented by [4]:

$$P_{source} = \frac{(P_E - P_A)h}{L_{AE}} + \frac{(P_E - P_B)h}{L_{EB}} \quad (12)$$

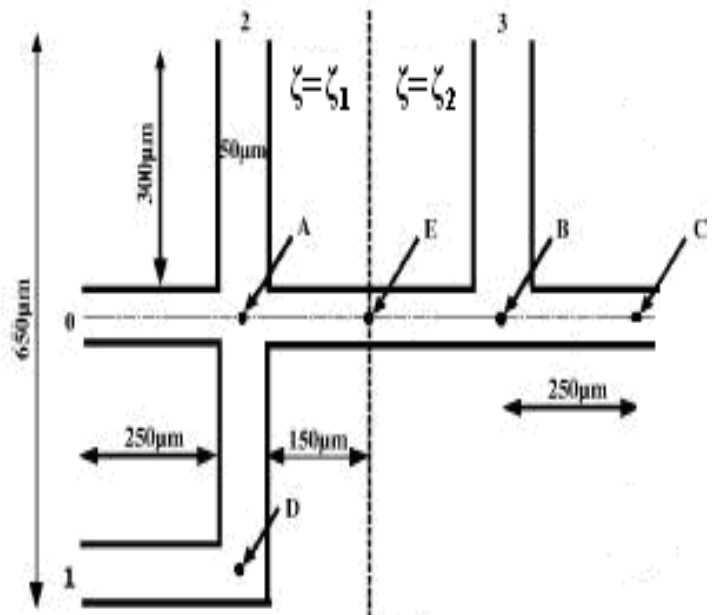


Fig. 2. A typical network for liquid transport. All channels have the same width 50 μm .

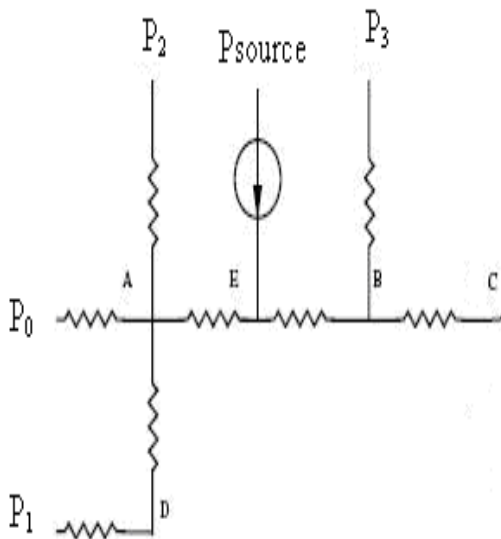


Fig. 3. A circuit model to compute the pressure distribution for micro fluidic network shown in figure2 .

TABLE I. FULL SIMULATION AND CIRCUIT MODEL PRESSURE DISTRIBUTION RESULTS IN MICRO FLUIDIC NETWORK SHOWN IN FIGURE2.

<i>P</i>	<i>Simulation results</i>	<i>Circuit model results</i>
P_A	-0.44452pa	-0.42040pa
P_E	-1.07561pa	-1.0630pa
P_B	-0.54427pa	-0.53366pa
P_D	-0.20100pa	- 0.19689pa

TABLE II. FULL SIMULATION AND CIRCUIT MODEL POTENTIAL DISTRIBUTION RESULTS IN MICRO FLUIDIC NETWORK SHOWN IN FIGURE2.

ϕ	<i>Simulation results</i>	<i>Circuit model results</i>
ϕ_A	1.85.57v	2.85.66v
ϕ_B	3.42.87v	4.43.22v
ϕ_D	5.93.82v	6.93.14v

CONCLUSION

We investigated pressure and potential distribution in an integrated micro fluidic channel using numerical and circuit modelling. In these results are very near. Circuit models who would like to a useful to micro fluidic designers quickly evaluate new design concepts as they are simplified models, very fast compared to detailed numerical simulators.

REFERENCES

- [1] R.Chien and J.w.Parce, Multiport flow-control system for lab-on-chip microfluidic devices, *Fresenius'J.Anal.Chem*,vol.371,pp,2001,106-111.
- [2] R.F.Probstein, *Physiochemical Hydrodynamics*. New York: Wiley,1994.
- [3] P.A.Greenwood and G.M.Greenway, Sample manipulation in micro total analysis systems, *Trends Anal,Chem*,vol.21,pp,2002,726-740.
- [4] R. Qiao and N.R. Aluru, A Compact model for electroosmotic flows in microfluidic devices, 2002,625-634.
- [5] Aavek N.Chatterjee and N.R.Aluru, Combined Circuit/Device Modeling and Simulation of Integrated Microfluidic System,2005.
- [6] Mitchell M ,Qiao R and Aluru N 2000, Meshless analysis of steady-state electro-osmotic transport *J.Microelectromech,Syst*.9435-49.
- [7] Comsol multiphysics software.

In this simulation $\rho=1$, $\mu=0.001$ PaS, $\epsilon=78.4939$ and ζ potential change from -10mv to -30mv.

Pressure and potential distribution results of full simulation by Comsol [7] and circuit model analysis are given in 1 and 2 tables.

Optimum Seismic Isolation System Design for Retrofitting and Upgrading Existing Concrete Bridges

Mohammad AlHamaydeh and Nader Aly

Abstract—In this paper, the performance of an upgraded bridge with natural rubber bearings and viscous fluid dampers is investigated. The impact of varying the isolation and damping parameters is explored to propose a range of feasible combinations. Seismic isolation systems elongate the bridge natural period, and thus different possibilities are explored. The performance of the isolated bridges are obtained from nonlinear time history analyses subject to 22 far-field earthquake ground motion with 1000-years return period. The main parameters investigated are Top of Deck Acceleration Ratio (TDAR) of the isolated bridge to the fixed base bridge, Total Maximum Displacement (D_{TM}) in isolators and Peak Damper Force (P_{DF}). It is concluded that using viscous fluid dampers is more effective in reducing TDAR at shorter natural periods. Moreover, high-damping-coefficient dampers are most effective in controlling the D_{TM} for bridges with longer natural periods. The lowest levels of damper forces P_{DF} are associated with lower damping exponent and coefficient for long-period bridges.

Keywords—Base Isolation, Bridge, Far-Field, Isolators, Viscous Fluid Dampers.

I. INTRODUCTION

Bridges are very crucial elements in any transportation network; they serve as a major link in highways to ease the flow of traffic in different directions. Usually, bridges are designed for 75-years life span. Therefore, it is critical that bridges do not collapse under any type of loading during its lifetime. Static loads are easier to predict when compared to earthquake loads with varying intensity, frequency and probable impact. Enough precautions should be taken when designing bridges to be constructed in areas that are susceptible to frequent seismic hazards. In addition, proposed upgrade alternatives should be available when the bridge location gets re-categorized as a zone with higher seismic hazard during the bridge life. Seismic Isolation [(SI) or Base Isolation (BI)] is one of the upgrade alternatives to promote

better seismic performance. It is not only limited to newly designed bridges, but it also works as a feasible alternative to retrofit and to upgrade existing bridges. Failure of bridges during an extreme event such as ground shaking is not only limited to collapse of the structure, but would also severely disturb the restoration of normal life after the event. BI separates the structure from most of the adverse effects of ground shaking. The isolation system effectively shifts the fundamental period of the structure into significantly lower acceleration region of the response spectrum and dissipates the transmitted energy using inherent damping or added damping devices such as viscous fluid dampers [1]. Additionally, the isolation system aids in dissipating the seismic energy transmitted to the structure from the ground motion.

The deployment of BI systems is very simple when it comes to bridges especially in retrofitting and upgrading. This is due to the fact the bridges are normally separated from their supporting columns by bearings that allow for temperature and other effects. Normal bearings can be simply replaced with base isolating elastomeric bearings or sliding frictional bearings. Several studies were conducted previously to investigate the behavior of base isolated bridges. A study of the base isolation concepts, design standards and comparison of the behavior of seismically isolated bridges with varying damping parameters was done by Mayes, Buckle, Kelly and Jones [2]. Moreover, it included the bidirectional nature of earthquakes and its effects on isolated bridges. Most of the published work regarding the base isolation of bridges focuses on investigating the behavior of base isolated bridges and explore the different isolating and damping devices. Furthermore, many research investigated the soil structure interaction in base isolated bridges and the consequences of excluding it from modeling. The implementation of base isolation in bridges had been very successful in many countries using elastomeric bearings and sliding bearings [1]. Furthermore, the concept of using base isolation in retrofitting existing bridges by replacing the conventional bearings and adding energy dissipaters was studied by some researchers [3], [4] and [5]. They presented many successful examples for base isolation and upgrade of existing bridges. Furthermore, many studies concerned with base isolation for buildings can be found in the literature [6], [7] and [8].

M. AlHamaydeh is a Civil Engineering Associate Professor at the American University of Sharjah, Sharjah, UAE (phone: +9716-515-2647; fax: +9716-515-2979; e-mail: malhamaydeh@aus.edu).

N. Aly is a Civil Engineering Graduate Student at the American University of Sharjah, Sharjah, UAE (phone: +9716-515-2929; fax: +9716-515-2979; e-mail: b00028143@alumni.aus.edu).

In this paper, the upgrade of an existing Concrete bridge using base isolators is investigated. The existing bridge is proposed to be base isolated to lengthen its fundamental period and reduce the expected damage from ground motions. Additionally, viscous fluid dampers will be installed to limit the bridge displacement to within allowable limits. The three main isolation parameters considered, isolator's stiffness (K), damping coefficient (C) and damping exponent (α), are varied to investigate the bridge behavior under different combinations. Three different values for each parameter are used to investigate the resulting behavior of the isolated system. The response of the isolated bridge is investigated using 22 selected far-field earthquake records obtained from PEER NGA Database [9]. The earthquake records are obtained from 14 events with magnitudes M6.5-M7.6 and M7.0 average magnitude. The records are scaled to match a very high hazard level with 1000-years return period. The Top of Deck Acceleration Ratio (TDAR) of the base isolated bridge to the fixed base bridge, Total Maximum Displacement (D_{TM}) in isolators and Peak Damper Force (P_{DF}) are investigated with respect to different combinations of isolation stiffness, damping exponent and damping coefficient. The fixed base bridge refers to the extreme case that represents monolithic bridges and most normal bridges with short piers having a natural period ranging from 0.2-1.2 seconds [1].

II. PROBLEM DESCRIPTION

The chosen concrete bridge is a two span continuous straight bridge. The bridge superstructure is made of post-tensioned concrete box girder and each span is 37m. The substructure of the bridge consists of two abutments and a single pier, all of which are assumed to be fixed at the foundation level. The proposed isolation system consists of 9 natural rubber isolators installed by replacing the conventional rubber bearings, three isolators at each abutment wall and another three at the pier. In addition, at each abutment two dampers are installed one aligned with the span and the other one perpendicular to it. A FEM model is created for the bridge and a nonlinear time-history analysis is performed using CSI Bridge software [10].

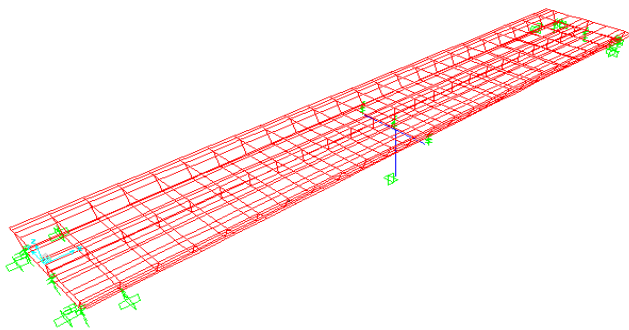


Fig. 1 bridge FEM

Figure 1 shows the FEM of the bridge while Table 1 lists the 22 far-field earthquake records as well some of their parameters.

Table 1: earthquake records [11]

No.	Magnitude	Event Name	Station	PGA (g)	PGV (cm/s)
1	6.7	1994 Northridge	Beverly Hills-Mulhol	0.52	63
2	6.7	1994 Northridge	Canyon Country-WLC	0.48	45
3	7.1	1999 Duzce, Turkey	Bolu	0.82	62
4	7.1	1999 Hector Mine	Hector	0.34	42
5	6.5	1979 Imperial Valley	Delta	0.35	33
6	6.5	1979 Imperial Valley	El Centro Array #11	0.38	42
7	6.9	1995 Kobe, Japan	Nishi-Akashi	0.51	37
8	6.9	1995 Kobe, Japan	Shin-Osaka	0.24	38
9	7.5	1999 Kocaeli, Turkey	Duzce	0.36	59
10	7.5	2000 Kocaeli, Turkey	Arcelik	0.22	40
11	7.3	1992 Landers	Yermo Fire Station	0.24	52
12	7.3	1992 Landers	Cool Water	0.42	42
13	6.9	1989 Loma Prieta	Capitola	0.53	35
14	6.9	1990 Loma Prieta	Gilroy Array #3	0.56	45
15	7.4	1990 Manjil, Iran	Abbar	0.51	54
16	6.5	1987 Superstition Hills	El Centro Imp. Co.	0.36	46
17	6.5	1987 Superstition Hills	Poe Road (temp)	0.45	36
18	7	1992 Cape Mendocino	Rio Dell Overpass	0.55	44
19	7.6	1999 Chi-Chi, Taiwan	CHY101	0.44	115
20	7.6	2000 Chi-Chi, Taiwan	TCU045	0.51	39
21	6.6	1971 San Fernando	LA - Hollywood Stor	0.21	19
22	6.5	1976 Friuli, Italy	Tolmezzo	0.35	31

Figure 2 shows a cross section of the chosen concrete bridge with form work details. However, reinforcement details and post-tensioning cables are not shown since it is out of scope of the paper.

The fixed base bridge has a fundamental period of 0.37sec and for the isolated bridge 2sec, 4sec and 6sec time periods are investigated to cover a wider range of retrofitted bridges. The total number of time history runs is 594 (3 damping exponents* 3 damping coefficients * 3 natural periods * 22 records = 594). The three main parameters that are

investigated under the different combinations are TDAR, D_{TM} and P_{DF} . The purpose of examining 27 different combinations of the isolation and damping parameters is an attempt to come up with an array of practical BI systems that will be feasible for most bridges and can be used in retrofitting or upgrading existing straight bridges.

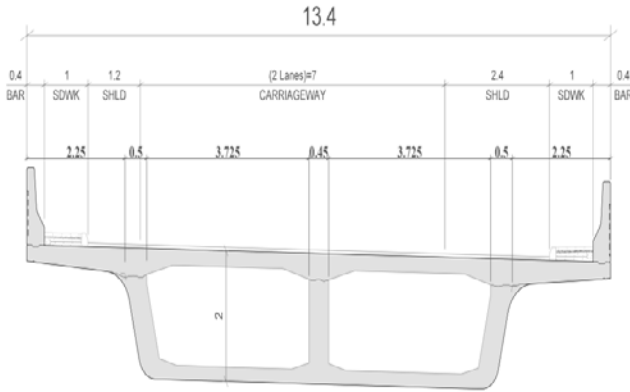


Fig. 2 typical bridge cross section at mid span

III. RESULTS AND DISCUSSION

The envelope of the time-history analysis results for the three main response parameters TDAR, D_{TM} and P_{DF} are obtained through the CSI Bridge commercial software package [10]. The data is processed on excel sheets and combined using the Square Root of the Sum of the Squares (SRSS). The peak response parameters from all of the 22 far-field earthquake records are described using the median of the individual peak response parameters to filter out the record-to-record variations. The peak response parameters TDAR, D_{TM} and P_{DF} are summarized using graphs shown in figure 3 to represent the behavior of the isolated bridge with varying isolation and damping parameters.

Figure 3 shows the relation between the bridge peak response parameters and the varying isolation and damping parameters. For instance, the TDAR of the bridge is always inversely proportional to the fundamental period for the different damping coefficients. Additionally, TDAR reduction rate is lesser for higher natural periods than shorter natural periods. Furthermore, for low damping coefficients the effect of damping exponent is very limited on reducing TDAR and it increases with the increase in natural period. Also, the efficiency of using dampers to control TDAR gets reduced as the natural period is increasing. Table 2 shows TDAR isolation efficiency calculated as the ratio between TDAR with dampers to TDAR without dampers for the different damping levels. Thus, the smaller the ratio, the more efficient the damping system is.

It is indicated that adding viscous fluid dampers to the system enhances the bridge performance by reducing TDAR. However, the enhancement is not uniform, and it is seen that dampers are more effective in reducing TDAR at lower natural periods. TDAR is higher when there are no dampers installed for bridges with short fundamental time period. Nevertheless, at longer fundamental periods and higher damping

coefficients, TDAR for bridges with no dampers are lesser than the damped counterparts. This exhibited phenomenon could be attributed to the fact that bridges have shorter height for the center of mass as compared to buildings; in essence, the isolated bridges' behavior is dominated by Single-Degree-Of-Freedom (SDOF) response and effects. Having such a short height for the center of mass, there is little accelerations transmitted from the isolation plane along the height of the bridge deck. The least TDAR is experienced when the bridge has a relatively long fundamental period, low damping coefficient (175 KN-s/m) and high damping exponent ($\alpha=0.7$). This combination reflects situation where the bridge is very flexible and augmented with modest levels of supplemental damping. Therefore, the optimum combination of isolation system producing the least TDAR (or highest efficiency) is for short-period bridges with high damping levels but with slight nonlinearity in the damper ($T_n=2\text{sec}$, $C=525\text{ kN-s/m}$, $\alpha=0.7$).

Figure 3 displays a clear inverse relation between the D_{TM} and the damping coefficient. However, increasing the damping exponent slightly reduces the efficiency of dampers in decreasing D_{TM} at the expense of the TDAR. Confirming intuition and conventional wisdom, D_{TM} is directly proportional to the bridge fundamental period. However, D_{TM} increase rate is lesser at longer periods. Table 3 shows D_{TM} isolation efficiency calculated as the ratio of D_{TM} with dampers to D_{TM} without dampers. Again, the smaller the ratio, the more efficient the damping system is.

Table 2: TDAR isolation efficiency

T(sec)	C=175 KN-s/m			C=350 KN-s/m			C=525 KN-s/m		
	2	4	6	2	4	6	2	4	6
$\alpha=0$	1	1	1	1	1	1	1	1	1
$\alpha=0.3$	0.76	0.73	0.83	0.70	0.87	1.27	0.69	1.10	1.73
$\alpha=0.7$	0.75	0.70	0.69	0.67	0.70	0.86	0.64	0.78	1.06
$\alpha=1$	0.75	0.71	0.71	0.67	0.72	0.89	0.65	0.81	1.10

In table 3, D_{TM} damping efficiency is consistently less than unity confirming that adding dampers is an effective method for controlling D_{TM} in isolated bridges. Again, dampers are found to be most effective in controlling D_{TM} for flexible structures, especially for high levels of damping. The least D_{TM} occurs when the bridge has the lowest fundamental period coupled with high levels of damping (highly nonlinear devices, i.e. low damping exponent, combined with high damping coefficient). The optimum combination of isolation system producing the least D_{TM} (or highest efficiency) is for long-period bridges with high damping levels and with significant nonlinearity in the damper ($T_n=6\text{sec}$, $C=525\text{ kN-s/m}$, $\alpha=0.3$).

It can be seen that achieving optimum isolation is not a trivial task with several competing and contradictory factors. What constitutes an optimum solution for short-period bridges is not the same as for their long-period counterparts. Furthermore, even for short-period or long-period bridges, the optimum isolation solution has to be achieved by

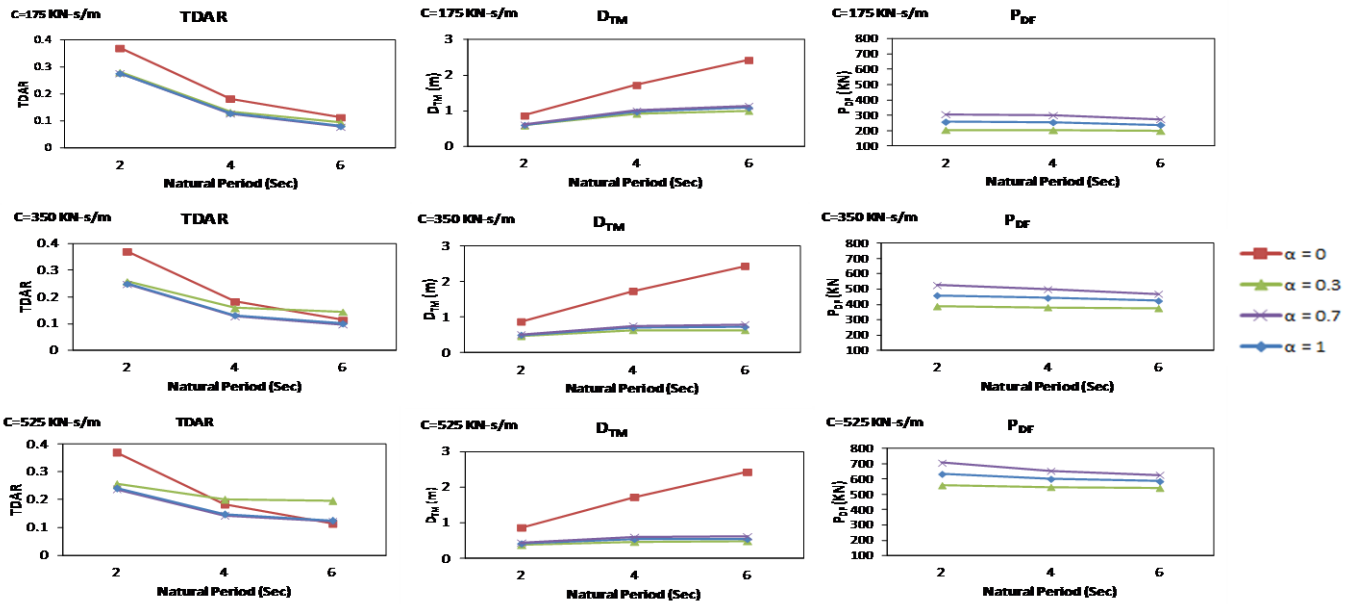


Fig. 3 summary of peak response parameters versus natural period

compromising and reconciliation of all performance parameters amongst themselves. Finally, figure 3 shows that P_{DF} is inversely proportional to the fundamental period of the bridge. The least P_{DF} occurs at longer periods, lowest damping coefficient and lowest damping exponent.

IV. SUMMARY AND CONCLUSION

Upgrading bridges using base isolation is one of the most efficient alternatives to enhance the bridge performance during seismic events with lesser impact on cost compared to replacing the bridge with a new design/construction. Due to the relatively long life span of bridges, the location of the bridge may be re-categorized as a seismically active zone during its life. Therefore, seismic isolation is found to be one of the best solutions. Base Isolation has been a widely used technique in both buildings and bridges in new as well as retrofit designs. This paper investigates the feasibility of upgrading bridges using natural rubber bearings and viscous fluid dampers. Various combinations of the isolation system parameters are studied to produce an array of possible solutions for the upgrade of existing bridges. A nonlinear time-history analysis is done using 22 far-field earthquake records with very high hazard level. The performance of the bridge isolation system is judged based on three main parameters which are TDAR, D_{TM} and P_{DF} . These parameters are investigated for the different combinations of isolation systems. The peak response of each parameter due to individual earthquake records is represented by their median values to screen the record-to-record variation. It is found that TDAR is inversely proportional to the bridge natural period, but its reduction rate is lesser at higher natural periods. The effect of damping exponent on TDAR is very poor at low damping coefficients and gets higher with the increase in damping. Additionally, using dampers is most effective in reducing TDAR for bridges with short natural periods. However, in reducing D_{TM} damping is more effective for longer natural periods. D_{TM} is directly proportional to bridge natural period; nevertheless the increase rate is lower for longer natural periods. Finally P_{DF} is found to be directly proportional to natural period, damping exponent and damping coefficient.

Table 3: D_{TM} isolation efficiency

	C = 175 KN-s/m			C = 350 KN-s/m			C = 525 KN-s/m		
T_n (sec)	2	4	6	2	4	6	2	4	6
$\alpha = 0$	1	1	1	1	1	1	1	1	1
$\alpha = 0.3$	0.68	0.54	0.41	0.54	0.36	0.26	0.43	0.27	0.20
$\alpha = 0.7$	0.70	0.57	0.45	0.57	0.41	0.30	0.49	0.32	0.23
$\alpha = 1$	0.71	0.58	0.47	0.59	0.44	0.33	0.51	0.35	0.26

Due to the finite number of considered retrofit/upgrade solutions, global optimization allowing trade-off can be achieved rather simply. Simple averaging (since both parameters are equally important) of the isolation system efficiency for the TDAR and D_{TM} suggests selecting ($T_n=4$ sec, $C=525$ kN-s/m, $\alpha=0.7$) as the optimum combination with a system efficacy of 0.55. The selected combination reduces the D_{TM} to 32% of the un-damped response (1.73m) yielding a much more manageable level of displacement (0.42m). It is worth noting here that although the selected combination seems like a sound solution, it may not always be a feasible one. Had the selected isolation system without damping required accommodating very large displacement demands, the reduction with dampers would have been unfeasible using the current technologies. In such scenarios, another combination would need to be selected as the optimum. One useful practice, would be to pre-screen the analytical solutions that violate the physical/practical limitations prior to the differentiation process.

ACKNOWLEDGMENT

The authors would like to thank Dr. Husam Najm and Mr. Tejaswi Kuppa of Rutgers University for sharing the structural specifications for the considered bridge. The authors would also like thank Dr. Zia Zafir of Kleinfelder for his efforts in scaling the earthquake records.

REFERENCES

- [1] M. C. Kunde, R. S. Jangid, "Seismic behavior of isolated bridges: A-state-of-the-art review", *Electronic Journal of Structural Engineering*, P. 140-170, 2003.
- [2] R. L. Mayes, I. G. Buckle, T. E. Kelly and L. R. Jones. "AASHTO Seismic isolation design requirements for highway bridges", *Journal of Structural Engineering, ASCE*, Vol. 118, P. 284-304, 1992.
- [3] D. D. Matson, Buckland and P. G. "Experience with seismic retrofit of major bridges", *Proceedings of the National Seismic Conference on Bridges and Highways: "Progress in Research and Practice"*, California, P. 10-13, 1995.
- [4] I. G. Buckle and R. L. Mayes. "The application of seismic isolation to bridges", *Structures Congress '89: Seismic Engineering: Research and Practice, ASCE*, NY, P. 633-642, 1989.
- [5] J. Penzien. "Earthquake engineering for transportation structures-Past, Present and Future", *Earthquake Spectra*, Vol. 17, P. 1-34, 2001.
- [6] A. H. ElSinawi, A. Jhemi, and M. H. AlHamaydeh. "Adaptive seismic isolation of structures using MR-fluid dampers". *5th International Conference on Modeling, Simulation and Applied Optimization (ICMSAO)*, 2013.
- [7] M. H. AlHamaydeh, S. A. Barakat, and F. H. Abed. "Multiple regression modeling of natural rubber seismic-isolation systems with supplemental viscous damping for near-field ground motion". *Journal of Civil Engineering and Management*, 19(5), 665-682, 2013.
- [8] S. M. Hussain, M. H. AlHamaydeh, and N. E. Aly "Jakarta's First Seismic-Isolated Building-A 25 Story Tower". *The 15th World Conference on Earthquake Engineering (15 WCEE)*, 2012.
- [9] PEER, 2010, PEER NGA Database, Pacific Earthquake Engineering Research Centre, University of California, Berkeley, California, Available at <http://peer.berkeley.edu/nga/>.
- [10] Computers and Structures, Inc. (2012). CSI Bridge, Berkeley, California.
- [11] Federal Emergency Management Agency (FEMA). *Quantification of Building Seismic Performance Factors*, FEMA P695, prepared for the Federal Emergency Management Agency, Prepared by the Applied Technology Council, Redwood City, CA, 2009.

A Study of Pressure Distribution Droplets Motion in Convergence-Divergence Shape Microchannel

Maryam Ghelichkhani

Abstract— Micro fluid devices enable the transport nano liters fluids in micro scale channels [1, 2]. Very devices built in this case, for example genome sequencing or using micro droplet as chemical reactors [1-3]. In this paper, we introduce a model of micro channel in order to investigate the dynamics of micro droplets. This model is derived of level set method. Further more, we investigate pressure distribution around micro droplet motion in this convergence-divergence micro channel. This device can be used in many applications for example it can be considered as convergence-divergence digital switch in digital micro fluidic.

Keywords-pressure distribution,micro channel,micro droplet

I. INTRODUCTION

Micro fluidic devices compose micro scale channels that minimize many chemical processes [4]. The Study of droplets, as the most common carriers for bio chemical is very important [4,5]. These channels transport fluids for many applications for example genome sequencing, using micro droplet as chemical reactors, reagent mixing, separation and detection [6]. Understanding droplets motion in micro channels is necessary in order to achieve the follow control needed in practical applications [1]. Pressure distribution is one of important parameters in micro channels. In this paper, we employed two phase level set method for numerical simulation two fluids transport in a convergence-divergence micro channel then investigated pressure distribution in this channel. This micro channel can be employed as a convergence-divergence digital switch. This paper is organized as follows, equation governing presented in section II and numerical simulation described in section III.

II. EQUATION GOVERNING

A. Level set equation

The level set method (sometimes abbreviated as LSM) which purposed by Sussman and et al, is a numerical technique for tracking interfaces and shapes. The advantage of the level set

method is that one can perform numerical computations involving curves and surfaces on a fixed Cartesian grid

without having to parameterize these objects (this is called the Eulerian approach). [7] Also, the level set method makes it very easy to follow shapes that change topology. To describe the droplet motion is necessary to simulate its shape variation and evolution of interface $f(X, t) = 0$ between the water and droplet. Driving this expression in time becomes equation (1) [8]:

$$\frac{\partial f}{\partial t} + U \cdot \nabla f = 0 \tag{1}$$

This method describes the evolution of interface between the two fluids tracing an isopotential cure of level set function ϕ . Zero level set function is demonstrated the interface motion at time. The more dense and more viscous fluids placed in the zone where the level set function is positive ($\phi > 0$) and less dense and less viscous one situated in the domain where the level set function is negative ($\phi < 0$). When the underling velocity field u is specified, the advection step involves the solution of the scalar transport equation for ϕ [3]:

$$\frac{\partial \phi}{\partial t} + U \cdot \nabla \phi = 0 \tag{2}$$

U is the fluid velocity.

B. Navier stock equation

Further more Level set equation, Navier-Stokes equations compose momentum (3) and continuity (4) equations for incompressible fluids are used [8]:

$$\rho \frac{\partial U}{\partial t} - \nabla \cdot [\eta (\nabla U + (\nabla U)^T)] + \rho (U \cdot \nabla) U + \nabla P = F \tag{3}$$

$$\nabla \cdot U = 0 \tag{4}$$

Where p is the pressure, $U = (u, v)^T$ is the velocity, ρ is the density, η is the viscosity and F is a volume force field such as gravity or surface tension

III. NUMERICAL SIMULATION

In this section, we consider the convergence-divergence shape micro channel shown in figure1.



Figure 1. A typical convergence-divergence shape micro fluidic channel.

The first, water with $\eta=1.95 \times 10^{-3}$ Pa.S and velocity 0.0166 m/s enter in this channel from B inlet then droplets with $\eta=6.7 \times 10^{-3}$ Pa.S and velocity =0.0083 m/s enter the channel from A inlet. Surface tension coefficient was considered 5×10^{-3} N/m in this simulation. We investigated droplets motion in length of B-C channel in different step.

In the first step, one droplet is in the first of convergence channel. Schematic of dynamic viscosity fluids in micro channel in this step at $t=0.065$ s shown in figure 2. When the first droplet is received to end of convergence channel, another droplet enters the channel. Dynamic viscosity figure of fluids in this step at $t=0.09$ s shown in figure 3.

Figure 3. Dynamic viscosity schematic of fluids in micro channel figure1 at $t=0.09$ s.

At $t= 0.095$ s, first droplet received in middle of micro channel where width of channel is smaller than over there. Channel is pinched in this zone, because droplets have more viscosity. Dynamic viscosity figure of fluids in this time indicated in figure4. At $t=0.12$ s the first droplet received to the divergence channel, third droplet entered the channel and because second droplet is near the middle of channel, pressure different increase in first and middle end of channel. Dynamic viscosity figure in this case shown in figure5.

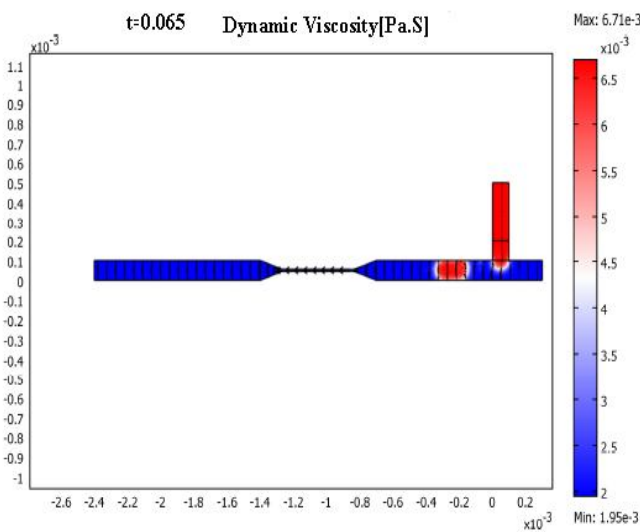


Figure 2. Dynamic viscosity schematic of fluids in micro channel figure 1 at $t=0.065$ s.

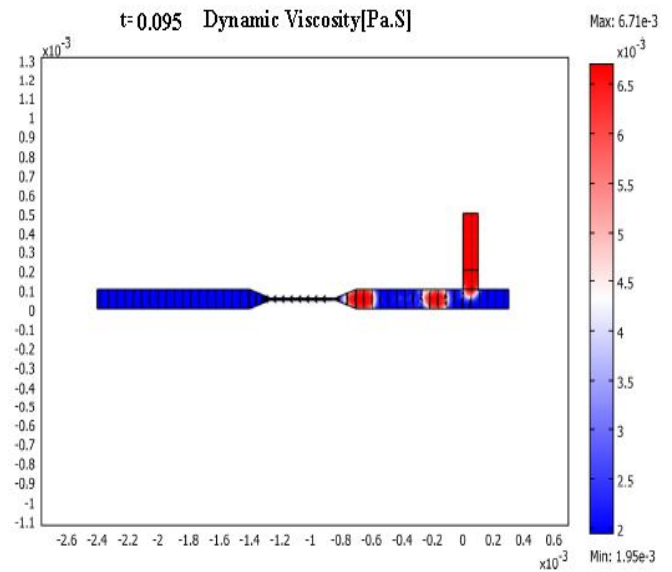


Figure 4. Dynamic viscosity schematic of fluids in micro channel figure1 at $t=0.095$ s.

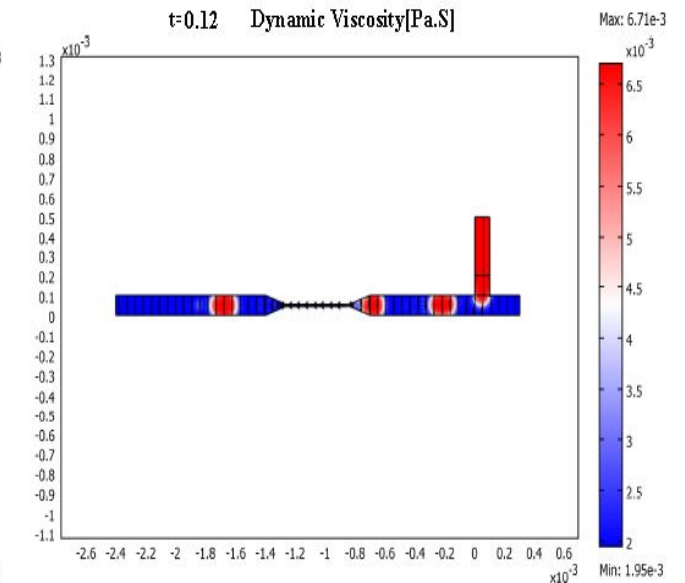
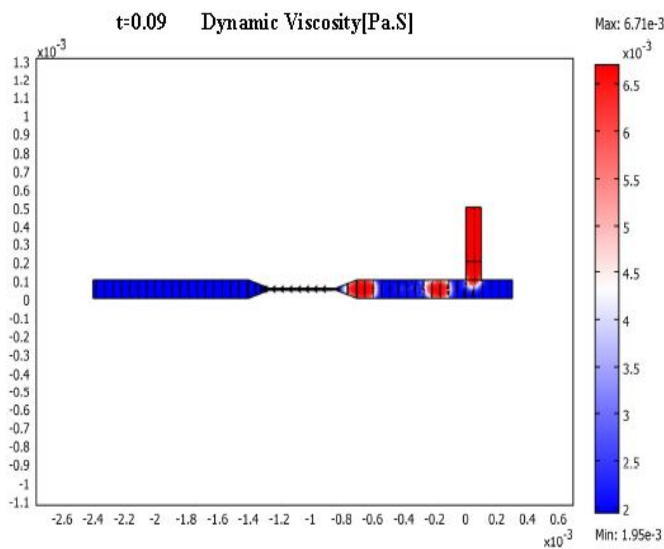


Figure 5. Dynamic viscosity schematic of fluids in micro channel figure1 at $t=0.12s$.

At $t=0.145s$ two droplets are in divergence and convergence channels. Dynamic viscosity figure of fluids in this time shown in figure6. At end of simulation five droplets are in micro channel three droplets are in divergence channel and two droplets are in convergence channel. Dynamic viscosity figure at $t=0.16s$ shown in figure 7. The pressure different in across the convergence channel is constant but in middle of channel where width of channel is smaller than over there, pressure decrease as linear in this zone. And pressure gradient again is constant in divergence channel. If droplet will be in convergence or divergence channel, pressure will be increase in this point. When droplet is in middle of channel with small width, channel pinch in this zone and the pressure different in convergence and divergence channels are very much. This case observe in $t=0.095s$. We can use of this property in digital micro fluidic and consider this channel as digital switch. A comparison of pressure distribution in these times demonstrated in figure 8.

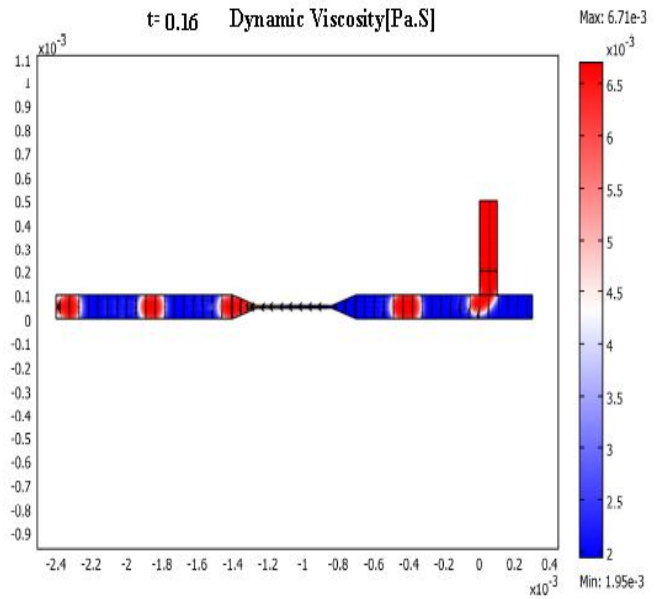


Figure 7. Dynamic viscosity schematic of fluids in micro channel figure1 at $t=0.16s$.

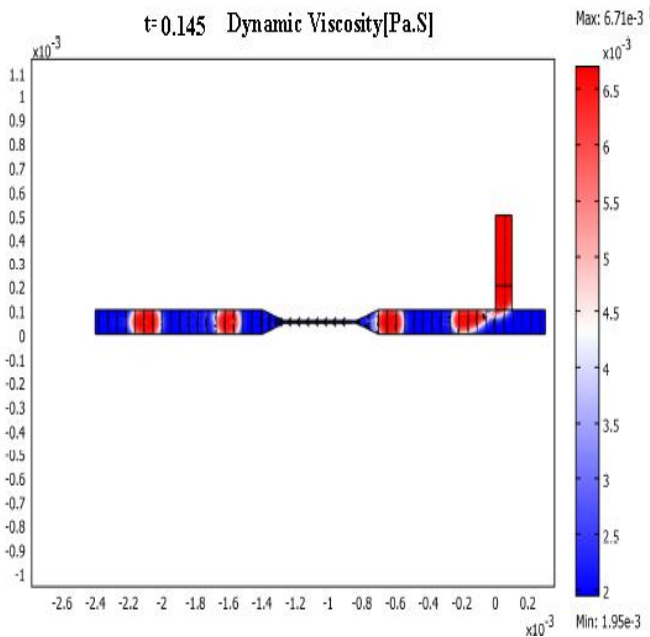


Figure 6. Dynamic viscosity schematic of fluids in micro channel figure1 at $t=0.145s$.

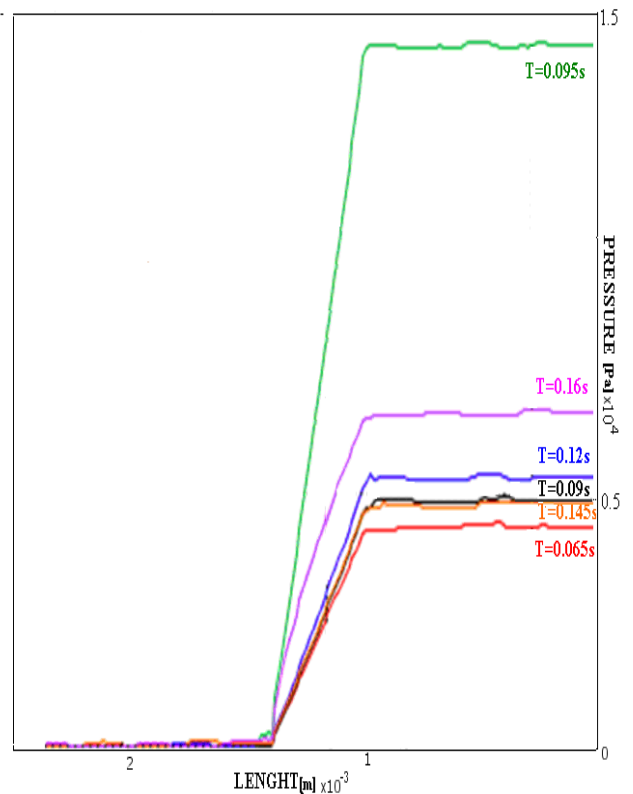


Figure 8. Comparison of pressure gradient along the line B-C in figure1 in various times.

CONCLUSION

We investigated pressure gradient in convergence-divergence shape micro channel when droplets move in this channels. When droplets are received to middle of channel where width of channel is smaller than over there. Pressure different is very much in length of channel. We can use of this property for many applications in digital micro fluidic.

REFERENCES

- [1] Paul Vigneaux, "Droplets in Microchannels with Level Set Method," 2008.
- [2] A. J. deMello. "DNA amplification moves on, Nature," Vol. 422 , 6 March, 2003.
- [3] E. Bovet, L. Preziosi, B. Chiaia, F. Barpi and Politecnico di Torino, "The Level Set Method Applied to Avalanches", 2007.
- [4] Dongdong He, Huaxiong Huang, Yongji Tan a" Numerical simulation for a droplet fission process of electrowetting on dielectric device," 2009.
- [5] R.Chien and J.w.Parce, "Multiport flow-control system for lab-on-chip microfluidic devices," *Resenius J. Anal. Chem.*, Vol. 371, pp. 106-111, 2001.
- [6] P.A.Greenwood and G.M.Greenway, "Sample manipulation in micro total analysis systems," *Trends Anal. Chem.*, vol. 21, pp. 726-740, 2002.
- [7] Osher, S. & J. A. Sethian (1988), "Fronts propagating with curvature-dependent speed: Algorithms based on Hamilton-Jacobi formulations", *J. Comput. Phys.* **79**: 12-49.
- [8] S. Osher and R. Fedkiw. "Level Set Methods and Dynamic Implicit Interfaces," 1st Edition, Applied Mathematical Sciences, Vol. 153, Springer, 2003

Design of Heat Exchanger

Eng. Ahmed Lajili Ali¹, Eng. Abdulmunam Shaban ².

Abstract— This paper has been done to design a heat exchanger to pasteurize milk by steam in a dairy plant. Milk is to flow through a bank of 1.2 cm internal diameter tubes while steam condenses outside the tubes at 1 atm. Milk is to enter the tubes at 4°C, and it is to be heated to 72°C at a rate of 15 L/sec. We did all calculation processes to specify the tube length and the number of tubes, and the pump for the heat exchanger.

Keywords— Exchanger- pasteurize milk- tube length- pump-



I. INTRODUCTION

According to Y. A. Cengel in his book Heat Transfer: a Practical Approach, 2nd ed,

“Heat exchangers are devices that facilitate the exchange of heat between two fluids that are at different temperature while keeping them from mixing with each other. Heat exchangers are commonly used in practice in a wide range of applications, from heating and air-conditioning systems in a household, to chemical processing and power production in large plants. Heat exchangers differ from mixing chambers in that they do not allow the two fluids involved to mix.” (Cengel, 2007)

There are many applications for heat exchanger in industrial field. In food industrial, heat exchanger is being used to transfer heat from hot to cold or vice versa.

Pasteurizing milk is one type of heat exchanger using in food applications. Design calculations are used to evaluate the efficiency of heat exchanger or to design new one for new purpose. By using this method, engineers can determine the rate of heat of both exit fluid cold and hot. Also, it can be used to estimate the power consumption.

Design a new heat exchanger is complicated process that is composed of many aspects. In this paper, we will discuss all the processes that involves in thermal side. Also, we will mention the characteristics of the material that we have picked up to be used in our design of this exchanger.

II. DESIGN CALCULATIONS FOR THE EXCHANGER

In heat exchanger design, the overall surface area of heat exchanger plays role in both inlet and outlet temperatures of product fluid and heating fluid. The flow rate of the fluid is also related to the surface area. Moreover, surface area plays a role in choosing the flow direction and pressure drop. Determining the total surface area, which is composed of tubes diameter, shell diameter and other geometrics, is important in heat exchanger designing.

Heat exchangers are named according to the direction of cold fluid and hot fluid to two kinds, Fig 1. Parallel flow is occurred in devices that the flow of both hot and could flow is moving in the same direction. In this case, usually the outlet temperature of heating fluid is more than the outlet temperature of cold fluid. Counter flow is existed when the cold and hot fluids are moving in the opposite direction of each other. In this case, the outlet temperature of cold fluid is sometimes more than the outlet temperature of heating fluid.

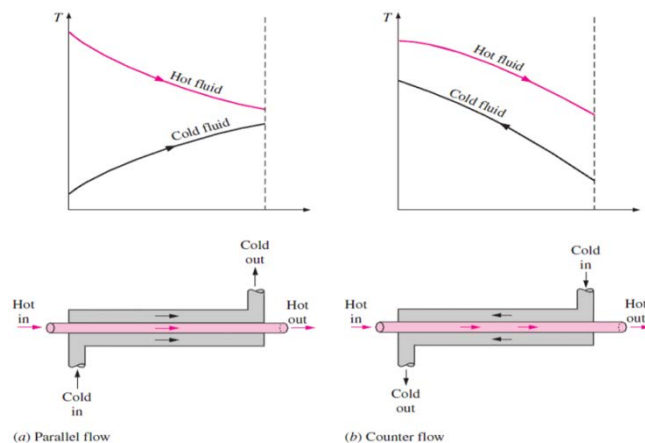


Fig 1, Parallel and counter flow configurations with corresponding temperature profiles (Cengel, 2007)

III. Materials involved

Stainless steel pipe and tubing are used for a variety of reasons: to resist corrosion and oxidation, to resist high temperatures for cleanliness and low maintenance costs, and to maintain the purity of materials which come in contact with stainless. The inherent characteristics of stainless steel tubing permit the design of thin wall piping systems without fear of early failure due to corrosion. The use of fusion welding to join such piping eliminates the need for threading.

Type 304 stainless is the most widely used analysis for general corrosive resistant tubing and pipe applications. It is used in chemical plants, refineries, paper mills, and food processing industries. Type 304 has a maximum carbon

content of 0.08%. It is not recommended to be used in temperature range between 800° F and 1650° F due to carbide precipitation at the grain boundaries which can result in inter-granular corrosion and early failure under certain conditions.

Type 316L as well as 304L is held to a maximum carbon content of 0.03%. This permits its use in welded assemblies without the need of final heat treatment. It is used extensively for pipe assemblies with welded fitting.

Other fields where stainless steel pipe and tubing are used are: aviation, electronics, automotive, cryogenic, marine, air conditioning and heating, medical, food preparation equipment, architectural and textiles.

IV. Calculation Processes

$$T_{in,Milk} = 4\text{ }^{\circ}\text{C}$$

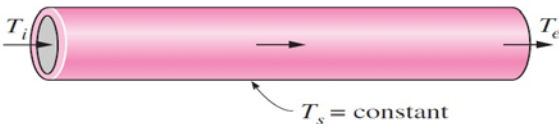
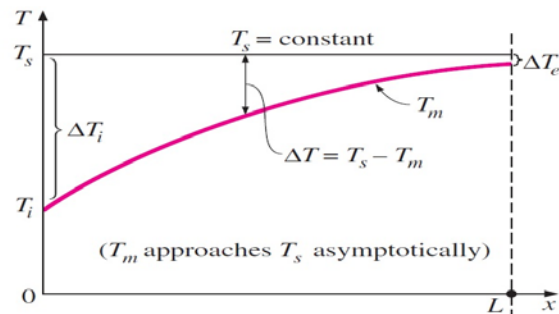
$$T_{out,Milk} = 72\text{ }^{\circ}\text{C}$$

$$\dot{m}_{total} = 15\text{ L/sec}$$

$$d_i = 1.2\text{ cm}$$

$$T_f = \frac{72+4}{2} \gg T_f = 38\text{ }^{\circ}\text{C}$$

We assumed that:



1. The number of tubes is 30 tubes.
2. The properties of milk equal to the water properties.

$$C_p = 4178.5 \frac{\text{J}}{\text{kg}\cdot\text{K}}$$

$$Pr = 4.572$$

$$\rho = 993.7 \frac{\text{kg}}{\text{m}^3}$$

$$K = 0.627 \frac{\text{W}}{\text{m}\cdot\text{K}}$$

$$A_c = \frac{\pi}{4} D_i^2$$

$$A_c = 1.131 \times 10^{-4} \text{ m}^2$$

$$\mu = 0.759 \times 10^{-3} \frac{\text{kg}}{\text{m}\cdot\text{s}}$$

$$\nu = \frac{\mu}{\rho} \text{ "Kinematic viscosity"}$$

$$\nu = 7.638 \times 10^{-7} \frac{\text{m}^2}{\text{s}}$$

$$\dot{Q} = \dot{m} C_p (T_{C,out} - T_{C,in})$$

From table

$$1\text{ kg/sec} = 1.0753\text{ liter/sec}$$

$$\dot{m}_{30\text{ tubes}} = \frac{15}{1.0753} = 13.95\text{ kg/sec}$$

$$\dot{m}_{\text{one tube}} = \frac{13.95}{30} = 0.465\text{ kg/sec}$$

$$\dot{Q} = 0.465 \frac{\text{kg}}{\text{s}} \times 4178.5 \frac{\text{J}}{\text{kg}\cdot\text{K}} (72\text{ }^{\circ}\text{C} - 4\text{ }^{\circ}\text{C})$$

$$\dot{Q} = 132.124\text{ Kw}$$

$$\dot{m} = \rho V_{avg} A_c$$

$$V_{avg} = \frac{\dot{m}}{\rho \cdot A_c} \gg V_{avg} = \frac{0.465}{993.7 \times 1.131 \times 10^{-4}}$$

$$V_{avg} = 4.138 \frac{\text{m}}{\text{s}}$$

$$Re = \frac{V_{avg} \cdot D_i}{\nu} \gg Re = \frac{4.138 \times 1.2 \times 10^{-2}}{7.638 \times 10^{-7}}$$

$$Re = 65011.78 \gg Re > 10,000$$

Since Reynolds number is more than 10,000, the flow is TURBULENT.

Nusslet Number is:

$$Nu = 0.023 Re^{0.8} Pr^n \gg$$

$$Nu = 0.023 (65011.78)^{0.8} (4.572)^{0.4} \gg \text{for heating, } n \text{ is } 0.4$$

$$Nu = 299.34$$

From the equation $Nu = \frac{h_i \cdot D_i}{k}$ then,

$$h_i = \frac{Nu \cdot K}{D_i} \gg h_i = \frac{299.34 \times 0.627}{1.2 \times 10^{-2}}$$

$$h_i = 15640.515 \frac{W}{m^2 \cdot K}$$

From the equation, $Q = h A_s \Delta T_{lm} \gg A_{s, \text{one tube}} = \frac{Q}{h \Delta T_{lm}}$

$$\Delta T_s = T_s - T_{milk \text{ out}} \gg \Delta T_s = 100 \text{ }^\circ\text{C} - 72 \text{ }^\circ\text{C} = 28$$

$$\Delta T_i = T_s - T_{milk \text{ in}} \gg \Delta T_i = 100 \text{ }^\circ\text{C} - 4.0 \text{ }^\circ\text{C} = 96$$

$$\Delta T_{lm} = \frac{\Delta T_s - \Delta T_i}{\ln(\Delta T_s / \Delta T_i)} \gg \Delta T_{lm} = \frac{28 - 96}{\ln(28/96)}$$

$$\Delta T_{lm} = 55.188$$

$$A_{s, \text{one tube}} = \frac{Q}{h \Delta T_{lm}} \gg A_s = \frac{192124.17}{15640.515 \times 55.188}$$

$$A_s = 0.153 \text{ m}^2$$

From the equation, $A_s = \pi n D_i L$ where $n=1$

$$L_{\text{one tube}} = \frac{A_s}{\pi n D_i} \gg L = \frac{0.153}{\pi \times 1.2 \times 10^{-2}}$$

$$L = 4.058 \text{ m}$$

The friction factor is:

$$f = 0.184 Re^{-0.2} \gg f = 0.184 (65011.78)^{-0.2} \gg$$

$$f = 0.02$$

$$\dot{W} = \dot{V} \Delta P$$

$$\Delta P = f \frac{L}{D} \cdot \frac{\rho v_m^2}{2} \gg \Delta P = 0.02 \frac{4.058}{1.2 \times 10^{-2}} \cdot \frac{999.7 (4.138)^2}{2}$$

$$\Delta P = 57539.63$$

$$\dot{V} = V_m \cdot A_c \cdot n \gg \dot{V} = 4.138 \times 1.131 \times 10^{-4} \times 30$$

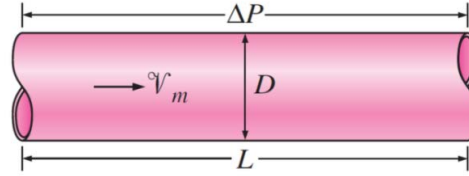
$$\dot{V} = 0.014 \frac{m^3}{s}$$

$$\dot{W} = \dot{V} \Delta P \gg \dot{W} = 0.014 \times 57539.63$$

$$\dot{W} = 805.554 \text{ W}$$

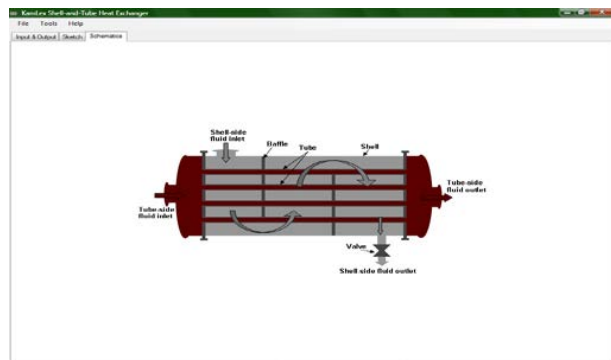
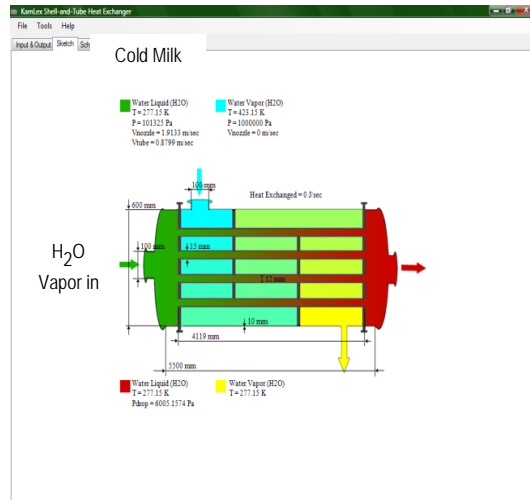
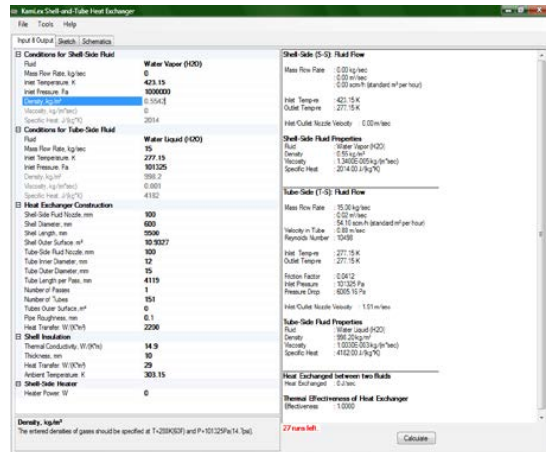
The power of pump is $W/745.7$ (Hp)

The power of pump is 1.08 hp



$$\text{Pressure drop: } \Delta P = f \frac{L}{D} \rho v_m^2$$

V. Calculate the Size of Heat Exchanger



VI. Conclusion

The calculation of thermal design assistance in the design and operation efficiency of heat exchangers. Is usually used routinely LMTD method to estimate the changes in temperature in the fluid and the size of heat exchangers. The method is based on the assumption that the properties of liquids LMTD constant along the heat exchanger (but we did not use LMTD due to lack of knowledge steam temperature in/ out of our system). To overcome these assumptions, the design calculations must be performed using computational techniques. Estimated coefficient of heat transfer surface could be the most difficult design because of its dependence on the flow of fluid and thermal properties, and flow conditions and heat exchanger engineering, and surface roughness. Can modern tools such as computational fluid dynamics to help determine the values of surface heat transfer coefficient.

For n tubes	
Q=	142069
tubes # =	30
V rate (l/s) =	15
mass flow rate (kg/s)	0.5
Ac (m2)	0.000113097
V ave =	8.897789051
Re # =	139792.4438
Nu # =	552.2774139
h (W/m2 . K) =	28856.49487
As (m2) =	0.089209497
L (m) =	2.366355403
f=	0.017207631
DP=	133477.8842
Volume rate (m3/s) =	0.030189487
W (W) =	4029.628853
Power of Pump (hp) =	5.403820374

VII. NOMENCLATURE

- A area of heat exchange surface (m²)
- Cp specific heat of fluid (J/kg _C)
- F correction factor (dimensionless)
- H surface heat transfer coefficient (W/m² K)
- K thermal conductivity (W/m K)
- L length of a cylindrical tube (m)
- LMTD log mean temperature difference (_C)
- \dot{m} mass flow rate (kg/sec)
- Q heat flow rate (W)
- Re Reynolds number (dimensionless)
- Pr Prandtl number (dimensionless)
- Rt total thermal resistance of heat exchange surface (K/W)
- Rf fouling factor (m² K/W)
- T temperature (Celsius or Kelvin)
- ΔT_{lm} log mean temperature difference
- U overall heat transfer coefficient (W/m² K)

IX. References

1. Bell, D., & Mueller, D. (2001). Wolverine Engineering Data Book II.
2. Cengel, Y. A. (2007). *Heat and Mass Transfer – a Practical Approach, 3rd Edition*. McGraw-Hill.
3. Singh, P. P. (2007). Thermal Design of Heat Exchangers. University of Idaho, Moscow, Idaho, U.S.A.

VIII. Microsoft Excel Calculations

The Microsoft Excel used to make formats that can help in calculation in this design.

Authors Index

Abdelhadi, B.	97	Marques, H. C.	68
Abu-Hamdeh, N. H.	107	Matei, P. G.	86
Aichouni, M.	49	Maximov, Yu. V.	116
Al Hamaydeh, M.	135	Meslem, A.	60
Ali, A. L.	144	Mihaila-Andres, M.	86
Aly, N.	135	Mokrejš, P.	55
Askarova, A. S.	116	Montagné, B.	60
Beketaeva, M. T.	116	Moshfeghi, M.	121
Bekmukhamet, A.	116	Muruganandam, T. M.	127
Bolegenova, S. A.	116	Nguyen, M. T.	112
Bragança, P.	60	Oliveira, R. F.	68
Charvátová, H.	55	Ospanova, Sh.	116
Dhont, J. K. G.	42	Phan, D. T.	112
Djedid, T.	97	Retiel, N.	49
Drga, R.	55	Rotaru, C.	86
Edu, R. I.	86	Said, B. O.	49
Ghelichkhani, M.	132, 140	Seo, J.-M.	75
Han, S. G.	92	Shaban, A.	144
Hur, N.	121	Shateyi, S.	102
James, J. K.	127	Shim, J.-H.	92
Janáčková, D.	55	Shin, Y. I.	92
Jung, I. S.	75	Sodjavi, K.	60
Kang, K.	42	Sohrab, S. H.	19
Kim, J.-H.	75	Song, C. K.	92
Kiselev, A. B.	38	Suh, J. S.	92
Kolomazník, K.	55	Teixeira, J. C.	68
Kristiawan, M.	60	Teixeira, S. F.	68
Lee, S.-W.	112	Vašek, V.	55
Maciel, E. S. G.	79	Yoon, C. H.	92